National Technical University of Athens
School of Mechanical Engineering
Department of Mechanical Design and Automatic Control
Vehicles Laboratory

Optimization of vehicle dynamic behavior

PhD Dissertation

submitted to the School of Mechanical Engineering
of the National Technical University of Athens

for the degree of
Doctor of Philosophy in Engineering of N.T.U.A.

by
Georgios Papaioannou
Mechanical Engineer of NTUA

supervised by
Dr. Dimitrios V. Koulocheris
Assistant Professor of NTUA

Athens, 2019

National Technical University of Athens
School of Mechanical Engineering
Department of Mechanical Design and Automatic Control
Vehicles Laboratory

Optimization of vehicle dynamic behavior

A dissertation submitted to the School of Mechanical Engineering
of the National Technical University of Athens

by

Georgios Papaioannou
Mechanical Engineer of NTUA

Advisory Committee

Assistant Professor Dr. Dimitrios Koulocheris	Professor Dr. Ioannis Antoniadis	Professor Dr. Christofer Provatidis

---

Examination Committee

Assistant Professor Dr. Dimitrios Koulocheris	Professor Dr. Ioannis Antoniadis	Professor Dr. Christopher Provatidis
Associate Professor Dr. Leonidas Alexopoulos	Professor Dr. Athanasios Michailidis	Professor Dr. Dimitrios Manolakos

Assistant Professor
Dr. Vasileios Spitas

Athens, 2019

National Technical University of Athens
School of Mechanical Engineering
Department of Mechanical Design and Automatic Control
Vehicles Laboratory

Abstract

The current thesis focuses on the optimization of vehicle and seat suspension systems. A vehicle suspension system cannot eliminate the compromise between the parts of the most prominent conflict in automotive industry, i.e. the passenger's ride comfort and the vehicle's stability. However, they are able to combine the above-mentioned parts optimally. Considering the importance of a good suspension design, in this thesis, its optimization is studied extensively. Firstly, the most common mathematical models for simulation of vehicle dynamics are compared and investigated in order to conclude to the most appropriate for our research. Afterwards, an assessment of the optimization procedure in single and multiple objective optimization problems is conducted with respect to the efficiency of both the objective functions and the optimization algorithms. Then, an approach for handling the objective functions in multi-objective optimization problems is presented in order to minimize their number and save computational time. The research for a high quality suspension system included also the study of semi-active suspensions and resulted in the development of a novel distribution-based control strategy (CDF) for skyhook control algorithms . Later, the conclusions regarding the optimization procedure are applied to various semi-active control algorithms, which also adopt the novel control strategy, in order to find their optimum design solution. However, the optimum design of a vehicle suspension system is not the only prerequisite for ride comfort. Seat suspension systems, are considered important and necessary so as to further isolate the passengers from the adverse effects of their exposure to vibration. In this respect, the modeling and the optimization of seat suspension systems is studied in this thesis. More specifically, a novel isolator with embedded negative stiffness elements (KDamper), which has proven efficient in other applications, is applied in a seat suspension and is benchmarked against the most common isolators in seat design, conducting an extensive dynamic analysis.

To sum up, in respect with the above, this thesis is organized as follows:

The **first chapter** discusses and reviews the literature regarding the four areas, where this thesis emphasized: (a) the mathematical models for the simulation of vehicle dynamics, (b) the semi-active suspensions, (c) the optimization of both passive and semi-active suspension systems and (d) the modeling and the optimization of seat suspensions. More specifically, the current chapter presents the evolutionary process of the research and exposes the technological attempts, perspectives and limitations resulted by various researchers working in the above-mentioned subjects.

The **second chapter** illustrates all the mathematical models used in this thesis, in order to study the dynamic behavior of the vehicle. Also, the equations of linear and nonlinear suspension systems are presented along with the control algorithms of semi-active suspension systems. Then, the vibration isolators applied to seat suspensions, in this thesis, in addition with a passenger model are described and their governing equations are presented. In order to assess the vehicle performance and the seat discomfort, the ride comfort and important aspects of suspension design are quantified and displayed. Last but not least, the modeling of discrete and continuous road irregularities is discussed in order to test the vehicle and the seat response under different conditions.

The **third chapter** illustrates a comparative work regarding the accuracy of vehicle models, and investigates if there is need for additional complexity, either by using a model with more degrees of freedom or by adding more elements in the one selected (anti-roll bars, tire dampers etc.). Thus, four vehicle models with various configurations are compared in terms of accuracy with respect to different performance metrics. More specifically, both passive and semi active suspensions are employed to the models, while the effect of adding anti-roll bars and tire dampers is also investigated. The transient behavior of the suspension system and the overall vehicle performance are assessed in terms of ride comfort, vehicle handling and road holding using different road excitation.

The **fourth chapter** presents a novel distribution-based skyhook (SH) control strategy of semi-active vehicle suspensions. The novelty of this strategy lies upon the use of an appropriate threshold in the control algorithm's operational conditions. More specifically, the proposed strategy quantifies the severity of the operational conditions and controls the damper's state based on their magnitude and not based on their sign. The value of the threshold depends on the induced vibrations by the road profile, but not from class. The strategy is applied to two SH control algorithms and is tested by using a quarter car model excited by four different road excitation. Additionally, a sensitivity analysis for various threshold values is performed for all the random road profiles, investigating the impact of adopting CDF strategy to various performance metrics.

The **fifth chapter** investigates the optimization procedure of suspension systems. More specifically, not only the efficiency of different optimization methods is studied but also the efficiency of various fitness and objective functions. In order to investigate thoroughly the optimization procedure, both single (SOO) and multi-objective optimization (MOO) approaches have been adopted. The single objective approach offers a limited insight in the suspension optimization problem but due to its simplicity it is often preferred over the more complex and time consuming multi-objective approach.

A simple multi-objective dealing strategy, known as pseudo-MOO techniques, is used in this thesis and suggests the combination of multiple objective functions using weighting factors. Also, three (3) optimization algorithms are used (Genetic Algorithms, Gradient Based and a hybridization of them) for the optimization of the five (5) most common objective functions in the literature, which follow SOO and pseudo-MOO approaches. The results are compared using figures illustrating the relation between the objectives, tables displaying the optimal design variables and important performance metrics regarding the dynamic behavior of the vehicle. Also, a benchmark against all the solutions is illustrated.

The **sixth chapter** focus on an approach of minimizing the computational time needed for the Pareto method, allowing the GAs to be attractive again in the optimization of suspension systems. Researchers sometimes end up using more than one objective function representing the same requirement and the dimension of the optimization problem grows. Thus, the optimization procedure becomes very quickly ineffective and the merits of the GAs are put aside because of the increased computational time of the simulations. Applying this approach, this thesis proves that the increasing use of objective functions, which depict the same requirement, doesn't help the optimizer to converge to more "optimal" solutions. In order to prove the above, at first, four SOO problems using the most common functions are presented (Part A) and a sorting algorithm is implemented in order to obtain the optimum solution among them. Afterwards, this thesis presents an approach for handling the objective functions, where they are divided in main and supplementary ones (Part B). The main ones (3) are introduced in the multi-objective genetic algorithm (MOGA), while the supplementary ones (3) are introduced in the sorting algorithm (KE) in order to rank the Pareto alternatives and vet the optimum solution. Afterwards, the six objective functions, the three main and the three supplementary of Part B, are introduced to the MOGA (Part C) and then they resulting solutions of the Pareto front are implemented in the sorting algorithm. The optimum solutions of the three parts are compared in terms of the objectives, the design variables and important metrics indicating the vehicle performance.

The **seventh chapter** investigates the optimization of semi-active suspension systems operating with various skyhook (SH) control algorithms. In addition, the novel distribution-based control strategy (CDF) proposed in this thesis is applied to them. In contrast to the literature that focus mainly on ride comfort and road holding, in this thesis we investigate the design of semi-active suspensions with respect to more performance aspects. More specifically, apart from ride comfort and road holding, the trade-off between the dissipated energy and the vibration control performance is considered. Furthermore, the chatter in the response of the vehicle is used as a design criterion. However, in order to consider all these objectives without costing computational time in the optimization procedure, the approach based on KEMOGA algorithm is applied, as described in Chapter 7. Firstly, the vehicle model is optimized with respect to ride comfort and road holding using a multi-objective genetic algorithm (MOGA). Each of these two objectives is represented by a single performance index, considering the outcomes of Chapter 6. Then, a sorting algorithm (KE) is applied so as to seek the optimum solution among the alternatives from MOGA considering the extra objectives.

The **eighth chapter** illustrates the application of a novel isolator (KDamper) in seat suspensions and its benchmark against four established isolators in seat design. The isolators are optimized using MOO methods (Pareto) and then their pareto fronts are compared. The optimum solutions occur for the excitation of the isolators with the response of the sprung mass of a vehicle, when it drives over random road profiles of different classes. Furthermore, an extensive dynamics analysis of the isolators is conducted. Three types of analysis are used for comparing the models and extracting conclusions for the levels of the isolation, the adaptability and the universality of the models in different excitations corresponding to different road classes and in different seated passengers. Moreover, three solutions of the Pareto Front of each model are selected according to the Pareto Theory, and the seat to head transmissibility of each is investigated.

In the **ninth chapter**, conclusions are summed up and suggestions for further work are presented.

To my girlfriend, my parents, my sister and her partner,
five chapters whose contribution to this thesis
is above any reference.

Acknowledgments

First and foremost, I would like to thank my supervisor Assist. Prof. Dr.-Ing Dimitrios Koulocheris for giving me the opportunity to pursue a PhD in Vehicles Dynamics, and extend a collaboration that started in 2013 for the purpose of my Diploma Thesis. I am grateful for his faith in me and the freedom to take initiatives regarding my research. His encouragement and support to participate in many international conferences offered me important experience. Thank you for helping me improve as a researcher.

Furthermore, I would like to thank Prof. Dr.-Ing Ioannis Antoniadis, member of my consultative committee, for his sincere willingness to work with me and our meetings. Thank you for giving me a different research perspective.

I also want to thank Prof. Dr.-Ing Christopher Provatidis, member of my consultative committee, for the feedback and support. In addition, I would like to thank Accos. Prof. Dr.-Ing Leonidas Alexopoulos, Prof. Dr.-Ing Dimitrios Manolakos, Prof. Dr.-Ing. Athanasios Michailidis and Dr.-Ing. Assist. Prof. Vasileios Spitas for being the examination committee of my PhD.

I would also like to thank all the members of Vehicles Laboratory for their help, but mostly Mr. Dionysis Asvestas for our early-morning discussions and his technical support all these years, Mr. Kostas Fouskas for welcoming me in M005 six years ago and helping me settle in and Dr.-Ing Clio Vossou for her company in M005.

A special thanks to Dr.-Ing Efstathios Velenis, Senior Lecturer at Cranfield University, because my 4-month Erasmus+ visit there was a motivating research experience and I learned a lot under his guidance.

A big thanks to my friends but mostly to Giorgos, Nikos and Vardis, for being there even when I was choosing to study for my PhD rather than go out with them. Thank you for your support, even if it was from Skype.

Last but not least, there are five people who were always there. Each one in his/her way and all together supported me in difficult times, putting sometimes their needs aside. The least I could do is to dedicate to them this PhD.

Smaragda, Mom and Dad, Katerina and Giorgos thank you for everything.

Georgios Papaioannou
Athens, 14^{th} February 2019

Part of the current PhD dissertation was funded by E.L.K.E. of N.T.U.A .

Contents

List of Figures

List of Tables

CHAPTER 1

Introduction

The ride comfort [1] is related to the passenger's perception of the moving vehicle's environment, while road holding is the degree to which a car maintains contact with the road surface in various types of directional changes. When the vehicle is employed with a high quality suspension system or it drives through smooth roads, the typical magnitude of the vibration entering the seat is low, whereas when it lacks of good suspension or drive over off-road ride, the seat is exposed to high vibration magnitudes. Therefore, the use of both vehicle and seat suspension systems in a vehicle are needed so as to to isolate the passengers from the adverse effects of their exposure to vibration [4, 18].

Regarding the vehicle suspensions [19], the passenger's ride comfort and the vehicle stability [20] are the parts of the most prominent conflict in the automotive industry . A good design for a suspension system cannot eliminate the compromise between ride comfort and vehicle stability, but it can combine them optimally. Thus, the optimization of suspension systems is discussed extensively in the literature, where different algorithms, methods and approaches are proposed in order to obtain the optimum design solution [21–27]. Also, various suspension systems have been proposed and they are classified by the way they are controlled in three categories: passive [28–31], semi-active [32–35] and active [36–40]. In contrast to the restricted use of active suspensions [41–44], semi-active ones have been used commercially providing many of the advantages of fully active systems while incurring less cost and being less complex in design. Since 1970s, semi-active suspensions have received much more attention and the research in their field follows two main mainstreams. The first one focuses on the study of new technologies for the actuation of damping in semi-active suspensions (like electro-hydraulic, electro-rheological and magnetorheological damper), with representative examples being

the works of Probakar et al. [45, 46] and Ahmadian et al. [47–49]. The second mainstream, in which we have focused also in this thesis, studies the design of semi-active control algorithms [50, 51]. The design of an algorithm for changing the damping ratio is a very interesting opportunity for a suspension designer so as to improve vehicle's suspension performance, and it is highly challenging when these changes could happen every 5 milliseconds. Therefore, the optimization of them has been discussed extensively in the literature [17, 50, 51].

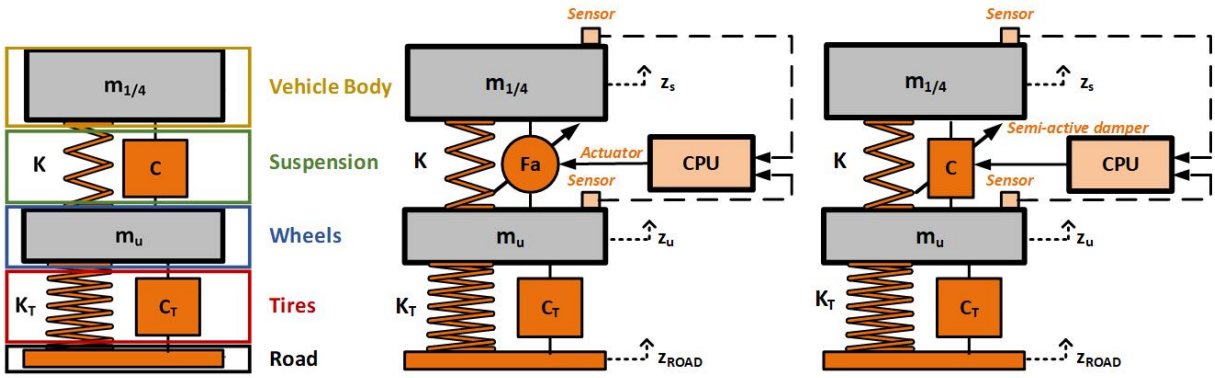

Figure 1.1: Quarter car vehicle models with (a) passive, (b) active and (c) semi-active suspensions.

As far as the seat suspensions are concerned, their comfort has proven to be dependant on both "static comfort" (e.g. seat stiffness) and "dynamic comfort" (e.g. vibration magnitude) [52]. The concept of Ebe's model describes this relation. When the vehicle is employed with a high quality suspension system or it drives through smooth roads, the typical magnitude of the vibration entering the seat is low. Thus, the dynamic seat factors are less important and the interest is turned on the static factors, i.e. seat stiffness, fit adjustments, seat shape and posture. However, when the seat is exposed to high vibration magnitudes, it might not perform very well, resulting in a poor "ride" for the occupant, due to the lack of good suspension or an off-road ride. Then, the dynamic factors can be as (or more) important as the static factors and therefore improved comfort would require optimisation of both static and the dynamic seat factors [53]. This relation is illustrated in Figure 1.2, as presented by Mansfield [1], and displays the conflict in the seat suspension systems, where the increasing initial deformation of the system leads to better isolation of the accelerations, and hence a more comfortable seat.

Considering the above, a good seat suspension system, occurred either from modeling or from optimization, can improve to some extent dynamic comfort, but cannot eliminate the compromise with the static comfort. To study the isolation of vibrations using a seat suspension, linear springs and dampers are typically used in the literature for their modeling. However, the standard commercial seats suspended by the use of conventional passive suspension systems have reached their full potential despite attempts in the literature to optimize them and obtain their optimal design [54–60]. Moreover, the semi-active and active suspensions [8, 61–64] despite being gradually used more in

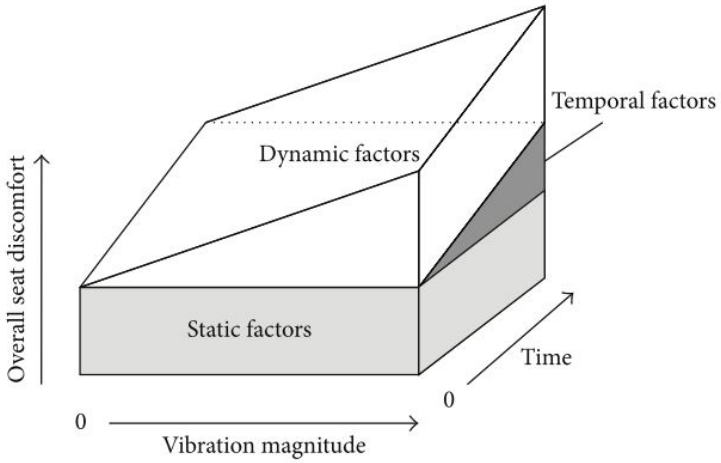

Figure 1.2: A model of vehicle seat discomfort including static, dynamic, and temporal factors (from Mansfield [1] page 33)

the seats and having increased industrial and academic interest, they are more expensive, complicated and less reliable than passive suspension systems. As a result, they have been put aside to some extent because of their disadvantages. Therefore, the modeling and the optimization of different types of vibration isolators, such as the ones with the embedded negative stiffness elements, are discussed extensively in this thesis [65, 66].

To sum up, this thesis focuses on four research areas and reviews the literature regarding them:

- Simulation of vehicle dynamics [19, 21]
- Semi-active suspensions [50, 51].
- Optimization of vehicle dynamics behavior [17, 22–27]
- Modeling and optimization of seat suspension [65, 66]

1.1 Simulation of vehicle dynamics

Multibody dynamics and rigid bodies have been used extensively by automotive industry so as to model and design the vehicle and its parts, as shown in Figure 1.3. In order to investigate the behavior of a vehicle, the discrete modeling employing lumped masses is usually used. A lumped mass model is a simplified representation of the vehicle, where the suspension system is assumed to act as a single lumped mass which can only translate forcesin the vertical direction with respect to the vehicle body. This mass is connected to the vehicle body at the wheel center with a translational joint, allowing only the vertical motion.

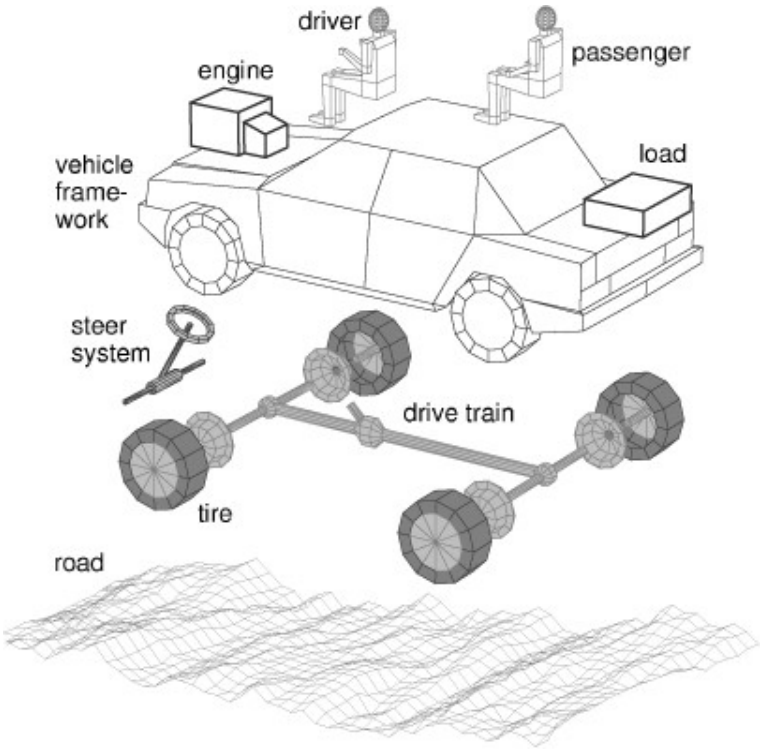

Figure 1.3: The vehicle model structure as presented by Rill [2].

Depending on the focus of each study, various models have been used in order to simulate the dynamic behavior of a vehicle by modeling the tires, the body and the suspension system. Simple models of one or two degrees of freedom (quarter car model [67, 68], can be found in literature. Since the quarter car model does not take into account any rotational degrees of freedom, its usage is limited to fairly simple suspension design optimization problems and preliminary results. For more accurate results, though, models of higher level of complexity should be used. Koulocheris et al. [26] used a half car model with degrees of freedoms the vertical displacement and the roll angle of the sprung mass and the displacements of the rear right and left unsprung masses comparing the results of the simulation with tire forces evaluated experimentally. Similar half car model were used also by Papaioannou et al. [27] and Koulocheris et al. [17, 25] including the pitch angle in the dynamic behavior of the vehicle.

Full car models are the most complex ones with seven or eight degrees of freedom offering the most accurate simulation. Despite being time consuming, they are widely used in research such as the works of Shirahatti et al. [69] and Gobbi et al. [70]. Seifi et al. [71] used a full car ride model along with a full car lateral model to study the rollover dynamics of a vehicle. In addition, more detailed models have been developed studying the lateral dynamics of the vehicle simultaneously with the vertical ones, such as the work of Shim et al. [72, 73] and Cao et al. [74]. Although, the need of knowing many vehicle parameters is an important disadvantage along with the fact that they are the most time consuming of all.

However, the selection of the most suitable model for suspension design is never explained and many times unnecessary complexity is added, either by using a model with more degrees of freedom or by adding more elements in the one selected (anti-roll bars, tire dampers etc.). The decision regarding the most appropriate model doesn't depend only on the fact that the pitch or the roll phenomena, should be investigated. The researchers have to consider if the increase in the DoFs of the model or the elements included will provide more accurate results and the computational time demanded will worth it. Thus, the decision has to be made based on the intended application, i.e. road excitation, reason of simulations (ride comfort or road holding), optimization of the suspension etc., without neglecting the complexity and the computational time. Based on the above, this thesis conducts an assessment regarding the accuracy of the four most common vehicle models. In contrast to Faris et al. [75] and Ihsan et al. [33, 76], who conducted comparative works more with respect to different semi-active control algorithms than with respect to different vehicle models, in this thesis, different vehicle models with various configurations are compared in terms of accuracy with respect to different performance metrics. More specifically, both passive and semi active suspensions are considered, while the effect of adding anti-roll bars and tire dampers is also investigated. The transient behavior of the suspension system and the overall ride performance of the vehicle are assessed in terms of ride comfort and road holding using different road excitations. Important conclusions are derived regarding their accuracy.

1.2 Semi active suspension systems

The design of various control algorithms for semi-active suspensions follows the skyhook (SH) concept. Skyhook damping is an ideal concept, which assumes that the shock absorber can deliver a force proportional to the chassis speed only. Even if an ideal SH damping cannot be implemented with semi-active suspensions, the SH behavior is typically approximated using two-states (SH-2) [77] or linear (SH-L) shock absorbers [78]. Many researchers have proposed various control strategies based on these two. Savaresi et al. [79] propped the Acceleration-Driven-Damper (ADD) control algorithm, which minimizes the vertical body acceleration when no road-preview is available. Later, Savaresi et al. [80, 81] combined the complementary characteristics of skyhook 2 states (SH-2) and Acceleration

Driven Damper (ADD) to two new algorithms (SH-ADD-1 and SH-ADD-2). The latter exploits the use of a frequency selector and is implemented with the use of only one sensor.

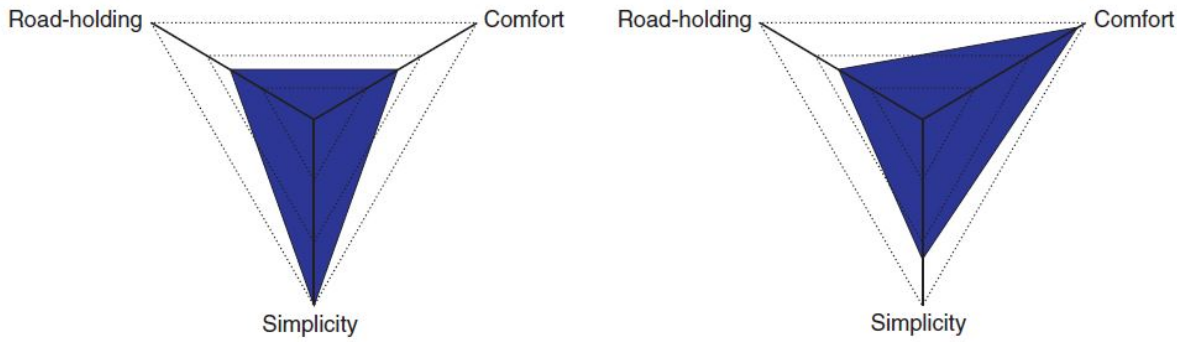

Figure 1.4: The radar diagram of performance and complexity of (a) SH-2 and (b) SH-L, as presented by Savaresi et al. [3].

Based on these algorithms, Van Der Sande et al. [82] proposed a rule-based controller for a semi-active suspension to reach minimal vertical acceleration, which performed much better than SH and ADD and slightly better than the mixed SH-ADD. Another controller was proposed by Nie et al. [83], achieving a good trade-off between ride quality and road-holding, by using the properties of the invariant points and employing a novel frequency selector. Besides the creation of new control algorithms, researchers have conducted extended surveys of the available controllers of semi-active suspensions with emphasis on different methods, such as: (a) the comparison of simulations with experimental results [84, 85], (b) the analysis in the frequency domain [86] and (c) in time domain [87] with comparisons with other control laws and (d) the comparison of the Pareto Fronts [17] occurred from the multi-objective optimization of semi-active suspensions operating with various control algorithms. In contrast to the existing works that prioritized the conflict between ride comfort and road holding, in this work, we propose a novel skyhook control strategy aiming to exploit the capabilities of classical control SH algorithms and reach significant improvements in various performance aspects.

In this framework, we will not focus only on overcoming the well-known trade-off of vehicle dynamics or improving one part of it, but also on eliminating another trade-off that has appeared due to the use of controlled suspension. The second trade-off consists of the dissipated energy and the vibration control performance, as shown in Figure 1.5. In semi-active suspensions of SH variety, in which we focus on this work, the vibration control performance is related to the number of switches in the damper's states or the sample time of checking the operational conditions. Better control performance demands more switches in the damper's states and it leads to more dissipated energy. Therefore, the fatigue in the damper's components and the elevated temperatures inside the damper (fluid, seals and other components) are increased and hence their expected life is decreased. Both of the above are not desired in a semi-active suspension. However, existing works allow the damper to switch states without it being necessary, neglecting the importance and the detrimental effect that could have in

the damper's components. Also, they don't consider the dissipated energy and the switches as an important design criteria in semi-active suspensions. As far as the dissipated energy is concerned, recently, only Smith et al. [88] and Crews et al. [89] considered the damper's dissipated energy as an important design criterion of semi-active suspensions. For instance, Crews et al. [89] demonstrated a method for determining the optimality of control algorithms based on two performance objectives, the ride quality represented by the absorbed power, and the thermal performance of the dampers, measured by the dissipated power in the suspension damper. In contrast to the traditional control algorithms, our control strategy avoids the redundant switches in the damper's states and achieves an important decrease in the dissipated energy.

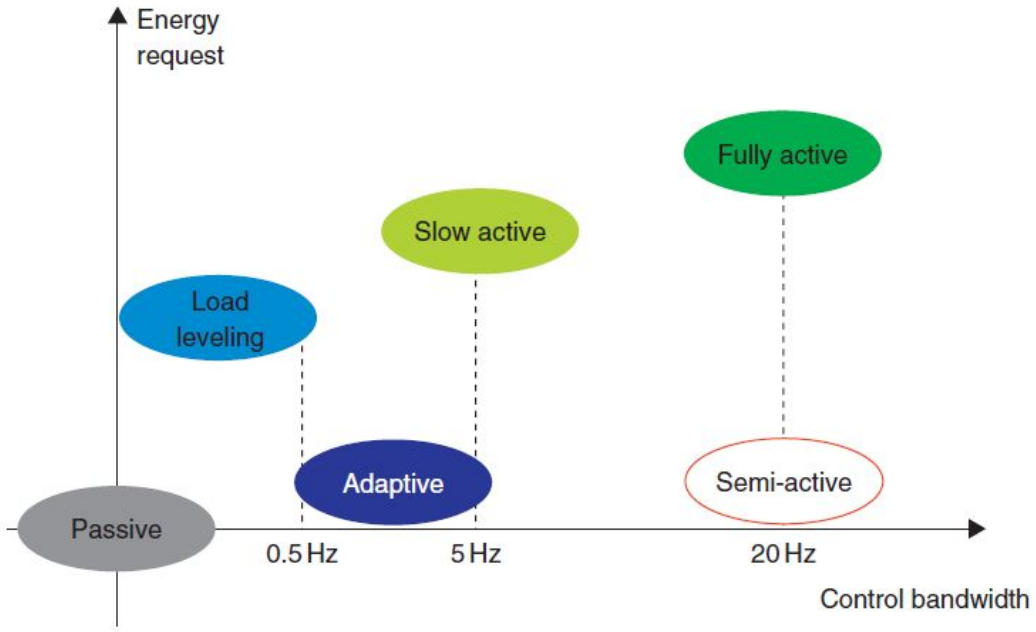

Figure 1.5: Graphic representation of suspension system classification: energy request with respect to the available control bandwidth, as presented by Savaresi et al. [3].

As far as the semi-active suspensions' are concerned the chattering effect of SH algorithms is investigated extensively in this work. The switches between the states that define the damper introduce nonlinearities into the system through the nonlinear damping force and the discontinuous command signal, as shown in Figure 1.6. This phenomenon is referred to as chatter. However, there is no relevant metric in the literature quantifying it. Eslaminasab et al. [90] decreased the chattering by suppressing all the nonlinearities of the control algorithm appearing around 30-40Hz, while Tsampardoukas et al. [91, 92] related the number of the switches in the damping ratio with the level of the chatter. Existing algorithms in the literature considered the decrease in the chattering and were compared with traditional SH algorithms [83, 90–93]. As Liu et al. [94] and Margolis et al. [95] stated, the use of the sign for the control of the operational conditions is the main reason for the occurring chattering, and many attempts have been made so as to suppress it. Our control strategy is based on

the use of an appropriate threshold in the algorithms' operational conditions in order to decrease both the chattering effect of the control algorithm and the switches of the damper's states.

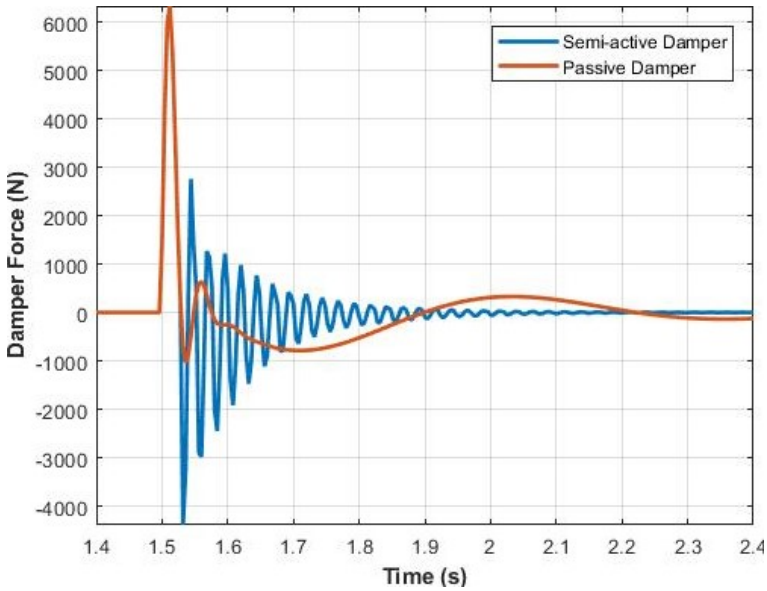

Figure 1.6: The chatter in the damper force of a semi-active damper compared to the continuous signal of a passive one.

The decrease both in the dissipation energy and in the chattering through the reduction of the damper's switches are intended to be achieved without a decrease either in the ride quality or in the vehicle stability (=handling+road holding). Instead, an increase in these aspects or at least in one of them is desired. Based on the above, the contribution of this work consists of a novel control strategy of semi-active suspensions benchmarked against the traditional ones for ride comfort [96], road holding and handling [38, 70], damper's dissipated energy [97, 98] and algorithm's chattering effect [90, 91, 94]. Our control strategy is based on the use of an appropriate threshold in the algorithms' operational conditions, which quantifies the severity of the operational conditions and controls the damper's state based on their magnitude and not based on their sign. It depends on the vibrations induced by the road profile that the vehicle drives through and is evaluated based on the cumulative distribution function of the operational conditions. For example in the case of SH-2, the algorithm considers the direction of the movement of the upper mass and if it is getting close with the unsprung or not. After fitting the operational conditions with a t-student distribution and using its cumulative function (CDF), the percentage of the operational conditions have values larger than zero -i.e. the damper works with the stiff state- is evaluated around to the 55% of the sample. Instead, the damper could be set to operate with the stiff state for a percentage of the sample around 30%, excluding the less dangerous conditions and avoiding to stiffen the damping coefficient if there isn't a severe situation. This could be achieved by applying the CDF control strategy in the SH-2 algorithm. Then, the SH-2-CDF control algorithm is introduced and considers the movement of the upper mass and how fast the unsprung mass is getting close to the sprung rather than if they are just getting close.

In this thesis, the proposed control strategy is applied to two traditional SH control algorithms (SH-2 and SH-ADD-2). Afterwards, the SH-2-CDF and the SH-ADD-2-CDF are benchmarked against the traditional ones for important aspects of vehicle's suspension performance. The simulations are performed by using a quarter car model and exciting it by four different road excitations. Moreover, a sensitivity analysis is performed in order to test thoroughly our control strategy. The comparison of SH-2-CDF and SH-ADD-2-CDF with the traditional ones is presented for three different random road profiles for various values of the thresholds. The sensitivity analysis outlines the change of all the performance metrics by applying our control strategy to the traditional control algorithms and varying the threshold.

1.3 Optimization of suspension systems

1.3.1 Passive suspension systems

The development of modern optimization methods opened new perspectives in the field of suspension design. In order to address the conflicting targets of ride comfort and road holding mentioned above, single (SOO) and multi-objective (MOO) methods have been formed. The single objective method offers a limited insight in the suspension optimization problem but due to its simplicity it is often selected over the more complex and time consuming multi - objective approach. Kuznechov et al. [99] used as objective function the root mean square of the frequency - weighted steady - state acceleration of the body based on ISO-2631, while Sun et al. [100] used the variance of the dynamic vehicle load. On the contrary, multi - objective approach (MOO) is commonly used in order to receive indicative results concerning many conflicting targets leading to simultaneous minimization of all the objectives, offering an insight of the conflicted targets through the Pareto front. A simple multi-objective dealing strategy, known as pseudo - MOO techniques, suggests the combination of multiple objective functions using weighting factors, so as to convert the multi-objective problem into a single-objective one, scalarizing the objective function. The drawback of such a scalarization is that the designer must include subjective information and preferences a priori for the weighting factors, i.e., before the results of the optimization process are known. Koulocheris et al. [26] compared the efficiency of various objective functions in SOO and pseudo-MOO approaches in the optimization of suspension systems of a heavy vehicle with three different optimization methods (gradient based, genetic and hybrid algorithms) conducting important conclusions regarding the solutions in terms of the results and the convergence of the problem.

In order to avoid the need to prespecify arbitrary weighting coefficients various methodologies have already been applied successfully in many engineering areas. The most common methods entail the Pareto Front approach where the different targets of the optimization are separated throughout the optimization process and are simultaneously minimized. The Pareto Front approach is very popular

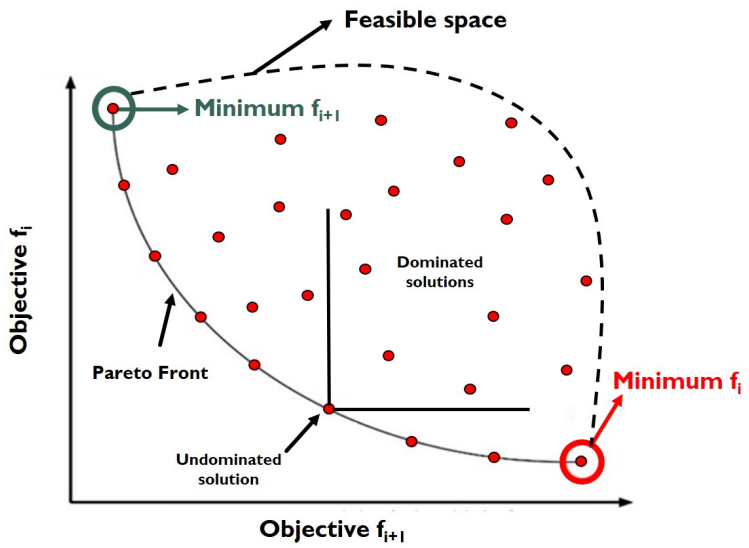

Figure 1.7: Pareto Front approach.

among optimization problems with conflicting optimization targets, because it allows the engineers to select various objective functions and overcome their conflicting character. Nariman et al. [101] investigated the use of a uniform-diversity Genetic Algorithm in the Pareto optimization method, selecting five targets including tire displacements and velocities concentrating mainly in the handling and the road holding of the vehicle. Whereas, Gadhvi et al. [30] also dealt with the use of different optimization techniques, mainly variations of Genetic and Evolutionary Algorithms in order to minimize the root mean squared values of (i) the vertical acceleration experienced by the passenger's seat, (ii) the front tire deflection and (iii) the rear tire deflection, selecting objective functions depicting the ride comfort and the road holding. The selection of objective functions in the work of Gadhvi et al. [30] followed the work of Koulocheris et al. [26] regarding the importance of the objective functions where the variance of the vertical acceleration as well as the one of the tire deflections were highlighted as the most important ones. On the other hand, Morardi et al. [102] used thirteen objective functions combining them through weighting factors in order to find the optimal suspension design in a full car model and P. Nagarkar et al. [103, 104] selected seven objective functions in order to compare the optimization algorithms NSGA-II and MOPSO-CD in a nonlinear suspension system.

Genetic Algorithms (GA) are time consuming optimization methods, but because of their important advantages, as mentioned by Marler et al. [105], Gobbi et al. [70] and Konak et al.[106], they are widely used in the field of automotive engineering. More specifically, in vehicle dynamics oriented MOO problems, the most common method is the Pareto Front, whose selection becomes very quickly ineffective based on the configuration of the problem. For instance, researchers add uncontrollably objective functions in order to find the optimum design of a suspension system, despite the fact that there are specific performance aspects which need to be optimized in vehicle dynamics. Thus, they sometimes end up using more than one objective function for the same performance aspect increasing

the dimension of the optimization problem, such as the works of Morardi et al. [102] and P. Nagarkar et al. [103, 104]. Also, in this way, the merits of the optimization algorithm used are put aside because the computational time required for convergence is essentially increased. Thus, in this thesis the attention is given in an approach of minimizing the computational time needed for the Pareto set allowing the GAs to be attractive again. Moreover, this approach aims at proving that the increasing use of objective functions depicting the same requirement doesn't help the optimizer to converge to the most "optimal" solutions. In the literature, a few papers mention this topic and the attention is on the issue of selecting the optimum solution among the Pareto alternatives, Gobbi et al. [70, 107] introduced the k- ε optimality method, which is implemented in this paper, and he presented the KEMOGA algorithm later [108]. Earlier, Das [109] introduced the k-optimality method which is based on the partial dominance between the solutions and was the basis of the k- ε optimality method. In Taboada's et. al work [110], two methods are presented to filter the Pareto optimal set to determine a subset of promising solutions based on data clustering. Moreover, in Venkat's et al. research [111], the Greedy Reduction algorithm is introduced and analyzed. The method is used for obtaining subsets of Pareto optimal set in multi-objective optimization by assuming that a certain preference weight is associated with each objective function. Another important work used to find out the local minima, is the one of Zhu et al. [112] who developed the adjoint sensitivity approach of multibody systems in the context of the penalty formulation applying it in a fourteen degree of freedom vehicle model.

To sum up, the Pareto selection becomes very quickly ineffective as the dimension of the problem grows in terms of the number of the objective functions. In this respect, the current thesis focuses on the issue of the inconsiderate selection of objective functions in the optimization of vehicle's suspension system noticed in the literature. The optimization problem, which is used as a case study, is the one of the optimum design of the suspension systems of a vehicle model excited by a specific road excitation. At first, three SOO cases for the main targets re presented along with one pseudo-MOO case of the same optimization problem (Part A) and a sorting algorithm is implemented for these four cases. Secondly, an alternative approach for handling the optimization targets is presented by selecting six optimization targets which are divided in main and supplementary ones (Part B). The main targets of the study are introduced in the multi-objective genetic algorithm (MOGA), while the supplementary ones are calculated later with simulation of the models. Then, the set of the main targets along with the supplementary ones are introduced in the sorting algorithm. Thirdly, all the six optimization targets are introduced in the multi-objective-optimization process (Part C) and then the resulting solutions of the Pareto front are implemented in a sorting algorithm so as to find the optimum solution among the Pareto alternatives. Finally, the optimum solutions occurred from the sorting algorithms were compared in terms of the values of each target, of the design variables, and of important metrics describing the dynamic behavior of the vehicle.

1.3.2 Semi-active suspension systems

The main reason that various optimization techniques have been suggested through the years is so as to overcome the well-known automotive conflict between ride comfort and road holding. The level of this compromise depends highly from the suspension system's design, but the trade-off between is never eliminated. The only thing that changes regarding the suspension type is the level of the isolation. Thus, the proposed approach of handling the objectives functions is applicable to any other suspension type. However, other constraints could be added such as the number of switches in an on-off or a continuous semi–active suspension instead the contribution of the nonlinear part in the spring force. Therefore, in this thesis, the approach for handling the objective functions in MOO problems is applied also to the optimization of semi-active suspension systems.

In any suspension type, the idea of the separations of the objectives could be followed and the supplementary objectives could be selected because they either enhance the main objectives or they are crucial to the suspension design. The supplementary objectives selected in this thesis for the optimization of semi-active suspensions is the dissipated energy and the number of switches in the damper's state. A decrease in the dissipated energy of the damper is really crucial considering that it may offer simultaneous benefits to hardware temperature and forward power requirements. Thus, due to the importance of the dissipated energy, we consider it as an important design criterion of semi-active suspensions and therefore we incorporate it in the optimization procedure as a supplementary objective. Moreover, the number of the switches in the damper's states and the chattering are considered as a supplementary objective. This thesis proposes the consideration of the number of the switches in the damper's states as an important design criterion of semi-active suspensions not only because of its effect on chattering, but also because their decrease increases the expected life of the damper's component by reducing their fatigue and the temperatures occurred in the fluid, the seals and the damper's components.

However, despite the importance of the extra objectives, the inconsiderate selection of objective functions grows the dimension of the optimization problem, costing computational time without providing "more optimum" solutions. Thus, the approach based on KEMOGA algorithm [56], which is proposed in this thesis in order to minimize the objective functions, is adopted. This approach suggests to separate the indexes of the design criteria to main and supplementary. The main objectives are used to the MOGA in order to obtain the Pareto front, while the supplementary ones are added in the sorting algorithm (KE) in order to rank the Pareto alternatives and vet the one solution with "something more" than the others. The supplementary objectives consist of performance metrics which either enhance the main ones or are of crucial importance in the design of the semi-active suspension and should be considered. To sum up, in this work, the design of semi-active suspensions is investigated and the optimization approach based on KEMOGA algorithm is applied to a passenger vehicle in order to optimize its suspension systems. The suspension systems operate with various SH control algorithms. Firstly, the vehicle model is optimized with respect to ride comfort and road holding with a multi-

objective genetic algorithm (MOGA) by considering two performance indexes as objective functions. Then, a sorting algorithm (KE) is applied considering the extra objectives of the dissipation energy and the number of switches in the damper's states as objective functions due to their importance in the suspension design. Finally, the optimum solution of each case and the optimum among all are pointed out. Conclusions regarding the design solutions are extracted in addition with the benchmark of them in terms of their objective's values and their design variables.

1.4 Modeling and optimization of seat suspensions

The stiffness of an isolation system has a considerable influence on isolation effectiveness and as a results of higher stiffness a more-susceptible-to-vibrations-system will occur. However, reducing the system's stiffness leads to decreasing the load support capacity of the isolation system. The above remark explains further the conflict of seat suspensions, which many researchers have focused on overcoming or at least suppressing. The last decade, this is attempted to be compromised with mechanisms combining negative stiffness elements with a positive stiffness one. In this way, the suspension allows the combination of high static stiffness, for safety in the machine handling, with low dynamic stiffness, for ride comfort.

Carrella et al. [5–7] proposed useful vibratory isolation models, which comprise a negative stiffness structure in parallel with the positive stiffness structure. Due to the conflicted effects of the negative and positive stiffness structures, low dynamic stiffness is achieved. Another mechanism with negative stiffness was designed by Lee et al. [113], so as to improve a railroad vibratory isolation system subjected to hazardous frequency vibrations. Later, Lee et al. [114] introduced a strategy for inserting into helicopter vibration isolation systems with springs of adjustable sign-changing stiffness for controlling the stiffness of the system. As far as the automotive industry and the seat design are concerned, Thanh Danh Le et al. [9] proposed a passive vibratory isolation system using negative stiffness structure and later an active damper was added[8]. The effectiveness of this model was also investigated experimentally [10] and further regarding its stiffness by Xiaojie Wang et al. [115]. Yan et al. [13] designed a novel nonlinear seat suspension structure by using the conceptual design of cam-roller-spring mechanisms (CRSMs) for off-road vehicles. Its static characteristics and seat-human dynamic response were modeled and analyzed, and experiments were conducted to verify the theoretical solutions. A similar model was also proposed by Zhou et al. [116]. Additionally, Zhao et al. [117] developed a new type of seat suspension with a hollow composite rubber spring. The results showed that the new suspension can attenuate more effectively the low frequency from the uneven ground, while, it can provide a more stable support so that the driver can control the vehicle effectively. Jeong Ho et al. [118] evaluated commercially available seat suspensions to reduce whole body vibration exposures in mining heavy equipment vehicle operators.

Apart from all the above, a novel type of oscillator has been proposed by Antoniadis et al. [14], incorporating a negative stiffness element, without presenting the drawbacks of the traditional linear oscillator, or of the quasi static zero stiffness designs. Later, Antoniadis et al. [15, 119] extended their work by presenting the KDamping concept. In their work, the KDamper does not require any reduction in the overall structural stiffness, overcoming the corresponding inherent disadvantage of the quazi zero stiffness isolators, which require a drastic reduction of the structure load bearing capacity. The KDamper concept is already implemented in a large variety of technological applications such as seismic isolations [120], the control of a marine shaft [121] and the wave damping within matamaterials [122].

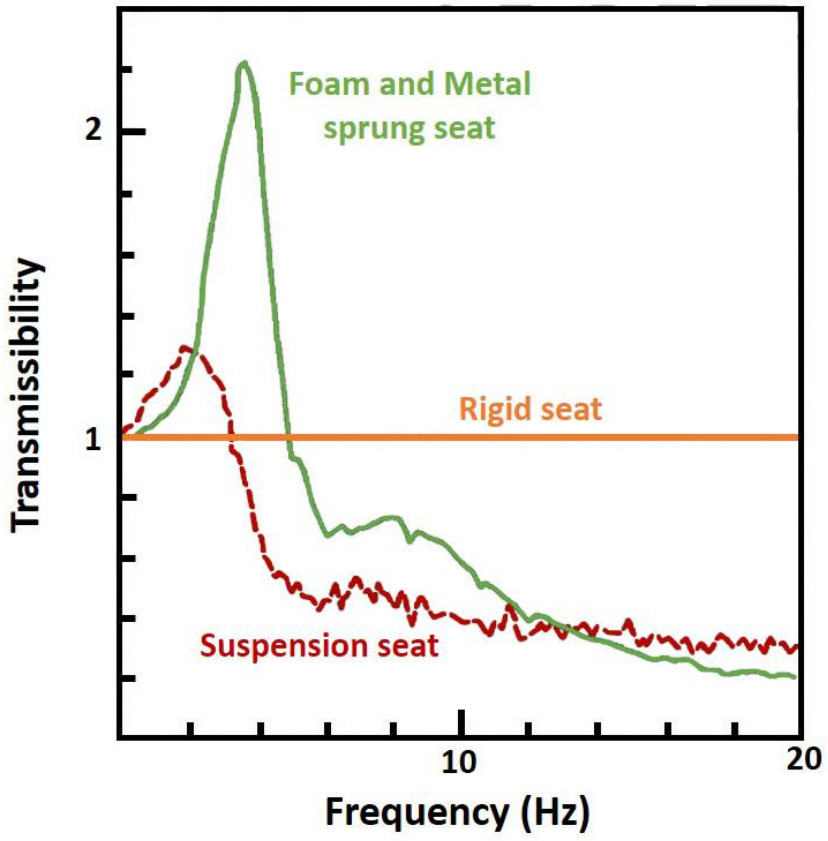

Figure 1.8: Comparison of the transmissibilities of a suspension seat, a rigid seat and a foam and metal sprung vehicle seat as presented by Griffin [4].

In this thesis, the main aim is apply the KDamper [15, 119] in seat suspensions and benchmark it against the four established vibration isolators in seat suspensions. More specifically the comparison is conducted between the conventional suspension, the one of Carrella et al. [5–7], Le Thanh Danh et al. [9] and Yan et al. [13] are used. In order to compare them, the suspension systems are optimized with genetic algorithms in respect to ride comfort and the safety of the machine handling by applying constraints aiming not only to a compact structure able to fit in a passenger vehicle but also

to a comfortable seat. A genetic algorithm (GA) is employed considering the fact that increases the probability of finding the global optimum solution and avoids convergence to a local minimum which is a drawback of gradient-based methods. The vibration of the vehicle's floor when driving in a road of class A is used as an excitation to the system for the optimization. Then, except from comparisons between the optimal solutions occurred in the Pareto front of each case study, three types of analysis are illustrated. Firstly, the optimum solutions of the Pareto Fronts are simulated for another two excitation, which correspond to the vibrations induced to the vehicle's floor by driving in two different road classes (B and C). Secondly, the system's mass (passengers and seat) is varied by increasing and decreasing it by 20 kg from the initial one. The optimum solutions obtained from the Pareto front, are simulated for the two different masses, i.e. two different passengers. Finally, a passenger model is added in the seat model and three solutions of the Pareto Fronts are selected based on the Pareto theory and the seat to head transmissibilities (STHT) of these solutions are compared. These three types of analysis except from allowing to test the applicability of KDamper in a seat suspension, provide information and conclusions regarding the sensitivity and the adaptability of the studied suspension systems in different passenger's masses and in driving under different road profiles. Also, the use of the multi-objective optimization, and more specifically the Pareto method, allowed as to compare numerous possible designs simultaneously.

CHAPTER 2

Simulation models

Suspension systems are used in a vehicle in order to isolate the passengers from the adverse effects of their exposure to vibrations, and improve their comfort and their safety [20]. As far as the main vehicle suspensions are concerned, various simulations models have been developed for vehicle dynamic analysis using lumped masses and rigid body theory. A lumped mass model is a simplified representation of the vehicle, where the suspension system is assumed to act as a single lumped mass which can only translate in the vertical direction with respect to the vehicle body. This mass is connected to the vehicle body at the wheel center with a translational joint, allowing only the vertical motion. The main models existing in the literature are the quarter car (QC), the half car (HC1 and HC2), considering either the right and the left wheel of one axle (HC1) or the front and rear axle of the vehicle (HC2), and the full car model (FC). For their modelling, the following assumptions are considered [18]:

1. The tires are always in contact with the ground, which is true at low frequency but might not be true at high frequency. Also, the camber angle between the wheels and the body is considered constant.

2. The aerodynamic forces, as well as the rolling resistance of the tires are neglected.

3. The center of gravity of the vehicle is assumed to be above the roll and pitch centers.

4. The deflections in the roll and pitch planes are small enough to use the approximate theory for small angles.

Moreover, the simulation models, which we study in this thesis, are modeled considering four basic subsystems, as shown in Figure 2.1, :

- the sprung mass, which represents the vehicle body,
- the unsprung masses, which represent the wheels of the vehicle and all the rotating parts,
- the suspension systems, which connect the sprung with the unsprung masses and each is modeled as a spring and a damper, and
- the tires, which are also modeled as a spring and a damper and the irregularities of the road profile are applied to them as inputs of the models .

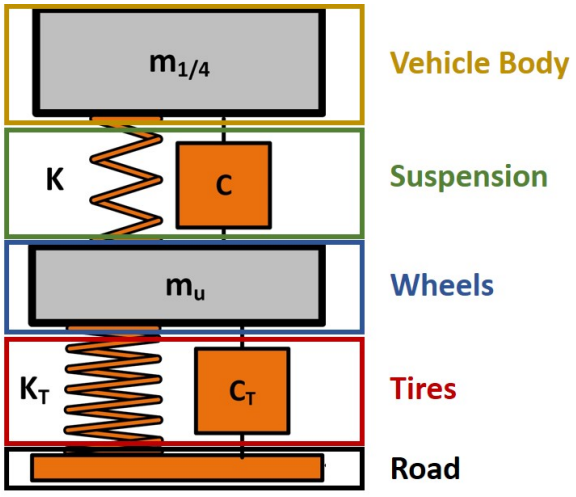

Figure 2.1: The elements considered from the vehicle models, which study ride dynamics

Apart from the primary suspensions, the secondary, such as seat suspension, have attracted much more attention recently. In a seated posture, humans are most sensitive to whole-body vibrations under low-frequency excitation. Therefore, biodynamic responses of a seated human body when exposed to vertical vibrations are considered an important knowledge. They require an understanding of the cause-effect relationships among the transmission of vibrations through the body and its health, comfort and performance [123]. Thus, the vehicle models are usually extended with the addition of seat and passenger models, which are also investigated in this thesis.

Nomenclature

Parameter	Unit	Description	Subscripts	Description
z	$[m]$	vertical motion coordinate of mass (m_s)	s	sprung mass
φ	$[rad]$	roll motion coordinate of mass (m_s)	u	unsprung mass
θ	$[rad]$	pitch motion coordinate of mass (m_s)	K	spring
z_{road}	$[m]$	road excitation	C	damper
F	$[N]$	forces applied to the subsystems	T	tire
M	$[Nm]$	moments applied to the subsystems	l	linear
m	$[kg]$	mass	nl	nonlinear
k	$[N/m]$	spring stiffness	AR	antiroll bar
c	$[Ns/m]$	damping coefficient	F	front axle
I_x	$[kgm^2]$	longitudinal moment of inertia	R	rear axle
I_y	$[kgm^2]$	lateral moment of inertia	1	right wheel
b	$[m]$	distance between CG and each side	2	left wheel
a	$[m]$	distance between CG and each axle	x	x-axis
w	$[m]$	track width	y	y-axis

Table 2.1: Nomenclature of the parameters used in the all the four vehicle models (QC, HC1, HC2 and FC).

2.1 Simulation of Vehicle Dynamics

2.1.1 Quarter Car Model (QC)

The quarter car model (QC), as shown in Figure 2.2a, is considered as a rigid body of mass $m_{1/4}$, equal to the one quarter of the vehicle's total mass ($m_{1/4} = m_s/4$). It represents any of the four suspension systems of the vehicle and the degrees of freedom (DoFs) are the displacements of both the sprung mass (z_s-m_s) and the unsprung mass (z_u-m_u). The effects of coupled masses are neglected in this model. The governing equations of the QC occur from its free body diagram, as presented in Figure 2.1 and are the following (Equations 2.1- 2.2). The nomenclature of the parameters included in the equations is presented in Table 2.2.

Body Bounce:

$$m_{1/4}\,\ddot{z}_s + F_C + F_K = 0 \tag{2.1}$$

Wheel Bounce:

$$m_u\ddot{z}_u - F_C - F_K + F_{CT} + F_{KT} = 0 \tag{2.2}$$

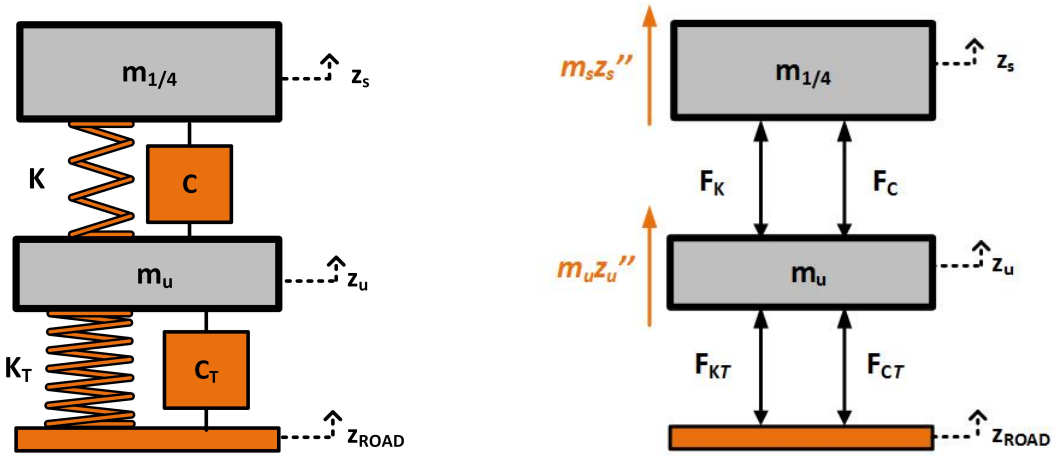

(a) The model with its elements.

(b) Free body diagram.

Figure 2.2: Quarter car model representing one wheel of the vehicle

where F_K and F_C correspond to the forces applied by the suspension spring and damper respectively, and they depend on the suspension travel and its velocity, while F_{KT} and F_{CT} correspond to the forces applied by the tire spring and damper respectively and are related with the tire deflection and its velocity. As far as the forces applied to the model are concerned, more detailed description is presented in the next sections. The suspension travel (ST) and the tire deflection (TD), as evaluated for the quarter car, are given by the equations 2.3 and 2.4, respectively.

$$ST = z_s - z_u \tag{2.3}$$

$$TD = z_u - z_{road} \tag{2.4}$$

2.1.2 Half Car Model (HC1 - right and left)

Another version of the half car model (HC1), as shown in Figure 2.3a. The body of the vehicle is considered as a rigid mass $m_{1/2}$, equal to the half of the vehicle's total mass ($m_{1/2} = m_s/2$), with a longitudinal moment of inertia I_{xx}, equal to the half of the total moment of inertia ($I_{xx} = I_x/2$). Furthermore, the right (z_{F1}) and the left (z_{F2}) wheel of one axle of the vehicle are considered as unsprung masses. Additionally, the half car model (HC1) may also include an antiroll bar with torsional stiffness k_{AR}, which provides a torque M_{AR} proportional to the roll angle φ of the sprung mass (Equation 2.11). The degrees of freedom (DOFs) of the model are the heave motions of the sprung (z_s) and

unsprung masses (z_{F1} *and* z_{F2}) and the roll angle (φ). In addition, the governing equations of the HC1 occur from its free body diagram, as presented in Figure 2.3b and are the following (Equations 2.5- 2.8). The nomenclature of the parameters included in the equations is presented in Table 2.2.

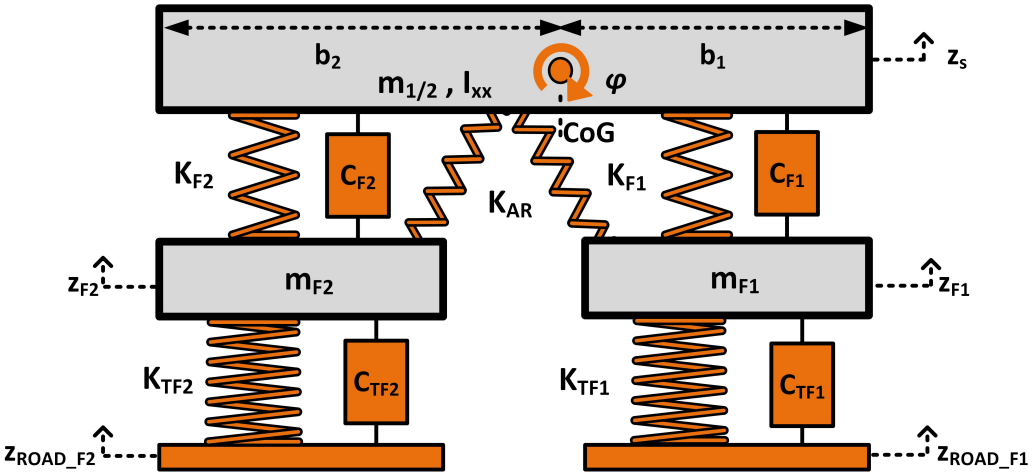

(a) The model with its elements.

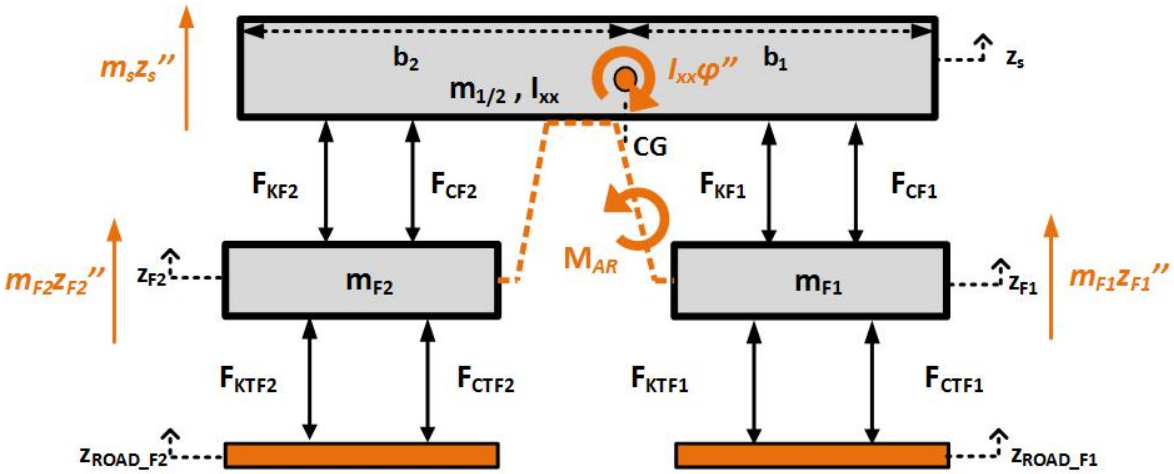

(b) Free body diagram.

Figure 2.3: Half Car Model considering the right and the left wheels of either the front or rear vehicle's axle

Body Bounce:

$$m_{1/2}\ddot{z}_s + F_{C_{F1}} + F_{C_{F2}} + F_{K_{F1}} + F_{K_{F2}} = 0 \tag{2.5}$$

Roll Bounce:

$$I_{xx}\ddot{\varphi} + b_1 F_{C_{F1}} - b_2 F_{C_{F2}} + b_1 F_{K_{F1}} - b_2 F_{K_{F2}} - M_{AR} = 0 \tag{2.6}$$

Right Wheel Bounce:

$$m_{F1}\ddot{z}_{F1} - F_{C_{F1}} - F_{K_{F1}} + F_{KT_{F1}} + F_{CT_{F1}} + F_{AR} = 0 \tag{2.7}$$

Left Wheel Bounce:

$$m_{F2}\ddot{z}_{F2} - F_{C_{F2}} - F_{K_{F2}} + F_{KT_{F2}} + F_{CT_{F2}} - F_{AR} = 0 \tag{2.8}$$

where F_{K_i} and F_{C_i} correspond to the forces applied by the spring and the damper either of the right ($i = F_1$) or the left ($i = F_2$) suspension system respectively, while F_{KT_i} and F_{CT_i} correspond to the forces applied by the spring and the damper either of the right ($i = F_1$) or the left ($i = F_2$) tire. As far as the forces applied to the model are concerned, more detailed description of them, is presented in the next sections. The suspension travel (ST_i) and the tire deflection (TD_i), as evaluated for the half car model (HC1), are given by Equations 2.9 and 2.10, respectively.

$$ST_i = \begin{cases} z_s - z_{F1} + b_1\varphi, & i = F1 \\ z_s - z_{F2} - b_2\varphi, & i = F2 \end{cases} \tag{2.9}$$

$$TD_i = \begin{cases} z_{F1} - z_{road_{F1}}, & i = F1 \\ z_{F2} - z_{road_{F2}}, & i = F2 \end{cases} \tag{2.10}$$

Additionally, as far as the antiroll bar is concerned, the torque it provides (M_{AR}) is calculated according to the Equation 2.11, while the force (F_{AR}) that the antiroll bar applies to the wheels is given by Equation 2.12.

$$M_{AR} = -k_{AR}\varphi \tag{2.11}$$

$$F_{AR} = \frac{M_{AR}}{w} \tag{2.12}$$

2.1.3 Half Car Model (HC2 - front and rear)

In order to study the pitch motion of a vehicle, the half car model (HC1) is modeled as shown in Figure 2.4a and it includes the front ($F1$) and the rear ($R1$) axle of the vehicle. It considers the body of the vehicle as a rigid mass $m_{1/2}$, equal to the half of the total mass of the vehicle ($m_{1/2} = m_s/2$), with a lateral moment of inertia I_{yy}, equal to the half of the total body's lateral moment of inertia ($I_{yy} = I_y/2$). The DOF's are the bounce motions of the sprung mass (z_s) and the ones of the two unsprung masses (z_{F1} *and* z_{R1}) and the pitch angle (ϑ) . The governing equations of HC2 occur from

its free body diagram, as presented in Figure 2.4b, and are the following (Equations 2.13- 2.16). The nomenclature of the parameters included in the equations is presented in Table 2.2.

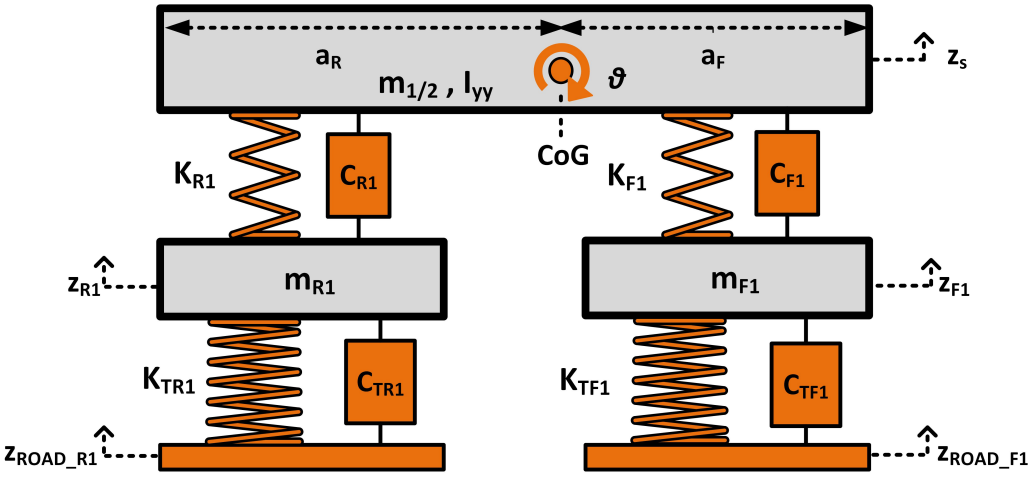

(a) The model with its elements.

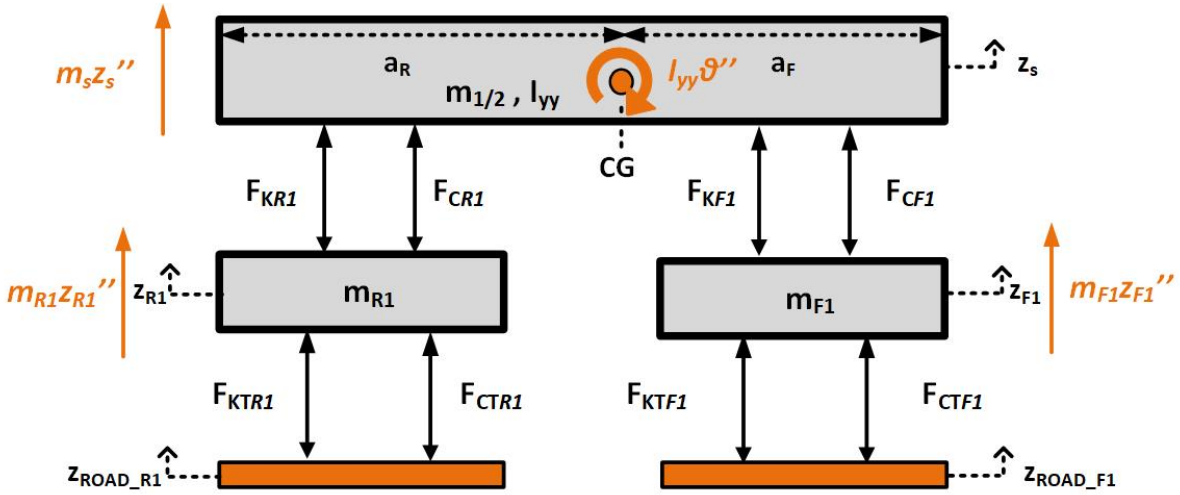

(b) Free body diagram.

Figure 2.4: Half Car Model considering the front and the rear vehicle's wheel

Body Bounce:

$$m_{1/2}\ddot{z}_s + F_{C_{F1}} + F_{C_{R1}} + F_{K_{F1}} + F_{K_{R1}} = 0 \tag{2.13}$$

Pitch Bounce:

$$I_{yy}\ddot{\vartheta} - a_1 F_{C_{F1}} + a_2 F_{C_{R1}} - a_1 F_{K_{F1}} + a_2 F_{K_{R1}} = 0 \tag{2.14}$$

Front Wheel Bounce:

$$m_{F1}\ddot{z}_{F1} - F_{C_{F1}} - F_{K_{F1}} + F_{KT_{F1}} + F_{CT_{F1}} = 0 \tag{2.15}$$

Rear Wheel Bounce:

$$m_{R1}\ddot{z}_{R1} - F_{C_{R1}} - F_{K_{R1}} + F_{KT_{R1}} + F_{CT_{R1}} = 0 \tag{2.16}$$

where F_{K_i} and F_{C_i} correspond to the forces applied by the spring and the damper either of the front ($F1$) or the rear (R_1) suspension system respectively, while F_{KT_i} and F_{CT_i} correspond to the forces applied by the spring and the damper either of the front ($i = F1$) or the rear ($i = R_1$) tire. As far as the forces applied to the model are concerned, more detailed description of them, is presented in the next sections. The suspension travel (ST_i) and the tire deflection (TD_i), as evaluated using the half car model (HC2), are given by Equations 2.17 and 2.18, respectively.

$$ST_i = \begin{cases} z_s - z_{F1} - a_F\theta, & i = F1 \\ z_s - z_{R1} + a_R\theta, & i = R1 \end{cases} \tag{2.17}$$

$$TD_i = \begin{cases} z_{F1} - z_{road_{F1}}, & i = F1 \\ z_{R1} - z_{road_{R1}}, & i = R1 \end{cases} \tag{2.18}$$

2.1.4 Full Car Model (FC)

The most detailed vibrating model of a vehicle is the so called full car model, as illustrated in Figure 2.5. This model is of seven degrees of freedom (DOFs) including the roll (φ) and the pitch angle (ϑ) of the sprung mass, as well as the heave motions of the vehicle body (z_s) and of the vehicle's wheels (z_{F1}, z_{F2}, z_{R1} *and* z_{R2}). The current model considers the vehicle body as a rigid mass m_s, equal to the total mass of the vehicle, with longitudinal and lateral moment of inertia I_x and I_y, respectively. Additionally, an antiroll bar with torsional stiffness k_{AR_i} providing a torque M_{AR-i} for front ($i = F$) and rear ($i = R$) axle. The governing equations of FC occur from its free body diagram, as presented in Figure 2.5 and are the following (Equations 2.19- 2.25), while the nomenclature of the parameters included in the equations is presented in Table 2.2.

Body Bounce:

$$m_s\ddot{z}_s + F_{C_{F1}} + F_{C_{F2}} + F_{C_{R1}} + F_{C_{R2}} + F_{K_{F1}} + F_{K_{F2}} + F_{K_{R1}} + F_{K_{R2}} = 0 \tag{2.19}$$

Roll Bounce:

$$\begin{aligned} I_x\ddot{\varphi} + b_1F_{C_{F1}} - b_2F_{C_{F2}} - b_1F_{C_{R1}} + b_2F_{C_{R2}} \\ + b_1F_{K_{F1}} - b_2F_{K_{F2}} - b_1F_{K_{R1}} + b_2F_{K_{R2}} - M_{ARF} - M_{ARR} = 0 \end{aligned} \tag{2.20}$$

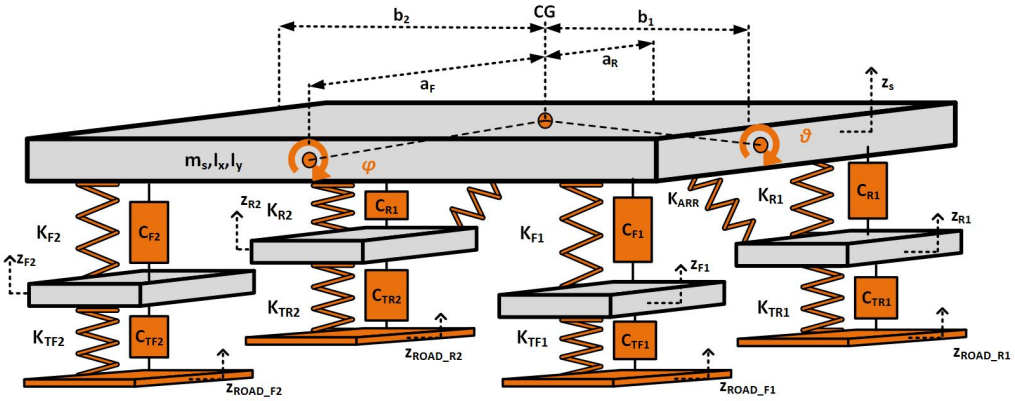

(a) The model with its elements.

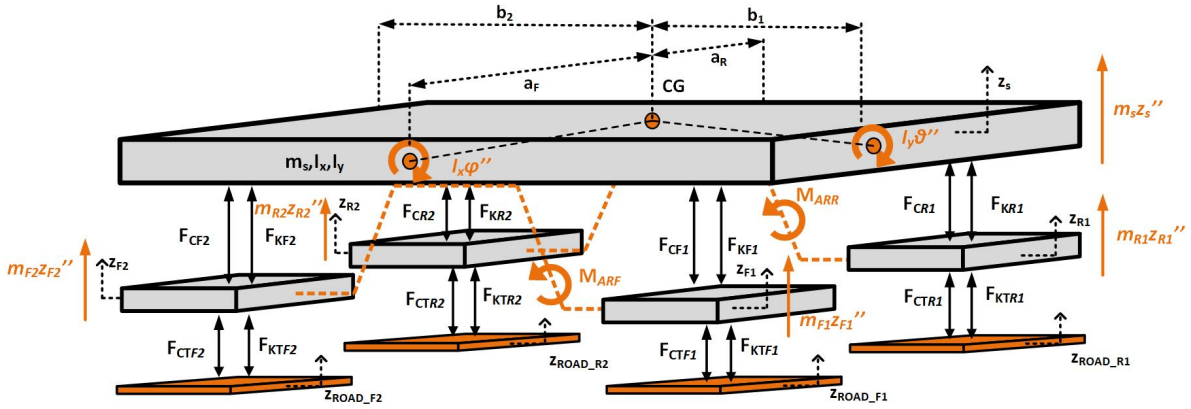

(b) Free body diagram.

Figure 2.5: Full car model considering all the wheels of the vehicle

Pitch Bounce:

$$I_y\ddot{\vartheta} - a_1F_{C_{F1}} - a_1F_{C_{F2}} + a_2F_{C_{R1}} + a_2F_{C_{R2}} - a_1F_{K_{F1}} - a_1F_{K_{F2}} + a_2F_{K_{R1}} + a_2F_{K_{R2}} = 0 \tag{2.21}$$

Front Right Wheel Bounce:

$$m_{F1}\ddot{z}_{F1} - F_{C_{F1}} - F_{K_{F1}} + F_{KT_{F1}} + F_{CT_{F1}} + F_{AR_F} = 0 \tag{2.22}$$

Front Left Wheel Bounce:

$$m_{F2}\ddot{z}_{F2} - F_{C_{F2}} - F_{K_{F2}} + F_{KT_{F2}} + F_{CT_{F2}} - F_{AR_F} = 0 \tag{2.23}$$

Rear Right Wheel Bounce:

$$m_{R1}\ddot{z}_{R1} - F_{C_{R1}} - F_{K_{R1}} + F_{KT_{R1}} + F_{CT_{R1}} + F_{AR_R} = 0 \tag{2.24}$$

Rear Left Wheel Bounce:

$$m_{R2}\ddot{z}_{R2} - F_{C_{R2}} - F_{K_{R2}} + F_{KT_{R2}} + F_{CT_{R2}} + F_{AR_R} = 0 \tag{2.25}$$

where F_{K_i} and F_{C_i} correspond to the forces applied by the spring and the damper of the i^{th} suspension systems ($i = F_1,\ F_2,\ R_1\ and\ R_2$), while F_{KT_i} and F_{CT_i} corresponds to the forces applied by the spring and damper of i^{th} tire ($i = F_1,\ F_2,\ R_1\ and\ R_2$). As far as the forces applied to the model are concerned, more detailed description of them, is presented in the next sections. The suspension travel (ST_i) and the tire deflection (TD_i), as evaluated for the full car model (FC), are given by Equations 2.26 and 2.27, respectively.

$$ST_i = \begin{cases} z_s - z_{F1} + b_1\varphi - a_F\theta, & i = F1 \\ z_s - z_{F2} - b_2\varphi - a_F\theta, & i = F2 \\ z_s - z_{R1} - b_1\varphi + a_R\theta, & i = R1 \\ z_s - z_{R2} + b_2\varphi + a_R\theta, & i = R2 \end{cases} \tag{2.26}$$

$$TD_i = \begin{cases} z_{F1} - z_{road_{F1}}, & i = F1 \\ z_{F2} - z_{road_{F2}}, & i = F2 \\ z_{R1} - z_{road_{R1}}, & i = R1 \\ z_{R2} - z_{road_{R2}}, & i = R2 \end{cases} \tag{2.27}$$

2.1.5 Forces applied by the tires and the suspension

Tire stiffness

The force due to the tire spring is calculated by multiplying the spring constant of the tire (k_{T_i}) with the tire deflection (TD_i), as shown in Equation 2.28.

$$F_{KT_i} = k_{T_i} TD_i \tag{2.28}$$

The tire deflections of the quarter car model (QC), the half car models (HC1 and HC2) and the full car model are evaluated by Equations 2.4, 2.18, 2.10 and 2.27, respectively.

Tire damping

As far as the force by the tire damper is concerned, it is given by the Equation 2.29, and it is calculated as the product of the tire damping coefficient (c_{T_i}) and the tire deflection velocity ($\dot{TD}_i$). However, in ride dynamics it is common to consider it as zero.

$$F_{CT_i} = c_{T_i} \dot{TD}_i \tag{2.29}$$

The tire velocities of the quarter car model (QC), the half car models (HC1 and HC2) and the full car model are evaluated by the integration of Equations 2.4, 2.18, 2.10 and 2.27, respectively.

Suspension spring

The force by the suspension spring is given in Equation 2.30 and it is calculated by multiplying the spring constant (k) with the suspension travel (ST_i), as presented in Equations 2.3, 2.17, 2.9 and 2.26 for the quarter car model (QC), for the half car models (HC1 and HC2) and for the full car model, respectively:

$$F_{K_i} = k_i \, ST_i \tag{2.30}$$

where $i = \emptyset,\ F1,\ R1,\ F2,\ R2$. Ideally, a suspension system should adjust its characteristics in order to function properly under different road conditions. This adjustment is achieved through the use of

controllers (active and semi active suspensions) or through added nonlinearities in the components of the suspension (springs and dampers). In this thesis, the case of adding a nonlinear term in the suspension spring force is also studied and it is described in Equation 2.31 .

$$F_{K_i} = k_{l_i}\, ST_i \pm k_{nl_i}\, ST_i^3 \tag{2.31}$$

where $i = \emptyset,\ F1,\ R1,\ F2,\ R2$, k_{li} is the linear term and k_{nl_i} is the nonlinear term of the spring force. Equation 2.31 represents a Duffing oscillator which simulates with higher accuracy, compared with the linear force of Equation 2.30, a variable coil spring or a variable coil pitch or a suspension spring placed with a caster or a camper angle. The Duffing oscillator is presented in Figure 2.6 and it displays the effect of adding nonlinear terms ($\pm k_{nl_i}\, ST_i^3$) to the linear term ($k_{l_i}\, ST_i$). Based on Figure 2.6, the nonlinear spring force of Equation 2.31 stiffens the suspension system further compared to the linear spring force of Equation 2.30, providing greater forces at the same displacement.

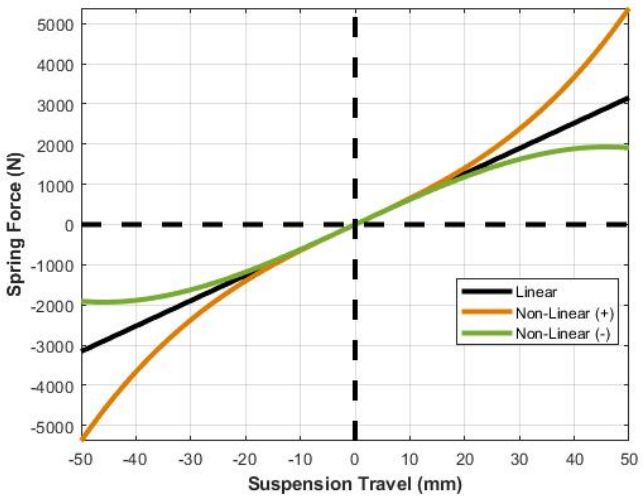

Figure 2.6: The effect of adding nonlinear terms ($\pm k_{nl_i}\, ST_i^3$) to the spring force

Suspension damper

As far as the damper is concerned, the force applied is presented in Equation 2.32 and it is calculated by multiplying the viscous damping coefficient (c) with the suspension travel velocity $\dot{ST}_s$).

$$F_{C_i} = c_i\, \dot{ST}_i \tag{2.32}$$

where $i = \emptyset,\ F1,\ R1,\ F2,\ R2$. The suspension stroke velocities ($\dot{ST}_i$) occur from the integration of Equations 2.3, 2.17, 2.9 and 2.26 for the quarter car model (QC), for the half car models (HC1 and HC2) and for the full car model, respectively. As far as the passive dampers are concerned, they are considered to operate with a constant coefficient ($c_i = const.$). Additionally, in this thesis, the suspension systems of the vehicle models (QC, HC1, HC2 and FC), presented before, are employed with semi-active suspensions operating with various control laws. The control laws studied are presented in separate section extensively.

2.1.6 Semi-active damper

Semi-active control strategies can maintain the reliability of passive devices using a very small amount of energy, providing simultaneously the versatility, the adaptability and the higher performance of fully active systems. Various control methods have been employed for years to vehicle suspensions. Linear controllers are normally based on the optimal control (LQR/LQG), the skyhook principle or robust control (H∞ and μ-synthesis). In this thesis, we will concentrate on the skyhook principle.

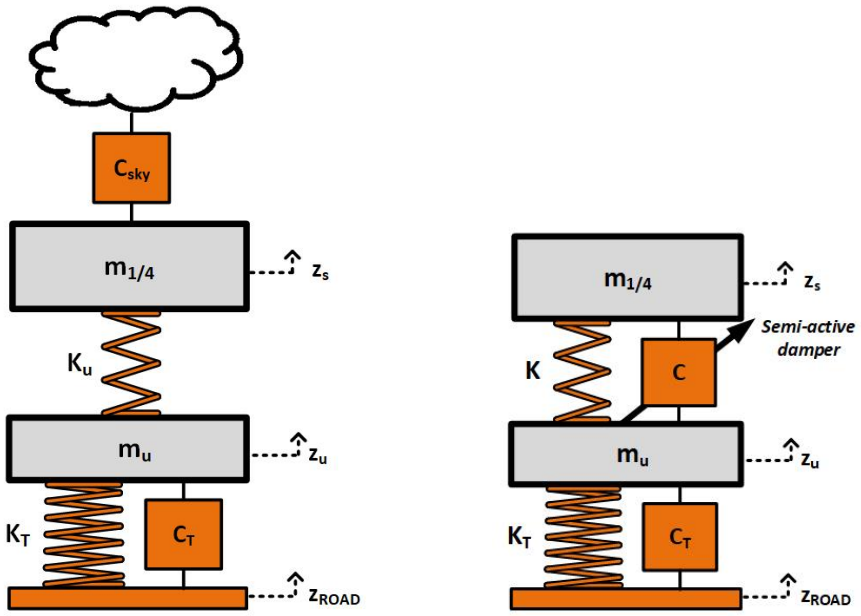

(a) The ideal concept. (b) The practical concept.

Figure 2.7: The quarter car representations of skyhook control algorithms

The ideal skyhook concept is presented in Figure 2.7, where a passive damper (C_{sky}) is hooked to an imaginary inertial reference point (i.e., sky, a ceiling that remains vertically fixed relative to a ground reference). With this configuration, when the upper mass is moving up and the two masses are getting closer, the damping constant should ideally be zero, whereas when the upper mass is moving down and the two masses are getting closer, the skyhook control ideally calls for an infinite

damping constant (C_{sky}). However, this is impractical, because the damper could achieve nor a zero neither an infinite damping constant in reality due to its physical limitations. Thus, a soft and a stiff damping are applied instead of a zero and infinite value, respectively. The above is achieved through the use of a controllable damper (C_i), as it is presented in Figure 2.7b, where the damping constant switches between soft and stiff damping coefficient with respect to operational conditions set by the suspension designer. Therefore, the Logical control strategy of Equation 2.33 is employed and is the most common control law that has been implemented for semi-active suspension systems in order to approach the ideal skyhook concept.

$$C_i = \begin{cases} C_{min} & ,if\ condition \leq 0 \\ f(C_{max}) & ,if\ condition > 0 \end{cases} \tag{2.33}$$

where $i = \emptyset,\ F1,\ R1,\ F2,\ R2$.

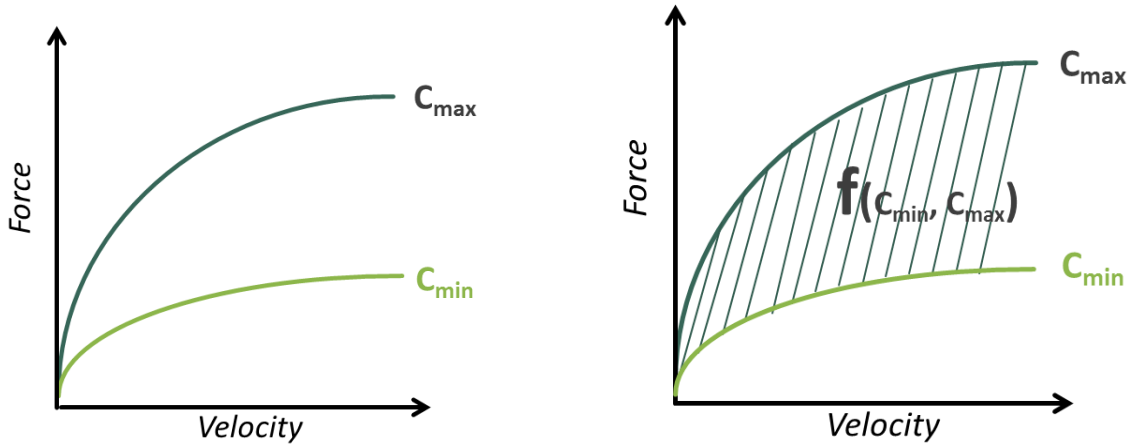

(a) On-off semi-active damper.

(b) Continuous semi-active damper.

Figure 2.8: The types of semi-active dampers according to the switching function of the damping coefficient

As far as the Logical Control Strategies are concerned, the two most common types of logical semi active dampers are the "on-off" and the continuous ones, as it is presented in Figure 2.8. For the on-off logical dampers (Figure 2.8a) the damping is switched between the minimum and maximum level based on conditions that define the damper, while for the continuous logical dampers, (Figure 2.8b), the damping is adjusted in the whole range between the minimum and maximum levels. The main types of logical semi active dampers are the Skyhook 2 states Control (SH-2), Skyhook Linear Control (SH-L), Acceleration Driven Damper Control (ADD), and two different versions of the combination of Skyhook and ADD Control (SH-ADD-1 and SH-ADD-2). All the above are comfort oriented, improving the ride comfort of the passengers by adjusting the damping coefficient of the suspension system according to the dynamic behavior of the vehicle and its response to the applied road excitation.

Many different versions of these algorithms have been presented in the past, by changing slightly their operational conditions.

Skyhook two states damper control (SH-2).

The 2-states control is an on-off strategy consisting of two states in which the damping factor (C_i) switches between soft and stiff damping coefficient according to the sign of the product of $\dot{ST}$ and $\dot{z}_s$. The effect of the Skyhook control scheme is to minimize the absolute velocity of the upper mass. The equation describing the control algorithm is presented in Equation 2.34:

$$C_i = \begin{cases} C_{min} & , \quad if\ \dot{ST}\ \dot{z}_s < 0 \\ C_{max} & , \quad if\ \dot{ST}\ \dot{z}_s > 0 \end{cases} \tag{2.34}$$

where $\dot{ST}$ is the stroke velocity of the damper, and C_{min} and C_{max} are the minimum and maximum damping factors achievable by the considered controlled damper, depicting the soft and the stiff damping coefficient respectively.

Skyhook linear approximation damper control (SH-L).

An improved version of Skyhook control is used to achieve variable damping for additional energy saving. The linear approximation of the Skyhook control includes the change of the damping factor C_u according to the sign of the product of $\dot{ST}$ and $\dot{z}_s$:

$$C_i = \begin{cases} C_{min} & , \quad if\ \dot{ST}\ \dot{z}_s < 0 \\ \frac{\alpha C_{max}\ \dot{ST} + (1-\alpha)\ C_{max}\ \dot{z}_s}{\dot{ST}} & , \quad if\ \dot{ST}\ \dot{z}_s > 0 \end{cases} \tag{2.35}$$

where $\alpha \in [0,1]$ is a tuning parameter that modifies the closed-loop performances and enables the controller to adjust its stiff value (C_{max}) according to the needs of the application and save more energy. More specifically, when a = 1, this control law is equivalent to the two-state Skyhook control. The difference relies on the fact that, according to the third expression (when $\dot{ST}\dot{z}_s > 0$), such a control provides an infinite number of damping coefficients, providing the ability of tuning it to be continuous.

Acceleration driven damper control (ADD).

This strategy has proven to be optimal in the sense that it minimizes the vertical body acceleration when no road information is available. The current control law is similar to the SH-2 approximation

of the Skyhook algorithm, with the difference that the switching law depends on body acceleration $\ddot{z}_s$ rather than the body speed $\dot{z}_s$.

$$C_i = \begin{cases} C_{min} & , \quad if \quad \dot{ST}\ \ddot{z}_s \leq 0 \\ C_{max} & , \quad if \quad \dot{ST}\ \ddot{z}_s > 0 \end{cases} \tag{2.36}$$

The ADD design is well adapted to comfort improvement but not to road-holding, being mainly road comfort oriented. The switching may influence the closed-loop performances, increasing the chatter effect significantly due to the swift changing of values of the sprung acceleration which is involved in the operational conditions.

Mixed Skyhook-Acceleration driven damper control (SH-ADD-1).

The SH and ADD algorithms present complementary behaviors in terms of performance, with SH providing the best performance at low frequency (around the body resonance), and ADD ensuring optimality at mid and high frequency (beyond the body resonance). Therefore, a mixed control law has been propped using a very simple but effective frequency range selector.

$$C_i = \begin{cases} C_{SH-2} & , \quad if \quad \ddot{z}_s^2 - a^2\dot{z}_s^2 \leq 0 \\ C_{ADD} & , \quad otherwise \end{cases} \tag{2.37}$$

$$C_i = \begin{cases} C_{min}, & if \quad \left(\ddot{z}_s^2 - a^2\dot{z}_s^2 \leq 0 \quad and\ \dot{ST}\dot{z}_s \leq 0\right) \\ & or \quad \left(\ddot{z}_s^2 - a^2\dot{z}_s^2 > 0 \quad and\ \dot{ST}\ddot{z}_s < 0\right) \\ C_{max}, & otherwise \end{cases} \tag{2.38}$$

The parameter "α" represents the frequency limit between the low and the high frequency ranges. Specifically, the value of "α" is set at the crossover frequency (in rad/s) between SH and ADD. This law is almost optimal as it provides a mix of the best performance of the SH and ADD.

Mixed Skyhook-Acceleration driven damper control with 1 sensor (SH-ADD-2).

The current law compromises the complementary performances of soft and stiff passive suspensions. Stiff suspension is able to damp optimally the body resonance, but without a desiring filtering at high frequencies. On the other hand, a soft suspension ensures the best filtering but with the drawback of a poorly damped body resonance. This law operates according to the current value of $\ddot{z}_s^2 - a^2\dot{z}_s^2$, as shown in Equation 2.39

$$C_i = \begin{cases} C_{min}, & if \quad \ddot{z}_s^2 - a^2 \dot{z}_s^2 \geq 0 \\ C_{max}, & if \quad \ddot{z}_s^2 - a^2 \dot{z}_s^2 < 0 \end{cases} \tag{2.39}$$

The soft damping condition is selected when it is positive, otherwise the hard-damping condition is used. Similarly to the mixed SH-ADD-1, the amount $\ddot{z}_s^2 - a^2 \dot{z}_s^2$ can be considered as a simple "frequency-range selector", where the parameter "a" represents the limit between the ranges of low and high frequency.

2.2 Seat Dynamics

The ride quality concept sweeps over many disciplines in automotive engineering, such as suspension design, the temperature control inside the cabin, the ergonomics of the car and many other factors. In this thesis, we are concerned with one aspect of these and more specifically the design of the seat suspensions, which is mainly related to ride dynamics.

A good design of a seat suspension, can improve to some extent dynamic comfort, but cannot eliminate the compromise with the static comfort. The above fact implies the conflict in the seat suspension systems, where the increasing initial deformation of the system leads to better isolation of the accelerations and a more comfortable seat. To isolate vibrations using a seat suspension, linear springs and dampers are typically used mainly in the literature for their modeling. However, the standard commercial seats suspended by the use of conventional passive suspensions have reached their full potential despite attempts in the literature to optimize them and obtain their optimal design. Moreover, the semi-active and active suspensions despite being gradually used more in seats and having increased industrial and academic interest, they are more expensive, complicated and less reliable than passive suspensions. Thus, respectively with the passive ones, they have been put aside to some extent because of their above disadvantages. Therefore, the modeling and the optimization of different types of vibration isolators, whose structures could be fitted in seat suspensions, have been discussed extensively in the literature. The main ones using negative stiffness elements are studied in this work.

2.2.1 Passive Suspension (PS)

The classic 1DoF model, illustrated in Figure 2.9, is often used to isolate the vibrations of a mass (m_{se}) and consists of a linear stiffness spring (K_v) and a damper (C_v). Its governing equation is presented in Equation 2.40:

$$m_{se}\, \ddot{z}_s + C_v(\dot{x} - \dot{z}_s) + K_v(x - z_s) = 0 \tag{2.40}$$

where z_s (m) is the response of the vehicle's body displacement and $\dot{z}_s$ its velocity (m/s). These are used as the excitation of the system.

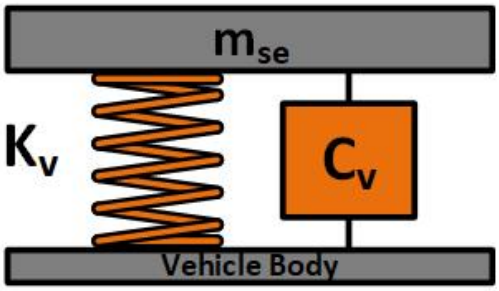

Figure 2.9: Passive seat suspension system with linear spring and damper (PS)

2.2.2 Negative Stiffness Suspension 1 (Carrella et al. - NSS1)

Generally, "quasi-zero-stiffness" (QZS) mechanisms can be achieved by combining a negative stiffness element with a positive stiffness element. A simple model is described by Carrella et al. [5–7] and the structure is presented in Figure 2.10. The main feature of this system is the use of two symmetric negative stiffness structures, including of one inclined spring (K_h), coupled with a positive stiffness structure (K_v). When the suspension system is loaded, all the springs are compressed so that the springs (K_h) are in horizontal position and the static load is applied entirely to the vertical spring (K_v). This is the static equilibrium, while the displacement around it is where the research interest lies. The inclined springs provide a negative stiffness in the vertical direction and they compensate the positive stiffness of the vertical spring.

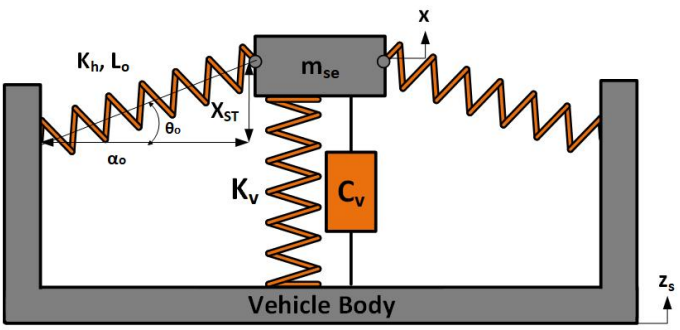

Figure 2.10: Seat suspension system based on Carrella et al. [5–7] at a random position x under the excitation of z_s (NSS1)

The vertical component of the force applied by the inclined springs is:

$$f_N = 2 * K_h * (L_o - L_h) * \sin\theta \tag{2.41}$$

Nomenclature		
Parameter	**Unit**	**Description**
x	$[m]$	displacement of mass (m) from the desired static E.P.
$\dot{x}$	$[m/s]$	velocity of mass (m)
$\ddot{x}$	$[m/s^2]$	acceleration of mass (m)
m_{se}	$[kg]$	total mass of seat (13.6 kg) and passenger (81.4 kg)
K_h	$[N/m]$	horizontal spring stiffness
K_v	$[N/m]$	vertical spring stiffness
C_v	$[N.s/m]$	damping coefficient
X_{ST}	$[m]$	initial deformation of vertical spring
L_o	$[m]$	initial length of underformed horizontal spring
a_o	$[m]$	distance from the wall
α	-	spring stiffness ratio (K_h/K_v)
Additional Nomenclature for NSS1		
θ_o	$[deg]$	initial angle of horizontal spring
Additional Nomenclature for NSS2		
b	$[m]$	bar length
Additional Nomenclature for NSS3		
R	$[m]$	cam radius
r	$[m]$	roller radius
d	$[m]$	distance from cam center
u_2	$[m]$	precompression of horizontal spring (=0.01 m)
Additional Nomenclature for NSS4		
K_S	$[N/m]$	vertical spring's stiffness
b	$[m]$	bar length
u_o	$[m]$	distance from horizontal level
m_d	$[kg]$	inner mass (=1 kg)

Table 2.2: Nomenclature of the parameters used in the seat models PS, NSS1, NSS2, NSS3 and NSS4

where L_h is the length of the compressed spring and θ is the angle between the spring's position and the vertical plane, as shown in Figure 2.10, and by defining L_o and L_h as:

$$L_o = \sqrt{X_{ST}^2 + a_o^2} \;\; and \;\; L_h = \sqrt{x^2 + a_o^2} \tag{2.42}$$

Finally, the equation of force applied by the negative element results in Equation 2.43:

$$f_N = 2K_h \left(\frac{\sqrt{X_{ST}^2 + a_o^2}}{\sqrt{x^2 + a_o^2}} - 1 \right) x \tag{2.43}$$

Additionally, the geometrical parameters, which are related with the negative structures, are defined as $\gamma = a_o/L_o = cos\theta_o$. When $\gamma = 0$, the inclined springs are initially vertical, while, when $\gamma = 1$, they lie horizontally. At the static equilibrium $(x = 0)$, the load is fully supported by the vertical linear spring and the inclined springs are aligned to the horizontal plane. By applying the Hooke's Law in the equilibrium, the following relationship occurs regarding the initial deformation of the system, $K_{\mathrm{v}}X_{ST} = mg$. In any other position where the force f_N (Equation 2.43) is applied on the mass, the following equation (Equation 2.44) applies:

$$m_{se}\,\ddot{x} + C_v(\dot{x} - \dot{z}_s) + K_{\mathrm{v}}(x - z_s) - f_N = 0 \tag{2.44}$$

and by applying Taylor's series around the equilibrium position $(x = 0)$ of f_N and keeping the polynomials below 3rd order, Equation 2.45 occurs:

$$\begin{aligned} m_{se}\,\ddot{x} + C_v(\dot{x} - \dot{z}_s) + K_{\mathrm{v}}(x - z_s) - K_{\mathrm{v}}\left(2\alpha\frac{1-\gamma}{\gamma}\right)(x - z_s) \\ + K_{\mathrm{v}}\left(\frac{\alpha}{L_o^2\gamma^3}\right)(x - z_s)^3 = 0 \end{aligned} \tag{2.45}$$

where z_s (m) is the response of the vehicle's body displacement and $\dot{z}_s$ its velocity (m/s). These are used as the excitation of the system.

2.2.3 Negative Stiffness Suspension 2 (Thahn Le et al. - NSS2)

To improve the isolation of seat vibrations under low excitation frequencies, a model based on the concept of the previous QZS is proposed by T. D. Le et al. [8–12]. The main feature of this system is the use of two symmetric negative stiffness structures, consisting of one inclined bar (b) and one horizontal spring (K_h) each, coupled with a positive stiffness element (K_{v}). Applying the current design, the load carrying capacity of the system is the same as a conventional suspension and the overall size of the construction is reduced for easier practical application. The proposed system has a wider frequency range compared to a non-NSS system.

The conditions that have to be satisfied so to ensure that the suspension system has the widest possible range of permissible displacements for which its dynamic stiffness is almost zero and the size of the construction is as small as possible, are shown in Equation 2.46 - 2.48:

$$\gamma_2 \approx 1 \;\; but \;\; \gamma_2 > 1 \tag{2.46}$$

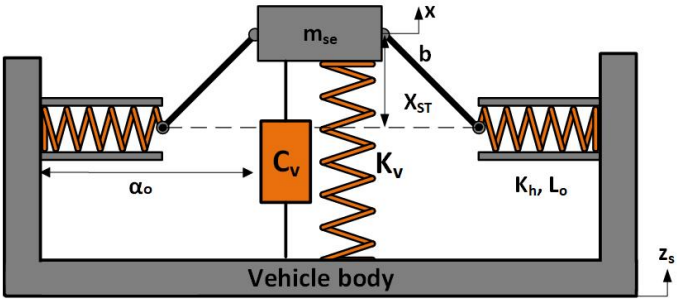

Figure 2.11: Seat suspension model system on T. D. Le et al. [8–12] at a random position x under the excitation of z_s (NSS2)

$$\gamma_2 \leq \gamma_1 \tag{2.47}$$

$$\alpha \leq \frac{\gamma_1}{2(1+\gamma_1-\gamma_2)} \tag{2.48}$$

The negative force of the mechanism, applied by the horizontal springs is :

$$f_N = 2K_h\left(\frac{L_o}{\sqrt{b^2-x^2}} - \frac{a_o}{\sqrt{b^2-x^2}} + 1\right)x \tag{2.49}$$

Considering that the initial deformation occurs as $X_{ST} = \sqrt{b^2-(a_o-L_o)^2}$, that the Hooke's Law implies $mg = K_v X_{ST}$ in the equilibrium, and finally that based on the design of the system $\gamma_1 = \frac{b}{L_o}$ and $\gamma_2 = \frac{a_o}{L_o}$, Equation 2.49 is converted to 2.50:

$$f_N = 2K_h\left(\frac{1}{\sqrt{\gamma_1^2-x^2}} - \frac{\gamma_2}{\sqrt{\gamma_1^2-x^2}} + 1\right)x \tag{2.50}$$

Thus, based on the above, the equation of motion of the seat results in:

$$m_{se}\,\ddot{x} + C_v(\dot{x}-\dot{z}_s) + K_v(x-z_s) - f_N = 0 \tag{2.51}$$

and finally, by applying Taylor series expansion to f_N around the static equilibrium ($x = 0$) and by keeping the until 3rd order polynomials, the equation of motion of the system in the steady state is approximated by Equation 2.52:

$$m_{se}\,\ddot{x}+C_v(\dot{x}-\dot{z}_s)+K_{\mathrm{v}}(x-z_s)-K_{\mathrm{v}}\left(2\alpha\frac{1-\gamma_2+\gamma_1}{\gamma_1}\right)(x-z_s) \\ +\alpha\frac{K_{\mathrm{v}}}{L_o^2}\left(\frac{\gamma_2-1}{\gamma_1^3}\right)(x-z_s)^3=0 \tag{2.52}$$

where z_s (m) is the response of the vehicle's body displacement and $\dot{z}_s$ its velocity (m/s). These are used as the excitation of the system.

2.2.4 Negative Stiffness Suspension 3 (Yan et al. - NSS3)

An innovative non-linear seat suspension is the conceptual design of cam–roller–spring mechanisms (CRSMs) proposed by Yan et al. [13], whose particular behavior differs a lot from the existing ones in the literature. The current model is presented in Figure 2.12. This suspension comprises a scissor-like frame, a vertical spring, a negative stiffness mechanism and a damper. When load is applied, the upper frame with the curved end descends, the bearings roll into the curved edge disc and the horizontal springs are compressed. The system eventually balances and the bearings come into contact with the tops of inner disk. When driving the vibrations are transmitted to the driver's seat suspension frame. The edge curve component rises and descends with the center as a balancing point, thus it isolates the vibrations.

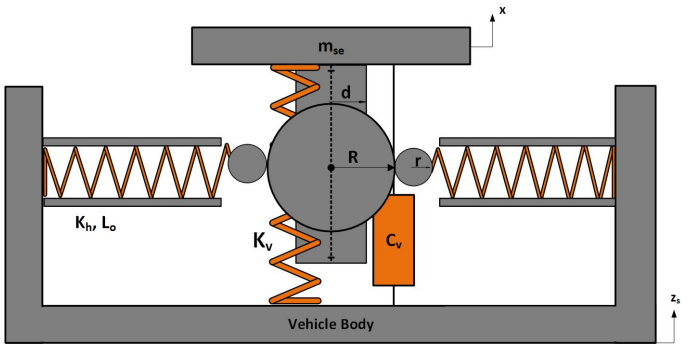

Figure 2.12: Seat suspension system based on Yan et al. [13] at a random position x under the excitation of z_s (NSS3)

The geometrical constraints needed to be satisfied, so as to ensure the proper function of the system, are the following:

$$r,d>0 \tag{2.53}$$

$$R > d \tag{2.54}$$

$$u_2 > 0 \tag{2.55}$$

The initial precompression u_2 of the horizontal springs is selected equal to 0.01 m, following also the constraint of Equation 2.55, for ensuring the contact of the roller with the cam in the extreme positions.

Considering the starting point of the coordinate system at the equilibrium, the initial deformation $X_{ST} = \sqrt{(R+r)^2-(d+r)^2}$ and the relation $K_v X_{ST} = mg$, occur by applying the Hooke's Law. Thus, by replacing in Equation 2.57 the negative force (f_N) of the mechanism of Equation 2.56, the Equation 2.58 gives us the equation of motion of the seat under excitation, :

$$\begin{aligned} f_N = {} & 2K_h u_2 \left(\frac{x}{\sqrt{(R+r)^2-x^2}} \right) \\ & +2K_h(\sqrt{(R+r)^2-x^2}-d-r)\left(\frac{x}{\sqrt{(R+r)^2-x^2}} \right) = 0 \end{aligned} \tag{2.56}$$

$$m_{se}\,\ddot{x} + C_v(\dot{x}-\dot{z_s}) + K_v(x-z_s) - f_N = 0 \tag{2.57}$$

$$\begin{aligned} & m_{se}\,\ddot{x} + C_v(\dot{x}-\dot{z_s}) + K_v(x-z_s) - 2K_h u_2 \left(\frac{x-z_s}{\sqrt{(R+r)^2-(x-z_s)^2}} \right) \\ & -2K_h(\sqrt{(R+r)^2-(x-z_s)^2}-d-r)\left(\frac{x-z_s}{\sqrt{(R+r)^2-(x-z_s)^2}} \right) = 0 \end{aligned} \tag{2.58}$$

where z_s (m) is the response of the vehicle's body displacement and $\dot{z}_s$ its velocity (m/s). These are used as the excitation to the system.

2.2.5 Negative Stiffness Suspension 4 (Antoniadis et al. - NSS4)

KDamper is an novel concept of passive suspension proposed by Antoniadis et al. [14, 15] and is based essentially on the ideal combination of appropriate stiffness elements, including a negative mechanism. The Kdamper concept is already implemented in a large variety of technological appli-

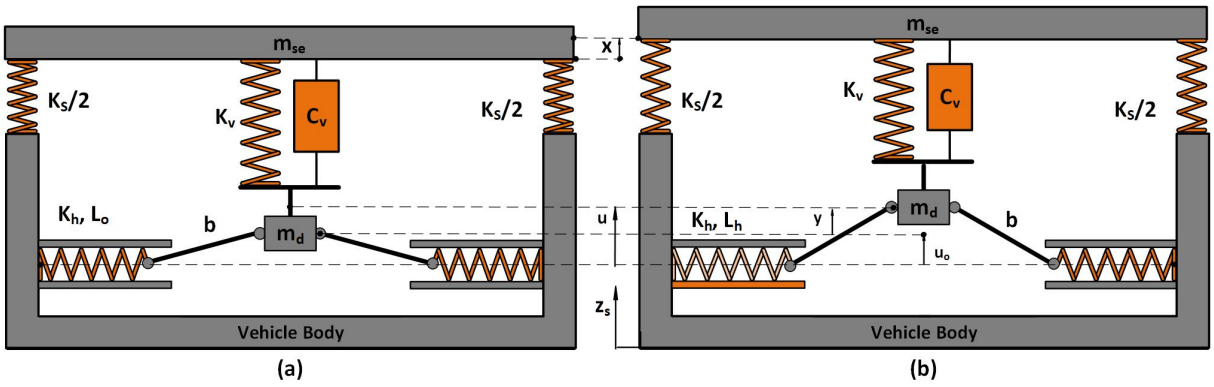

Figure 2.13: Seat suspension system based on Antoniadis et al. [14, 15] the left in the static equilibrium and the right at a random position x under the excitation of z_s (NSS4)

cations, and in this thesis is going to be applied in a seat suspension. The reason is that the model can provide much better vibration isolation and damping at low frequencies than other tuned mass damper models (TMD). The KDamper does not require any reduction in overall system stiffness, thus it overcomes the main drawback of QZS, which require less permissible load compared to the conventional linear oscillators.

KDamper is designed to exhibit the same overall (static) stiffness as a linear oscillator, but it is designed to be stable both statically and dynamically despite including a negative mechanism. It is designed as illustrated in Figure 2.13 and consists of a mass (m_{se}) which is supported by two parallel linear coil springs (K_S and K_v) and a damper (C_v). The damper (C_v) and the spring (K_v) are also connected to a smaller mass (m_d). The negative stiffness is achieved by a set of two symmetrical linear horizontal springs (K_h,) which support the internal mass (m_d) by means of a modular mechanism. The static equilibrium of the system is illustrated in Figure 2.13(a). The disturbed position after applying the excitation of the sprung mass is shown in Figure 2.13(b).

The equations of motion are the following:

$$m_{se}\,\ddot{x} + C_v(\dot{x}-\dot{y}) + K_S(x-z_s) + K_v(x-y) = 0 \tag{2.59}$$

$$m_d\ddot{y} - C_v(\dot{x}-\dot{y}) - K_v(x-y) + f_{ND}(u-z_s) = 0 \tag{2.60}$$

where:

$$f_{ND}(u) = f_N(u) - f_N(u_0) = f_N(u) - f_{N0} \tag{2.61}$$

$$u = u_0 + y \tag{2.62}$$

$$f_{N0} = f_N(u_0) \tag{2.63}$$

where u_o is $1mm$, and is close to zero so as to make a symmetric response around the equilibrium, and the inner mass is chosen to be constant and equal to 1 kg, i.e. approximately 1% of the mass of the entire load applied to the system. The selection of this value follows the work of Antoniadis et al. [124], who investigated the value of the ratio m_{se}/m$_d$, concluding in a value around 0.01.

The value of X_{ST} is extracted by Equation 2.64:

$$X_{ST} = [(m + m_D)g - f_{N0}]/K_S \tag{2.64}$$

Based on the above, the following expression for the nonlinear force (f_N), which is applied by the two symmetric horizontal springs (K_h), is obtained.

$$f_N(u) = -2K_h\left(1 + \frac{L_o - a_o}{\sqrt{b^2 - u^2}}\right)u = -2K_h\left(1 + c_I\frac{1}{(1 - \frac{u^2}{b^2})^{\frac{1}{2}}}\right)u \tag{2.65}$$

where L_o is the initial length of the undeformed spring K_h, while L_h (t) is the length of springs K_h and is defined as:

$$L_h = a_o - \sqrt{(b^2 - u^2)} \tag{2.66}$$

while a coefficient is defined as:

$$c_I = \frac{L_o - a_o}{b} \tag{2.67}$$

where when $c_I = 0$, the two horizontal springs are equivalent to a negative spring with constant stiffness $K_N = -2K_h$.

The final equations are shown below:

Equation of m$_{se}$:

$$m_{se}\,\ddot{x} + C_v(\dot{x} - \dot{y}) + K_S(x - z_s) + K_v(x - y) = 0 \tag{2.68}$$

Equation of m_d:

$$\begin{aligned} & m_d\ddot{y} - C_v(\dot{x}-\dot{y}) - K_v(x-y) \\ & -2K_h\left[1+c_I\left(\frac{1}{\sqrt{1-\frac{(u_o+y-z_s)^2}{b^2}}}\right)\right](u_o+y-z_s) \\ & +2K_h\left[1+c_I\left(\frac{1}{\sqrt{1-\frac{u_o^2}{b^2}}}\right)\right]u_o = 0 \end{aligned} \tag{2.69}$$

where z_s (m) is the response of the vehicle's body displacement and $\dot{z}_s$ its velocity (m/s). These are used as excitation to the system.

2.3 Passenger's Body Dynamics

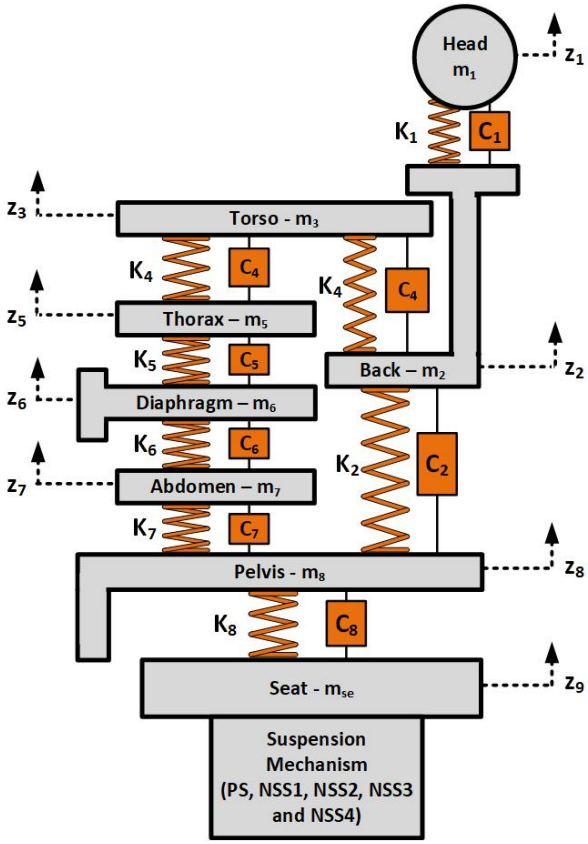

Figure 2.14: Seat-Passenger Model

In order to investigate in depth the ride comfort, the passenger is modeled as shown in Figure 2.14 [125]. Different parts of the human body such as the pelvis, the diaphragm, the thorax etc. are

described via several $m-c-k$ subsystems. The governing equations of the passenger model, are the following and the parameters of each body part are presented in Table 2.3.

Seat:

$$m_{se}\,\ddot{z}_9 + c_9(\dot{z}_9 - \dot{z}_s) + k_9(z_9 - z_s) - c_8(\dot{z}_8 - \dot{z}_9) - k_8(z_8 - z_9) = 0 \tag{2.70}$$

$$\begin{aligned} m_8\ddot{z}_8 - c_2(\dot{z}_2 - \dot{z}_8) - k_2(z_2 - z_8) - c_7(\dot{z}_7 - \dot{z}_8) - k_7(z_7 - z_8) \\ +c_8(\dot{z}_8 - \dot{x}) + k_8(z_8 - x) = 0 \end{aligned} \tag{2.71}$$

Abdomen:

$$m_7\ddot{z}_7 + c_7(\dot{z}_7 - \dot{z}_8) + k_7(z_7 - z_8) - c_6(\dot{z}_6 - \dot{z}_7) - k_6(z_6 - z_7) = 0 \tag{2.72}$$

Diaphragm:

$$m_6\ddot{z}_6 + c_6(\dot{z}_6 - \dot{z}_7) + k_6(z_6 - z_7) - c_5(\dot{z}_5 - \dot{z}_6) - k_5(z_5 - z_6) = 0 \tag{2.73}$$

Thorax:

$$m_5\ddot{z}_5 + c_5(\dot{z}_5 - \dot{z}_6) + k_5(z_5 - z_6) - c_3(\dot{z}_3 - \dot{z}_5) - k_3(z_3 - z_5) = 0 \tag{2.74}$$

Torso:

$$m_3\dot{z}_3 + c_3(\dot{z}_3 - \dot{z}_5) + k_3(z_3 - z_5) - c_4(\dot{z}_3 - \dot{z}_2) - k_4(z_3 - z_2) = 0 \tag{2.75}$$

Back:

$$m_2\ddot{z}\text{|`}_2 - c_4(\dot{z}_3 - \dot{z}_2) - k_4(z_3 - z_2) + c_2(\dot{z}_2 - \dot{z}_8) + k_2(z_2 - z_8) = 0 \tag{2.76}$$

Head:

$$m_1\ddot{z}_1 + c_1(\dot{z}_1 - \dot{z}_2) + k_1(z_1 - z_2) = 0 \tag{2.77}$$

Description	m_i **[kg]**	c_i **[N.s/m]**	k_i **[N/m]**
Seat (*se*)	13.6	–	–
Pelvis (8)	27.70	378	25500
Abdomen (7)	6.20	298	8941
Diaphragm (6)	0.46	298	8941
Thorax (5)	1.38	298	8941
Torso (3-4)	33.33	298	8941
Back (2	6.94	3651	53460
Head (1)	6.20	3651	53460
Passenger's Mass = $\sum_{i=1}^{8} m_i$ = 81.4 kg			

Table 2.3: Parameters of the passenger's model

2.4 Performance Metrics

In this thesis, we evaluate the vehicle's suspension systems, both primary and secondary, in terms of various aspects of performance. Thus, we do not focus only on the best ways of overcoming the well known trade-off of vehicle dynamics (ride comfort and vehicle stability = road holding and handling), but also we try to eliminate another trade-off that has appeared with the use of controlled suspensions, the one between the dissipated energy and the vibration control performance. In addition, we consider also the chatter effect as an important factor for suspension design, as far as semi-active suspension are concerned. In this Chapter, these aspects are investigated and quantified.

2.4.1 Transient Response

Systems like vehicles, which include energy storage, cannot respond instantaneously when they are subjected to disturbances and thus, they exhibit transient responses. The transient response depends on the initial conditions of the system. Moreover, for comparing transient responses, it is common to consider that the vehicle is initially at rest and all the time derivatives therefore are zero. Then, a step input is applied to the vehicle as an excitation, as shown in Figure 2.16. Hence, in order to specify the transient response characteristics, it is common to use few of the following metrics, as shown in Figure 2.15:

1. Rise Time (t_r) refers to the time required for a signal to change from a specified low value to a specified high value. Typically, these values are 10% and 90% of the maximum value (M_p).

2. Peak Time (t_p) is the time required for the response to reach the first peak of the overshoot and it displays the responsiveness of the system.

3. Peak, (M_p) is the maximum value of the response and corresponds to peak time (t_p).

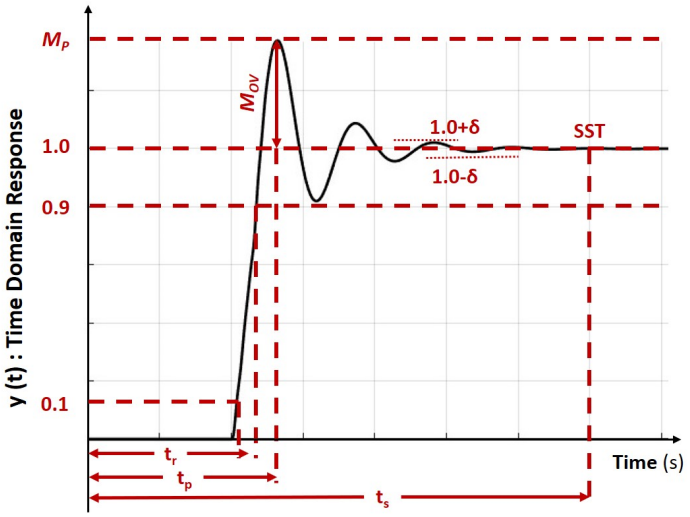

Figure 2.15: The time-domain metrics for transient response

4. Steady State (SST) is the value where the response of the system has settled at the settling time (t_s).

5. Overshoot (M_{OV}) is when a signal or function exceeds its target or the level of exceeding the steady state value (SST).

6. Settling Time (t_s) is defined as the time required for the system in order for the response to reach and stay within $\delta\%$ range of the steady-state value (SST). The settling time is related to the largest time constant of the system.

In vehicle dynamics, transient response is investigated for assessing the suspension performance, since vehicles are mostly time-domain systems and they have to exhibit acceptable time responses. Therefore, the time-domain metrics presented above are quite important. Except for certain applications where oscillations cannot be tolerated, it is desirable that the transient response be sufficiently responsiveness and damped.

2.4.2 Ride Comfort

A suspension system should be able to isolate a vehicle body from road disturbances, aiming to reduce vehicle body acceleration and provide good ride quality. The ride comfort can be quantified by the measurements of the sprung mass' vertical acceleration ($\ddot{z}_s$), when the measurements are not applicable in the seat or the passenger. More specifically, the ride comfort could be measured via the weighted root mean square (RMS) of the acceleration ($\ddot{z}$), Vibration Dose Value (VDV) and the Crest Factor (CF). These characteristics are proposed by the ISO-2631 standard which evaluates the

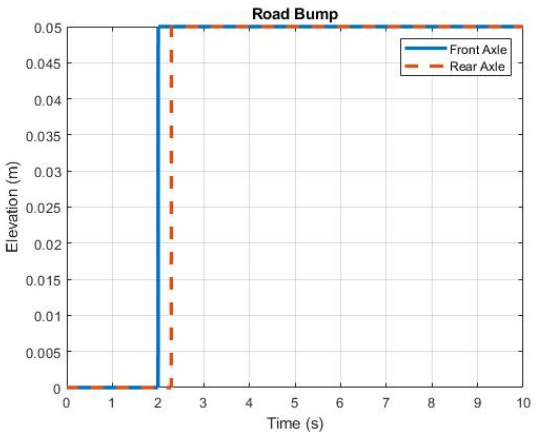

Figure 2.16: Step input used for evaluating transient response

human exposure to whole-body vibration [96]. More specifically, the weighted RMS acceleration is calculated as follows:

$$RC = RMS(\ddot{z}_{w_i}) = \left[\frac{1}{T}\left(\int_0^T \ddot{z}_{w_i}(t)^2 dt\right)\right]^{\frac{1}{2}} \tag{2.78}$$

where T is the duration of the measurement in seconds, $\ddot{z}_{w_i}$ is the weighted acceleration as a function of time (m/s^2) and i i is the selected subsystem of the driver or the vehicle model. In our case, where no seat model or passenger model are used, $i = s$. The frequency weighting curves, presented in the Figure 2.17, are based on ISO-2631 [96] and are applied according to Equation 2.79.

$$\ddot{Z}_{w_i} = WP_{i_1} * WA_{i_2} * \ddot{Z}_i \tag{2.79}$$

where $\ddot{Z}_i$ is the measured acceleration of $\ddot{z}_i$ in the frequency domain, WP are the principal frequency weightings related to health, comfort and perception depicting the weighting frequency for :

- for the z direction (i_1=k),
- for vertical recumbent direction except the head (i_1=k),
- for the x-y direction and for horizontal recumbent position (i_1=d)
- for motion sickness (i_1=f)

and finally WS is the additional frequency weightings related to

- seat back measurements (i_2=c),

- measurements for rotational vibrations (i_2=e),
- measurement of vibration under the head of recumbent person (i_2=j).

In case there is no need for additional weighting of the measurement, WA is equal to 1.

In cases where the basic evaluation may underestimate the effects of vibrations (high crest factors, occasional shocks and transient vibration), the running RMS value of the measured acceleration z_i is proposed as a metric along with the Maximum transient vibration value (MTVV), Vibration Dose Value (VDV) and the Crest Factor (CF) of the measurement is calculated through Equation 2.82 and 2.83, respectively.

$$RMS(\ddot{z}_{r_i}) = \left[\frac{1}{\tau}\left(\int_{t_0-\tau}^{t_0} \ddot{z}_{wr_i}(t)^2 dt\right)\right]^{\frac{1}{2}} \tag{2.80}$$

$$MTVV_i = max\left(\ddot{z}_i(t)\right) \tag{2.81}$$

$$VDV_i = \left[\int_0^T \left(\ddot{z}_i(t)\right)^4 dt\right]^{\frac{1}{4}} \tag{2.82}$$

$$CF_i = \frac{max(\ddot{z}_i)}{rms(\ddot{z}_i)} \tag{2.83}$$

where i is the selected subsystem of the driver or the vehicle model from Equation 2.1 - 2.2 so as to evaluate $\ddot{z}_i$, $\ddot{z}_{wr_i}(t)$ is the instantaneous frequency-weighted acceleration, τ is the integration time for running averaging, t is the time and t_0 is the time of observation. The additional metrics from Equation 2.80 - 2.83 are useful for evaluating health or comfort when:

$$\frac{MTVV(\ddot{z}_i)}{RMS(\ddot{z}_{w_i})} = 1.5 \tag{2.84}$$

$$\frac{VDV_i}{RMS(\ddot{z}_{w_i})T^{0.25}} = 1.75 \tag{2.85}$$

2.4.3 Seat-to-head transmissibility

The primary contact point for transmission of vertical whole body vibration (WBV) to drivers is through vehicle seat (amplifies or attenuates vibration at the base). Suspension seats, mostly used in off-road vehicles consist of low stiffness suspensions with low damping to attenuate vibration in

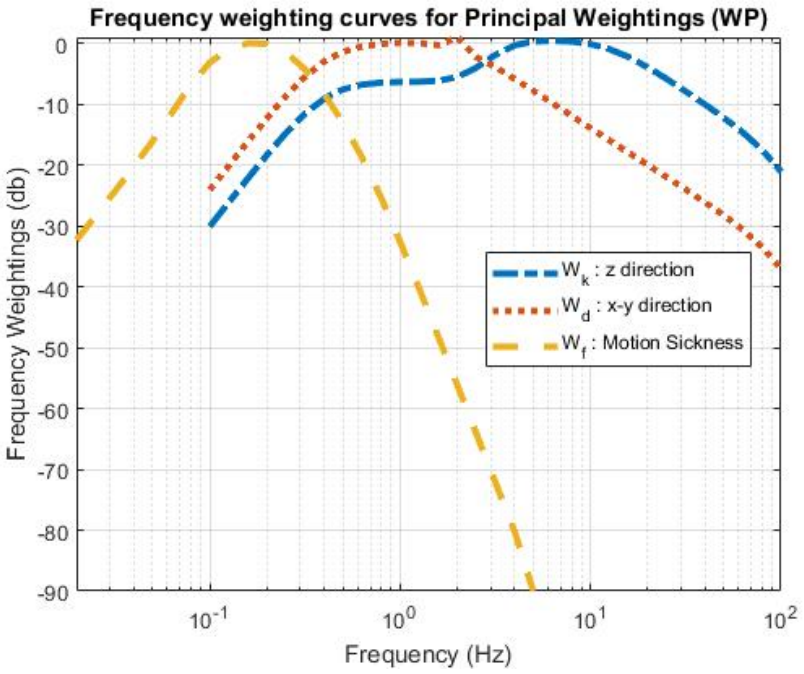

(a) Principal Frequency Weightings-WP.

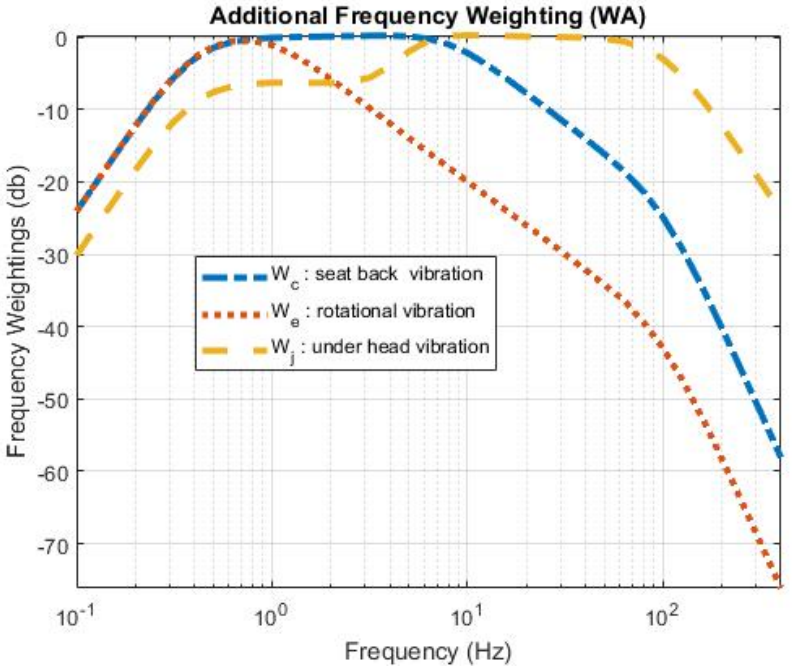

(b) Additional Frequency Weightings-WA.

Figure 2.17: Frequency Weightings of Measured Accelerations

some environments. The stiffness of the suspension has a considerable influence also in the isolation effectiveness and this could be depicted by Figure 2.18a. However, the efficiency of the seat still

depends on the vibration spectrum and the seat dynamics. The dynamic characteristics of a seat are measured by the transmissibility, which is a non-dimensional ratio of the vibration on the seat surface to the vibration of the seat base (sprung mass or chassis floor) as a function of frequency and can be used to quantify seat performance. Transmissibility (TR) is shown in the following equation:

$$TR = \frac{\ddot{z}_i}{\ddot{z}_{input}} \tag{2.86}$$

where $\ddot{z}_i$ (m/s^2) is the response of the seat (when i=seat) induced from the excitation of the system $\ddot{z}_{input}$ (m/s^2).

From Figure 2.18b, where the transmissibilities of the seat-input to the seat-output are presented, it is obvious that the use of a lower stiffness leads to a wider range of isolation frequencies. Designs 3 and 4 have a greater isolation performance than the other two, because of the decreased stiffness. Less stiffness leads to a greater static mass shift, and this relationship between isolation and static displacement is known as the main conflict in suspension designs, being outlined in Figure 2.18a. The frequency range in which a linear passive suspension operates is often limited by the maximum stiffness of the spring required to support a static constant mass load, and usually the system can only provide good efficiency for the high excitation frequencies. In the literature, more often the interest is turned on the transmissibility from seat to head (STHT), by using in Equation 2.86 with $i = 1 = head$. In biomechanical systems, researchers in the area of human response to whole-body vibration (WBV) consider the seat-to-head transmissibility (STHT) in capturing the perception of vibration of seated people for single-input/single-output motions [126–129]. Thus, in this thesis, STHT is studied by applying Equation 2.86 with $i = 1 = head$.

2.4.4 Road Holding and Handling

Important metrics indicating the dynamical behavior of the vehicle through the ride models (Figures 2.2, 2.3, 2.4 and 2.5) are the suspension travel and the tire deflection. The suspension travel (Equations 2.3, 2.9, 2.17 and 2.26) depicts the ability of the suspension system to support the vehicle's static weight. The vehicle static weight is well supported as long as the rattle space requirements of the vehicle are kept small. It can be quantified in terms of the variance of the suspension travel ($ST1$) or by the maximum value undergone by the suspension ($ST2$), as shown in Equations 2.87 - 2.88.

$$VST_i = \frac{1}{n}\sum_{j=1}^{n}(ST_{i,j} - \overline{ST})^2 = VAR(ST_i) \tag{2.87}$$

$$MST_i = MAX(ST_i) \tag{2.88}$$

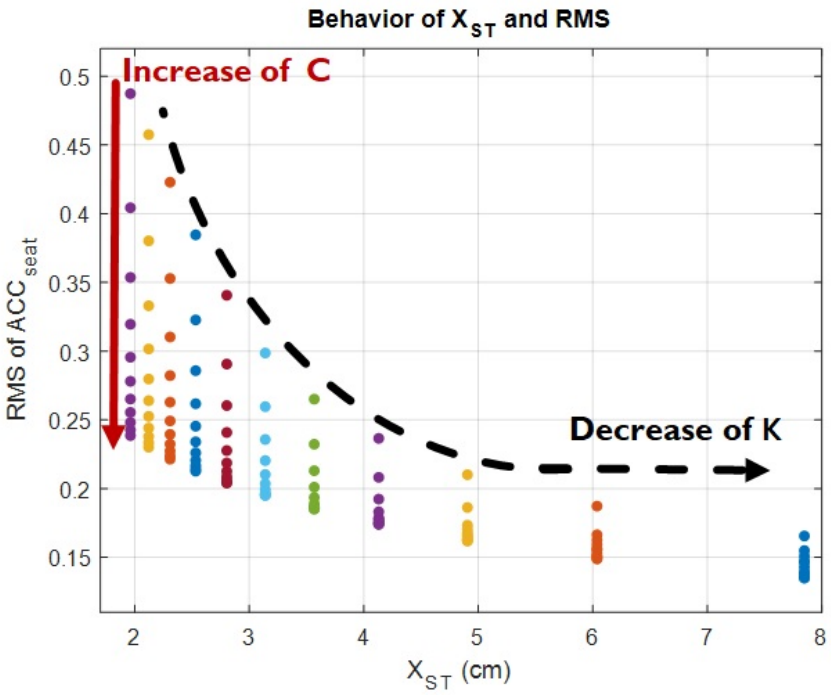

(a) Initial compression (X_{ST}) with the RMS of the vertical accelerations in the seat.

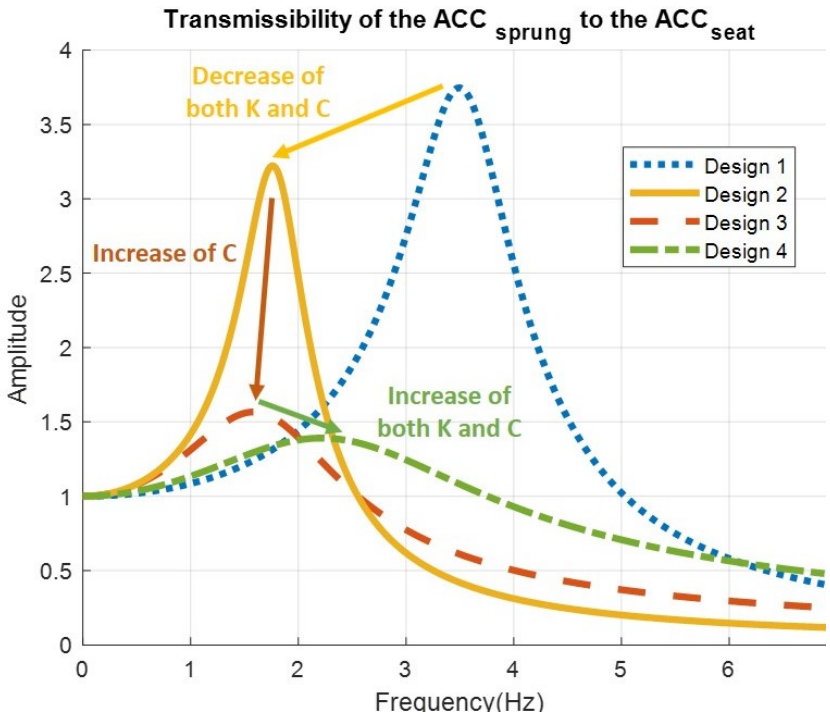

(b) Transmissibility ($\ddot{z}_{seat}/\ddot{z}_{sprung}$) of accelerations.

Figure 2.18: The conflict of the seat suspension for various values of stiffness (K_v) and damping (C_v)

On contrary, the tire deflection of the system and thus the normal tire forces illustrate the good road holding and handling of the vehicle (Equation 2.4, 2.10, 2.18 and 2.27). This performance can be characterized in terms of vehicle's cornering, braking and traction abilities. These abilities can be improved by minimizing the variations in normal tire loads, because the lateral and the longitudinal forces generated by a tire depend directly on the normal tire load. So, variations in normal tire load can be directly related to vertical tire deflection considering that a tire roughly behaves like a spring in response to vertical forces. Thus, both the variance of tire deflection and its maximum value could be good indexes for vehicle's road holding ($TD1$ and $TD2$, respectively), as shown in Equations 2.89-2.90.

$$VTD_i = \frac{1}{n}\sum_{j=1}^{n}(TD_{i,j} - \overline{TD})^2 = VAR(TD_i) \tag{2.89}$$

$$MTD_i = MAX(TD_i) \tag{2.90}$$

where $i = \emptyset,\ F1,\ F2,\ R1$ and $R2$. In addition the pitch angle is considered as an index for road holding, thus its variance is investigated.

$$PTC = \frac{1}{n}\sum_{j=1}^{n}(\theta_j - \overline{\theta})^2 = VAR(\theta) \tag{2.91}$$

2.4.5 Dissipated Energy

The damper is designed to absorb the vibrational energy and to dissipate it as heat, which leads to elevated temperatures in the hardware of the damper. Mean dissipated power (DE) is one of the main indexes used in the literature for thermal performance. DE depicts the average mechanical energy that a damper dissipates per second and it is directly proportional to the temperature rise in the damper. Elevated temperatures could have a detrimental effect to the components of the damper and the fluid, while the minimization of the dissipated energy may offer simultaneous benefits to hardware temperature, seals durability and forward power requirements. Therefore, the designers must include the damper's temperature rise while they design new control algorithms for active or semi-active suspensions. The mean dissipated power (DE) is evaluated as shown in Equation 2.92.

$$DE_i = \frac{\int_0^{t_f} F_{C_i} * \dot{ST}_i \ dt}{t_f} = \frac{\int_0^{t_f} C_i * \dot{ST}_i * \dot{ST}_i \ dt}{t_f} \tag{2.92}$$

where t_f is the total time of the simulation or the experiment and $i = \emptyset,\ F1,\ F2,\ R1$ and $R2$.

The dissipation energy is part of the second conflict that the suspension designers must face while controlled suspensions are designed. This conflict implies that greater vibration control demands more dissipated energy. This could be further and more accurately explained through the law of conservation of energy. In physics, the law of conservation of energy states that the total energy of an isolated system remains constant, it can neither be created nor destroyed; rather, it can only be transformed or transferred from one form to another.

In the case of SH control algorithms, which are studied in this thesis, greater vibration control corresponds to either greater number of switches - i.e times that the damper operates with C_{max}- or smaller sampling time in the control algorithm, which both are not desired. Therefore, the increase in the DE could lead to the decrease of either kinetic or potential energy and hence of z and $\dot{z}$, respectively, increasing the vibrational control performance.

2.4.6 Number of switches and chattering

The switches between the states that define the damper introduce nonlinearities into the system through the nonlinear damping force and the discontinuous command signal. This phenomenon is referred to as chatter. However, there is no relevant metric in the literature quantifying it. Eslaminasab et al. [90] minimized the chattering by suppressing the nonlinearities of vehicle's response around 30-40Hz, while Tsampardoukas et al. [91, 92] related the level of the chatter with the number of the switches of the damping coefficient. Many researchers proposing a new control algorithm considered the decrease in the chattering and compare their algorithms with the traditional SH algorithms [83, 90–93]. In this work, the effect of the chattering is studied through the number of switches in the damper's state (SW). By decreasing the chattering and thus the number of the switches (SW), we increase the expected life of the damper's component by reducing their fatigue and the temperatures occurred in the fluid, the seals and the other damper's components similarly with the dissipation energy. However, a significant decrease could affect the vehicle's performance and thus the vibrational control.

2.5 Road Profiling and Excitation

The irregularities on the road cause disturbances and are classified as shock or vibration. The first is related to discrete disturbances, usually associated with higher amplitudes, such as a bump or a pothole, while the latter is related to continuous irregularities, such as an unpaved road. Both types have different requirements for the suspension system, but in order for the designer to design one has to consider both these applications. One of the important aspects in the analysis of the dynamic behavior of a vehicle is the road profile that is used as an input function. The dynamic properties of the vehicle's suspension system, the vehicle speed and the elevation of the road surface unevenness

determine the vibration levels. Thus, road profile generation is a strong asset for the researchers, as it enables them to test the vehicle under different road conditions. The most common approach in the literature is the study of a vehicle under a road bump [17, 24, 25, 101, 130, 131] or a random road profile [16, 33, 34, 39, 40, 62, 132] generated based on ISO 8608:1995 [133].

2.5.1 ISO 8608 : Mechanical vibration and road surface profiles

Profiles taken along a lateral line show the superelevation and crown of the road design, plus rutting and other distress. Longitudinal profiles show the design grade, roughness, and texture (see Figure 2.19). In this thesis, we focus on the longitudinal profiles, whose classifications are based on ISO 8608:1995 [133]. ISO 8608:1995 is based on the assumption that a given road has equal statistical properties everywhere along a section and that the road surface is a combination of a large number of longer and shorter periodic bumps with different amplitudes. ISO has proposed road roughness classification using the power spectral density (PSD) values as shown in Figure 2.20 and Table 2.4. Paved roads are generally considered to be among road classes A to D.

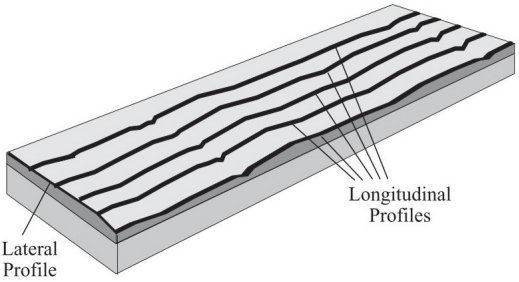

Figure 2.19: Road profile representation obtained by Tyan et al. [16]

Classification of Road Profiles

The road profile can be represented by a PSD function as shown in Figure 2.20 and Table 2.4. The power spectral densities of roads show a characteristic drop in magnitude with the wave number. To determine the power spectral density function, or PSD, it is necessary to measure the surface profile with respect to a reference plane. Random road profiles can be approximated by a PSD in the form of Equation 2.93:

$$\Phi(\Omega) = \Phi(\Omega_0)\left(\frac{\Omega}{\Omega_0}\right)^{-w} \tag{2.93}$$

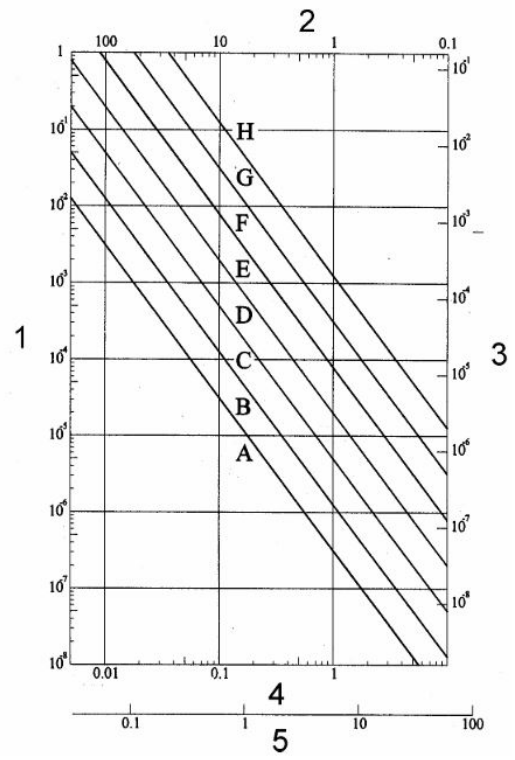

Figure 2.20: Road Surface Classification (ISO 8608) [16]. The axes surrounding the frame are defined as **1.** displacement psd, $\Phi(n)[m^3]$, **2.** wavelength, $\lambda[m]$, **3.** displacement psd, $\Phi(\Omega)[m^3]$, **4.** spatial frequency, n[cycle/m], **5.** angular spatial frequency, $\Omega[rad/m]$.

where $\Omega = \frac{2\pi}{L}$ in rad/m denotes the angular spatial frequency, L is the wavelength, $\Phi(\Omega_0)$ in $m^2/(rad/m)$ describes the values of the psd at the reference wave number $\Omega_0 = 1\ rad/m$, $n = \frac{\Omega}{2\pi}$ is the spatial frequency, $n_0 = 0.1\ cycle/m$ and w is the waviness, equal to 2 for most of the road surfaces.

Road Class	**Degree of roughness** $\Phi(\Omega_0)(10^{-6}\ m^3)$ *where* $\Omega_0 = 1\ rad/m$		
	Low limit	**Geometric mean**	**Upper limit**
A (very good)	-	1	2
B (good)	2	4	8
C (average)	8	16	32
D (poor)	32	64	128
E (very poor)	128	256	512

Table 2.4: Road roughness values classified by ISO expressed in terms of spatial frequency Ω

For a rough and quick estimation of the roughness quality, the following guidance is given:

1. New roadway layers, such as, for example, asphalt or concrete layers, can be assumed to have a good or even a very good roughness quality;

2. Old roadway layers which are not maintained may be classified as having a medium roughness ;

3. Roadway layers consisting of cobblestones or similar material may be classified as medium ("average") or bad ("poor", "very poor").

Road Profiles in Spatial and Temporal Domain

It is well-known that the amount of the road excitation imposed at the vehicle tire depends on two factors:

1. the road roughness, which is a function of the road roughness coefficient and

2. the vehicle velocity.

Let s be the path variable. By introducing the wavelength λ:

$$\lambda = \frac{2 * \pi}{\Omega} \tag{2.94}$$

and assuming $s = 0$ at $t = 0$, the term $\Omega * s$ can be written as:

$$\Omega * s = \frac{2 * \pi}{\Omega} * s = 2 * \pi \frac{V}{\lambda} t = \omega t \tag{2.95}$$

where $\omega(rad/sec)$ is the angular velocity in time domain, we end up with :

$$\Omega * V = \omega \tag{2.96}$$

Hence, in the time domain the excitation frequency is $f = \frac{\omega}{2*\pi} = \frac{V}{\lambda}$. For most of the vehicles the rigid body vibrations are between 0.5 - 15 Hz. This range is covered by waves which satisfy the condition $0.15Hz < \frac{V}{\lambda} < 15Hz$. For a given wavelength of $\lambda = 4m$, the rigid body vibration of a vehicle is excited if the velocity of the vehicle is varied from $V_{min} = 0.5Hz * 4m = 60/m/sec = 216km/h$. Thus, an excitation in the whole frequency range with moderate vehicle velocities profiles with different varying wavelengths is needed.

Sinusoidal Approximation

Based on the work of Tyan et al. [16] and Andren [134],various random road profiles of different classes could be generated using a sinusoidal approximation. If the vehicle is assumed to travel with a constant speed V over a given road segment with length (L_s), then a random road profile can be approximated by a superposition of N($\rightarrow \infty$) sine waves using Equation 2.97

$$y(t) = \sum_{n=1}^{N} A_n sin(n\omega_0 t - \phi_n) \tag{2.97}$$

where:

$$\omega_0 \triangleq V\Delta\Omega,\ \Delta\Omega \triangleq V\frac{2\pi}{L} \tag{2.98}$$

where :

$$A_i = \sqrt{\Phi(\Omega_i)\frac{\Delta\Omega}{\pi}},\ i = 1,...,N \tag{2.99}$$

$$\Delta\Omega = \frac{\Omega_N - \Omega_1}{N-1}(rad/sec) \tag{2.100}$$

The phase angles $\phi_n,\ n = 1,...,N$ are treated as random variables following a uniform distribution in the interval of $[0, 2\pi)$ and V is the vehicle's velocity which is considered constant.

2.5.2 Road Bumps

The irregularities on the road cause disturbances and the road bumps are related to shock and discrete disturbances, usually associated with higher amplitudes. For the design of a road bump, as the ones illustrated in Figures 2.22 and 2.23, the height of the bump h (=0.05 m), its length L (=20 m) and the vehicle's velocity V (=const = 10 m/s) are needed, as shown in Figure 2.21. As a function of time, the road bump is designed as sinusoidal or step input respectively by Equations 2.101 and 2.103 for models which include one axle, while for models including both the rear axle respectively by Equations 2.102 and 2.104. The excitation for the front wheels is illustrated in Figure 2.22, while when rear wheels are also included in the model the excitation is presented in Figure 2.23.

Road Bump of Sinusoidal Type:

$$Road_F = \begin{cases} h * sin(\omega * t) & \text{, if } t_0 \leq t < t_0 + \frac{L}{2*V} \\ 0 & \text{, otherwise} \end{cases} \tag{2.101}$$

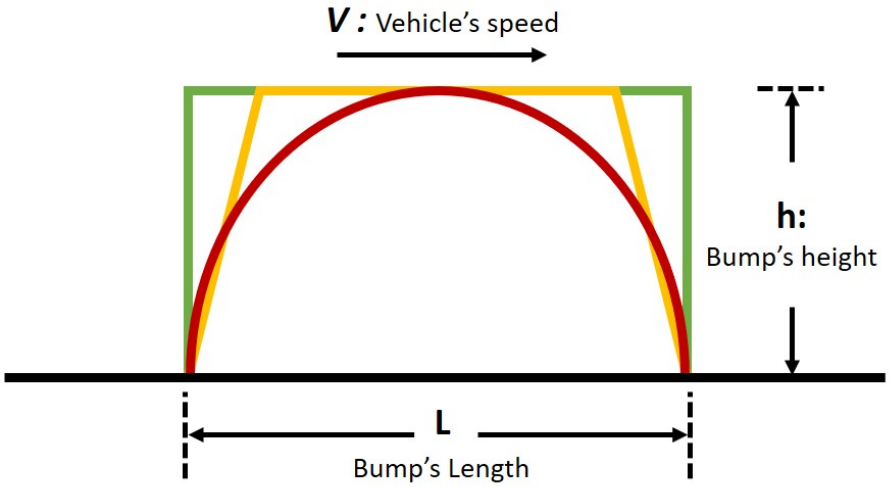

Figure 2.21: The design of a bump considering its height (h), its length (L) and the vehicle's velocity (V)

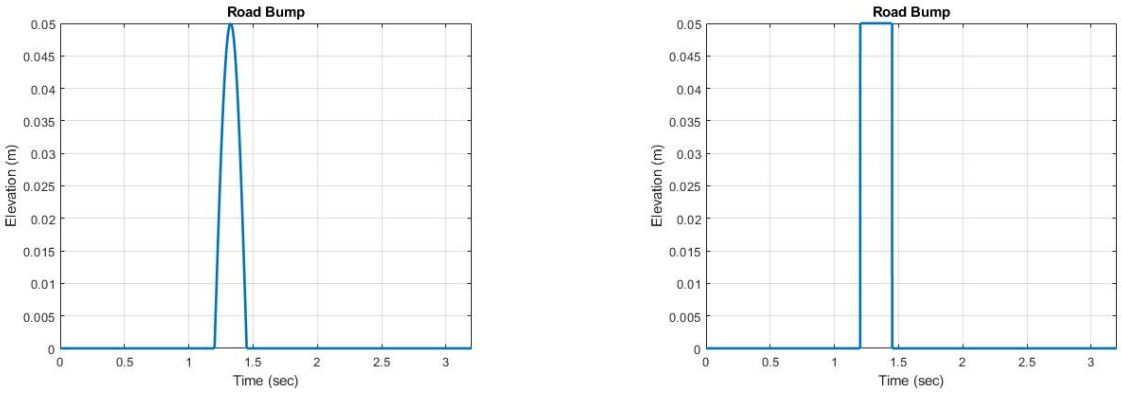

(a) Sinusoidal type.

(b) Step type.

Figure 2.22: Road bumps for vehicle models including one axle

$$Road_R = \begin{cases} h * sin(\omega * t) & \text{, if } t_0 + t_{distance} \leq t < t_0 + \frac{L}{2*V} + t_{distance} \\ 0 & \text{, otherwise} \end{cases} \tag{2.102}$$

Road Bump of Step Type:

$$Road_F = \begin{cases} h, & t_0 \leq t < t_0 + \frac{L}{V} \\ 0, & \text{otherwise} \end{cases} \tag{2.103}$$

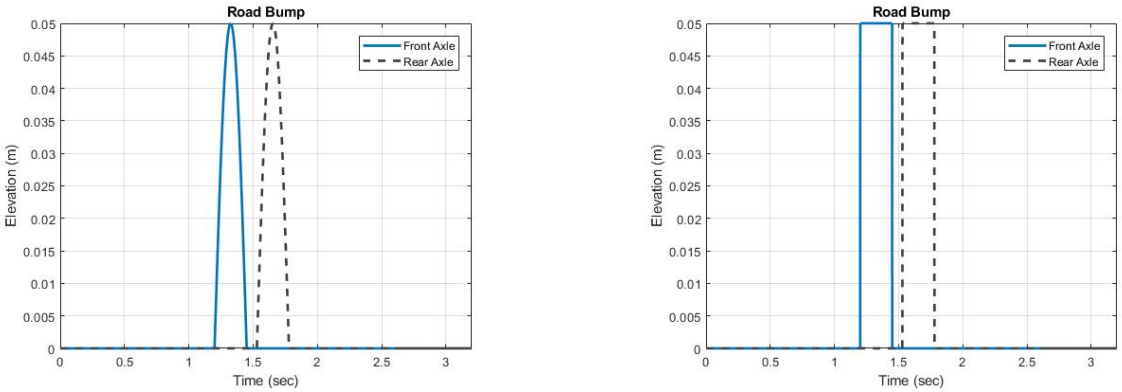

(a) Sinusoidal type.

(b) Step type.

Figure 2.23: Road bumps for vehicle models including both front and rear axle

$$Road_R = \begin{cases} h & ,\text{if } t_0 + t_{distance} \leq t < t_0 + \frac{L}{2*V} + t_{distance} \\ 0 & ,\text{ otherwise} \end{cases} \tag{2.104}$$

where t_0 is the starting time of the road bump, whilst ω is the excitation frequency $\frac{2\pi L}{V}$, $t_{distance}$ is the time lag between front and rear wheels $\frac{a_F + a_R}{V}$. More specifically, the front and rear wheels follow the same trajectory with a time delay $t_{distance}$, which is due to the distance $a_F + a_R$ of front and rear wheels.

CHAPTER 3

Comparative study of vehicle models with respect to dynamic performance

The selection of the most suitable model for suspension design is never explained and many times unnecessary complexity is added, either by using a model with more degrees of freedom or by adding more elements in the one selected (anti-roll bars, tire dampers etc.). The decision regarding the most appropriate model doesn't depend only on the fact that the pitch phenomena or the roll phenomena, should be investigated. The researchers have to consider if the increase in the DoFs of the model or the elements included will provide more accurate results and the computational time demanded will worth it. Thus, the decision has to be made based on the intended application, i.e. road excitation, reason of simulations (ride comfort or road holding), optimization of the suspension etc. without neglecting the complexity and the computational time. Based on the above, the aim of this paper is to conduct an assessment regarding the accuracy of the four most common vehicle models. In contrast to [75] and Ihsan et al. [33, 76] who conducted comparative works more with respect to different semi-active control algorithms than with respect to vehicle models, in this work the vehicle models with various configurations are compared in terms of accuracy and with respect to different performance metrics. More specifically, both passive and semi active suspensions are considered, while the effect of adding anti-roll bars and tire dampers is also investigated. The transient behavior of the suspension system and the overall ride performance of the vehicle are assessed in terms of ride comfort and road holding using different road excitation.

3.1 Materials & Methods

3.1.1 Simulation Models

This work intents to compare the main vehicle models in terms of their accuracy. As the degrees of freedom increase and the computational cost rises, it is of significant importance to investigate not only the loss of information but also the accuracy in evaluating the performance both of the vehicle and the suspension system. Therefore, different case studies are implemented, using different suspension systems under different road excitations, as presented in TAble 3.2. More specifically, they are presented below:

Parameter	**Unit**	**Value**	**Parameter**	**Unit**	**Value**
m_s	$[kg]$	1085	m_u	$[kg]$	40
I_x	$[kgm^2]$	820	I_y	$[kgm^2]$	1100
a_F	$[m]$	1.4	a_R	$[m]$	1.47
b_1	$[m]$	0.7	b_2	$[m]$	0.75
k	$[N/m]$	10000	c	$[Nm/s]$	800
k_T	$[N/m]$	150000	c_T	$[Nm/s]$	0
Additional Parameters for Part 1b					
c_{min}	$[Nm/s]$	400	c_{max}	$[Nm/s]$	1200
Additional Parameters for Part 2a					
k_R	$[Nm/rad]$	40000			
Additional Parameters for Part 2b					
c_T	$[Nm/s]$	49			

Table 3.1: Parameters of FC model used in this chapter.

1. Part 1: In this part, all the vehicle models (QC, HC1, HC2 and FC described in Chapters 2.1.1, 2.1.2, 2.1.3 and 2.1.4) are compared with respect to their transient and their dynamic behavior. Firstly, they are employed with passive (Part 1a) and then with semi-active suspension systems (Part 1b), while the tire damper ($c_{T_i} = 0$) and the anti-roll bars ($M_{AR_i} = 0$) are neglected. The semi-active suspension system operates with SH-2 control law, as presented in Equation 2.34 of Chapter 2.1.6.

2. Part 2: In this part, the impact of additional elements in vehicle modeling is investigated. Firstly, in Part 2a two full car models are compared. The former one is the one of Part 1a, whereas the latter considers the anti-roll bars both in front and rear axle ($M_{AR_i} \neq 0$). Secondly, two quarter car models are compared (Part 2b). The first one is the one of Part 1a, while the latter considers a non-zero tire damping coefficient ($c_{T_i} \neq 0$), as described in Equation 2.29.

Part	Description	Analysis for each part	Parameters studied
1a	Comparison of **QC, HC1, HC2 and FC** employed with passive suspensions. Tire damping and anti-roll bars are neglected.	**Transient Response**. A road bump is used as excitation	1. Time-domain responses of $\ddot{z}_s$ and z_s. 2. Transient metrics of Chapter 2.4 for $\ddot{z}_s$ and z_s. 3. Natural frequencies of the models. $*$. Time-domain response of ϕ and its transient metrics **only for Part 2a**.
1b	Comparison of **QC, HC1, HC2 and FC** employed with semi-active suspensions. **Tire damping and anti-roll bars** are neglected.		
2a	Comparison of **two FC** models with and without anti-roll bars. The models are employed with passive suspensions.	**Dynamic Response.** A random road profile is used as excitation	1. Time-domain responses of $\ddot{z}_s$ and z_s. 2. Transfer function of $\ddot{z}_s$. 3. Ride comfort metrics (RC and $max(\ddot{z}_s)$. 4. Vehicle stability metrics (VST, MST, VTD and MTD).
2b	Comparison of **two QC** models with and without tire damping. The models are employed with passive suspensions.		

Table 3.2: Parts, type of analysis and parameters studied in this chapter .

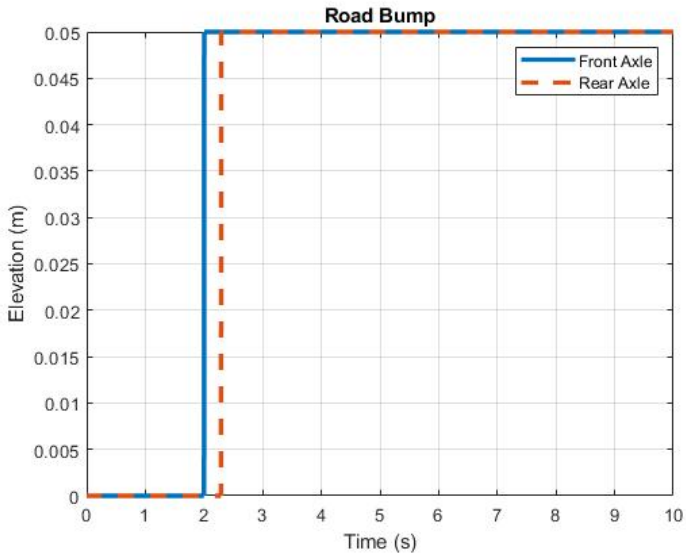

(a) Road bump.

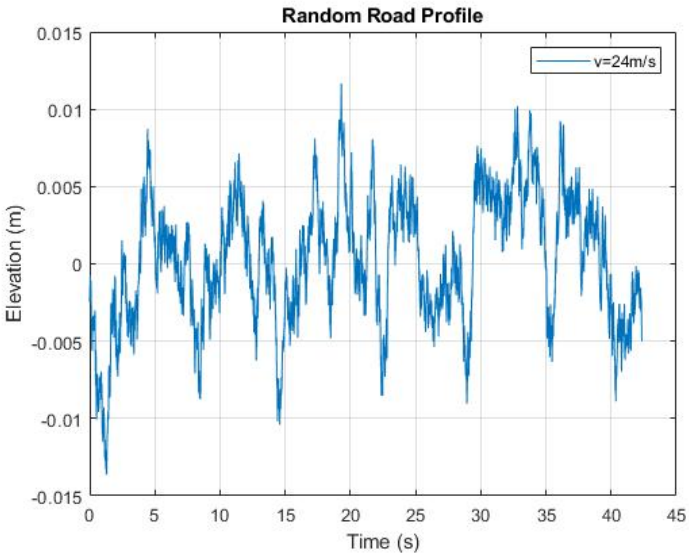

(b) Road Profile generated based on ISO-8608.

Figure 3.1: The road profiles used as excitation of the vehicle models in this chapter

3.1.2 Excitation

In this chapter, a road bump (Figure 3.1a) and a random road profile (Figure 3.1b) are generated, so as to thoroughly test the transient and dynamic response of the models .

Road Bump

The road bump that is used, is illustrated in Figure 3.1a. The height of the bump is set to h=0.05 m and its length to L=80 m. The vehicle velocity is constant and set to 10 m/s. The excitation takes place at t_0=2sec.

Road Excitation for the Vehicle Model

The second excitation involves a random road profile, generated based on the ISO 8608 regulation [133], which classifies road profiles according to the quality of the road. The velocity of the vehicle is set 86.4 km/h for the road profile. The road profile in time domain is illustrated in Figure 3.1b. Likewise, the front and rear wheels follow the same trajectory with a time delay $t_{distance}$, which is due to the wheelbase (a_F + a_R).

3.2 Results

For each part, two types of analysis are conducted.

1. The former type contains the analysis of transient response, thus the models are excited with a road bump (Figure 3.1a). In addition, the time-domain responses of the vehicle to the excitation are compared and the transient metrics regarding the acceleration ($\ddot{z}_s$) and the displacement (z_s) of the sprung mass are evaluated. Particularly for Part 2a, the transient metrics regarding the roll angle (ϕ) are investigated as well. Additionally, the natural frequencies (ω) of the models are calculated.

2. The second analysis concerns the dynamic behavior of the vehicle. In this respect the models are excited with a random road profile of class B, as illustrated in Figure 3.1b, and both time-domain and frequency-domain vehicle responses are compared. Furthermore, performance metrics concerning the ride comfort, the road holding and the vehicle handling are evaluated.

3.2.1 Comparative Study : Part 1a

In the first part, all the vehicle models (QC, HC1, HC2 and FC) are employed with passive suspension systems and are compared in terms of their accuracy. The springs of the suspension systems are considered linear (Equation 2.30), while the tire damping ($c_{T_i} = 0$) and the anti-roll bars ($M_{AR_i} = 0$) are ignored. The vehicle parameters are selected from the literature so as to represent a passenger vehicle and are illustrated in Table 3.1. In the following figures, the vehicle models are denoted as:

- Case Study 1: FC Model
- Case Study 2: HC1 Model
- Case Study 3: HC2 Model
- Case Study 4: QC Model

Transient Behavior

As it was mentioned before, in order to evaluate the transient behavior of the vehicle models, they are excited with a step input. The acceleration ($\ddot{z}_s$) and the displacement (z_s) of the sprung mass are compared in Figures 3.2 and 3.3, respectively. In addition, in Figures 3.4 and 3.5 the acceleration ($\ddot{z}_u$) and the displacement (z_u) of the front right unsprung mass are illustrated. The metrics of the sprung mass acceleration are compared in Table 3.3, while the ones of the sprung mass displacement are shown in Table 3.4. In these Tables the percentage of the difference of each model's metrics compared to the ones of the quarter car are evaluated ($\frac{X-X_{QC}}{X_{QC}}100\%$).

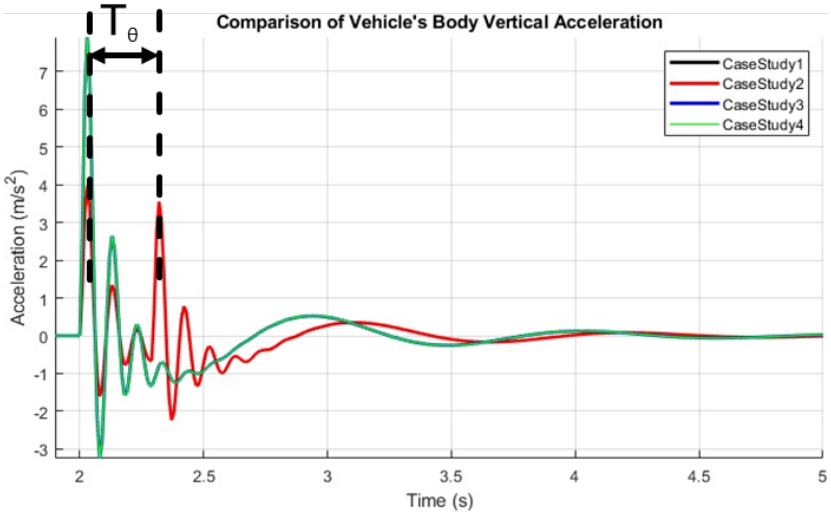

Figure 3.2: Part 1a - Transient Behavior: Sprung mass acceleration response.

	FC		**HC2**		**HC1**		**QC**
	Value	**%**	**Value**	**%**	**Value**	**%**	**Value**
Peak, M_p (m/s^2)	3.97	*50%*	3.97	*50%*	7.92	*0%*	7.92
t_p (s)	2.03	*0 %*	2.03	*0 %*	2.03	*0%*	2.03
t_s (s)	4.25	*-17%*	4.25	*-17%*	3.65	*0%*	3.65

Table 3.3: Part 1a - Transient Metrics: Sprung mass acceleration.

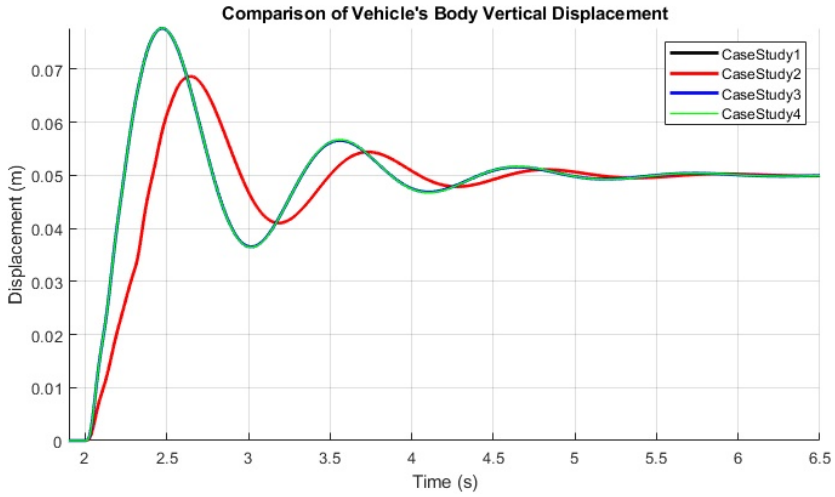

Figure 3.3: Part 1a - Transient Behavior: Sprung mass displacement response.

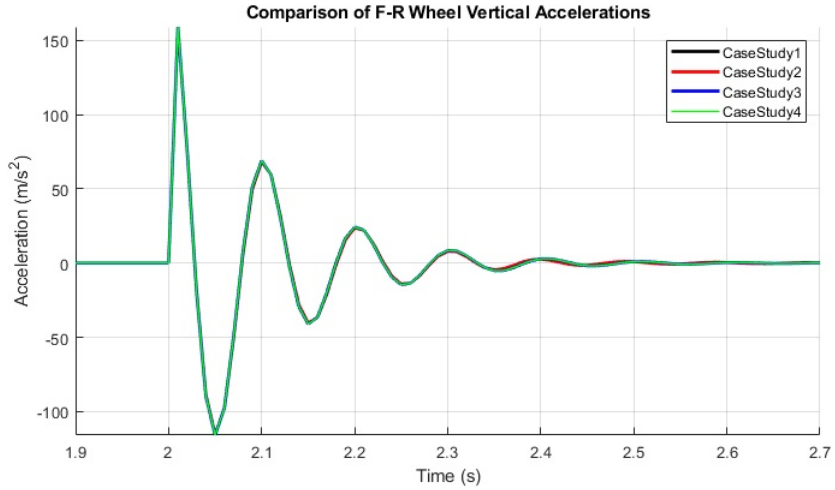

Figure 3.4: Part 1a - Transient Behavior: Unsprung mass acceleration response.

	FC		**HC2**		**HC1**		**QC**
	Value	**%**	**Value**	**%**	**Value**	**%**	**Value**
Peak, M_p (mm)	68.62	*12%*	68.62	*12%*	77.69	*0%*	77.69
t_p (s)	2.65	*-7%*	2.65	*-7%*	2.47	*0%*	2.47
t_s (s)	4.88	*-1.5%*	4.88	*-1.5%*	4.80	*0%*	4.81

Table 3.4: Part 1a - Transient Metrics: Sprung mass displacement.

Based on the sprung mass response (Figures 3.2 and 3.3), there are two groups of waveforms that dominate. The first consists of QC and HC1 models (group 1), which present identical response, while the latter illustrates common behavior between FC and HC2 models (group 2). The first group displays responses of greater magnitude, while all models have the same steady-state value. Additionally,

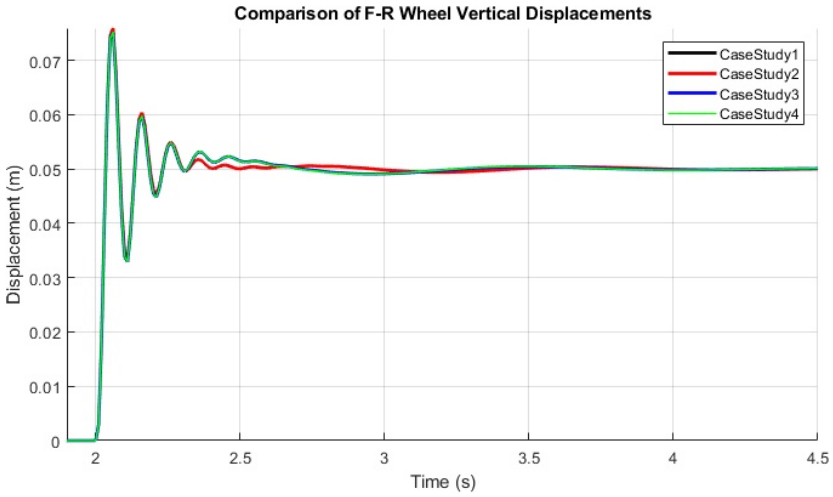

Figure 3.5: Part 1a - Transient Behavior: Unsprung mass displacement response.

according to the sprung mass acceleration response (Figure 3.2) the lack of the peak that corresponds to the pitch natural frequency is noticed ($T_\Theta = 2\pi/\omega_\Theta$. Also, the first group of models (QC and HC1) displays less damping. On the other hand, small differences between the responses of the unsprung mass (Figures 3.4 and 3.5) are noticed and they are related to the settling time of the displacement.

The above remarks are also confirmed by the tables of transient metrics (Tables 3.3 and 3.4). First of all, based on Tables 3.3 and 3.4 the separation of the models in two groups is verified. FC and HC2 present the same percentage of difference comparing their metrics to the ones of HC1 and QC. According to Table 3.3, the peak value of the acceleration of the QC and HC1 models is $\sim$50% increased compared to the other two models. On the other hand, these models display more damping in the sprung mass acceleration response, with their settling time being around 16.5% lower than the group 2. As far as the sprung mass displacement is concerned (Table 3.4), the differences between the metrics of the models are smaller. Likewise, the group 1 of models show greater peak value by $\sim$12%, while their settling time is $\sim$1.4% less. As far as the peak time variations are concerned, the second group of models have greater peaks of sprung mass displacement almost by 7.3%, in contrast to the acceleration, where no difference is noticed.

Dynamic Behaviour

In order to assess the dynamic behavior of the vehicle models, we apply as an excitation a random profile of class B. The responses of sprung mass acceleration and displacement in time-domain are compared in Figures 3.6 and 3.7, respectively, while the sprung mass acceleration response in frequency-domain is illustrated in Figure 3.8. Finally, the performance metrics regarding ride comfort are compared in Table 3.6, while the ones regarding the road holding and the vehicle handling are

	FC	HC2	HC1	QC
$\omega_{x_s}[Hz]$	0.93	0.93	0.94	0.93
$\omega_{\varphi}[Hz]$	0.78	-	0.78	-
$\omega_{\theta}[Hz]$	1.33	1.33	-	-
$\omega_{z_1}[Hz]$ $\omega_{z_2}[Hz]$ $\omega_{z_3}[Hz]$ $\omega_{z_4}[Hz]$	10.07	10.07	10.07	10.07

Table 3.5: Natural Frequencies of all the vehicle models (QC, HC1, HC2 and QC).

shown in Table 3.7. In these Tables the percentage of the difference of each model's metrics compared to the ones of the quarter car are evaluated.

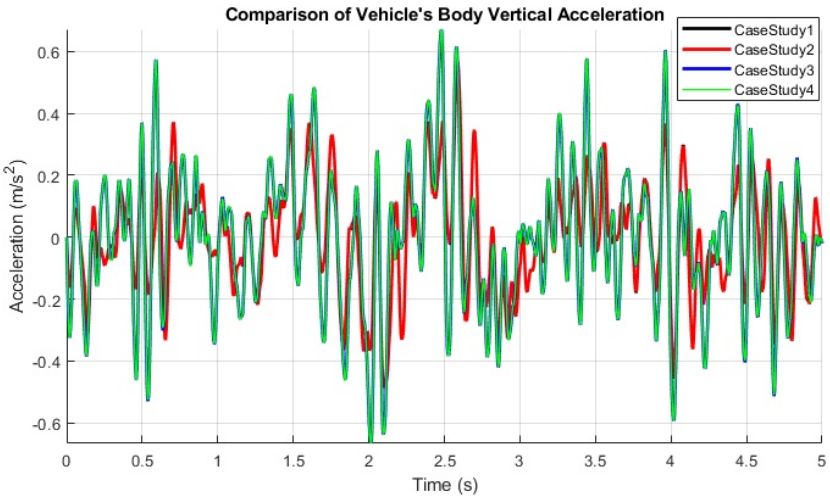

Figure 3.6: Part 1a - Dynamic Behavior: Sprung mass acceleration response in time-domain.

	FC		HC2		HC1		QC
	Value	**%**	**Value**	**%**	**Value**	**%**	**Value**
RC	0.15	*24%*	0.15	*24%*	0.19	*0%*	0.19
$Max(\ddot{z}_s)$ (m/s^2)	0.56	*18%*	0.56	*18%*	0.70	*-1%*	0.69

Table 3.6: Part 1a - Dynamic Behavior: Ride comfort Metrics.

According to figures, which present the time-domain responses of the sprung mass (Figures 3.6 and 3.7), the same conclusions, as the transient analysis, are derived. As far as the frequency-domain response of the sprung mass acceleration is concerned, all models have the same natural frequencies, while the QC and HC1 (group 1) display greater magnitudes compared to the FC and HC2 models (group 2), as shown both in 3.5 and Figure 3.8.

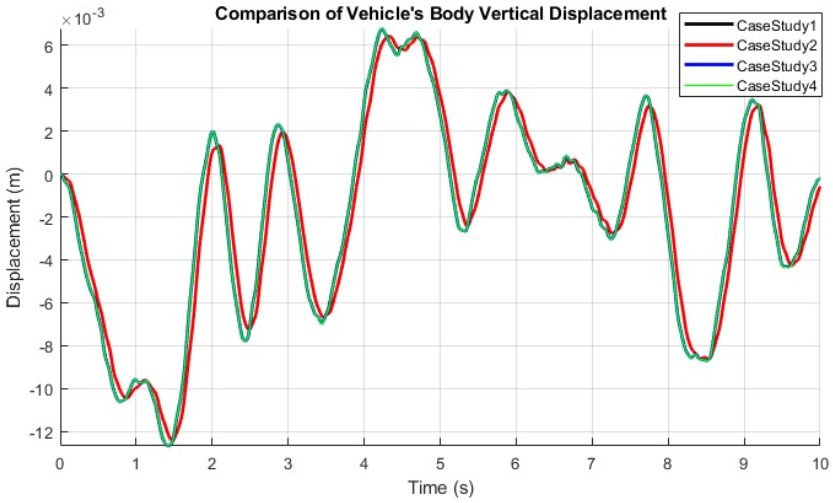

Figure 3.7: Part 1a - Dynamic Behavior: Sprung mass displacement response in time-domain.

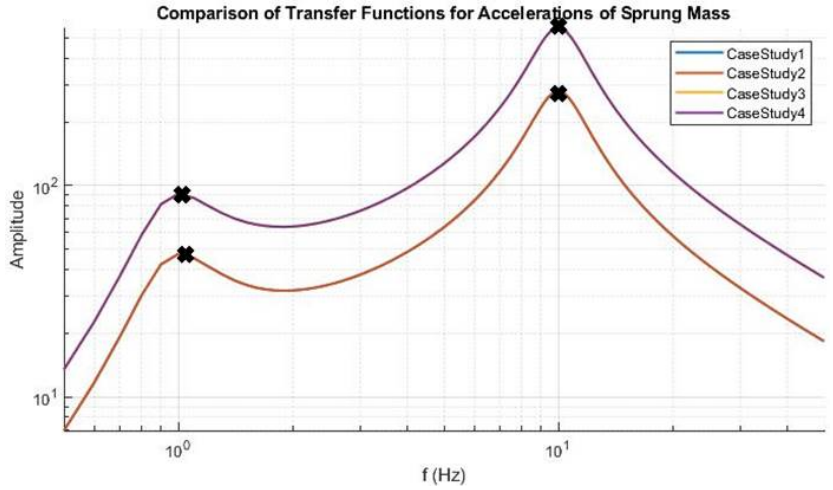

Figure 3.8: Part 1a - Dynamic Behavior: Sprung mass acceleration response in frequency-domain.

As far as the ride comfort is concerned, according to the Table 3.6, the QC and HC1 models have greater values not only of the maximum sprung mass acceleration ($Max(\ddot{z}_s)$) but also of the weighted RMS of acceleration (RC). Thus, the group 1 models estimate the levels of ride comfort with less accuracy, while overestimating these values. Additionally, according to the Table 3.7, the differences between the vehicle models are significant as far as the suspension travel is concerned. More specifically, the variances of the right and the left suspension travel of HC1 model differ compared to QC by $\sim$0.4% and $\sim$0.3%, respectively, while the maximum values of the right and the left suspension travel differ by $\sim$1.2% and $\sim$1.4 %, respectively. The difference between the suspension travels of HC1 and the one of QC is due to the consideration of the roll angle. Considering that the right and left excitations are the same, the differences are insignificant and thus they estimate the suspension

	FC		HC2		HC1		QC
	Value	**%**	**Value**	**%**	**Value**	**%**	**Value**
$VST_1(mm^2)$	6.22	*20%*	6.16	*21%*	7.77	*0%*	7.81
$VST_2(mm^2)$	6.11	*22%*			7.83	*0%*	
$VST_3(mm^2)$	8.79	*-13%*	8.88	*-14%*	7.77	*0%*	
$VST_4(mm^2)$	8.96	*-15%*			7.83	*0%*	
$MST_1(mm)$	9.07	*2%*	9.05	*3%*	9.41	*-1%*	9.30
$MST_2(mm)$	9.03	*3%*			9.17	*1%*	
$MST_3(mm)$	9.92	*-7%*	9.97	*-7%*	9.41	*-1%*	
$MST_4(mm)$	10.01	*-8%*			9.17	*1%*	
$VTD_1(mm^2)$	1.15	*-1%*	1.15	*-1%*	1.14	*0%*	1.14
$VTD_2(mm^2)$							
$VTD_3(mm^2)$	1.13	*0%*	1.13	*0%*			
$VTD_4(mm^2)$							
$MTD_1(mm)$	4.54	*-1%*	4.53	*-1%*	4.50	*0%*	4.49
$MTD_2(mm)$					4.47	*1%*	
$MTD_3(mm)$	4.46	*1%*	4.47	*1%*	4.50	*0%*	
$MTD_4(mm)$					4.47	*1%*	

Table 3.7: Part 1a - Dynamic Behavior: Vehicle handling and Road holding Metrics.

system's behavior similarly. Furthermore, the difference noticed between FC and HC2 is less than 1% and is also due to the consideration of the roll angle and the lateral load transfer.

On the other hand, as far as the comparison of FC and HC2 (group 2) with the QC is concerned, the values of the VST of group 2 regarding the front axle are by $\sim$21% less, while the variances regarding the rear axle are by $\sim$14% more. Accordingly, the maximum values of the suspension travel of group 2, regarding the front axle, are by $\sim$2.9% less, while the maximum values regarding the rear axle are less by $\sim$7.5% more. The differences between the front and rear axles is a result of including the pitch angle in the models of group 2 and the consideration of the longitudinal load transfer. Thus, the consideration of the pitch angle in a model affects the estimation regarding the behavior of the suspension system significantly. On the other hand, the differences in the tire deflection also exist, but they are negligible (differences less than $\sim$1%).

3.2.2 Comparative Study : Part 1b

This part investigates the vehicle models' accuracy while using semi-active suspension systems. In this respect, all the vehicle models (QC, HC1, HC2 and FC) are employed with semi-active suspension systems, operating with the SH-2 states control law, and are compared. The springs are considered

linear and all anti-roll bars ($M_{AR_i} = 0$) as well as the tire damping ($c_{T_i} = 0$) are neglected. The vehicle parameters are illustrated in Table 3.1. In the following figures, the vehicle models are denoted as:

- Case Study 1: FC
- Case Study 2: HC1
- Case Study 3: HC2
- Case Study 4: QC

Transient Behaviour

In Figures 3.9 and 3.10 the sprung mass acceleration ($\ddot{z}_s$) and the displacement (z_s) responses of all models are presented, respectively. In addition, the corresponding responses ($\ddot{z}_u$ and z_u) of the unsprung mass (front right wheel) are illustrated in Figures 3.11 and 3.12, respectively. Furthermore, the transient metrics of the sprung mass acceleration and the displacement are compared in Tables 3.8 and 3.9, respectively. In these Tables the percentage of the difference of each model's metrics compared to the ones of the quarter car are evaluated.

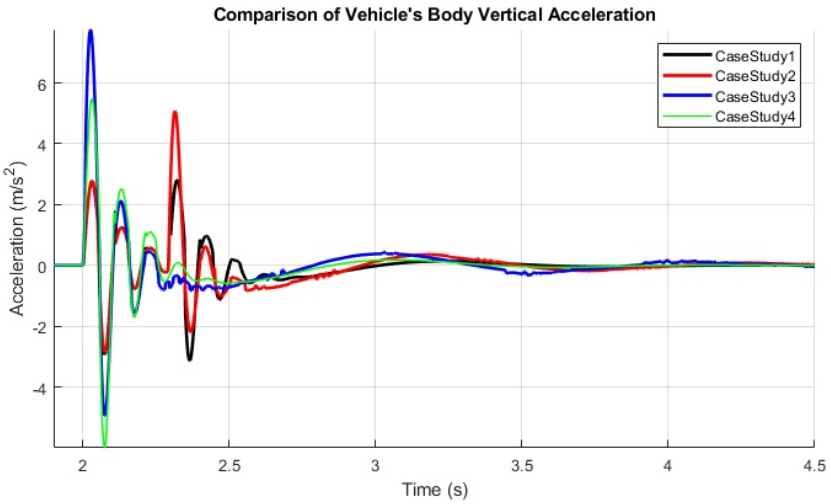

Figure 3.9: Part 1b - Transient Behavior: Sprung mass acceleration response.

According to Figures 3.9 - 3.12, all vehicle models' responses differ, regarding not only the magnitude but also the damping rate, in contrast to Part 1a, where two groups of models of similar response where identified. Specifically, both Figures 3.9 and 3.10 show that the FC model displays more damping with reduced magnitude, compared to the other models, being less responsive. Additionally, as described in Part 1a, all models have the same steady-state value of both sprung mass acceleration and displacement (Figures 3.9 and 3.10), while the QC and HC1 models lack of the peak that corresponds to the pitch natural frequency, as shown in Figure 3.9. On the other hand, unlike Part 1a, significant differences are

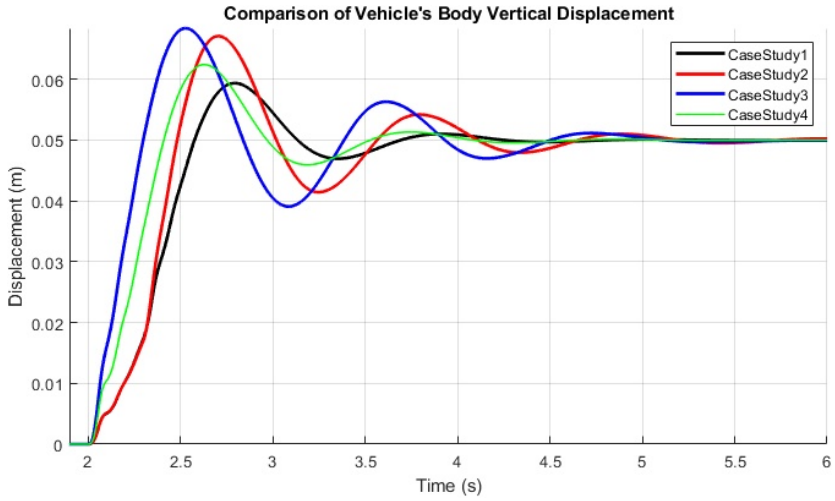

Figure 3.10: Part 1b - Transient Behavior: Sprung mass displacement response.

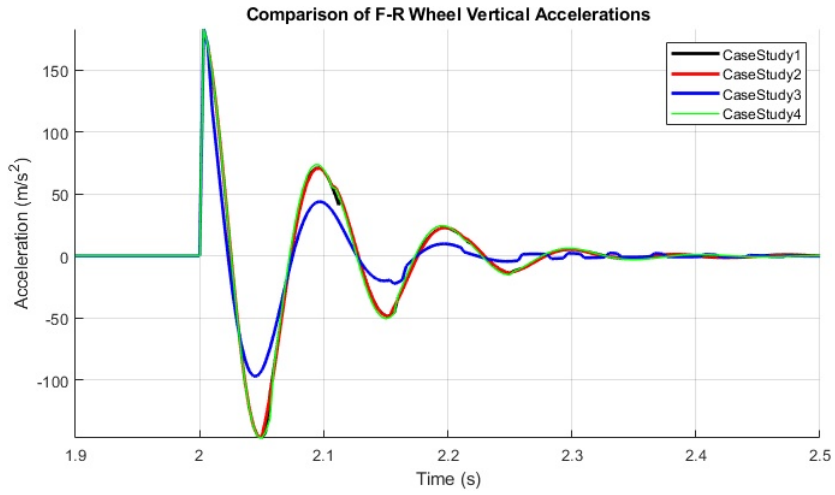

Figure 3.11: Part 1b - Transient Behavior: Unsprung mass acceleration response.

	FC		**HC2**		**HC1**		**QC**
	Value	**%**	**Value**	**%**	**Value**	**%**	**Value**
Peak, M_p (m/s^2)	2.81	*49%*	5.08	*7%*	7.76	*-42%*	5.48
t_p (s)	2.32	*-15%*	2.31	*-14%*	2.03	*0%*	2.03
t_s (s)	3.44	*-7%*	3.90	*-21%*	4.00	*-24%*	3.23

Table 3.8: Part 1b - Transient Metrics: Sprung mass acceleration.

illustrated regarding the unsprung mass responses. More specifically, Figures 3.11 and 3.12 illustrate that the HC1 model is more oscillatory and less damped, while it displays lower magnitude, compared to the rest of the models.

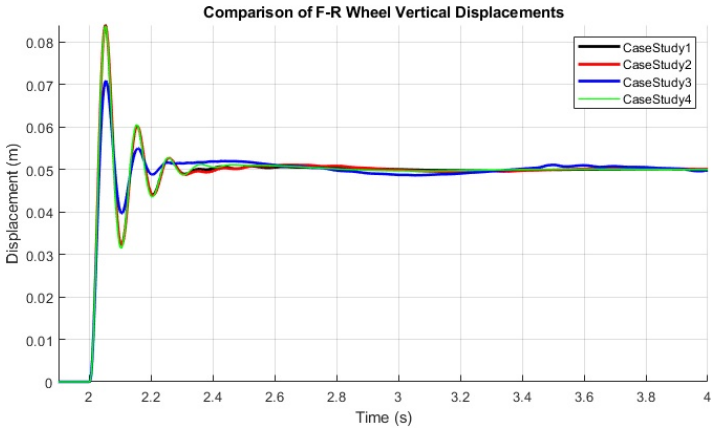

Figure 3.12: Part 1b - Transient Behavior: Unsprung mass displacement response.

	FC		**HC2**		**HC1**		**QC**
	Value	**%**	**Value**	**%**	**Value**	**%**	**Value**
M_p (mm)	59.36	*5%*	67.10	*-8%*	68.39	*-10%*	62.41
t_p (s)	2.79	*-6%*	2.71	*-3%*	2.53	*4%*	2.63
t_s (s)	3.92	*-1%*	4.91	*-27%*	4.83	*-24%*	3.88

Table 3.9: Part 1b - Transient Metrics: Sprung mass displacement.

The tables of transient metrics (Tables 3.8 and 3.9) confirm the above remarks. More specifically, the peak value of the acceleration of the FC model is ∼49% decreased compared to the QC value. As far as the peak time is concerned, both FC and HC2 models have ∼14% greater value compared to the other two models, which indicates less responsive behavior. Additionally, the settling time of FC and QC models is ∼20% decreased compared to the HC1 and HC2 models, and thus they settle faster. Finally, as far as the transient characteristics of the sprung mass displacement are concerned, the differences between the models are less intense, but reflect the same remarks. Likewise, the FC and HC2 models show greater peak time value (∼6.2% and ∼2.9%, respectively) compared to QC model, while the FC and QC models have settling time value ∼25-26% less compared to HC1 and HC2 models. As far as the peak values are concerned, the value of FC is around ∼5% less, while HC1 and HC2 have peak values ∼7.5% and ∼9.5% less compared to QC model.

Dynamic Behaviour

In order to assess the dynamic characteristics and the performance of the vehicle models using semi-active suspension systems, both the time-domain and frequency-domain responses are calculated. Specifically, the responses of the sprung mass acceleration and the displacement in time-domain are illustrated in Figures 3.13 and 3.14 respectively. The frequency-domain response of the sprung mass acceleration is shown in Figure 3.15. Finally, the performance metrics regarding ride comfort are

illustrated in Table 3.10, while the ones regarding the road holding and the vehicle handling are shown in Table 3.11. In these Tables the percentage of the difference of each model's metrics compared to the ones of the quarter car are evaluated.

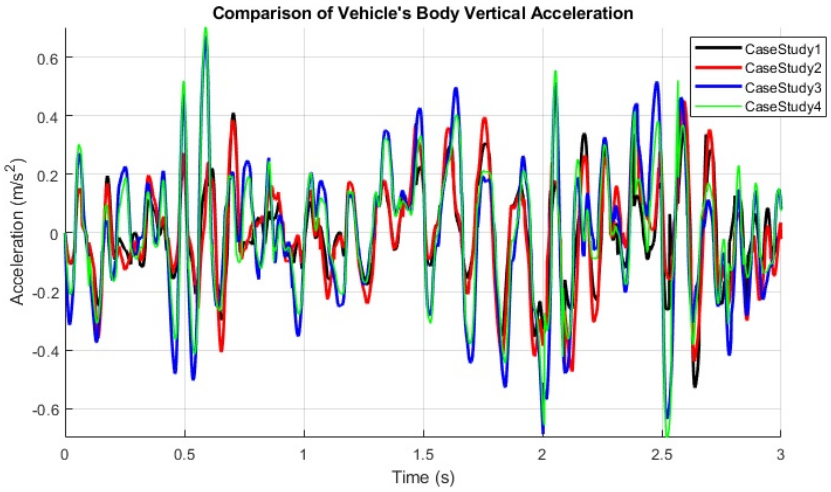

Figure 3.13: Part 1b - Dynamic Behavior: Sprung mass acceleration response in time-domain.

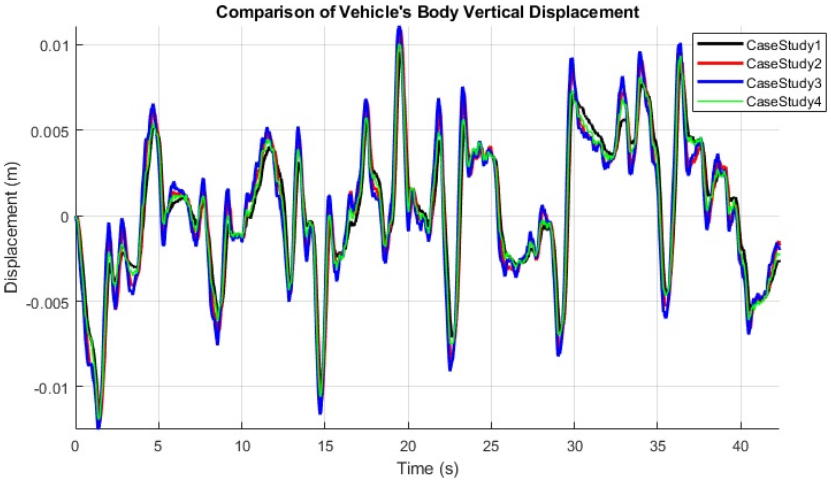

Figure 3.14: Part 1b - Dynamic Behavior: Sprung mass displacement response in time-domain.

	FC		**HC2**		**HC1**		**QC**
	Value	**%**	**Value**	**%**	**Value**	**%**	**Value**
RC	0.14	*25%*	0.16	*15%*	0.20	*-9%*	0.19
$Max(\ddot{z}_s)$ (m/s^2)	0.65	*19%*	0.60	*25%*	0.76	*6%*	0.80

Table 3.10: Part 1b - Dynamic Behavior: Ride comfort Metrics.

AS noticed in the transient analysis, the time-domain response of the sprung mass acceleration is different for every model, regarding the magnitude, as shown in Figure 3.13. On the other hand, the

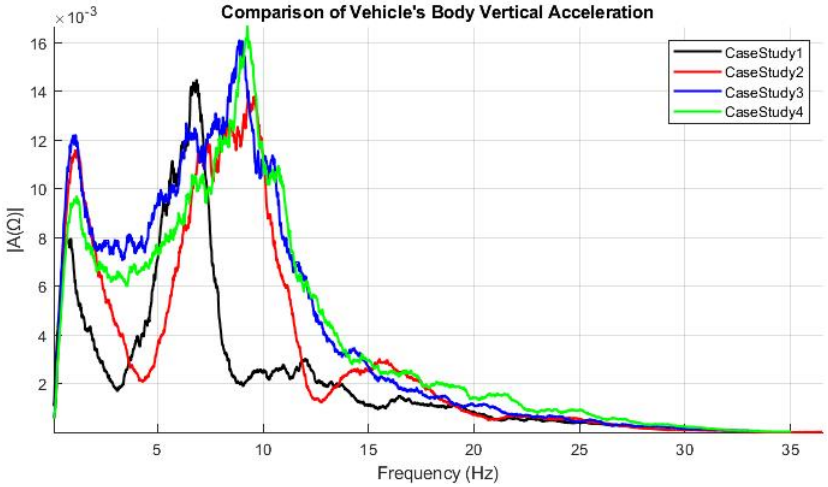

Figure 3.15: Part 1b - Dynamic Behavior: Sprung mass acceleration in frequency-domain.

	FC		**HC2**		**HC1**		**QC**
	Value	**%**	**Value**	**%**	**Value**	**%**	**Value**
$VST_1(mm^2)$	5.13	*10%*	5.65	*1%*	6.20	*-8%*	5.73
$VST_2(mm^2)$	5.14	*10%*			5.66	*1%*	
$VST_3(mm^2)$	8.34	*-46%*	5.09	*11%*	6.20	*-8%*	
$VST_4(mm^2)$	8.41	*-47%*			5.66	*1%*	
$MST_1(mm)$	7.28	*18%*	8.53	*4%*	8.72	*1%*	8.83
$MST_2(mm)$	7.23	*18%*			8.50	*4%*	
$MST_3(mm)$	10.33	*-17%*	7.33	*17%*	8.72	*1%*	
$MST_4(mm)$	10.36	*-17%*			8.50	*4%*	
$VTD_1(mm^2)$	1.37	*-7%*	1.19	*7%*	0.91	*29%*	1.29
$VTD_2(mm^2)$					1.25	*3%*	
$VTD_3(mm^2)$	1.56	*-21%*	0.88	*31%*	0.91	*29%*	
$VTD_4(mm^2)$					1.25	*3%*	
$MTD_1(mm)$	4.80	*1%*	4.82	*0%*	4.20	*13%*	4.83
$MTD_2(mm)$	4.79	*1%*			4.82	*0%*	
$MTD_3(mm)$	4.83	*0%*	4.12	*15%*	4.20	*13%*	
$MTD_4(mm)$					4.82	*0%*	

Table 3.11: Part 1b - Dynamic Behavior: Vehicle handling and Road holding Metrics.

differences between the models regarding the time-domain response of the sprung mass displacement (Figure 3.14) are insignificant, but similarly the HC1 model displays greater magnitude. Figure 3.15 illustrates that FC model has lower natural frequency of the unsprung mass, compared to the other models. In addition, lower values of the magnitude of FC model's response are also noticed, while the area around 2-5 Hz of the responses of QC and HC1 models is over weighted. As far as the ride comfort is concerned, according to the Table 3.10, the FC and HC2 models have similar values of both

the maximum and the RMS value. Specifically, the maximum values of acceleration of the FC and BC models are by ∼18.8% and ∼25% less, while the *RC* values are by ∼25.4% and ∼14.91% less, compared to the QC model, respectively. These values indicate that the FC and HC2 model estimate more accurate ride comfort. Additionally, according to the Table 3.11, the most important difference between the models regard the VST. More specifically, the rear suspension travel variances of the FC model have greater value compared to the QC model by ∼46%. Furthermore, it is noticed that the differences between the suspension systems of each model is greater, in contrast to the Part 1a. This phenomenon is due to the semi active control law, which includes the roll and/or pitch angle in its operational conditions ($\dot{ST}$). Therefore, in few cases, the models use different state in the damper's condition under the same excitation, as displayed in Figure 3.16, in two different time intervals of the simulations. As a result of the above, greater variations occur in the response.

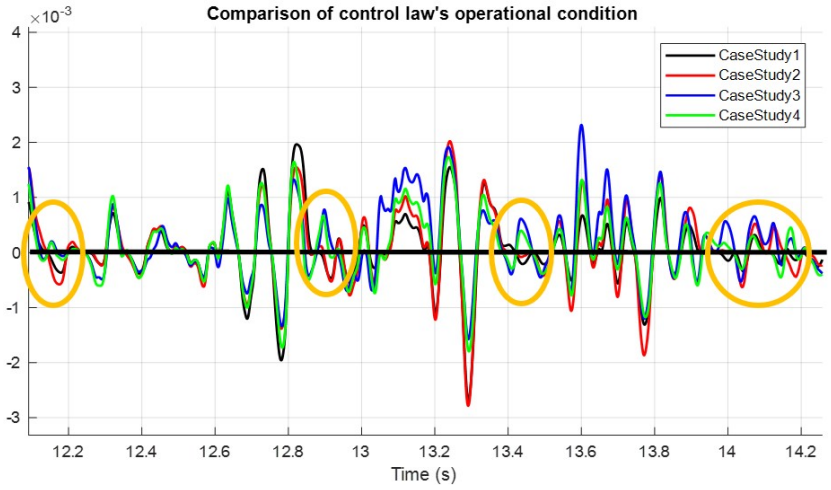

(a) Simulation interval between 12-14 sec.

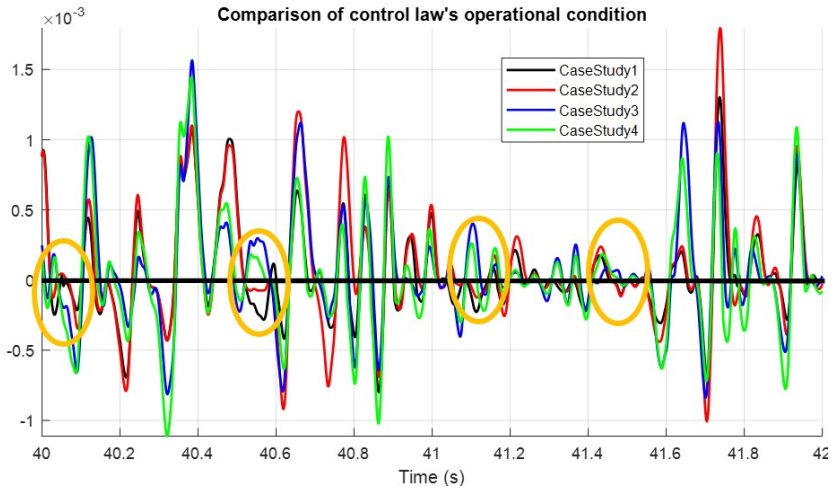

(b) Simulation interval between 40-42 sec.

Figure 3.16: Dynamic Behavior: Control's law operational conditions of SH-2 in two different simulation interval

3.2.3 Comparative Study : Part 2a

This part investigates the effect of including an anti-roll bar in the vehicle models, in terms of their accuracy. Specifically, we intent to evaluate which aspects of the vehicle's transient and steady-state responses are affected. Thus, two full car models are compared, where in the former one the anti-roll bars are neglected, while the latter includes both front and rear anti-roll bars. In both models the tire damping is neglected ($c_{T_i} = 0$). In this study, the road excitation is applied only to the right side of the vehicle, in order to excite the roll plane, while investigating the vertical dynamics, and understand the importance of considering an anti-roll bar in the vehicle model. The vehicle parameters are illustrated in Table 3.1. In the following figures, the vehicle models are denoted as:

- Case Study 1: FC without anti-roll bar.
- Case Study 2: FC including anti-roll bar.

Transient Behaviour

In order to study the transient behavior of the vehicle models, the sprung mass acceleration ($\ddot{z}_s$) and the displacement (z_s) are compared in the Figures 3.17 and 3.18, respectively. In Figure 3.19 the roll angle (φ) is illustrated. The transient metrics of the sprung mass acceleration and the displacement are compared in Tables 3.12 and 3.13, while the ones of the roll angle are shown in Table 3.14. In these Tables the percentage of the differences of the metrics' values of the full car model with anti-roll bar compared to the ones of the full car model without anti-roll bar are evaluated.

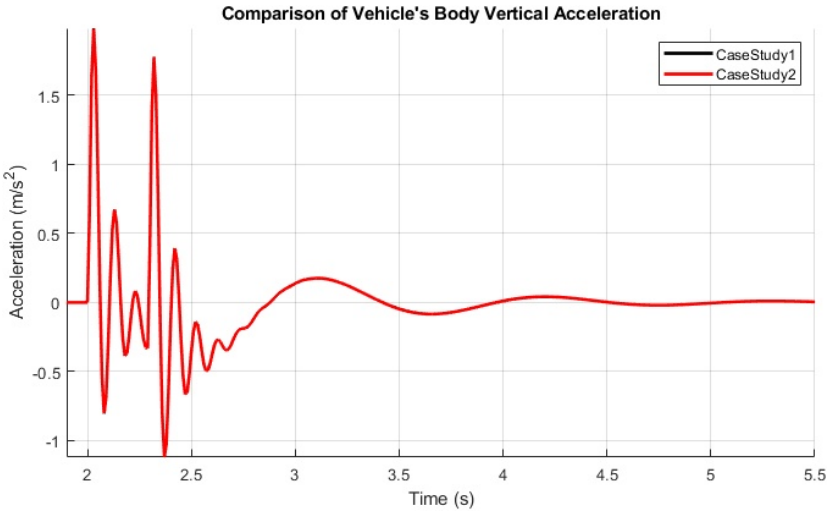

Figure 3.17: Part 2a - Transient Behavior: Sprung mass acceleration response.

The figures regarding the sprung mass response (Figures 3.17 and 3.18) show that the use of the anti-roll bar does not affect the sprung mass responses. However, the Figure 3.19 displays a significant

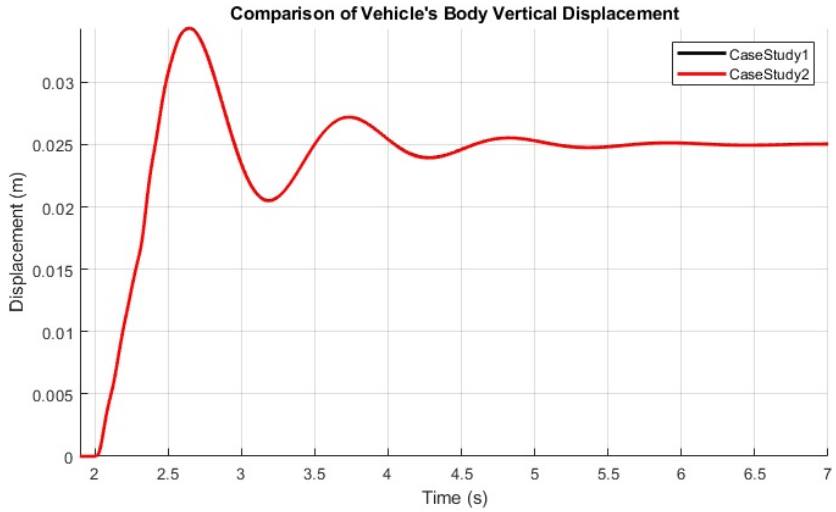

Figure 3.18: Part 2a - Transient Behavior: Sprung mass displacement response.

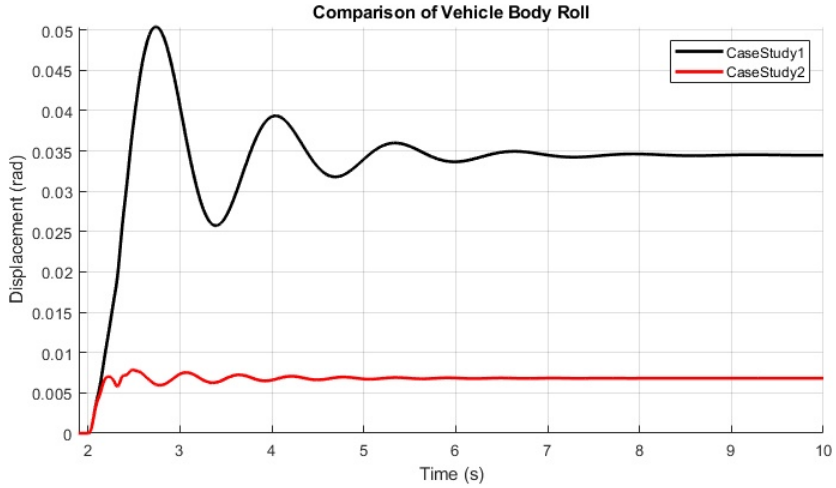

Figure 3.19: Part 2a - Transient Behavior: Roll angle response.

	FC With A.R.		**FC Without A.R.**
	Value	**%**	**Value**
Peak, M_p (m/s^2)	1.98	*0%*	1.99
t_p (s)	2.03	*0%*	2.03
t_s (s)	4.25	*0%*	4.25

Table 3.12: Part 2a - Transient Metrics: Sprung mass acceleration.

difference between the models, regarding both the magnitude and the damping rate. Specifically, the FC model employed with the anti-roll bars is less oscillatory and its steady-state value is less compared to the other model. The tables of transient metrics (Tables 3.12 and 3.13) confirm that the use of the anti-roll bar has no impact on the sprung mass response. Additionally, Table 3.14 shows that the use of

	FC With A.R.		**FC Without A.R.**
	Value	**%**	**Value**
Peak, M_p (mm)	34.32	*0%*	34.34
t_p (s)	2.65	*0%*	2.65
t_s (s)	4.88	*0%*	4.87

Table 3.13: Part 2a - Transient Metrics: Sprung mass displacement.

	FC With A.R.		**FC Without A.R.**
	Value	**%**	**Value**
Peak, M_p (rad)	$7.86{*}10^{-3}$	*84%*	$5.04{*}10^{-2}$
t_p (s)	2.49	*9%*	2.74
t_s (s)	4.82	*21%*	6.10
Steady-State, SST (rad)	$6.80{*}10^{-3}$	*80%*	$3.45{*}10^{-2}$

Table 3.14: Part 2a - Transient Behavior: Roll angle.

	FC Without A.R.	**FC With A.R.**
$\omega_{z_s}[Hz]$	0.93	0.93
$\omega_{\varphi}[Hz]$	0.78	0.97
$\omega_{\theta}[Hz]$	1.33	1.33
$\omega_{z_1}[Hz]$ $\omega_{z_2}[Hz]$ $\omega_{z_3}[Hz]$ $\omega_{z_4}[Hz]$	10.07	10.07

Table 3.15: Part 2a - Natural frequencies.

the anti-roll bar decreases not only the peak ($\sim$84%) and peak time ($\sim$9%) values but also the settling time ($\sim$21%) of roll angle. This indicates a more responsive and less oscillatory behavior of the roll angle.

Dynamic Behaviour

In Figure 3.20 the response of roll angle in time-domain is compared. More specifically, in Figure 3.20a the roll angle of the complete simulation is shown. However, due to the use of the random profile, the evaluation of the response in a smaller time interval, in order to achieve a better viewing, is needed. Thus, in Figure 3.20b the same response is illustrated, but for simulation interval between 0-15 (s). The roll acceleration response in frequency-domain is shown in Figure 3.21. Finally, the performance metrics regarding the ride comfort are compared in Table 3.16, while the ones regarding

the road holding and the vehicle handling are illustrated in Table 3.17. In these Tables the percentage of the differences of the metrics' values of the full car model with anti-roll bar compared to the ones of the full car model without anti-roll bar are evaluated.

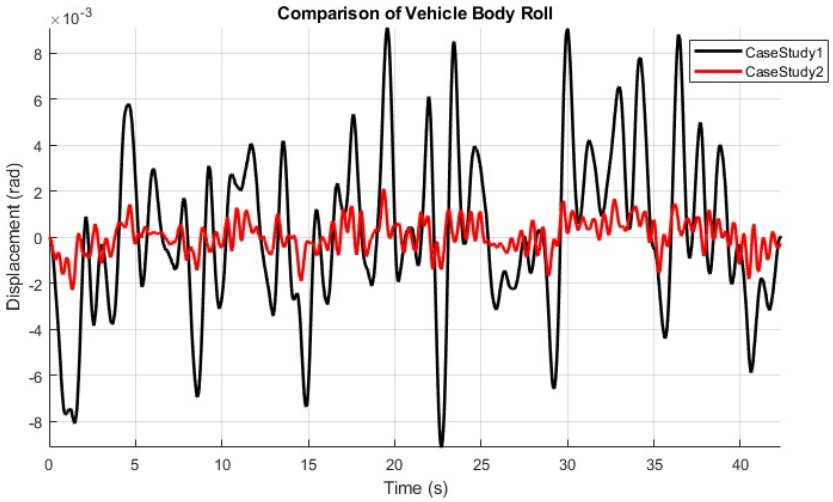

(a) .

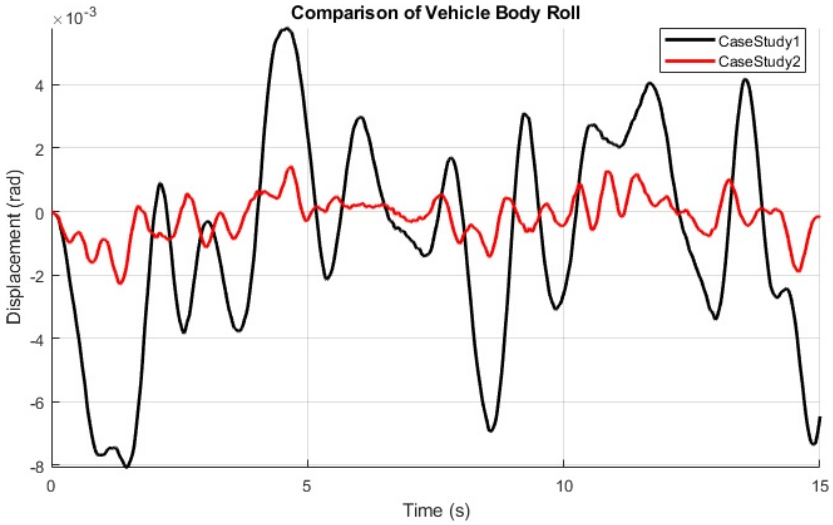

(b) .

Figure 3.20: Part 2a - Dynamic Behavior: Roll angle response in time-domain (a) Complete Simulation, (b) Simulation interval: [0,15 s].

	FC With A.R.		**FC Without A.R.**
	Value	**%**	**Value**
RC	0.07	*0%*	0.07
$Max(\ddot{z}_s)$ (m/s^2)	0.27		0.27

Table 3.16: Part 2a - Dynamic Behavior: Ride comfort Metrics.

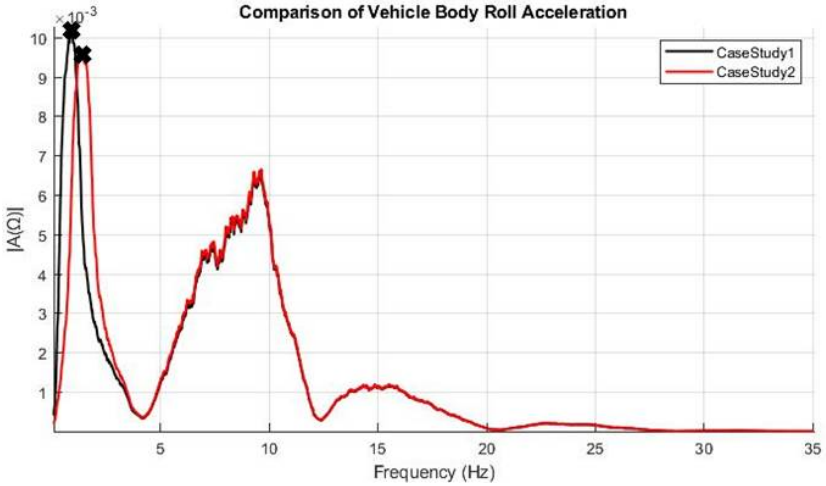

Figure 3.21: Part 2a - Dynamic Behavior: Roll acceleration in frequency-domain.

	FC With A.R.		**FC Without A.R.**
	Value	**%**	**Value**
$VST_1(mm^2)$	6.28	*2%*	6.40
$VST_2(mm^2)$	5.39	*-14%*	4.72
$VST_3(mm^2)$	7.12	*4%*	7.43
$VST_4(mm^2)$	5.88	*15%*	6.92
$MST_1(mm)$	7.82	*1%*	7.92
$MST_2(mm)$	6.48	*-15%*	5.64
$MST_3(mm)$	8.43	*0%*	8.42
$MST_4(mm)$	6.41	*10%*	7.15
$VTD_1(mm^2)$	1.13	*0%*	1.13
$VTD_2(mm^2)$	18.2	*0%*	18.2
$VTD_3(mm^2)$	1.11	*0%*	1.11
$VTD_4(mm^2)$	18.1	*0%*	18.0
$MTD_1(mm)$	4.05	*2%*	4.15
$MTD_2(mm)$	14.25	*0%*	14.22
$MTD_3(mm)$	4.06	*2%*	4.15
$MTD_4(mm)$	14.11	*0%*	14.15

Table 3.17: Part 2a - Dynamic Behavior: Vehicle handling and Road holding Metrics.

According to Figure 3.20, the differences concerning the time-domain roll angle response are significant. As presented in the transient analysis, the use of the anti-roll bar significantly decreases the magnitude of the roll angle. As far as the frequency-domain response of the roll acceleration is concerned, Figure 3.21 illustrates not only the decrease of the magnitude of the response, but also the increase of the roll angle natural frequency (ω_ϕ). This remark is confirmed by Table 3.15, which displays the natural frequencies of the models with and without the use of the anti-roll bar. Specifically,

it illustrates that the roll angle natural frequency (ω_ϕ) has increased from 0.78 Hz to 0.97 Hz, while using the anti-roll bars, whereas the rest of the natural frequencies remain the same.

As far as the performance metrics are concerned, both the ride comfort (Table 3.16) and the vehicle handling and road holding (Table 3.17) do not display significant differences. Nevertheless, according to the Table 3.17, a divergence of $\sim$10 - 15% of the variances and the maximum values of the left suspension travels is noticed (VST_2, VST_4, ST_2 and ST_4). This increase is induced since the anti-roll bar attempts to diminish the roll vibration, at the expense of the suspension travel.

3.2.4 Comparative Study : Part 2b

In order to simplify and reduce the required time of the calculations, usually the tire damping is neglected. This assumption is made as the damping of tires is much smaller than the damping of shock absorbers. In this case study, an investigation of the effect of including the tire damping in the vehicle models is conducted. For that reason, it was chosen to compare two quarter car models employed with passive suspension systems, where the former has zero tire damping, while the latter considers this coefficient non-zero. The vehicle parameters are illustrated in Table 3.1. In the following figures, the vehicle models are denoted as:

- Case Study 1: QC without tire damping.
- Case Study 2: QC including tire damping.

Transient Behaviour

In Figures 3.22 and 3.23 the acceleration ($\ddot{z}_s$) and the displacement (z_s) of the sprung mass are illustrated, respectively. The transient metrics of the sprung mass acceleration are compared in Table 3.18, while the ones of the sprung mass displacement are shown in Table 3.19. In these Tables the percentage of the differences of the metrics' values of the quarter car model with tire damping compared to the ones of the quarter car model without tire damping are evaluated.

	QC With Tire Damper		**QC Without Tire Damper**
	Value	**%**	**Value**
Peak, M_p (m/s^2)	7.86	*0%*	7.92
t_p (s)	2.03	*0%*	2.03
t_s (s)	3.65	*0%*	3.65

Table 3.18: Part 2b - Transient Metrics: Sprung mass acceleration.

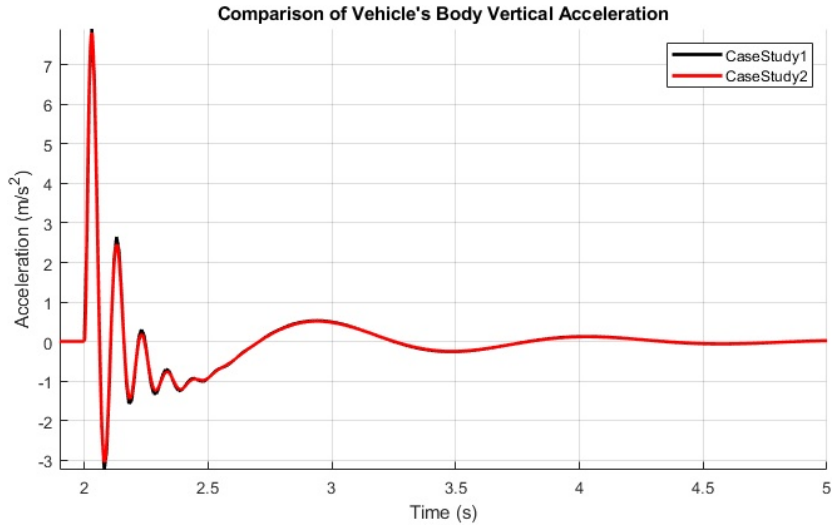

Figure 3.22: Part 2b - Transient Behavior: Sprung mass acceleration response.

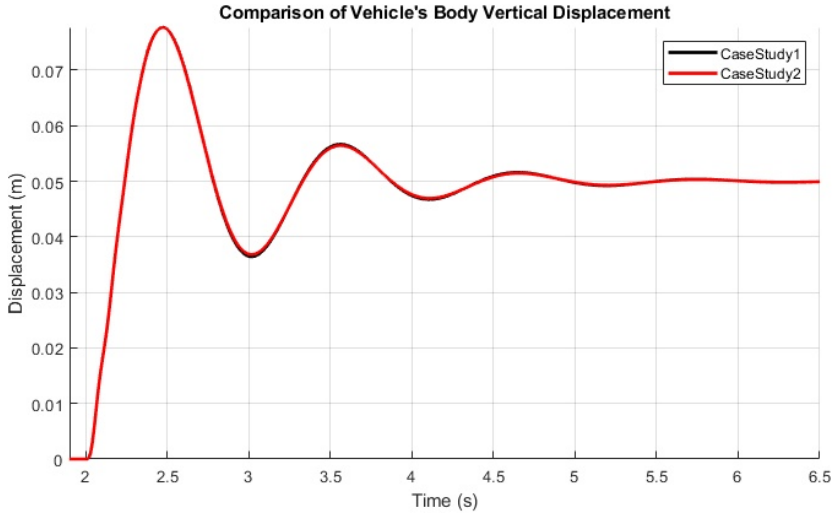

Figure 3.23: Part 2b - Transient Behavior: Sprung mass displacement response.

	QC With Tire Damper		**QC Without Tire Damper**
	Value	**%**	**Value**
Peak, M_p (mm)	77.72	*0%*	77.72
t_p (s)	2.47	*0%*	2.47
t_s (s)	4.81	*0%*	4.17

Table 3.19: Part 2b - Transient Metrics: Sprung mass displacement.

In Figures 3.22 - 3.23, the acceleration ($\ddot{z}_s$) and the displacement (z_s) of the sprung mass are presented respectively. The transient metrics of the sprung mass acceleration and the ones of the sprung mass displacement are not displayed because of the insignificant differences showed in Figures 3.22 - 3.23.

The figures regarding the sprung mass response illustrate that the inclusion of the tire damper in the models does not influence neither the acceleration nor the displacement. Therefore, we conclude that the assumption of zero tire damping coefficient does not affect the transient behavior of the suspension system.

Dynamic Behaviour

Considering the identical responses of Figure 3.22, only the response of the sprung mass acceleration in frequency-domain is illustrated in Figure 3.24. Also, in order to evaluate the effect of including the tire damping in the vehicle model, the performance metrics regarding the ride comfort are given in Table 3.20, while the ones regarding the road holding and the vehicle handling are shown in Table 3.21. In these Tables the percentage of the differences of the metrics' values of the quarter car model with tire damping compared to the ones of the quarter car model without tire damping are evaluated.

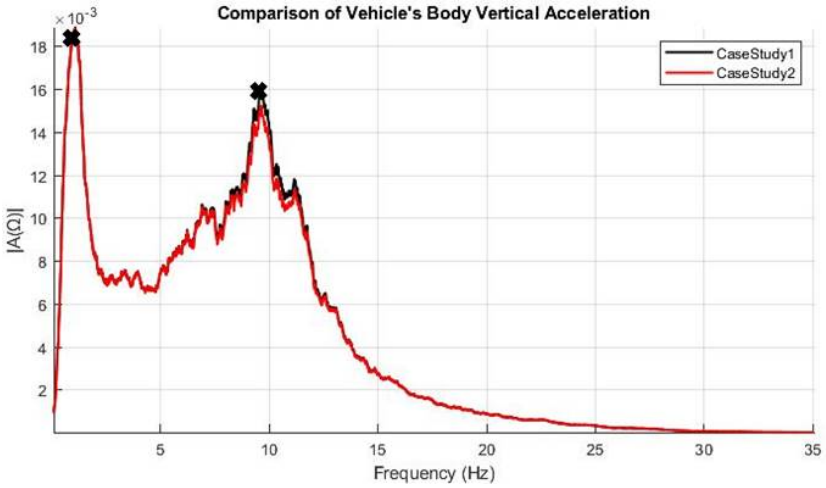

Figure 3.24: Part 2b - Dynamic Behavior: Sprung mass acceleration in frequency-domain.

	QC With Tire Damper		**QC Without Tire Damper**
	Value	**%**	**Value**
RC	0.19	*0%*	0.19
$Max(\ddot{z}_s)$ (m/s^2)	0.67	*4%*	0.69

Table 3.20: Part 2b - Dynamic Behavior: Ride comfort Metrics.

As far as the frequency-domain response of the sprung mass acceleration is concerned (Figure 3.24), the models have the same natural frequencies, while the QC model including the tire damper display a small decrease of the magnitude. According to the Table 3.20, the models have the same weighted RMS value of acceleration (RC), but the maximum value in the case of including the tire damper is reduced by $\sim$3.8%. Additionally, according to the Table 3.21, the vehicle models have not significant

	QC With Tire Damper		QC Without Tire Damper
	Value	**%**	**Value**
$VST(mm^2)$	7.74	*1%*	7.81
$MST(mm)$	9.18	*1%*	9.30
$VTD(mm^2)$	1.07	*6%*	1.14
$MTD(mm)$	4.42	*2%*	4.49

Table 3.21: Part 2b - Dynamic Behavior: Vehicle handling and Road holding Metrics.

differences between the values of the suspension travel as well as the maximum value of tire deflection, while the variance of the latter in the case of including the tire damper is increased by $\sim$5.6%. Despite that, the models are similar in terms of vehicle handling.

3.3 Conclusions

In this chapter, the most common vehicle models with various configurations are compared in terms of accuracy and with respect to different metrics. More specifically, both passive and semi active suspensions are considered, while the effect of adding anti-roll bars and tire damping is investigated. The transient behavior of the suspension system and the overall vehicle performance are assessed using different road excitations.

To sum up, in case of the models with passive suspension systems, two groups of models with identical responses occur. The first, which includes the QC and HC1 models, estimates vehicle's behavior with less accuracy than the latter group, which consists of the HC2 and FC models. The differences between the models of each group are negligible, therefore the higher accuracy models are not necessary to be used. However, the higher accuracy models should be used only if different excitation are intended to be applied, which will trigger the roll dynamics. This remark could save significant computational time from the researchers and specifically when optimization procedures are applied, which are extremely demanding. Moreover, in the case of employing the models with semi-active suspension systems, all the models display different responses to the excitation without illustrating a similar trend likewise the passive suspensions. This is because both pitch and roll angle are included in the operational conditions of the control law studied when the model considers them as DoFs. Therefore, the operational conditions differ significantly between the vehicle models and in few cases, the dampers use different state in their conditions. Therefore, in vehicle models with control laws that include the roll angle or the pitch angle, the loss of information may be greater if QC is used for example instead of HC or FC.

As far as the additional elements are concerned, the use of the anti-roll bar affects only the roll response, increasing the natural frequency, decreasing the magnitude and affecting the transient characteristics of the roll angle. However, the consideration of the anti-roll in the vehicle doesn't affect the metrics depicting the ride comfort of the passengers. Therefore, in such cases where the attention is turned on ride comfort, we may neglect the anti-roll bars without costing accuracy in our results. Last but not least, the consideration of the tire damper in the models has no significant impact to neither the transient nor the dynamic behavior of the models, and thus the assumption of zero damping does not affect the accuracy of the models, validating the proposal of researcher to neglect it.

CHAPTER 4

A Distribution-Based Control Strategy (CDF)

Semi-active control strategies can maintain the reliability of passive devices using a very small amount of energy, providing simultaneously the versatility, adaptability and the higher performance of fully active systems. The most common types of semi active dampers are the 2-States Skyhook (SH-2), the Skyhook Linear (SH-L), the Acceleration Driven Damper Control (ADD) and two different combinations of Skyhook and ADD (SH-ADD-1 and SH-ADD-2). They are mainly comfort oriented, improving the ride comfort of the passengers by adjusting the damping coefficient of the suspension system according to the response of the vehicle to the applied road excitation. Many different versions of these algorithms have been presented in the past, by changing slightly their operational conditions, such as the recent work of Van Der Sande et. al [82] and Nie et. al [83].

In this thesis, the operational conditions of two SH control strategies (SH-2 and SH-ADD-2) are modified based on a proposed control strategy in an attempt to improve the vehicle's performance. Afterwards, the SH-2-CDF and the SH-ADD-2-CDF are benchmarked against the traditional ones for important aspects of vehicle's suspension performance. The simulations are performed by using a quarter car model and exciting it by four different road excitations. Moreover, a sensitivity analysis is performed in order to test thoroughly our control strategy. The comparison of SH-2-CDF and SH-ADD-2-CDF with the traditional ones is presented for three different random road profiles for various values of the thresholds. The sensitivity analysis outlines the change of all the performance metrics by applying our control strategy to the traditional control algorithms and varying the threshold.

4.1 Materials & Methods

4.1.1 Vehicle model

A quarter car model is selected in this work (Figure 2.2), in order for the vertical vibrations induced by the road surface to be investigated. The suspension system consists of a linear spring (K) and a controllable damper (C) using SH algorithms, as presented in Chapter 2.1.6. As far as the controllable damper is concerned, the control algorithms of SH-2 and SH-ADD-2 are applied and afterwards they adopt a novel control strategy presented in this thesis. The values of the model's parameters are presented in Table 4.1 and they represent a passenger vehicle.

Parameter	Unit	Value	Parameter	Unit	Value
m_s	$[kg]$	260	m_u	$[kg]$	25
K_u	$[N/m]$	28100	C_{min}	$[Nm/s]$	1734
K_{Tu}	$[N/m]$	200000	C_{max}	$[Nm/s]$	4873

Table 4.1: Parameters of the QC Model used in this chapter based on optimization results from Koulocheris et al. [17].

4.1.2 Road Excitation

In this chapter, a road bump (Figure 4.1) and three random road profiles (Figure 4.2) are generated, so as to thoroughly test the CDF control strategy against the traditional control algorithm. The road bump is illustrated in Figure 4.1. Moreover, the road profiles are illustrated in Figure 4.2, displaying them both in time domain (Figure 4.2a) and in frequency domain (Figure 4.2b). The velocity is set at 120, 85 and 50 km/m for the road profiles of class A, B and C respectively, according to the limits of the national roads.

4.2 A Distribution Based Control Strategy (CDF)

In recent literature, various versions of Skyhook (SH) control algorithms use the control law of Equation 4.1 in order to change the damper's state in accordance with the sign of the operational condition. However, the use of the sign for the control of the operational conditions is the main reason of the occurring chattering as Liu et al. [94] and Margolis et al. [95] concluded.

$$C_u = \begin{cases} C_{min} & ,if\ condition \leq 0 \\ f(C_{max}) & ,if\ condition > 0 \end{cases} \tag{4.1}$$

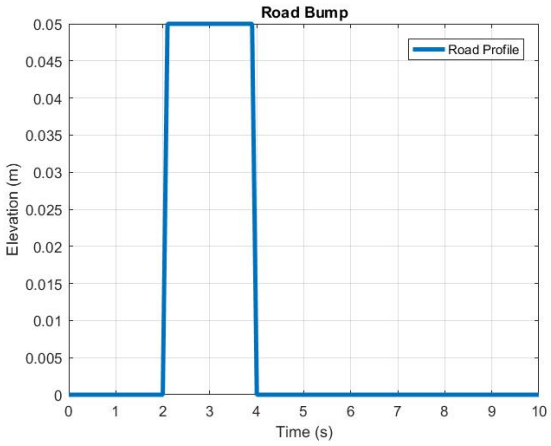

Figure 4.1: The road bump applied to the vehicle model of this chapter

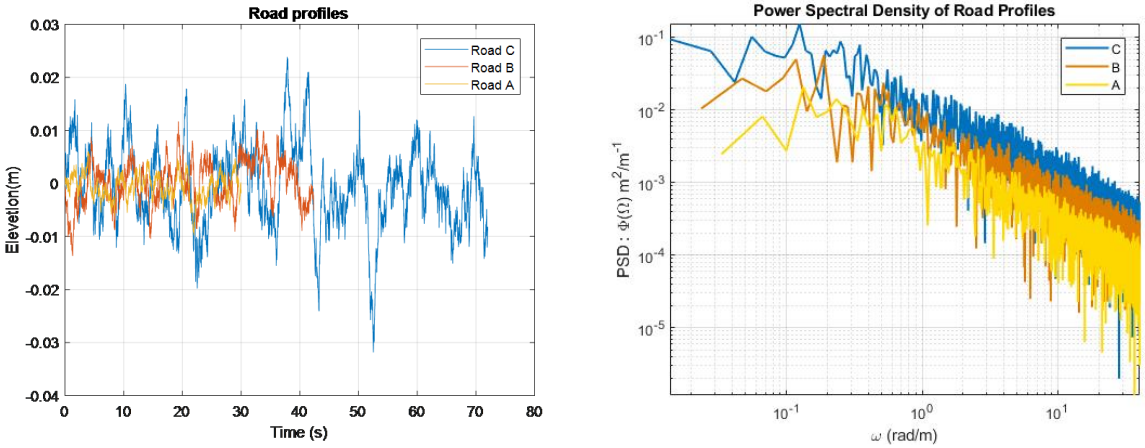

(a) Time Domain.

(b) Frequency Domain.

Figure 4.2: The random road profiles generated based on ISO-8608 and applied to the vehicle model of this chapter

In this thesis, a distibution based control strategy is proposed, which requires the use of an appropriate threshold in the algorithms' operational conditions, as shown in Equation 4.2.

$$C_u = \begin{cases} C_{min} & ,if\ condition \leq T_A, T_B \\ f(C_{max}) & ,if\ condition > T_A, T_B \end{cases} \tag{4.2}$$

This threshold decreases the chattering and improves significantly other aspects of the vehicle's performance, as it will be outlined in the next sections. The novelty of this modification lies upon the fact that this threshold quantifies the severity of the operational conditions and controls the damper's state based on their magnitude and not based on their sign. The values (T_A and T_B) used as thresholds of

the operational conditions depend on the vibrations induced by the road profile that the vehicle drives through and hence on the levels of the operational conditions. However, as it is explained later, their evaluation require neither the identification of the road profile nor its class as a prior knowledge. The increase of the threshold's value corresponds to the decrease of the percentage of the sample operating with C_{max}.

In this work, the operational conditions of two SH control strategies (SH-2 and SH-ADD-2) are modified based on the proposed control strategy so as to improve the vehicle's performance. The control algorithms are digitally implemented for ΔT=4 ms, which is much higher than the one used from other researchers [35, 80, 83, 135] who who tested their control algorithms for ΔT $\sim$1-2 ms. The importance of the higher sampling time lies upon the fact that the smaller the sampling time of the controller its response is much better but its implementation is more difficult. Thus, the more realistic sampling time in terms of design is preferred in our work compared to small sampling time which could exploit more the advantages of our algorithm.

4.2.1 Skyhook two states damper control with CDF control strategy (SH-2-CDF).

The 2-states control is an on-off strategy that switches between soft and stiff damping coefficient. This control law consists of two states in which the damping factor C changes according to the sign of the product of $(\dot{z}_s - \dot{z}_u)$ and $\dot{z}_s$. When the upper mass (m_s) is moving up, and the two masses (m_s and m_u) are getting closer, the damping constant should ideally be zero. However, due to the physical limitations of a damper, a damping constant of zero is not practical and a low damping constant is used. When the upper mass (m_s) is moving down and the two masses are getting closer (m_s and m_u), the Skyhook control policy ideally calls for an infinite damping constant. Since an infinite damping constant is not physically attainable, in practice the adjustable damping constant is set to a maximum.

By applying the modification in SH-2, the control algorithm does not consider the direction of the movement of the upper mass or if it is getting close with the unsprung. Instead, it quantifies the severity of this movement considering how fast they are getting close. Then, it selects to not change the damping coefficient in "less harmful and dangerous" situations, and continue using the soft value of the damper's state. In Equation 4.3, the control law of SH-2-CDF is introduced with the use of a threshold in the operational conditions ($T_A \neq 0$). If the threshold's value is zero ($T_A = 0$), the algorithm is converted to the traditional SH-2.

$$C = \begin{cases} C_{min}, & if\ (\dot{z}_s - \dot{z}_u)\,\dot{z}_s < T_A \\ C_{max}, & if\ (\dot{z}_s - \dot{z}_u)\,\dot{z}_s > T_A \end{cases} \tag{4.3}$$

where C_{min} and C_{max} are the soft and the stiff damping coefficient achievable by the considered controllable damper, respectively.

4.2.2 Mixed Skyhook and Acceleration driven damper with CDF control Strategy (SH-ADD-2-CDF).

The SH-ADD-2 algorithm compromises the complementary performances of soft and stiff passive suspensions and using a single sensor. Stiff suspensions are able to damp optimally the body resonance, but without a desiring filtering at high frequencies. On contrary, soft suspensions ensure the best filtering with the drawback of a poorly damped body resonance. This law operates according to the value of $\ddot{z}_s^2 - a^2\dot{z}_s^2$, which is a simple "frequency-range selector".

By applying the CDF strategy, we check the value of the frequency selector with respect to the threshold (T_B). This threshold is evaluated with the cumulative distribution function of the operational conditions, selecting the percentage of the sample that operates with C_{max}. In Equation 4.4, the control law of SH-ADD-2-CDF is introduced with the use of a threshold in the operational conditions ($T_B \neq 0$). If the threshold's value is zero ($T_B = 0$), the algorithm is converted to the traditional SH-ADD-2.

$$C = \begin{cases} C_{min}, & if\ \ddot{z}_s^2 - a^2\dot{z}_s^2 \geq T_B \\ C_{max}, & if\ \ddot{z}_s^2 - a^2\dot{z}_s^2 < T_B \end{cases} \tag{4.4}$$

where the parameter "α" represents the limit between the ranges of low and high frequency. It operates as a tuning coefficient and is selected at 6 Hz (39 rad/sec) for passenger vehicles based on optimization results of the same vehicle model [17].

4.2.3 Design of CDF controller

In this section, the design of the controller proposed is presented and is applied to the quarter car model of Table 4.1, whose suspension system operates initially with SH-2. The only prerequisite for the function of the controller is the measurements required for evaluating the operational conditions of the control algorithm ($\dot{z}_s$ and $\dot{z}_u$), while nor the trajectory of the road profile or its class are needed. Therefore, no additional sensors are required.

Firstly, we consider the case in which the suspension operates completely with SH-2. After the simulation of the vehicle under a random excitation, the values of the control algorithms' operational conditions (X = $\left(\dot{z}_s - \dot{z}_u\right)\ \dot{z}_s$) are fitted to a t-student distribution with a mean value μ and a standard deviation σ. The fit of the operational conditions to the t-student distribution is presented in Figure 4.3a, while due to the large number of the data ($\rightarrow \infty$) the cumulative distribution function (CDF) of t-student, presented in Figure 4.3b, corresponds to the one of the normal distribution [136]. Therefore, using the CDF, the percentage of the sample ($P(X1 < 0)$) which operates with C_{min} is evaluated, after calculating through Equation 4.5 the standardized score $Z1$ that corresponds to $X1 = 0$:

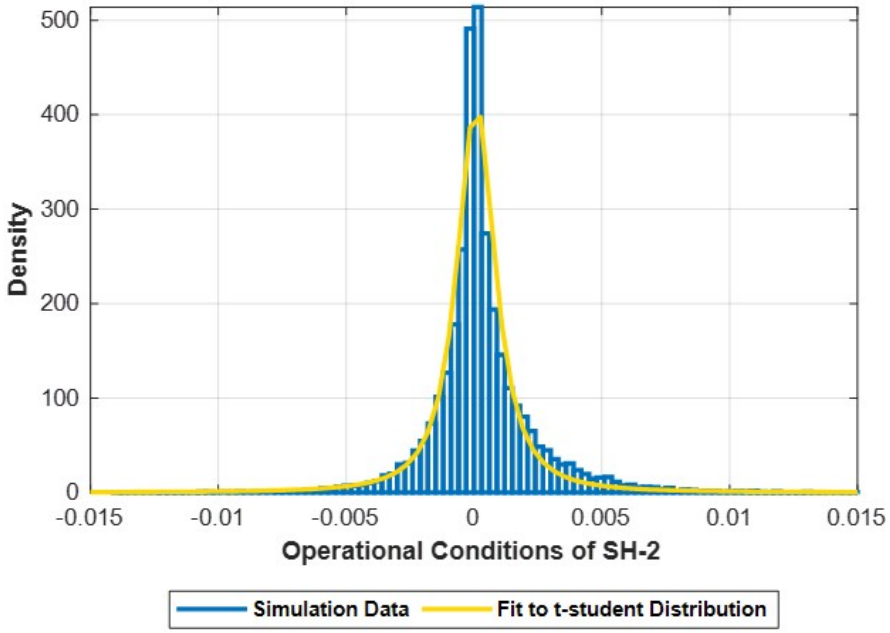

(a) The fit to a t-student distribution.

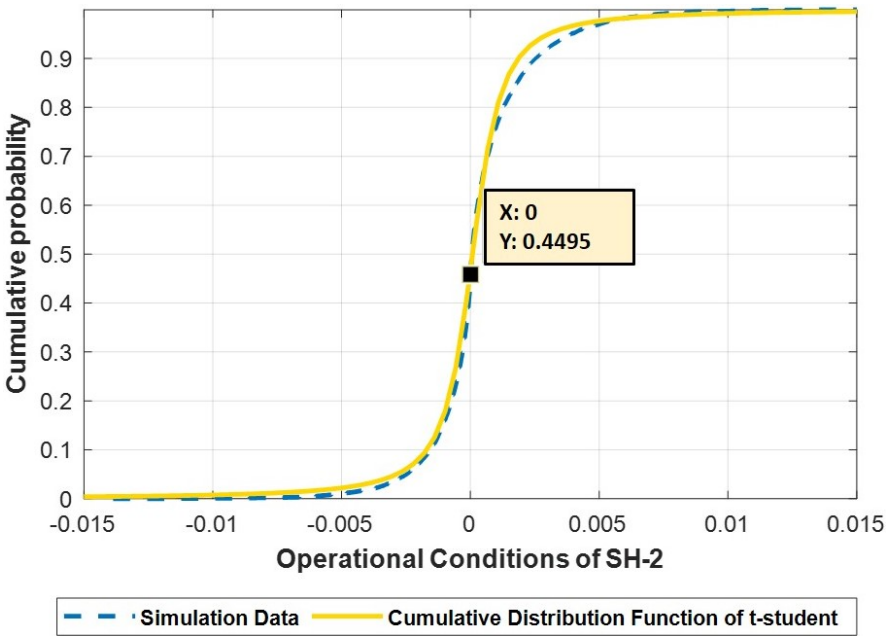

(b) The cumulative function of the distribution.

Figure 4.3: The distribution in which the operational conditions of SH-2 have been fitted in order to evaluate the value of T_A using its cumulative function

$$Z1 = \frac{X1 - \mu}{\sigma} \tag{4.5}$$

The probability of $P(Z1 < \frac{X1-\mu}{\sigma})$ concludes to be equal with the 45%, as it is pointed out in Figure 4.3b. Thus, the damper operates with C_{min} $(N\%)$ and C_{max} $(1 - N\%)$ for the 45% and 55% of the sample respectively, when the suspension is working completely with SH-2.

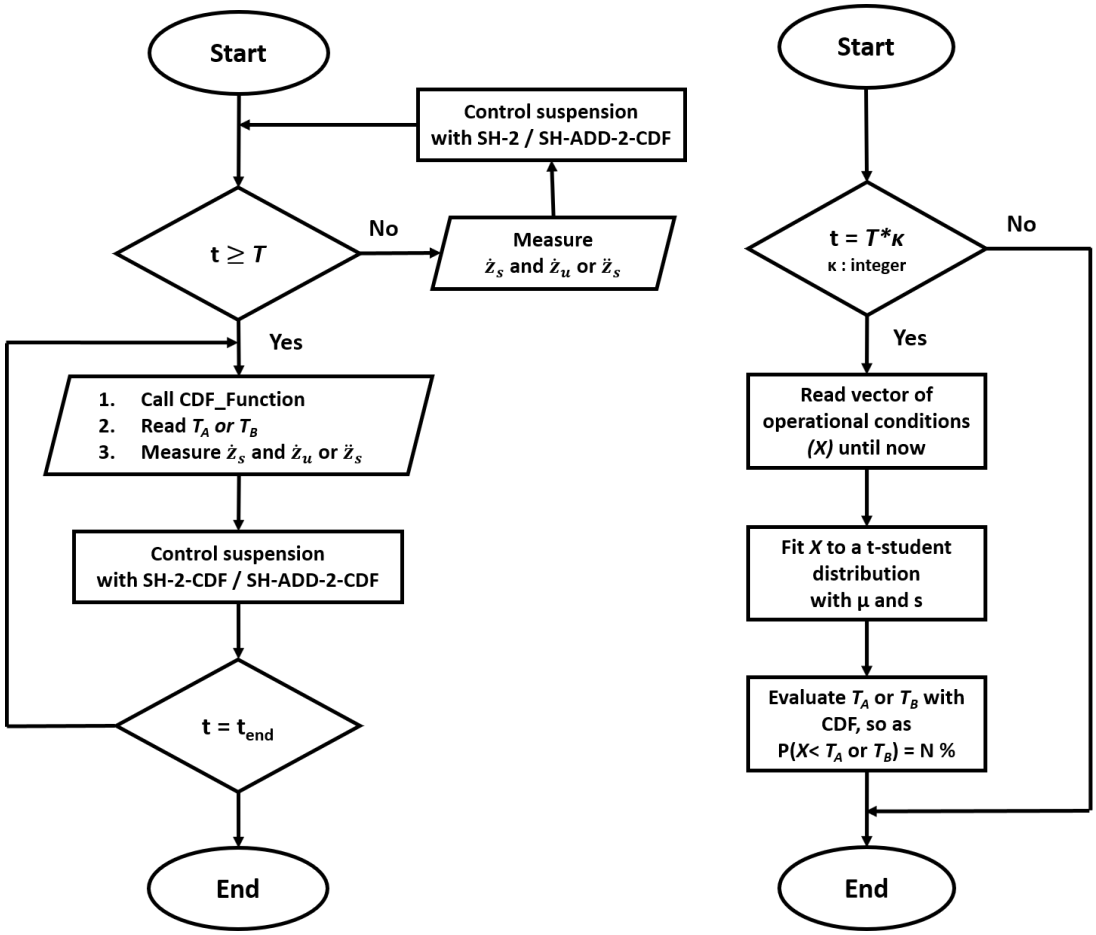

(a) The main function (Main_Function) and the simulation of the vehicle.

(b) The evaluation of the thresholds (CDF_Function).

Figure 4.4: The design of the CDF controller

Considering the above, the control strategy aims to decrease the number of the switches between the damper's states, by decreasing the percentage of the sample operating with C_{max} $(1 - N\%)$. The implementation of the CDF control strategy applied to SH-2 or SH-ADD-2 is presented in Figure 4.4. Based on Figure 4.4a, the suspension system of the quarter car model operates initially with SH-2 for few seconds until t becomes greater or equal to T $(t \geq T)$. Then, the CDF function, shown in Figure 4.4b, is called and operates every $\kappa * T$ so as to reevaluate the threshold's value (T_A or T_B), if

needed. More specifically, the CDF function reads the vector of the operational conditions (X), which have been evaluated until the current point, and it fits the data to a t-student distribution (μ, σ). Later, considering the selected percentage ($N\%$) of the sample operating with C_{min}, either as selected by the suspension designer before or by the driver during the ride, the corresponding threshold is evaluated so as :

$$P(X < T_A) = N\% \tag{4.6}$$

In this case, the percentage of the sample operating with C_{max} $(1 - N\%)$ is reduced around 30% of the sample compared to the 55% of the traditional SH-2. Therefore, the percentage of the sample operating with C_{min} $(N\%)$ is increased around 70%. Then, the corresponding threshold (T_A), which corresponds to probability P($X < T_A$) equal to 70% , is evaluated using the CDF of the distribution. Using the standard normal distribution table [136], the corresponding normalized $Z2$ score for P($X < T_A$) is equal to 0.61. By solving Equation 4.5 for X2, the threshold T_A occurs to be $15{*}10^{-4}$:

$$X2 = \frac{Z2 + \mu}{\sigma} = T_A \tag{4.7}$$

Afterwards, this value is applied to the operational conditions of the SH-2 algorithm (Figure 4.4a) instead of the zero value (Equation 4.1), introducing the SH-2-CDF (Equation 4.2).

4.3 Results

In this Section, the effect of the CDF control strategy is studied taking into consideration the performance metrics that were presented extensively in Section 2.4.2-2.4.6.The SH-2-CDF and SH-ADD-2-CDF are benchmarked against SH-2 and SH-ADD-2 respectively, by investigating thoroughly the impact of our control strategy using figures and tables. More specifically,

1. The values of the CDF algorithms' operational conditions for the random road profile of Class C, the threshold (T_A and T_B) and the switches of damper's states are illustrated in figures. These figures depict the function of our control strategy. (**Fig. 4.5 and 4.8)**

2. After selecting thresholds (T_A and T_B) which correspond to the 27% of the sample operating with C_{max}, the CDF algorithms are compared with the traditional ones for all the road profiles (road bump, random road profile of class A, B and C) by evaluating the percentage of the change ($\frac{X-X_{CDF}}{X}100\%$) in the performance metrics (RC, ST, TD, DE and SW). Also, the threshold values evaluated for each excitation are presented. **(Tables 4.2 - 4.3)**

3. The response of the vertical acceleration of the sprung mass ($\ddot{z}_s$) in time and frequency domain is illustrated, so as to point out the effect of our control strategy on $\ddot{z}_s$. (**Fig. 4.6 and 4.9**)
   More specifically:

   - The response of $\ddot{z}_s$ in time domain is outlined for the case of the road bump for SH-2-CDF and SH-ADD-2-CDF compared to the traditional ones. (**Fig. 4.6a and 4.9a**)
   - The frequency responses of $\ddot{z}_s$ of SH-2-CDF and SH-ADD-2-CDF compared with the SH-2 and SH-ADD-2 respectively, are presented for all the random road profiles. As far as the frequency domain is concerned, two areas will be investigated: (a) the area around 12-10 Hz regarding ride comfort and (b) the area around 30-40 Hz regarding the isolation of the nonlinearities due to the chattering. (**Fig. 4.6b - 4.6d and Fig. 4.9b - 4.9d**)

4. The sensitivity analysis outlines the change of the performance metrics by applying our CDF control strategy to the traditional SH control algorithms and varying the threshold. The thresholds' values correspond to the percentages of the sample operating with C_{max} $(1-N\%)$ from 20 to 70%. In these figures, the operating point of the traditional and the CDF algorithms are pointed out. (**Fig. 4.7 and 4.10**)

4.3.1 Skyhook 2 states control law with CDF control strategy (SH-2-CDF).

The CDF control strategy is applied to the SH-2 algorithm and it is tested for four road profiles. The threshold (T_A) is evaluated as described in the corresponding section and the values occurred are

$3.3*10^{-2}$, $2.4*10^{-4}$, $6*10^{-4}$ and $15*10^{-4}$ respectively for the four road profiles studied (road bump, class A, B and C respectively).

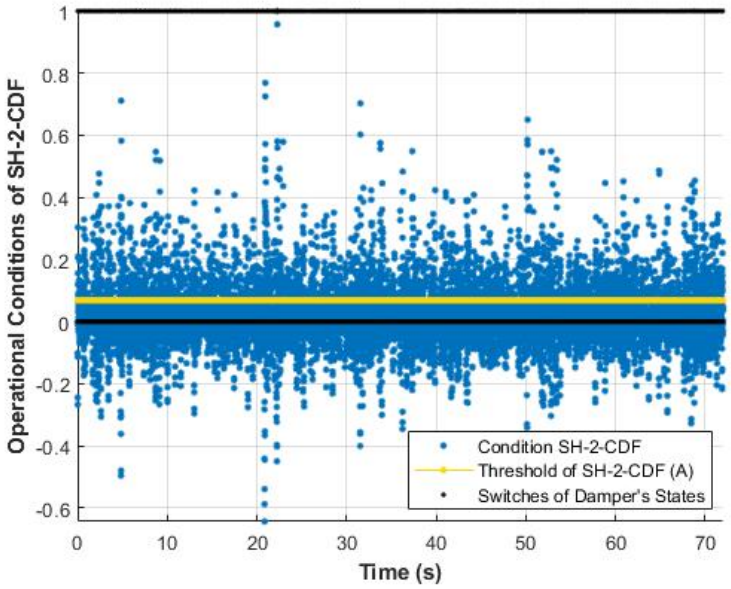

(a) Complete simulation duration.

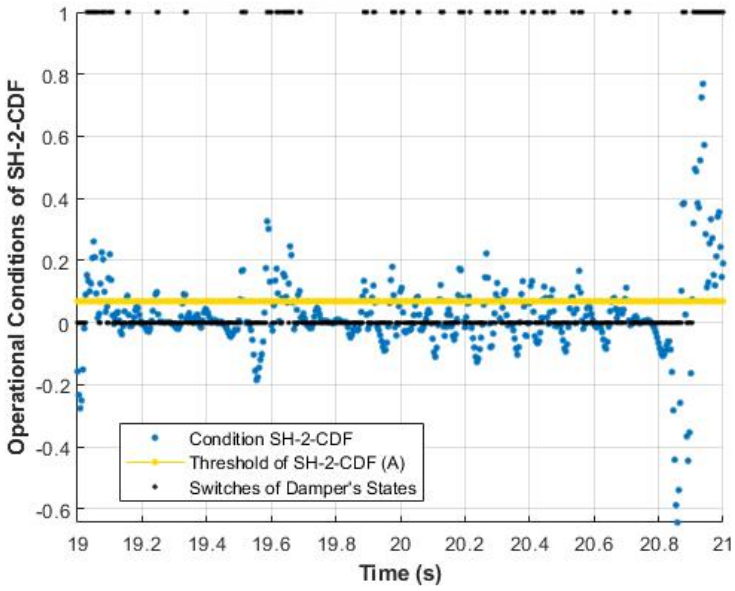

(b) Simulation interval between 19-22 s.

Figure 4.5: The operational conditions of SH-2-CDF, the threshold (T_A) and the switches in the damper's states

The values of the operational conditions of SH-2-CDF for a road profile of Class C, the threshold (T_A) and the switches of the dampers' states are illustrated in Fig. 4.5. Thus, this figure depicts the main

idea of the CDF control strategy, which is the use of a threshold in the operational conditions of SH-2 instead of the zero value. In this figure, the stiff state (C_{max}) of the semi-active damper is designated unity, while the soft state (C_{min}) is designated zero. Also, the operational conditions are normalized with their maximum values, so as to be able to fit in the same figure with the damper's switches. As shown in Fig. 4.5b, where a simulation interval between 19 and 22 *sec* is presented, when the value of the operational condition is above the limit of threshold T_A, C_{max} is applied. In contrast to the SH-2 algorithm, where the C_{max} would have been applied if the value of the operational condition was above zero.

Road Bump / $T_A = 3.3 * 10^{-2}$				
Index	**Unit**	**SH-2**	**SH-2-CDF**	**Percentage**
Switches	[#]	281	71	74.73%
RC	$[m/s^2]$	1.67	1.66	0.60%
ST	$[mm]$	8.00	8.40	-5.00%
TD	$[mm]$	3.15	3.13	0.63 %
DE	$[kJ/s]$	3.71	3.57	3.59%
Road Class A / $T_A = 2.4 * 10^{-4}$				
Switches	[#]	1638	958	41.51%
RC	$[m/s^2]$	0.28	0.25	10.71%
ST	$[mm]$	0.88	0.92	- 4.55%
TD	$[mm]$	0.44	0.42	4.55%
DE	$[kJ/s]$	0.74	0.62	15.92%
Road Class B / $T_A = 6 * 10^{-4}$				
Switches	[#]	2254	1360	39.66%
RC	$[m/s^2]$	0.45	0.41	8.89%
ST	$[mm]$	1.35	1.40	-3.70%
TD	$[mm]$	0.71	0.68	4.49%
DE	$[kJ/s]$	1.88	1.67	10.93%
Road Class C / $T_A = 15 * 10^{-4}$				
Switches	[#]	3609	2188	39.37%
RC	$[m/s^2]$	0.68	0.62	8.82%
ST	$[mm]$	2.16	2.25	-4.17%
TD	$[mm]$	1.06	1.00	5.48%
DE	$[kJ/s]$	3.95	3.59	9.03%

Table 4.2: The comparison of the performance metrics (SW, RC, ST, TD and DE) of SH-2 and SH-2-CDF algorithms for all the road profiles

The SH-2-CDF algorithm is compared with SH-2 for all the road profiles by evaluating the percentage of the change in all the performance metrics of Section 2.4. The results are illustrated in Table 4.2. Regarding the road bump, there is no significant improvement and the performance metrics of SH-2

and SH-2-CDF are almost the same, except for a slight increase in the suspension travel (ST). Despite the fact that the vehicle's performance is unaffected based on the performance metrics, the switches in the damper's states have decreased up to 74 %. This is really crucial considering that a reduction in the number of switches is essential to avoid overheating, wear and reduced life of damper's components. However, despite the minor effect in the performance metrics, the change in the operational conditions affects the dynamic behavior of the vehicle, as shown in Fig. 4.6a. The sprung mass' acceleration response ($\ddot{z}_s$) in time domain (Fig. 4.6a) has less oscillatory behavior and is damped more effectively during the settling of the vibrations (after 1.7 sec and after 2.7 sec). This remark depicts the effect of the decreased switches on the measured acceleration and the dynamic behavior of the vehicle in general. However, this effect isn't illustrated in the RC metric of Table 4.2, because the acceleration in Eq. 2.78 is weighted as described in Section 2.4 and ISO 2631:1995 [96].

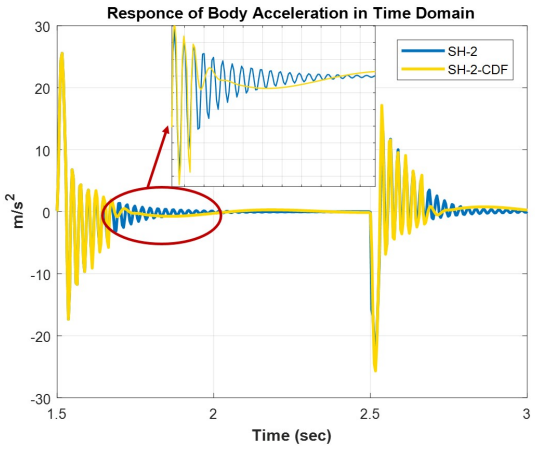

(a) Time Responce-Road Bump.

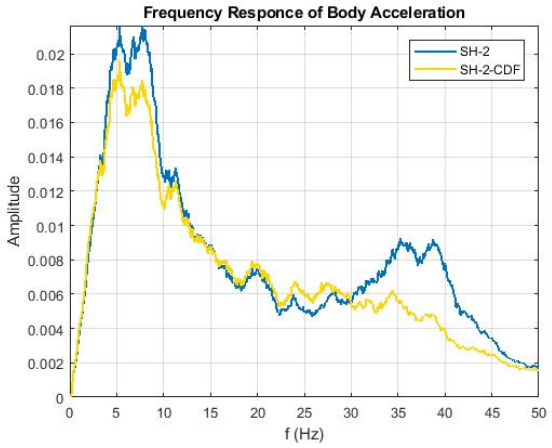

(b) Frequency Response-Road Class A.

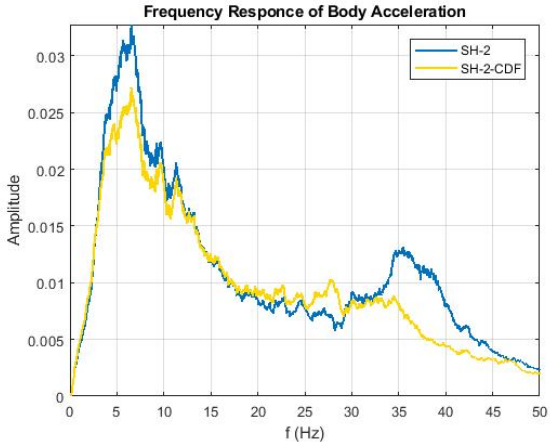

(c) Frequency Response-Road Class B.

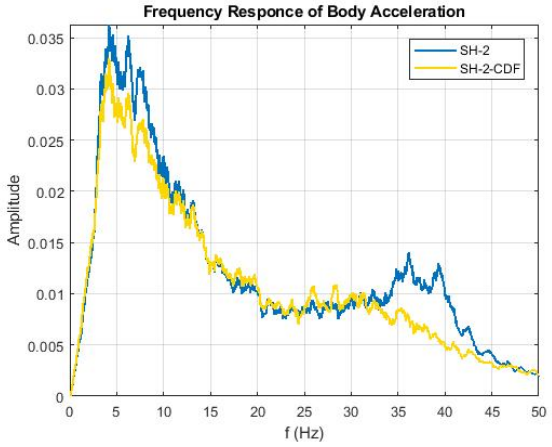

(d) Frequency Response-Road Class C.

Figure 4.6: Comparison of the response of $\ddot{z}_s$ between SH-2 and SH-2-CDF for all the road profiles

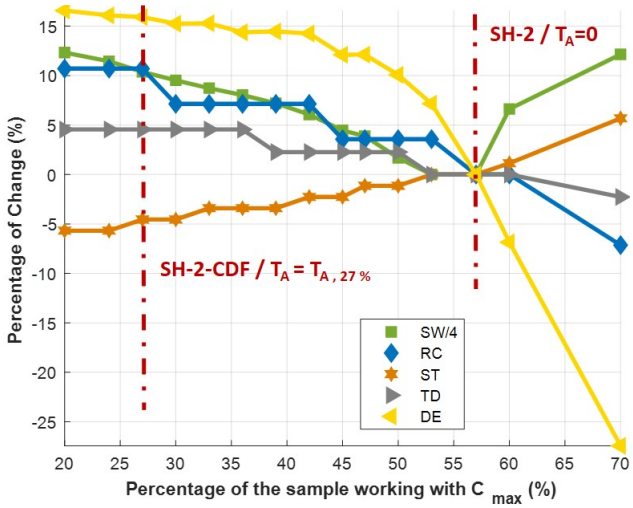

(a) Road A.

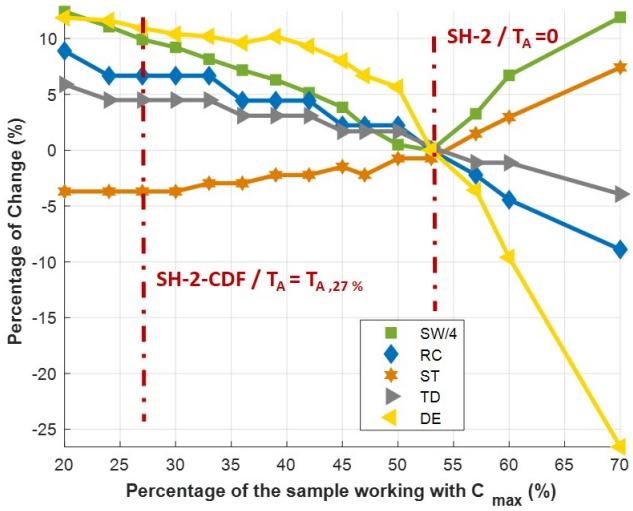

(b) Road B.

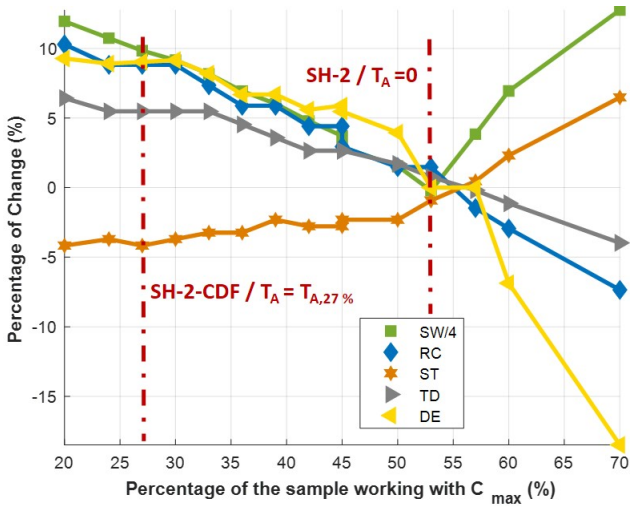

(c) Road C.

Figure 4.7: Sensitivity analysis of the difference in the performance metrics (SW, RC, ST, TD and DE) comparing SH-2 with SH-2-CDF for various threshold values corresponding to different percentages of the sample operating with C_{max} $(1-N\%)$ under the random road profile of (a) Class A, (b) Class B and (c) Class C.

In contrast to the road bump, while the vehicle drives through the random road profiles (Classes A, B and C) its performance is significantly improved simultaneously with a decrease in the switches of the damper's states. More specifically, the three profiles have an improvement in ride comfort around 8-10% and a reduce of 40% in the number of switches, in accordance to Table 4.2. The increase in the ride comfort is also illustrated from Fig. 4.6, where the peaks of the area around 1-10 Hz are isolated more compared to the SH-2. Fig. 4.6b, 4.6c and 4.6d present the results of the three road profiles of class A,B and C, respectively. The improvement in the isolation of the nonlinearities, and thus the suppression of the chattering, are illustrated in Fig. 4.6b - 4.6d, where the peaks of the area around 30-40Hz are better isolated in SH-2-CDF compared to the traditional SH-2 algorithm. Additionally, in all road profiles, a decrease of 9-16% is noticed in the dissipated energy of the damper, which is really crucial considering that the dissipated power may offer simultaneous benefits to hardware temperature and forward power requirements, as Crolla et. al [97] and Karnopp [98] concluded. Moreover, the tire deflection is improved by around 5% in all the random profiles, whereas the suspension travel is increased by the same levels balancing this change.

Finally, the impact of varying thresholds on the performance of the vehicle is illustrated in Fig. 4.7. As it was mentioned before, the threshold T_A is evaluated based on the percentage of the sample of the operational conditions operating with C_{max} $(1-N\%)$. Thus, the sensitivity analysis is conducted by finding the corresponding threshold in order to decrease the percentage of the sample operating with C_{max} between 20-70%. Then, the difference of the performance metrics comparing SH-2 with SH-2-CDF is evaluated and plotted. More specifically, Fig. 4.7 is the Table 4.2 for various thresholds. In this figure, the percentage of the switches (SW) in the damper's state is divided by four, so as to fit better in the y-axis limits of the other metrics. Also, the point where all the curves converge is when the threshold reaches zero and the suspension would have operated with the SH-2 algorithm. Based on Fig. 4.7, as the threshold increases and corresponds to less and less percentage of the sample working with C_{max}, the algorithm becomes more ride comfort oriented (decrease of RC) with a significant decrease in the switches of the damper's state. However, the suspension travel is slightly increased in all the cases, but it is balanced by a similar decrease in the tire deflection. Last but not least, even for the use of a small threshold corresponding to the use of C_{max} for 53% instead of 55%, the number of switches is decreased essentially and the vehicle's performance is improved.

4.3.2 Mixed Skyhook-Acceleration driven damper control with CDF control strategy (SH-ADD-2-CDF).

In Fig. 4.8, similarly with Fig. 4.5, the values of the operational conditions, the threshold (T_B) and the switches of the dampers' stated are illustrated. The threshold values are negative compared to the positive ones of SH-2-CDF due to the mean value (μ) and the standard deviation (σ) of the fitted distribution.

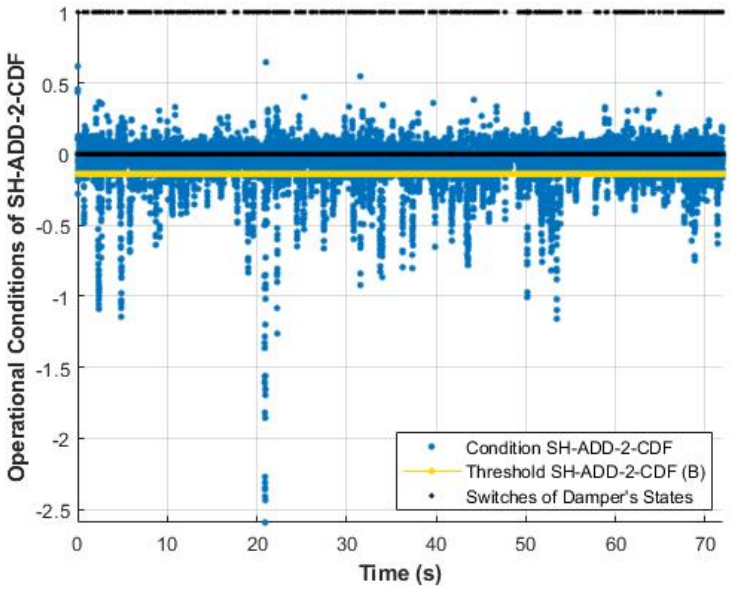

(a) Complete simulation duration.

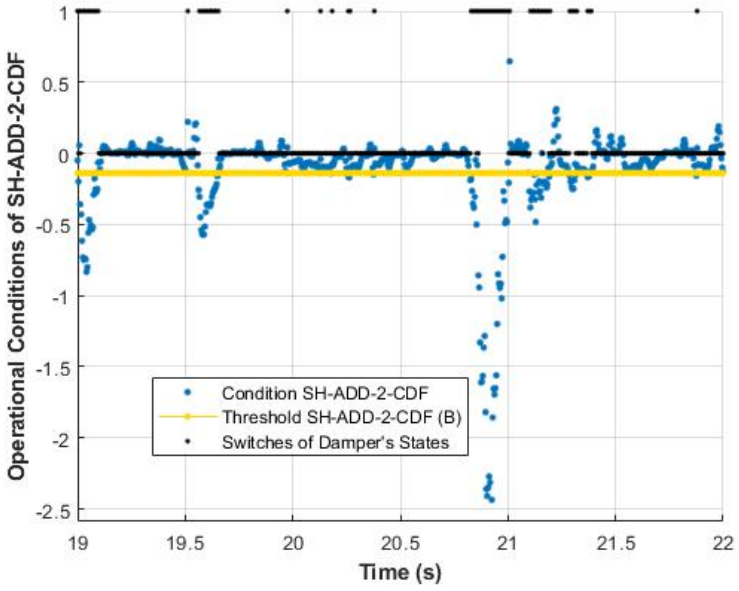

(b) Simulation interval between 19-22 s.

Figure 4.8: The operational conditions of SH-ADD-2-CDF, the threshold (T_B) and the switches in the damper's states

The comparison of SH-ADD-2-CDF with SH-ADD-2 using the performance metrics is illustrated in Table 4.3 for all the road profiles. As discussed in the previous case based on Table 4.2, in the case of the road bump there is no significant improvement in the performance metrics, except from a 5% improvement in the dissipation energy. However, with the use of the CDF control strategy there is a significant decrease in the switches of the damper's states up to 74%. This decrease is really important considering that the vehicle's performance is the same avoiding overheating, wear and reduced life of damper's components. Moreover, despite the minor changes in the metrics, the CDF approach has affected the dynamic behavior of the vehicle during its settling, as it could be seen from Fig. 4.9a. The response has less oscillatory behavior during the settling of the vibration after the wheel have ascended the bump (1.7 sec) or have descended it (2.7 sec). This is mainly due to the significant decrease in the switches.

Road Bump / $T_B = -31$				
Index	**Unit**	**SH-ADD-2**	**SH-ADD-2-CDF**	**Percentage**
Switches	[#]	165	43	73.94%
RC	$[m/s^2]$	1.61	1.60	0.62%
ST	$[mm]$	7.80	8.10	-3.85%
TD	$[mm]$	3.10	3.10	0%
DE	$[kJ/s]$	3.44	3.24	5.70%
Road Class A / $T_B = -0.31$				
Switches	[#]	2376	566	76.18%
RC	$[m/s^2]$	0.24	0.21	12.50%
ST	$[mm]$	0.91	1.00	-9.89%
TD	$[mm]$	0.42	0.40	4.76%
DE	$[kJ/s]$	0.62	0.54	12.90%
Road Class B / $T_B = -0.70$				
Switches	[#]	3453	702	79.67%
RC	$[m/s^2]$	0.39	0.35	10.26%
ST	$[mm]$	1.38	1.47	-6.52%
TD	$[mm]$	0.66	0.64	3.03%
DE	$[kJ/s]$	2.65	1.44	12.73%
Road Class C / $T_B = -2.10$				
Switches	[#]	5369	982	81.71%
RC	$[m/s^2]$	0.60	0.53	11.67%
ST	$[mm]$	2.28	2.49	-9.21%
TD	$[mm]$	0.99	0.94	5.05%
DE	$[kJ/s]$	3.65	3.24	11.23%

Table 4.3: The comparison of the performance metrics (SW, RC, ST, TD and DE) of SH-ADD-2 and SH-ADD-2-CDF algorithms for all the road profiles

(a) Time Response-Road Bump.

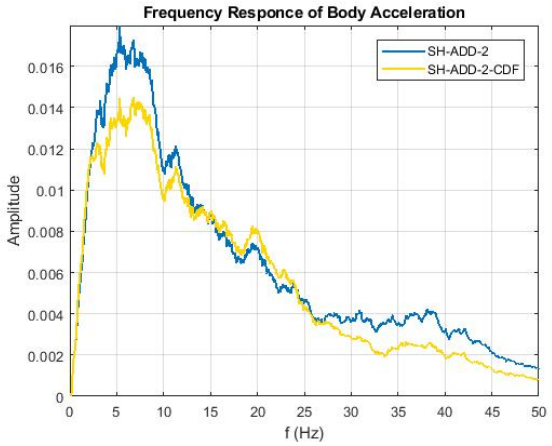

(b) Frequency Response-Road Class A.

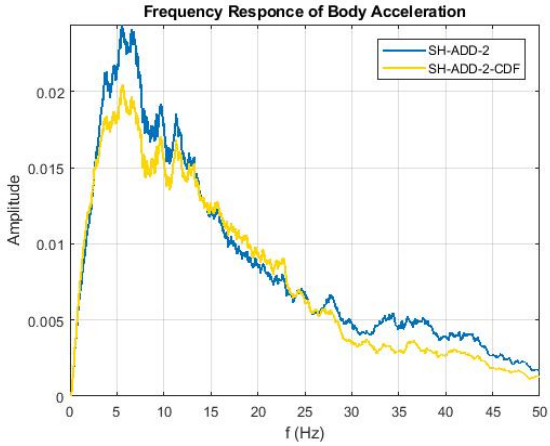

(c) Frequency Response-Road Class B.

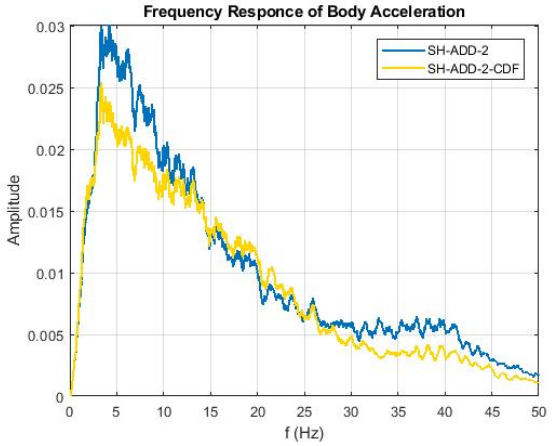

(d) Frequency Response-Road Class C.

Figure 4.9: Comparison of the response of $\ddot{z}_s$ between SH-ADD-2 and SH-2-ADD-CDF for all the road profiles

On the other hand, while the vehicle drives through the random road profiles its performance is significantly improved simultaneously with a decrease in the switches of the damper's states up to 82%. More specifically, in the three cases, there is an improvement in ride comfort around 10-13% based on Table 4.3. Also, this is illustrated from Fig. 4.9, where the peaks of the area around 1-10 Hz are isolated more successfully than the SH-ADD-2 algorithm. In addition, an improvement in the isolation of the nonlinearities is presented from Fig. 4.9. This improvement occurs due to the reduce of the switches which affect the chattering of the algorithm. Furthermore, in all the road profiles, a decrease of 12% is noticed in the dissipated energy of the damper. Regarding the vehicle stability, the tire deflection is slightly decreased in all the road profiles around 5 %, in contrast to the increase of the suspension travel around 10%.

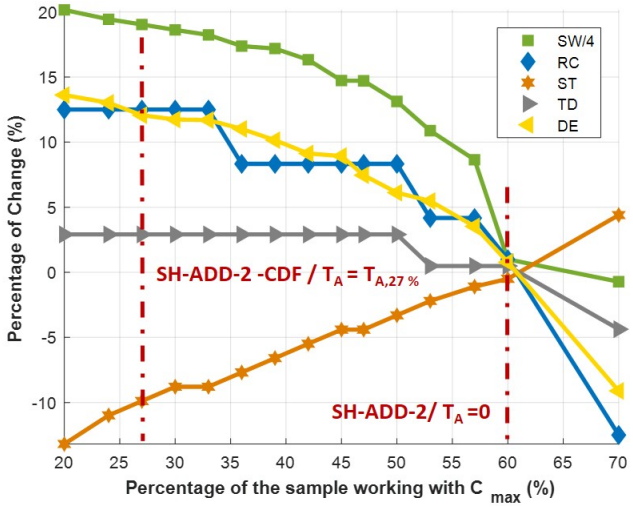

(a) Road A.

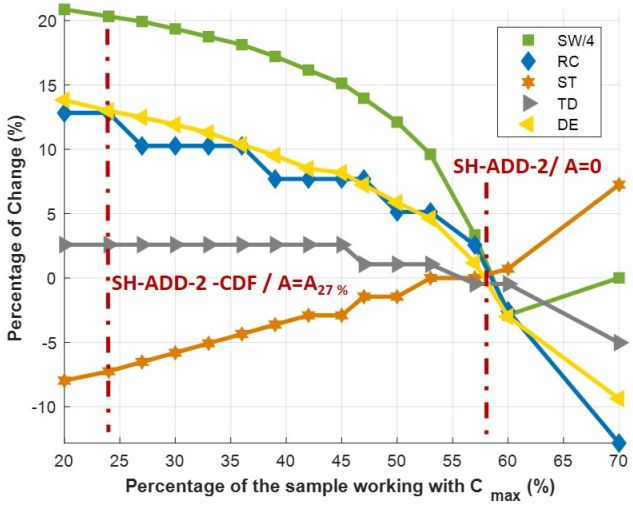

(b) Road B.

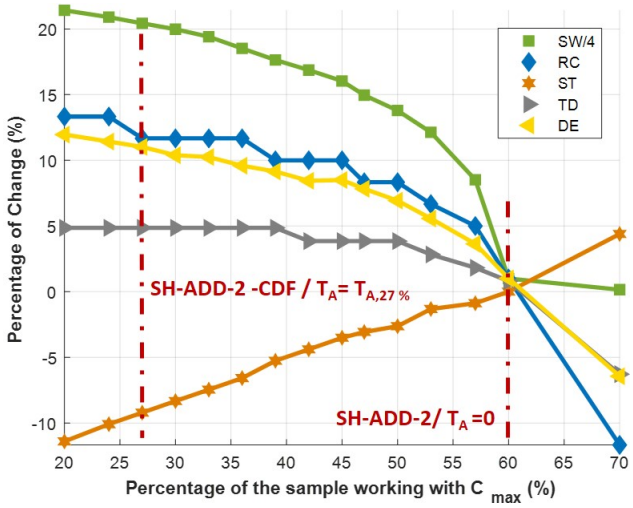

(c) Road C.

Figure 4.10: Sensitivity analysis of the difference in the performance metrics (SW, RC, ST, TD and DE) comparing SH-ADD-2 with SH-ADD-2-CDF for various threshold values corresponding to different percentages of the sample operating with C_{max} $(1-N\%)$ under a random road profile of (a) Class A, (b) Class B and (c) Class C.

Finally, the impact of different threshold's value on the performance of the vehicle is illustrated in Fig. 4.10, in accordance to Fig. 4.7. The point where all the curves converge is when the threshold is zero and the algorithm operates with the tranditional SH-ADD-2 algorithm, which is almost when the 60% of the sample operates with C_{max} $(1 - N\%)$. As the threshold corresponds to less and less percentage of the sample working with C_{max}, the algorithm becomes more ride comfort oriented, without costing road holding and decreasing significantly the switches of the damper's state.

4.4 Conclusions

To sum up, in this thesis, a new distribution-based control strategy for SH algorithms is proposed for a vehicle suspension system. The novelty of this work is the use of an appropriate threshold in the operational conditions, which quantifies the severity of the algorithm's operational conditions and controls the damper state based on their magnitude and not based on their sign. The CDF strategy is applied to two SH control algorithms and is benchmarked against them for various performance metrics. Its superior performance is shown through simulation results for a road bump and three random profiles, investigating the ride comfort and the road holding of the vehicle with respect to performance metrics (SW, RC, ST, RT and DE), which are widely used in the literature

We conclude that:

1. The CDF strategy leads to an improvement in the road holding of the vehicle and the ride comfort of approximately 6% and 13%, respectively. Even for the use of a small threshold corresponding to the 53% of the sample operating with C_{max} instead of the 55% in the case of the traditional algorithms, the number of switches is decreased significantly and the vehicle performance is improved. Thus, even then the application of the proposed algorithm is beneficial.

2. The CDF strategy manages to decrease the number of the damper's state switches for 40% and 82% without deteriorating the vehicle's performance. In addition, the dissipation energy of the damper is decreased up to 16%. Both of the above decreases are crucial for the damper's components life. The decrease in the switches could increase the expected life of the damper's component by reducing their fatigue, while the decrease in the dissipation energy reduces the temperatures of the fluid, the seals and the damper's hardware. In addition, the minimization of the mean dissipated power will offer simultaneous benefits to forward power requirements.

3. As far as chattering is concerned, the CDF control strategy eliminates to an important extend the nonlinearities originating from the switches of the damper's state. This is achieved without deteriorating the performance of the vehicle in any of the studied cases.

4. Last but not least, the CDF control strategy, as presented in this work, could be directly applied, without any changes, in a number of existing works. For instance, our control strategy is applicable to other well-known ride-comfort-oriented algorithms (SH-L, SH-ADD-1 and ADD), to some road-holding-oriented ones (Groundhook) and other recently proposed such as the one by Nie et al. [83]. Also, existing chassis control algorithms could adopt the CDF strategy and investigate its impact on their performance.

Considering the promising results of this work and that the topic of semi-active suspensions is talked and published for decades, the importance of our control strategy could be identified in the significant amount of existing works that could be applied. For instance, our control strategy could also be

applied to other well-known ride comfort oriented algorithms (SH-L, SH-ADD-1 and ADD), to some road holding oriented ones (Groundhook) [137–139] and other existing in the literature such as the one proposed by Nie et al.[83]. Also, existing chassis control algorithms [140] could adopt the CDF strategy and investigate its impact on their performance.

CHAPTER 5

Assessment of the optimization procedure for a suspension system

Ride comfort and road holding depict one of the main conflicts in vehicle dynamics and the optimization of the suspension systems with respect to these performance requirements, is discussed extensively in the literature. Researchers have been trying to find the optimum design of a suspension system using various objective functions and optimization methods.

In this chapter, the optimization procedure of suspension systems is investigated. More specifically, not only the efficiency of different optimization methods is studied but also the efficiency of various fitness and objective functions. In order to investigate thoroughly the optimization procedure, both single (SOO) and multi-objective optimization (MOO) approaches have been adopted. The single objective approach offers a limited insight in the suspension optimization problem but due to its simplicity it is often preferred over the more complex and time consuming multi-objective approach. A simple multi-objective dealing strategy, known as pseudo-MOO techniques, is used in this thesis and suggests the combination of multiple objective functions using weighting factors. Therefore, three (3) optimization algorithms are used (Genetic Algorithms, Gradient Based and a hybridization of them) for the optimization of five (5) objective functions, following SOO and pseudo-MOO approaches. The results are compared using figures illustrating the relation between the objectives, tables displaying the optimal design variables and important performance metrics regarding the dynamic behavior of the vehicle. Finally, a benchmark against all the solutions character is illustrated in order to extract conclusions regarding the efficiency of the objective functions and the optimization methods.

5.1 Materials & Methods

5.1.1 Optimization Methods

Stochastic Algorithms

Genetic Algorithms are stochastic global search and optimization methods. They simulate the metaphor of the natural biological evolution and are developed based on the Darwinian theory of the "survival of the fittest". Unlike other stochastic methods, genetic algorithms manipulate populations of possible solution instead of one possible solution at a time. GAs are suitable for finding the minimum of a function (or of a set of functions) by performing a semi-stochastic search. In genetic algorithms, the design variables are coded as finite length strings in binary representation most of the times (chromosomes). Each bit of the string can be either 0 or 1. Real coding was introduced later in more complex GAs variations. GA includes three major processes: selection, crossover and mutation. Each member of the current population is evaluated by the objective function and thus is given a value, which is called fitness. Depending on the selection criteria, the best or the "fittest" members of the population are selected as parents in order to breed children via the crossover function. There are various methods concerning the crossover such as single-point or two point-crossover etc. In this way the best characteristics of the parents (so far) are incorporated in the children. Mutation randomly changes a certain bit of the children's string from 0 to 1 and vice versa. Mutation is a very important procedure, despite its simplicity, because it increases the diversity of the population and prevents the method from being trapped into local minima. This is how a new generation is created and consequently is evaluated again. GAs are based on an elitist reproduction strategy, where the strongest members of the population (design solutions) are selected for reproduction and are given the opportunity to strengthen the chromosomal (i.e. genes, namely design variables) makeup of the next generation. Unlike many other search techniques, GAs consider multiple design solutions (a population) at each iteration. The previous steps are iterated until the stopping criteria imposed by the user are met. The stopping criteria may differ, depending on the preferences of the analyst. The convergence of the fitness function or a maximum number of generations are often used as stopping criteria of a genetic algorithm.

Deterministic Methods

Gradient Based Algorithms are developed to find the nearest local optimum. These algorithms work with calculating the gradient(s) of the search field at a point in question. The gradient can be calculated analytically from the gradient vector function, otherwise a pseudo-gradient is needed. The pseudo gradient can be calculated experimentally by producing the derivative of the search field with very small steps. The searching is moving towards based on the gradient, where the optimization

needs (maximum or minimum). The requirement of the gradient rise the need for continuous objective function and even the continuity of the first gradient of the objective function. The steepest descent method or the adjoint gradient method are well-known methods that fall into this category. In general, these methods work as follows: an initial set of values is assigned to the design variables, and the objective function is calculated. Depending on the method, the satisfaction of the constraints is checked afterwards, with penalties given to the objective function value if the constraints are not satisfied (KKT Method etc.). The method used in this report follows the previously described process. Its asset is that a large constraint problem is transformed to an unconstrained one due to the penalty given to the objective function. The penalty is imposed only to the active constraints (the ones that are not satisfied) using Lagrange Multipliers to balance the deviations that are due to the differences in magnitude. The last step in this iterative process is the calculation of the derivatives of the objective function and the assignment of new values to the design variables. The algorithms stops when a global or local minimum is found or if the desirable convergence is achieved.

Theoretical comparison of the methods

The main difference between the previously discussed methods lies in the core of their algorithms. Gradient Based methods are deterministic while the GAs are stochastic. Due to that fact G.As are more likely to find a global minimum, contrary to the Gradient Based Methods which are often trapped in a local minimum. In addition, the genetic algorithms do not require the calculation of any derivative. Thus, the fitness function of the GAs does not need to be continuous, so they are able to handle problems with discrete solution spaces. Furthermore, gradient based methods should be used when the area of the desired solution is known, in any other case the G.As have better results due to their stochastic nature. In order to validate these theoretical remarks, the two methods are compared in the next chapter of this report.

Hybrid Algorithms

Hybrid Algorithms form a new area of interest for the research community, and the optimization methods would not be the exception. Hybrid optimization algorithms combine two or more different optimization methods in order to solve a problem, switching between them over the course of the algorithm. In this way all the advantages of the involved methods are drafted in order to achieve the optimum result. For example, GA are more likely to find a global minimum, contrary to the GB which are often trapped, as well as the fact that the GA do not require the calculation of any derivative. Thus, the fitness function of the GA does not need to be continuous, so they are able to handle problems with discrete solution spaces. Furthermore, GB should be used when the area of the desired solution is known, in any other case the GA have better results due to their stochastic nature. Based on these points, a possible combination would be a stochastic method followed by a deterministic one. In

the beginning. GA will operate for a number of generations with large population in order to locate the area of the optimum solution. After that, GB is employed so as to locate the global minimum, knowing the area of the desired solutions. The GA set of optimal values is used as initial value for the GB method, and the upper and lower bounds are set in a symmetric area around the initial values. Thus, the ability of GB methods to converge to a local (in this case global) minimum is exploited. The genetic part in the hybrid algorithm was active for 10 generations.

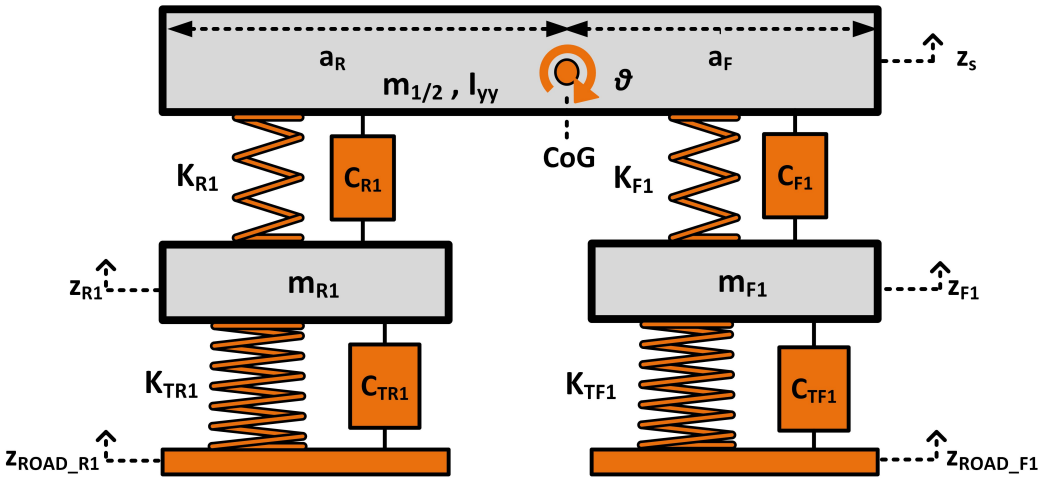

Figure 5.1: Half Car Model considering the front and the rear vehicle's wheel

5.1.2 Simulation Model

In the current study, as it was mentioned before, in order to investigate the efficiency of various objective functions, we use the HC2 car model, as shown in Figure 5.1 and described in Chapter 2.1.3. The springs of both the front and rear suspension systems of the vehicle model are considered non-linear and the force (F_K) applied by them is described by Equation 2.31. Moreover, the tire springs and the suspension dampers are modeled as linear elements and their forces follow Equations 2.28 and 2.32, respectively. In addition, the tire damper is neglected (C_T=0).

Parameter	Unit	Value	Parameter	Unit	Value
$m_{1/2}$	$[kg]$	2210	a_F	$[m]$	1.61
I_{yy}	$[kgm^2]$	1142	a_R	$[m]$	1.67
m_{F1}	$[kg]$	50	K_{TF1}	$[N/m]$	$4.00\ 10^5$
m_{R1}	$[kg]$	100	K_{TR1}	$[N/m]$	$8.00\ 10^5$

Table 5.1: Parameters of HC2 model used in this chapter

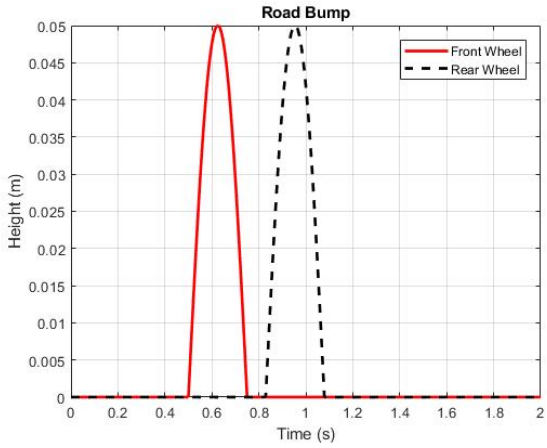

Figure 5.2: The road bump applied to the vehicle model of this chapter

5.1.3 Road Excitation

In this chapter, a road bump is generated using a sinusoidal function, as shown in Figure 5.2. The height (h) of the bump is set to $0.05m$ with an appropriate length (L) for the half-sinusoidal of $L = 2m$. The vehicle velocity (V) is constant at 40 km/h. The design of the road bump (L, h) as well as the high speed of the vehicle, constitute the road excitation intense allowing us to use the road bump instead of a random road profile. The front and the rear wheels follow the same trajectory with a time delay $t_{distance}$, which is due to the distance $a_F + a_R$ between the front and rear wheels.

5.2 Optimization Procedure

5.2.1 Design variables, Constraints and Objective Functions

In all the optimization scenarios that are implemented in this chapter, the key parameters of the suspension systems are selected as design variables and are presented in Equation 5.1 :

$$\text{design variables}=[K_{l_{F1}};C_{F1};K_{l_{R1}};C_{R1};K_{nl_{F1}};K_{nl_{R1}}] \tag{5.1}$$

where $K_{l_{F1}}$, $K_{nl_{F1}}$, $K_{l_{R1}}$ and $K_{nl_{R1}}$ are the linear and nonlinear coefficients of the front and rear spring forces (Equation 2.31) and C_{F1} and C_{R1} are the linear coefficients of the front and rear dampers (Equation 2.32). The upper and lower bounds of these design variables are shown in Table 5.2.

As far as the constraints of the problem are concerned, they are selected regarding the ride comfort of the passengers and the nonlinear part of the suspension springs as shown in Eq. 5.2 and 5.3 respec-

Design Variable	Unit	Lower Bound	Upper Bound
$K_{l_{F1}}, K_{l_{R1}}$	$[N/m]$	3.2 10^4	1.5 10^5
C_{F1}, C_{R1}	$[N.s/m]$	2.0 10^3	1.0 10^4
$K_{nl_{F1}}, K_{nl_{R1}}$	$[N/m^3]$	5.0 10^5	3.0 10^8

Table 5.2: Upper and lower bounds of the design variables

tively. The RCs, based on Equation 2.78, is required to be less than 0.8 m/s^2 and the maximum usage of the nonlinear part of the suspension force ($Ratio_i$) to be between 10 - 30%, based on Equation 2.31.

$$RC_s < 0.8\ m/s^2 \tag{5.2}$$

$$10\ \% < Ratio_i = max\left(\frac{K_{nl_i}x^3}{K_{l_i}x + K_{nl_i}x^3}\right) < 30\ \% \tag{5.3}$$

where $i = F1,\ R1$. As far as the objective functions are concerned, single-objective problems as well as pseudo multi-objective ones are investigated in terms of their efficiency and their convergence. Thus, three single-objective problems are formulated considering two different vehicle performance aspects to optimize. The first one is the ride comfort of the passengers, which is represented using objective f_1 (Equation 5.4-Case 1), as described in Chapter 2.4.2. The second one is the vehicle stability, which is represented by two performance metrics. The former one is the mean value of the variance of the front and rear suspension travels (f_2- Equation 5.5 - Case 2), representing vehicle handling as described in Equation 2.87 of Chapter 2.4.4. The latter is the mean value of the variance of the front and rear tire deflections (f_3- Equation 5.6 - Case 3), ensuring road holding as described in Equation 2.89 of Chapter 2.4.4.

$$f_1 = \frac{1}{n}\sum_{j=1}^{n}(\ddot{z}_{s_j} - \overline{\ddot{z}_s})^2 = VAR(\ddot{z}_s) \tag{5.4}$$

$$f_2 = \frac{1}{2}\left(VST_{F1} + VST_{R1}\right) \tag{5.5}$$

$$f_3 = \frac{1}{2}\left(VTD_{F1} + VTD_{R1}\right) \tag{5.6}$$

Moreover, due to the fact that the above objectives ($f_1,\ f_2$ *and* f_3) are in conflict, they are combined, so as to formulate a multi-objective problem and investigate the balancing between the objectives. In this respect, a pseudo-MOO technique is adopted and the objectives are combined with appropri-

ate balancing factors (w_1, w_2 and w_3) for each objective respectively (f_1, f_2 and f_3), as shown in Equation 5.7, converting the MOO problem to a SOO (Case 4 and 5).

$$f_{4,5} = w_1 f_1 + w_2 f_2 + w_3 f_3 \tag{5.7}$$

where w_1, w_2 and w_3 are the weighting factors. In order to investigate the multi-objective approach more accurately, two cases are tested. In the first case (f_4), the magnitudes of all the three objectives (f_1, f_2 and f_3) are balanced and set at the same order of magnitude (Case 4). On the other hand, in the second case (f_5) different weighting factors are selected. In this case (f_5), the main idea is the use of the two additional objectives as dynamic penalty functions rather than optimization targets. In this respect, f_1 is selected as the main objective and f_2 and f_3 as the penalty functions. Thus, the weighting coefficients are considered so as the magnitude of f_1 to be one order greater than the ones of the other two objectives, f_2 and f_3 (Case 5). The values of the weighting factors for Case 4 and 5 are selected based on random simulations of the model.

5.2.2 Scenarios

The optimization is implemented with the Optimization Toolbox of MATLAB R2016a, provided for academic use by NTUA. The optimization methods applied to the problem are a Genetic Algorithm (*ga* of MATLAB), a Gradient Based Algorithm (active set of *fmincon* of MATLAB) as well as a hybridization of the above. Thus, five different scenarios (S_1-S_5), regarding the optimization methods, are implemented for five (5) different cases as far as the fitness functions are concerned (Case 1-5). The optimization scenarios are illustrated in Table 5.3 in detail. In S_1 and S_3, the population size is set to 200 as proposed in MATLAB R2016a for problems with more than five (5) design variables (currently six), whilst in S_2 and S_4, the population size is set to 1000 in order to investigate the influence of the population size. As far as the hybrid method is concerned, the part of the genetic algorithm is active only for 10 generations and then the gradient based algorithm is enabled. For all the optimization scenarios the tolerance of the fitness function is set low at 10^{-6}.

Scenario	**Algorithm**	**Optimization Parameter 1**		**Optimization Parameter 2**	
S_1	Genetic	*Population Size*	200	*Fitness function tolerance*	10^{-6}
S_2			1000		
S_3	Hybrid		200		
S_4			1000		
S_5	Gradient Based	-			

Table 5.3: Implemented optimization scenarios for each case

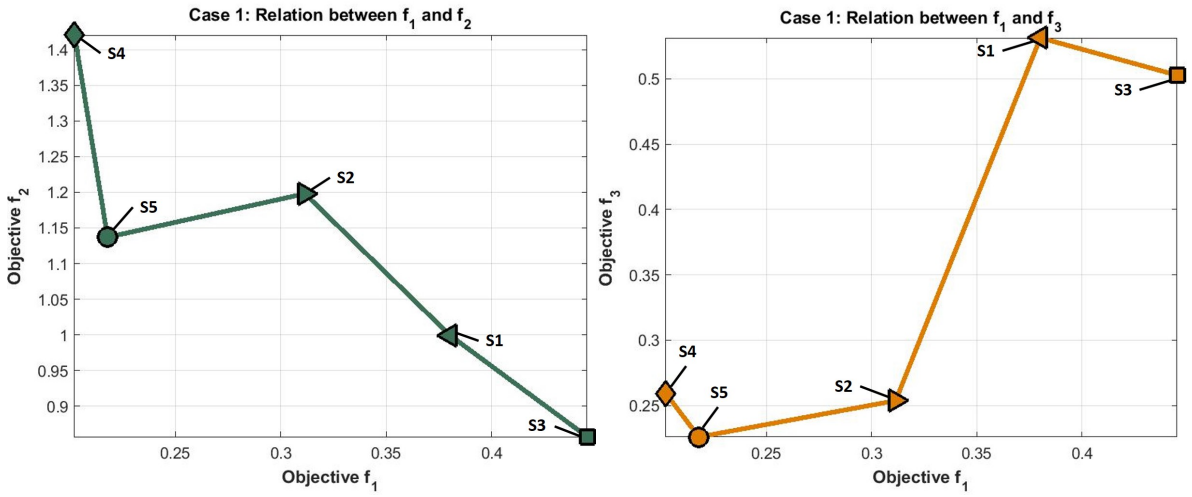

(a) (b)

Figure 5.3: The relation between the objectives (f_1, f_2 and f_3) of the optimal solutions for all the optimization scenarios (Case 1).

5.3 Results

The results are presented for each case (Case 1-5), i.e. for each fitness function, illustrating the relation between the optimization objectives (f_1, f_2 and f_3) in Figures 5.3-5.7. Additionally, in each case the optimal design variables and the computational time needed are presented for every optimization scenario ($S_1 - S_5$) in Tables 5.4, 5.6, 5.8, 5.10 and 5.12, while the performance of the vehicle for the optimal solutions is illustrated in Tables 5.5, 5.7, 5.9, 5.11 and 5.13.

5.3.1 Case 1 - Objective function f_1

In this case, the "best" optimal solution, in terms of the objective (RC_s - f_1), is attained by the optimization scenarios S_4 and S_5, which are the hybrid algorithm with population 1000 and the gradient based algorithm, respectively. In these scenarios, the fitness function (f_1), which represents the ride comfort, reaches the minimum value, as shown in Figure 5.3 which illustrates the relation of f_1 with f_2 and f_3. Moreover, as far as the design variables are concerned, these two scenarios converged to solutions with similar design variables. More specifically, as shown in Table 5.4, the solutions of S_4 and S_5 have similar values to four (C_{lF}, K_{lR}, K_{nlF} *and* K_{nlR}) out of six design variables. In addition, the solutions of these scenarios have similar values in their performance metrics, as shown in Table 5.5. Furthermore, the optimal solutions of the design variables reflect the general optimization objective of this case, i.e. ride comfort . In order to improve ride comfort, the optimization methods are trying to design a suspension system with low spring stiffness and low damping coefficient compro-

Design Variables	Optimization Scenarios					LB.	UB.	Units
	S_1	S_2	S_3	S_4	S_5			
K_{1F1}	102620	34479	105019	43094	36194	**32000**	**150000**	**N/m**
C_{F1}	6950	2000	5890	2050	2582	**2000**	**10000**	**N.s/m**
K_{1R1}	32352	74939	58027	33652	39741	**32000**	**150000**	**N/m**
C_{R1}	2083	5112	2155	2272	3228	**2000**	**10000**	**N.s/m**
K_{n1F1}	19.7	3.42	40.8	10.9	10.3	**0.5**	**30**	10^6 **N**/m^3
K_{n1R1}	8.58	44.7	13.0	9.19	11.8	**0.5**	**30**	10^6 **N**/m^3
Computational Time	886	9488	1364	5030	288	-	-	**sec**

Table 5.4: The optimal design variables and the computational time for all the optimization scenarios (Case 1).

mising the suspension travel and the road holding. Last but not least, the computational time needed for convergence in S_5 (288 *sec*) is almost the 6% of the computational time needed for S_4 (5030 *sec*).

Performance Metric	Optimization Scenarios					Unit
	S_1	S_2	S_3	S_4	S_5	
RC$_s$	0.63	0.56	0.68	0.45	0.47	**m/s**^{2}
MST$_{F1}$	25	37	24	40	37	**mm**
MST$_{R1}$	38	27	38	38	37	**mm**
Max(F_{KT_F})	4085	2249	3833	2991	2649	**N**
Max(F_{KT_F})	3061	3750	3275	2610	2791	**N**
Ratio$_{F1}$	11	12	19	29	28	%
Ratio$_{R1}$	27	30	24	29	28	%

Table 5.5: The performance metrics of the optimal solutions for all the optimization scenarios (Case 1).

5.3.2 Case 2 - Objective function f_2

In this case, the fitness function is the average of the variances of both the front and the rear suspension travels. In terms of the objective (f_2), the "best" optimal solution is attained by the optimization scenarios S_2, S_3 and S_4 which are the genetic algorithm with population 1000 and the hybrid ones with population 200 and 1000, respectively. In these scenarios, the fitness function, which represents the vehicle handling, reaches the minimum value of all the scenarios, as shown in Figure 5.4a where the relation of f_1 with f_2 is illustrated. Moreover, as far as the design variables are concerned, the two (S_2 and S_4) out of three scenarios have converged to similar solutions with design variables closed to each other. As illustrated in Table 5.6, the solutions of S_2 and S_4 have similar values to all the design variables, except from K_{nlF} which is significantly different.

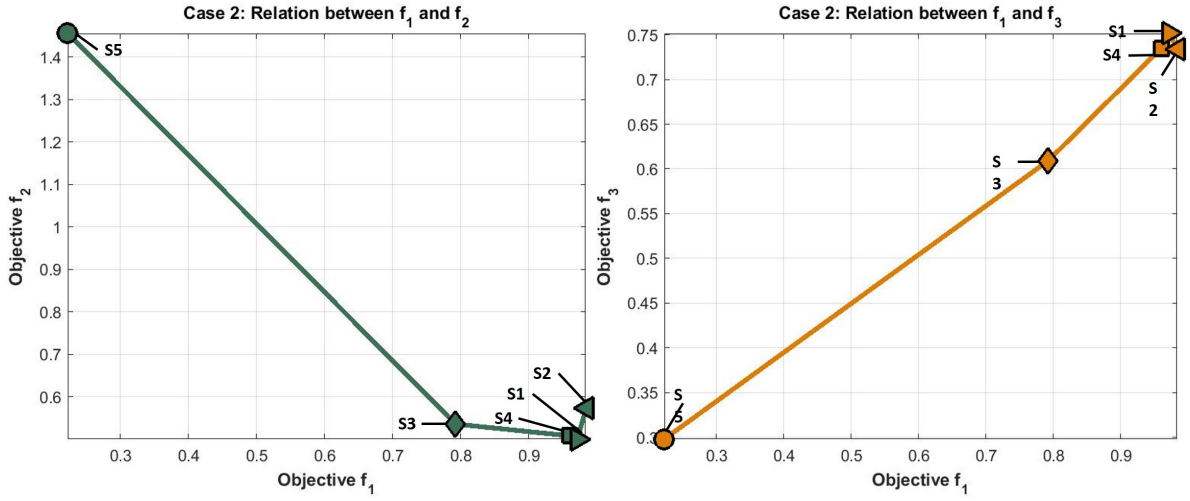

(a) (b)

Figure 5.4: The relation between the objectives (f_1, f_2 and f_3) of the optimal solutions for all the optimization scenarios (Case 2).

Design Variable	**Optimization Scenarios**					**LB.**	**UB.**	**Unit**
	S_1	**S_2**	**S_3**	**S_4**	**S_5**			
K_{1F1}	83283	51337	38952	57879	51377	**32000**	**150000**	**N/m**
C_{F1}	6635	9696	8003	8759	2003	**2000**	**10000**	**N.s/m**
K_{1R1}	70210	36651	47540	36934	36456	**32000**	**150000**	**N/m**
C_{R1}	9091	8757	8286	9376	2001	**2000**	**10000**	**N.s/m**
K_{n1F1}	25.7	24.8	25.6	13.0	75.6	**0.5**	**30**	10^6 **N/m^3**
K_{n1R1}	34.2	13.7	16.0	18.4	29.6	**0.5**	**30**	10^6 **N/m^3**
Computational Time	737	9398	4611	9371	315	-	-	**sec**

Table 5.6: The optimal design variables and the computational time for all the optimization scenarios (Case 2).

On the other hand, the optimization scenario S_3 differs mainly on the linear part of the spring both to the front and the rear suspensions, proving that a solution with different characteristics is selected. This is validated by the greater value of f_1 compared to the other scenarios (S_4 and S_5), as shown in Figure 5.5. However, this optimal solution not only delivers the smallest RC_s and the lowest MST_{F1} and MST_{R1} between the three, as shown in Table 5.7, but also it converges in the 50% less computational time compared to S_2 and S_4, as shown in Table 5.6 . Furthermore, the optimal design variables of the current case (Table 5.6) verify the target of the optimization. The suspension systems are designed with both high spring stiffness and high damping coefficient in order to secure the minimum suspension travel in contrast to Case 1, where low values of spring stiffness and damping coefficient

Performance Metric	Optimization Scenarios					Unit
	S_1	S_2	S_3	S_4	S_5	
RC$_s$	0.99	0.99	0.91	0.98	0.47	**m/s**^{2}
MST$_{F1}$	30	25	26	26	37	**mm**
MST$_{R1}$	20	21	22	38	37	**mm**
Max($F_{KT_{F1}}$)	4682	4168	3571	3957	3212	**N**
Max($F_{KT_{R1}}$)	3559	3276	3384	3364	3462	**N**
Ratio$_{F1}$	22	23	30	13	20	%
Ratio$_{R1}$	16	15	14	18	10	%

Table 5.7: The performance metrics of the optimal solutions for all the optimization scenarios (Case 2).

are required for more ride comfort. Last but not least, the gradient based algorithm (S_5) failed to deliver a proper solution with respect to the objective of the optimization. More specifically, the algorithm didn't manage to minimize f_2 considering that based on Table 5.7, the MST_{F1} and the MST_{R1} are the greatest among all the optimal solutions. However, it decreases significantly the RC_s value, indicating that possibly it was trapped in a local minima.

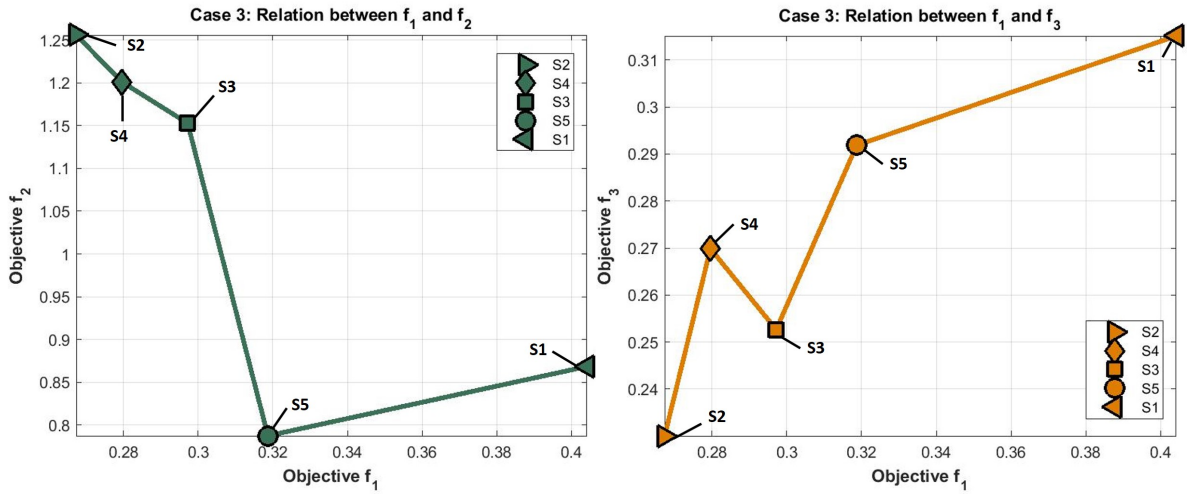

(a) (b)

Figure 5.5: The relation between the objectives (f_1, f_2 and f_3) of the optimal solutions for all the optimization scenarios (Case 3).

5.3.3 Case 3 - Objective function f_3

In this case, the fitness function is the average of the variances of both front and rear tire deflections (f_3). In terms of the objective function, the "best" optimal solution is found by the optimization

scenarios S_2 and S_3 which are the genetic algorithm with population 1000 and the hybrid one with population 200. In these scenarios, the fitness function (f_3), which represents the road holding, reaches the minimum value of all the scenarios, as shown in Figure 5.5b which illustrates ere the relation of f_1 with f_3. Moreover, as far as the design variables are concerned, the two scenarios (S_2 and S_3) have converged to solutions with design variables closed to each other. The above remark is illustrated in Table 5.8, where the solutions of S_2 and S_3 have similar values to all the design variables, except from K_{nlF} which is significantly different. The difference between K_{nlF1} in the two scenarios (S_2 and S_3) is also depicted in the contribution of the nonlinear part of the spring force of both front and rear suspensions, as shown in Table 5.9.

Design Variable	**Optimization Scenarios**					**LB.**	**UB.**	**Unit**
	S_1	**S_2**	**S_3**	**S_4**	**S_5**			
K_{1F1}	41279	33114	37028	47186	33583	**32000**	**150000**	**N/m**
C_{F1}	3632	2139	2092	2203	4242	**2000**	**10000**	**N.s/m**
K_{1R1}	77718	65367	67512	57595	37473	**32000**	**150000**	**N/m**
C_{R1}	4319	3661	4211	2713	5012	**2000**	**10000**	**N.s/m**
K_{n1F1}	14,4	4.95	11.1	8.54	12.3	**0.5**	**30**	10^6 **N/m**^{3}
K_{n1R1}	50.0	26.9	34.7	26.2	3.31	**0.5**	**30**	10^6 **N/m**^{3}
Computational Time	776	10510	850	4776	163	-	-	**sec**

Table 5.8: The optimal design variables and the computational time for all the optimization scenarios (Case 3).

Despite the different population used in these two scenarios (S_2 and S_3), the hybrid algorithm with the lower population (S_3) has proven to be superior compared to the genetic algorithm with the greater population (S_2). The hybrid algorithm overcame the disadvantage of the lower population exploiting the advantages of both the genetic and the gradient based algorithms. Also, it converged to to the optimal solution in less computational time (850 *sec*), which is almost 8% of the time required for convergence in optimization scenario S_2 (10510 *sec*). The superiority of the hybrid algorithm is confirmed due to the close solutions of the design variables (Table 5.8) as well as the values of the important performance metrics (Table 5.9). Finally, the effectiveness of the gradient based algorithm, in this current case, is based on the relation of the tire deflection and the vehicle's body acceleration, which is illustrated in Figures 5.3-5.5. Particularly, the increase or the decrease of the term f_1, which depicts the ride comfort, leads to the increase or the decrease of term f_3, which depicts the tire deflection, respectively. Therefore, there is no conflict between them so as to prevent the algorithm to converge to an optimum solution with respect to both objectives.

Performance Metric	Optimization Scenarios					Unit
	S_1	S_2	S_3	S_4	S_5	
RC$_s$	0.64	0.52	0.56	0.53	0.47	**m/s**^{2}
MST$_{F1}$	33	36	37	38	31	**mm**
MST$_{R1}$	25	32	29	31	40	**mm**
Max$(F_{KT_{F1}})$	2936	2226	2515	2853	2596	**N**
Max$(F_{KT_{R1}})$	3381	3537	3569	3006	3111	**N**
Ratio$_{F1}$	27	16	30	21	26	%
Ratio$_{R1}$	29	29	30	30	12	%

Table 5.9: The performance metrics of the optimal solutions for all the optimization scenarios (Case 3).

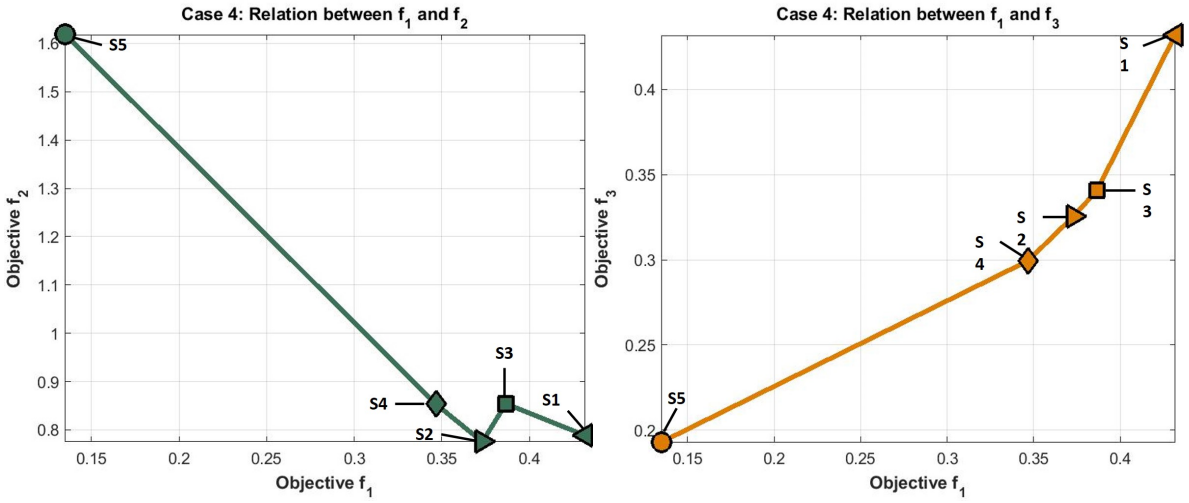

(a) (b)

Figure 5.6: The relation between the objectives (f_1, f_2 and f_3) of the optimal solutions for all the optimization scenarios (Case 4).

5.3.4 Case 4 - Objective function f_4

In this case, the fitness function is the sum of all the objectives (f_1, f_2 and f_3) which are balanced and at the same order of magnitude. First of all, as far as the effectiveness of the algorithms is concerned, the gradient based is not able to find a "good" optimal solution, getting trapped probably in a local minimum. The S_4 scenario decreased significantly objective f_1, as shown in Figure 5.6, neglecting the multi-objective character of the fitness function and therefore the minimization of the rest objectives. This is due to the fact that the minimization of the acceleration has proven enough so as to decrease the fitness function and finally converge. This remark is verified by the fact that all the design variables of S_5 reached the lower bounds, as shown in Table 5.10. Due to the multi-objective character of this case its difficult to understand which optimization scenarios converged to the "best"

optimal solutions. In addition, the optimal solutions of each optimization scenario differ significantly between them in terms of the optimal design variables. None of them are close enough to indicate the same characteristics in the optimal solutions. However, based on Table 5.11, the performance metrics of S_2-S_4 present similarities, such as the maximum suspension travels and the maximum tire forces.

Design Variable	**Optimization Scenarios**					**LB.**	**UB.**	**Unit**
	S_1	**S_2**	**S_3**	**S_4**	**S_5**			
K_{1F1}	81307	46116	63116	42377	32000	**32000**	**150000**	**N/m**
C_{F1}	5431	4129	3645	4002	2000	**2000**	**10000**	**N.s/m**
K_{1R1}	57264	45371	66731	60069	32000	**32000**	**150000**	**N/m**
C_{R1}	2877	5301	2753	3693	2000	**2000**	**10000**	**N.s/m**
K_{n1F1}	21.2	6.24	17.8	13.6	5.00	**0.5**	**30**	10^6 **N**/m^3
K_{n1R1}	9.52	27.3	34.7	28.6	10.8	**0.5**	**30**	10^6 **N**/m^3
Computational Time	840	6566	923	4674	430	-	-	**sec**

Table 5.10: The optimal design variables and the computational time for all the optimization scenarios (Case 4).

Performance Metric	**Optimization Scenarios**					**Unit**
	S_1	**S_2**	**S_3**	**S_4**	**S_5**	
RC$_s$	0.67	0.61	0.64	0.59	0.37	**m/s**^{2}
MST$_{F1}$	28	33	31	31	39	**mm**
MST$_{R1}$	33	27	28	29	48	**mm**
Max($F_{KT_{F1}}$)	3704	3096	3270	2802	2103	**N**
Max($F_{KT_{R1}}$)	2805	2785	2937	3105	3086	**N**
Ratio$_{F1}$	17	13	21	24	12	%
Ratio$_{R1}$	15	30	29	29	17	%

Table 5.11: The performance metrics of the optimal solutions for all the optimization scenarios (Case 4).

5.3.5 Case 5 - Objective function f_5

In this case, the fitness function is the sum of all the objectives (f_1, f_2 and f_3) like Case 4. However, in this case, the two additional objectives (f_2 and f_3) are used as dynamic penalty functions rather than optimization targets. Therefore, the objective f_1 is selected as the main term and the other two are set one order of magnitude lower using appropriate balancing factors. Because of this, the relation between the terms of the fitness function (f_1, f_2 and f_3) is not similar with before and greater dispersion is illustrated in Figure 5.7. As far as the effectiveness of the algorithms is concerned, the gradient based (S_5) focuses on the term f_1 only, ignoring the multi-objective character of the fitness

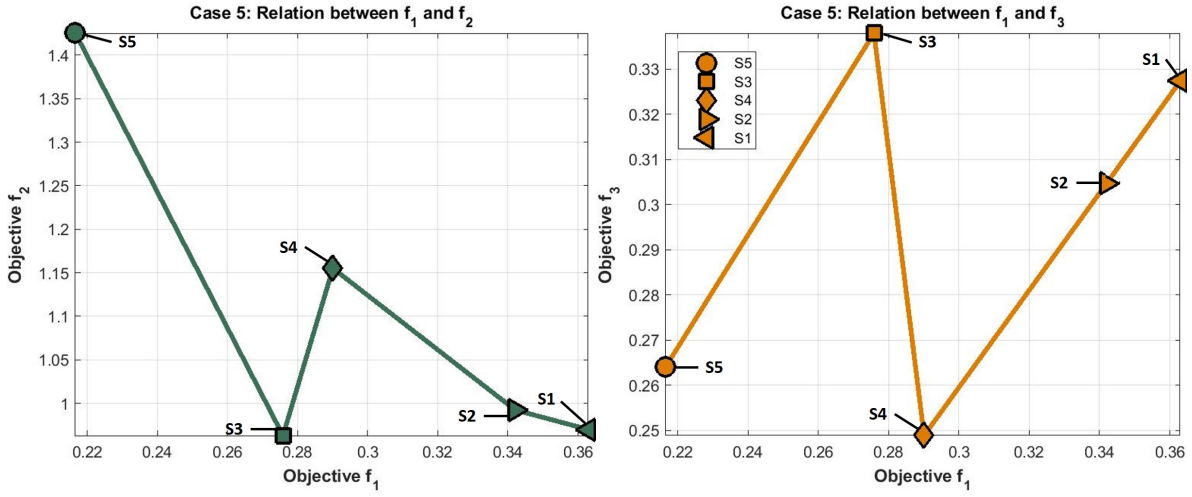

(a) (b)

Figure 5.7: The relation between the objectives (f_1, f_2 and f_3) of the optimal solutions for all the optimization scenarios (Case 5).

function and failing to find a "good" optimal solution. This problem is also pointed out in Table 5.12 and the design variables of this optimization scenario (S_5), where some of them are trapped in the upper or lower bounds. As far as the other optimization scenarios are concerned, due to the multi-objective character of this case it is difficult to understand which optimization scenarios converged to the "best" optimal solutions. In contrast to the previous case, neither the optimal design variables (Table 5.12) in every optimization scenario nor the performance metrics (Table 5.13) indicate similar characteristics in the optimal solutions.

Design Variable	**Optimization Scenarios**					**LB**	**UB**	**Unit**
	S_1	**S_2**	**S_3**	**S_4**	**S_5**			
K_{1F1}	59559	49457	43581	37635	44761	**32000**	**150000**	**N/m**
C_{F1}	2414	2164	5312	2096	2000	**2000**	**10000**	**N.s/m**
K_{1R1}	58680	56541	45694	65343	45798	**32000**	**150000**	**N/m**
C_{R1}	3901	6281	1910	4616	2000	**2000**	**10000**	**N.s/m**
K_{n1F1}	12.5	5.72	24.2	5.09	7.56	**0.5**	**30**	10^6 **N/m**^{3}
K_{n1R1}	43.4	44.0	5.89	33.2	3.56	**0.5**	**30**	10^6 **N/m**^{3}
Computational Time	767	9470	1123	4540	130	-	-	**sec**

Table 5.12: The optimal design variables and the computational time for all the optimization scenarios (Case 5).

Performance Metric	Optimization Scenarios					Unit
	S_1	S_2	S_3	S_4	S_5	
RC$_s$	0.61	0.59	0.54	0.54	0.47	**m/s**^{2}
MST$_{F1}$	38	40	26	38	40	**mm**
MST$_{R1}$	24	23	36	29	38	**mm**
Max($F_{KT_{F1}}$)	3556	3070	2829	2433	2836	**N**
Max($F_{KT_{R1}}$)	2549	2944	3154	3367	3302	**N**
Ratio$_{F1}$	17	13	21	24	12	%
Ratio$_{R1}$	15	30	29	29	17	%

Table 5.13: The performance metrics of all the optimal solutions for all the optimization scenarios (Case 5).

5.4 Comparison of the optimum solutions for all the cases

In order to compare the optimal solutions obtained from all the optimization Scenarios (S_1-S_5) of each Case ($1-5$), the fitness functions are scaled to the one of Case 4. All the solutions are benchmarked against Case 4, due to its multi-objective character and the fact that the objectives are balanced in one function. More specifically, the terms f_1, f_2 and f_3 of each optimal solution are used for calculating f_4 for each scenario of each case. Therefore, Figure 5.8 occurs and the value of f_4 for each optimization scenario (S_1-S_5 : different group of columns) for all the cases (Case 1-5 : columns of different color) is compared. In the table of data of Figure 5.8, the values of f_4 for all the optimal solutions are presented and the optimum solution for every Case is pointed out in borders with the corresponding color of the bar. The selection of the optimum solution is performed horizontally for every Case. Furthermore, in the top of each bar the computational time needed for convergence is displayed with the corresponding color of the bar. Moreover, Table 5.14 presents the values of the scaled terms f_1, f_2 and f_3 using the weighting factors of Case 4 as well as the sum of them (f_4) for the optimum solutions of each case. Also, the optimization scenario in which the optimum solution occurred is illustrated.

Optimization Targets	Case 1	Case 2	Case 3	Case 4	Case 5
	S_5	S_3	S_5	S_2	S_3
$w_1 * f_1$	0.218	0.792	0.319	0.373	0.316
$w_2 * f_2$	1.137	0.536	0.788	0.775	0.839
$w_3 * f_3$	0.226	0.609	0.292	0.326	0.336
$f_4 = w_1 * f_1 + w_2 * f_2 + w_3 * f_3$	1.581	1.937	1.398	1.474	1.491

Table 5.14: The design variables for all the optimal solutions of all the optimization scenarios (Case 5).

Based on Table 5.14 and Figure 5.8, the optimum solution among all the results is identified in Case 3/S_5, which was not expected because Case 4 is the ground case for the comparison of the optimal

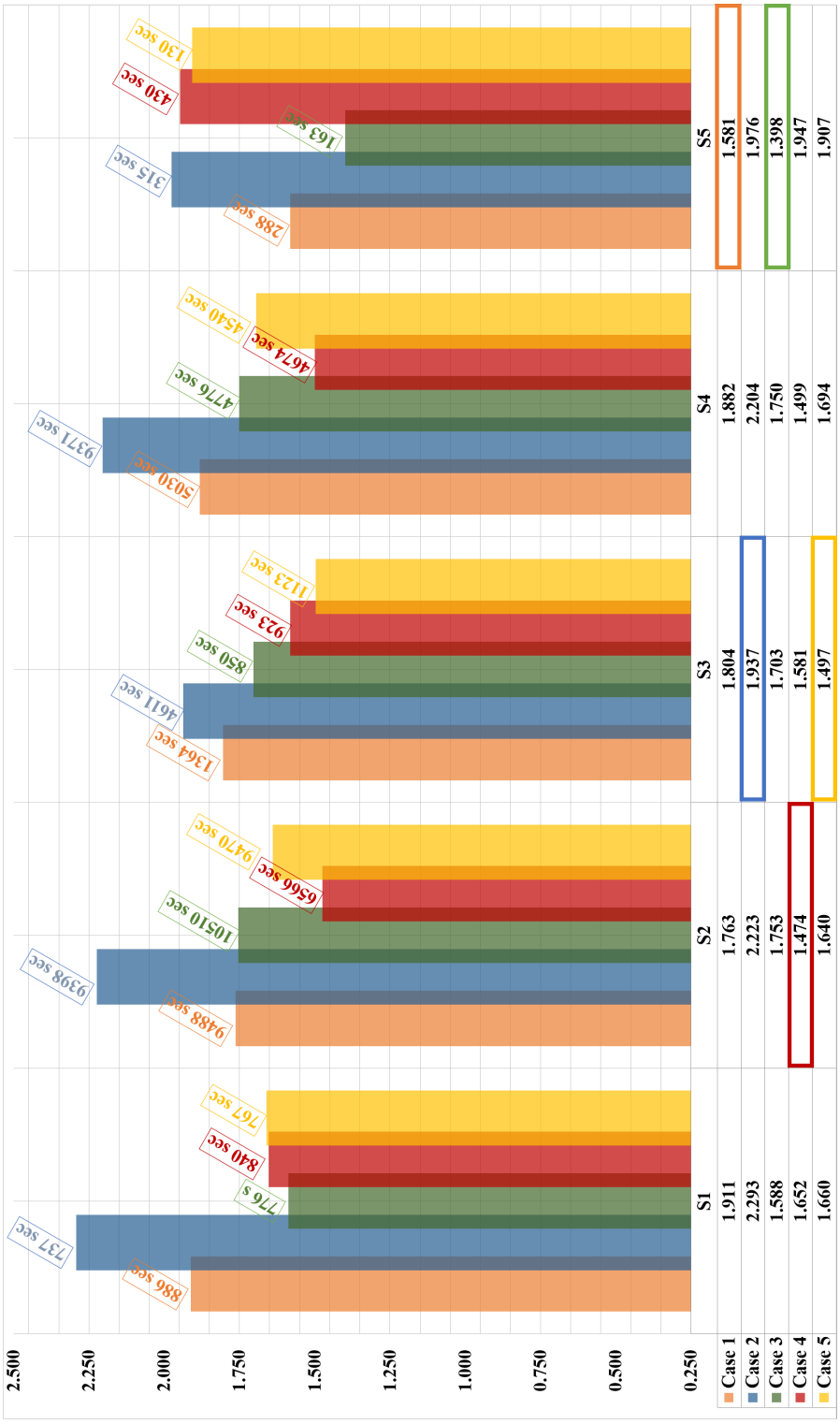

Figure 5.8: Benchmark of all the optimal solutions based on the fitness function (f_4) of Case 4.

solutions. The next two solutions closer to the optimum one, are the one of Case 4/S_2 as well as the one of Case 5/S_3. The computational time needed for convergence for Case 3/S_5 is around 3-5 % of the computational time needed for the next two closer solutions. This is due to the fact that the optimum solution (Case 3/S_5) is obtained with the gradient based algorithm, which seems to deliver the optimum solution in case of SOO fitness functions (Case 1 and Case 3). Based on Table 5.14, the close values of the terms f_1, f_2 and f_3 of these three solutions indicate that they have converged to similar design solution. The above remark is also verified by the optimal design variables of these solutions, as shown in Table 5.15. The slight differences in the design variables don't affect significantly the objectives (f_1, f_2 and f_3).

Design Variable	**Case 1**	**Case 2**	**Case 3**	**Case 4**	**Case 5**	**LP**	**UB**	**Units**
	S_5	**S_3**	**S_5**	**S_2**	**S_3**			
K_{1F1}	36194	38952	33583	46116	43581	**32000**	**150000**	**N/m**
C_{F1}	2582	8003	4242	4129	5312	**2000**	**10000**	**N.s/m**
K_{1R1}	39741	47540	37473	45371	45694	**32000**	**150000**	**N/m**
C_{R1}	3228	8286	5012	5301	2910	**2000**	**10000**	**N.s/m**
K_{n1F1}	10.3	25.6	12.3	6.24	75.6	**0.5**	**30**	10^6 **N**/m^3
K_{n1R1}	11.8	16.0	3.31	27.3	35.6	**0.5**	**30**	10^6 **N**/m^3
Computational Time	288	4611	163	6566	1123	-	-	**sec**

Table 5.15: The optimal design variables and the computational time for all the optimal solutions of all the optimization scenarios.

Regarding the optimization scenarios, the Hybrid Algorithm with population 200 (S_3) is proven to be the leading method together with the Gradient Based (S_5), as shown in Table 5.14 and Figure 5.8. The four out of the five optimal solutions are obtained using these algorithms, two each. The gradient based algorithm proved superior in the SOO cases (Case 1 and Case 3) in contrast to the other cases in which it failed to deliver. As far as the fitness functions are concerned, Case 5/S_3, where f_2 and f_3 are added as dynamic penalty functions, converged to a solution superior than one of Case 1/S_5, which is the SOO of term f_1. This implies that using the terms f_2 and f_3 as penalties, the optimization prioritizes the main term but takes slightly into consideration the other two. As a result, it leads to a middle ground solution better than the single objective case (Case 1). The solution of Case 5/S_3 it very similar to Case 4/S_4, which is the pseudo-MOO with f_4 as the fitness function and the terms (f_1, f_2 and f_3) balanced at the same order of magnitude.

As far as the different Cases are concerned, based on the data table of Figure 5.8, Case 3 seems to be superior than Case 1 due to the fact that the optimal solutions of Case 3 always deliver lower values of f_4 compared to the ones of Case 1, regardless the optimization scenarios. Moreover, in all the optimization scenarios, Case 3 not only delivered more satisfactory optimal solutions than Case 1 but

also converged in much less computational time, lowering it by 10-40% depending on the optimization scenario.

The argument regarding the superiority of Case 3, is validated from the fact that it delivers the optimum solution based on Figure 5.8, as explained in the previous paragraphs in detail. Case 3 converge to solutions taking into consideration not only the increase of the ride comfort but also the minimization of the suspension travel. The above indicates a multi-objective character in Case 3 even stronger than Case 4 and 5, despite having a single-objective fitness function. Moreover, based on Figure 5.8, Case 3 seems to be stable in providing satisfactory results in comparison with all the other cases which sometimes fail to deliver depending the optimization scenario.

5.5 Conclusions

To sum up, in this chapter, the optimization procedure of a vehicle suspension system is investigated. More specifically, not only the efficiency of different optimization methods is studied but also the efficiency of various fitness and objective functions.

The results of Case 3 outline the importance of tire deflection as a part of the objective function in the optimization procedure. This remark is illustrated from the superiority of Case 3 over Case 1 in all the scenarios of each case, which is the most common term of fitness functions in literature as far as the optimization of suspension systems is concerned. Also, the use of f_3 as an objective displays a multi-objective character in the optimum solutions, considering both the ride comfort and the road holding. Moreover, the consideration of f_2 and f_3 as additional terms to the main target of f_1 and their use as dynamic penalty functions is proven efficient. Case 5 converged to more optimal solutions compared to Case 1, where f_1 is the objective functions. Furthermore, the effectiveness of the hybrid algorithm proved promising in comparison with the other algorithms, while the efficiency of the gradient based algorithm with SOO cases is pointed out.

CHAPTER 6

An approach for minimizing the number of objective functions

Genetic Algorithms (GA) are time consuming optimization methods, as pointed out in the previous chapter, but because of their important advantages they are widely used in the field of automotive engineering. More specifically, in vehicle dynamics oriented MOO problems, the most common method is the Pareto Front, whose selection becomes very quickly ineffective based on the configuration of the problem. For instance, researchers add uncontrollably objective functions in order to find the optimum design of a suspension system, despite the fact that there are specific performance aspects which need to be optimized in vehicle dynamics. Thus, they sometimes end up using more than one objective function for the same performance aspect increasing the dimension of the optimization problem. Also, in this way, the merits of the optimization algorithm used are put aside because the computational time required for convergence is essentially increased.

In this chapter, we focus on an approach of minimizing the computational time needed for the Pareto method allowing the GAs to be attractive again in optimization of suspension systems. Applying this approach, we prove that the increasing use of objective functions, which depict the same requirement, doesn't help the optimizer to converge to more "optimal" solutions. In the literature, a few papers mention this topic. The purpose of this chapter is not the estimation of the suspension parameters but the proof that the optimum design variables could be achieved if the optimization procedure, and specifically the objective functions are set carefully. In order to prove the above, at first, three SOO cases of the most common objective functions and one pseudo-MOO case, which combines them, are presented (Part A). These cases are obtained from the previous chapter and are used as benchmark for the other parts of the analysis. Then, a sorting algorithm is implemented for these four cases in

order to obtain their optimum solution their optimum solution. Afterwards, we present an alternative approach for handling the objective functions, where they are divided in main and supplementary ones (Part B). The main objective functions (3) of the study are introduced in the MOO algorithm, while the supplementary ones (3) are introduced in the sorting algorithm in order to rank the Pareto alternatives and vet the optimum solution. The supplementary objectives consist of performance metrics which either enhance the main ones or are of crucial importance in the design of the suspension Thirdly, six objective functions, the three main and the three supplementary of Part B, are introduced in the MOO process (Part C) and then the resulting solutions of the Pareto front are implemented in the sorting algorithm so as to find the optimum solution of Part C. Finally, the optimum solutions occurred from the sorting algorithm are compared in terms of the objectives, of the design variables, and of important metrics indicating the vehicle performance.

6.1 Materials & Methods

6.1.1 Optimization Methods

In this chapter, a MOO algorithm is combined with a sorting algorithm. This approach is the tool to point out the effect of the inconsiderate selection of objective functions in vehicles suspension design and highlight the advantages of decreasing them, as proposed in this thesis.

In general, the optimization problem is expressed as a problem of minimization of the objective functions, with the selected design variables being subjected to a number of inequality constraints, making the problem a nonlinear programming one. In MOO problems, the objective function is not a scalar number, as in SOO problems, but a vector. Thus, in order to rank the different solutions, the concept of partial ordering is adopted. The Pareto dominance, which is used in this chapter, is based on this concept. The solutions of the Pareto set are non – dominated by any other solution and are considered as equally optimal solutions. When dealing with complex problems, the size of the Pareto set might be quite large and the designer must select which solution fits better the demands of the project in question. The selection of the optimum solution lies upon the designer, who is responsible of evaluating the solutions based on requested demands, because all the Pareto alternatives are equally optimal regarding the optimization targets. This process can be tiresome and time - consuming, due to the potentially large number of optimal solutions and the complexity of the problem in question. In order to overcome this problem, various sorting algorithms have been developed in order to assess the vetting process and consequently the reduction of the optimal set of solutions. The aim of these methods is to sort the solutions, according to various indexes, aiming to extract one optimum solution or to decrease the number of optimal solutions significantly. Carrillo et al. [141] introduced a process in which a solution sorting based on non-numerical ranking with random weight generation was proposed. Das [109] introduced the k-optimality method which is based on the partial dominance between the solutions, locating solutions which achieve a better trade – off between the optimization targets and eventually "offer something more" than the other optimal solutions. Based on the aforementioned method, Gobbi et al. [70, 107, 108] introduced the k - ε optimality method, which not only vets as the k-method, but also measures the entity of this variation. This algorithm is implemented in this chapter. In k - ε, the k index cannot receive only integer values on contrary with k method, but also real ones. In this way, a continuous degree of optimality is achieved. These two methods theoretically justify and mathematically define the designer's tendency to choose solutions that are "in the middle" of the Pareto-optimal set.

Formulation of the problem

A general multi-objective optimization problem can be expressed as follows:

$$min_{x \in R^n} f(\vec{x}) \tag{6.1}$$

$$h_j(\vec{x}) = 0, j = 1, ..., m_{eq} \tag{6.2}$$

$$g_j(\vec{x}) \leq 0, j = 1, ..., m_{ineq} \tag{6.3}$$

$$x \in X \tag{6.4}$$

where $\vec{f}$ is the objective function vector, $\vec{x}$ is the vector of the design variables, X is the definition domain of x and h_j, g_j are equality and inequality constraints, respectively. The set X can represent certain ranges of real values or certain types, such as integer or "standard" values, which are very often used in design specifications. The functions h and g in Equations 6.2 and 6.3 can be expressed with algebraic equations or computer simulations. If the functions h and g are all linear, the problem is a linear programming one. Otherwise, the problem is a nonlinear programming one. The Pareto-optimal solutions are defined mathematically as follows. Given the minimization problem with k objective functions and n design variables, a solution x_i is Pareto-optimal if there is no solution x_j such that:

$$\begin{cases} f_m(x_j) \leq f_m(x_i) \text{ , m } = 1, 2, 3, ..., k \\ \exists l : f_l(x_j) \leq f_l(x_i) \end{cases} \tag{6.5}$$

The definition of the Pareto dominance is presented in Equation 6.5 and it will be explained extensively later.

Pareto Dominance

As it is illustrated in Equations 6.1 - 6.5, in MOO problems the objective function is not a scalar value but a vector, which consists of the values of each target. On the other hand, in SOO problems the scalar objective function can be easily ranked and the derivation of one optimum solution is straightforward. In case of dealing with multi - objective functions arranged in vectors, the comparison operators ($<$, $>$, $\leq$, $\geq$) cannot be applied. Thus, in order to facilitate a ranking strategy, the concept of partial ordering is introduced. For every pair of vectors $\vec{a}$ and $\vec{b}$ a partial comparison relationship is introduced and described by Equation 6.6 - 6.9.

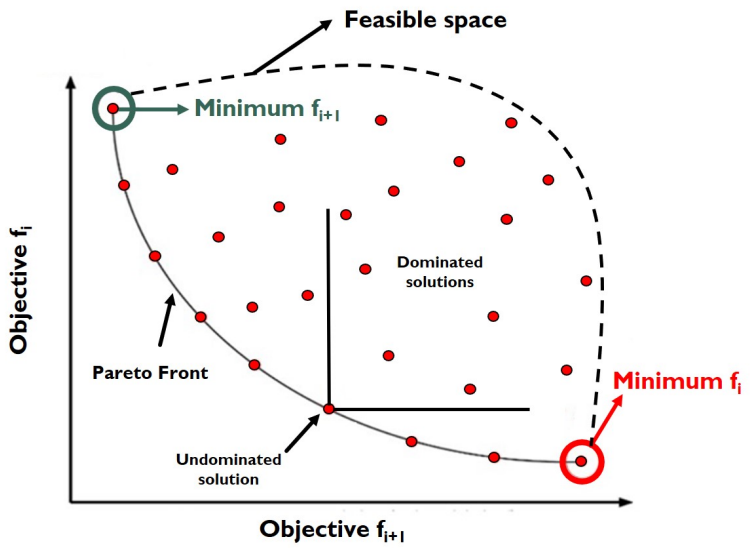

Figure 6.1: Pareto Dominance

$$\vec{a} = \vec{b}, \text{ when } a_i = b_i \forall \text{i} \tag{6.6}$$

$$\vec{a} \leq \vec{b}, \text{ when } a_i \leq b_i \forall \text{i} \tag{6.7}$$

$$\vec{a} < \vec{b}, \text{ when } a_i \leq b_i \forall i \text{ and } a_i < b_i \text{ for at least one i} \tag{6.8}$$

$$\text{i} = \text{ Number of Targets} \tag{6.9}$$

Thus, in terms of multi-objective optimization, the solution $\vec{a}$ dominates solution $\vec{b}$, i.e. $\vec{a} < \vec{b}$, when $f_i(\vec{a}) \leq f_i(\vec{b})$ for all targets and $f_i(\vec{a}) < f_i(\vec{b})$ for at least one target.

A Pareto set of optimal solutions contains solutions that are non-dominated by any other solution. More specifically a possible solution x* is part of the Pareto set if and only if there exists no other possible solution that $f_i(\vec{x}) \leq f_i(\vec{x^*})$ for all targets and simultaneously for at least one target $f_i(\vec{x}) < f_i(\vec{x^*})$. The concept of non-dominance is illustrated in Figure 6.1. As it was mentioned before, the Pareto dominance can be supported by various optimization methods, by imposing minor changes in their algorithm. In most cases evolutionary algorithms are used, in order to exploit their advantage of not being easily trapped in local minima due to their stochastic nature.

Selection of Optimum Solution

As the optimization problem becomes more complex, the number of solutions in a Pareto set increases. After the optimization process is over, the designer often acquires a relatively large group of potential optimal solutions. Depending on each problem, the vetting process can be a hard task even for experienced designers due to the large number of data. Thus, many post - Pareto selection methods have been developed, in order to acquire the one optimum solution of a complex problem. Das [109] introduced the k - optimality method which is based in the partial dominance of the possible optimal solutions. The goal of this method is to seek for solutions which remain Pareto-optimal, but they "have something more" than the others, being able to achieve a better trade-off between the objectives. According to Das [109], a solution is k - optimal if and only if it is Pareto optimal for all the subsets of the n-k objectives. Thus, if k=0 then the normal Pareto optimality is acquired, on the other hand if k=n-1, with n being the number of objectives, then the global optimum is acquired, which is called "utopia point". Mathematically the k - optimality method can be described with Equation 6.10.

$$\text{k}=min_Z\left(\sum_{i=1}^{n}\Gamma(\Delta f_i)\right)-1 \tag{6.10}$$

where n is the number of objectives and Δf_i is the difference between the i^{th} objective of the considered point and another point belonging to the solution space Z. $\Gamma(x)$ is a merit function which assigns appropriate values to each solution based on Equation 6.11, depending on their dominance over other solutions.

$$\Gamma(x)=\begin{cases}0\text{ , x }>0\\1\text{ , x }\leq 0\end{cases} \tag{6.11}$$

This merit function, in reality, is responsible for sorting out the solutions due to its logical character: if its value is true, then the solution is k - optimal, otherwise it is not. In this paper, though the k- ε optimality selection method is selected, which is able not only to vet solutions taking into consideration if an objective is better, but also to measure the entity of this variation. The mathematical description of the method remains the same as the one of k - optimality, except from the definition of the merit function. In this method, an indifference threshold ε is introduced so as to take also into account solutions that are "not so bad". If the difference Δf_i is not greater than ε, which is chosen by the user, the solution is characterized as "not so bad", without being sorted out as in k - optimality method.

$$\Gamma(x) = \begin{cases} 0\,, & \mathrm{x} \leq \varepsilon \\ 1 - \frac{x}{\varepsilon}\,, & 0 < x < \varepsilon \\ 1\,, & \mathrm{x} \leq 0 \end{cases} \tag{6.12}$$

with this change in the definition of the merit function, a continuous degree of optimality is achieved. The role of ε in this method is crucial determining the level of the variations in the solutions. If a small value of ε is chosen, then the k- ε optimality approaches the k - optimality method. If a relatively large value of ε is selected, then smoother variations in solutions will be achieved. A drawback of the k - optimality is that it is a crisp selection, k can be only an integer number. So, if the set of the points with the maximum value of k is still too large it is impossible to make a further selection, giving the same result with the simple Pareto-optimality. On the other hand, the k- ε optimality can always attain a single solution but requires the designer to specify an indifference threshold for each objective function. Also, it performs better as the number of targets increases above three.

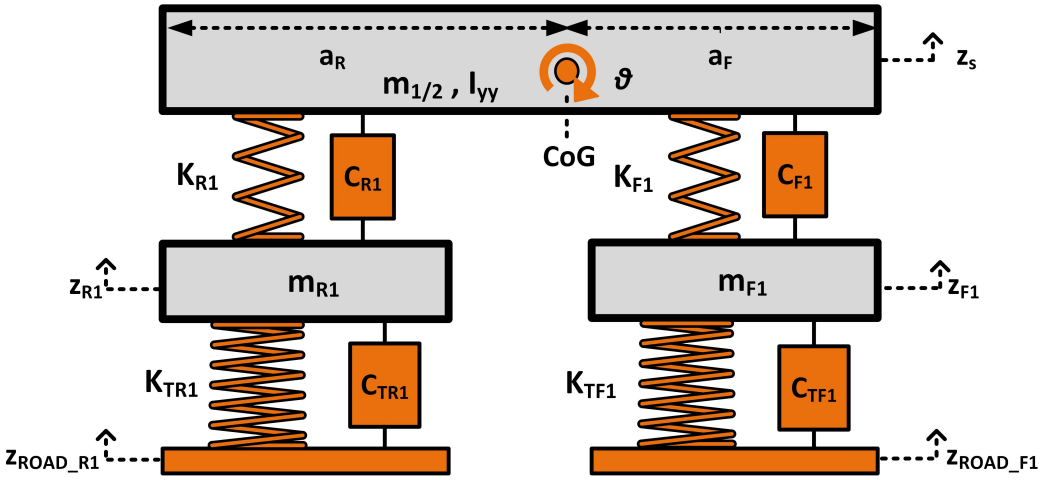

Figure 6.2: Half Car Model considering the front and the rear vehicle's wheel

6.1.2 Simulation Model

In this chapter, in order to prove the issue of inconsiderate selection of objective functions in suspension design, the same half car model (HC2 - Figure 6.2) as the one used in Chapter 5 is studied also in this chapter. Additionally, a seat, employed with a passive suspension (Figure 2.9 in Chapter 2.2.1), and a passenger (Figure 2.14 in Chapter 2.3), are added in order to investigate in depth the ride comfort. The seat-passenger model (Figure 6.3) is placed at the center of the vehicle and the seat is excited by the vibration of the sprung mass ($\ddot{z}_s$).

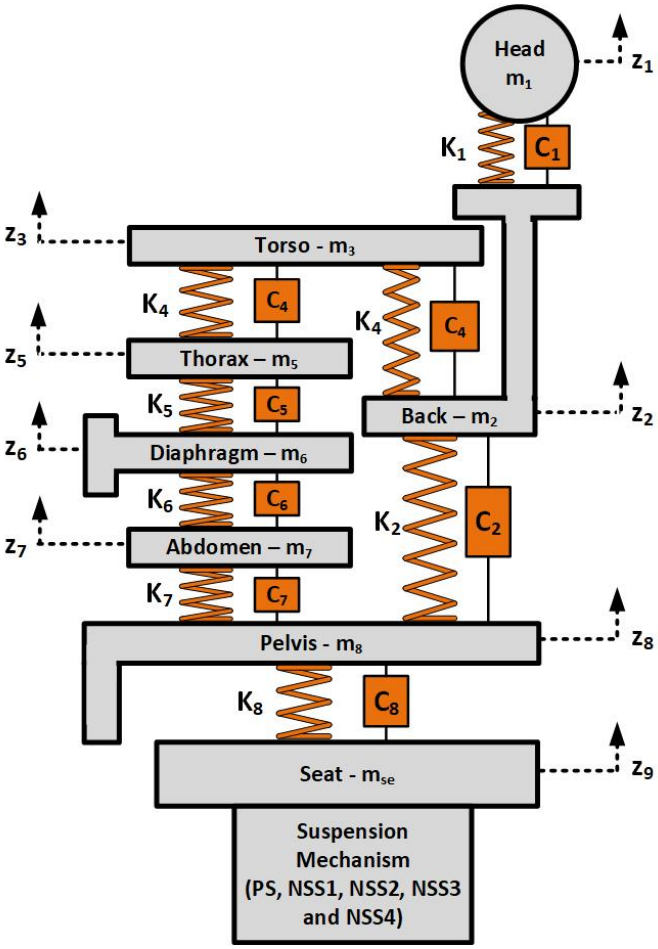

Figure 6.3: Seat-Passenger Model

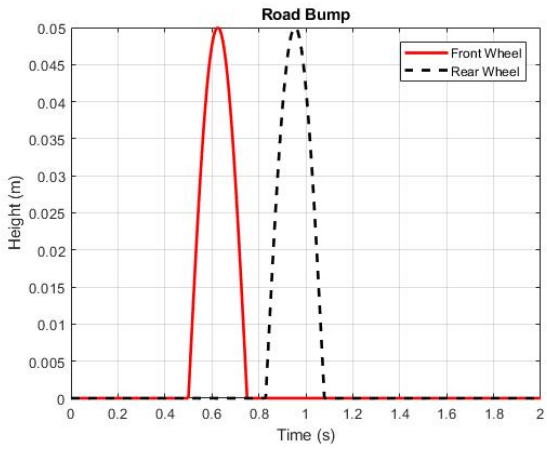

Figure 6.4: The road bump applied to the vehicle model of this chapter

6.1.3 Road Excitation

Likewise with the vehicle model, the same road excitation with Chapter 5 is used (Figure 6.4) .

6.2 Optimization Procedure

In this chapter, we aim to highlight the importance of choosing carefully the objective functions for the solution of an optimization problem. In this respect, a specific optimization problem is selected in order to conduct our experiments, the one of the optimum suspension design of a heavy vehicle under specific road conditions. However, the well-known automotive conflict between ride comfort and road holding, whose optimal compromise is the reason of applying different optimization techniques for the optimal design of the suspension system, is the same in every suspension type. The only thing that changes, depending on the suspension type, is the level of its compromise and the isolation of the vibrations induced by the road. Therefore, all the experiments could have been conducted in any other suspension type applying the concept of the proposed approach in order to exploit the algorithm's advantages. Although, the design variables, the constraints and other optimization parameters should change if needed based on the suspension system. The application of this approach in semi-active suspensions is presented in the next Chapter.

6.2.1 Design Variables, Constraints and Objective functions

The optimization problem investigated in this chapter is the same with the one of Chapter 5 in terms of the design variables, the bounds set to them and the constraints applied to problem.

The selection of the vector of the objective functions is of vital importance to the optimization procedure. Thus, we select six objective functions (f_i), which are widely used in the literature and represent either the ride comfort or the road holding. More specifically, the objective functions are:

(a) f_1, the variance of the acceleration of the body of the vehicle (Equation 5.4),

$$f_1 = \frac{1}{n}\sum_{j=1}^{n}(\ddot{z}_{s_j} - \overline{\ddot{z}_s})^2 = VAR(\ddot{z}_s) \tag{6.13}$$

(b) f_2, the average of the variances of the front and rear suspension systems (Equation 5.5),

$$f_2 = \frac{1}{2}\Big(VST_{F1} + VST_{R1}\Big) \tag{6.14}$$

(c) f_3, the average of the variances of the front and rear tire deflections (Equation 5.6),

$$f_3 = \frac{1}{2}\left(VTD_{F1} + VTD_{R1}\right) \tag{6.15}$$

(d) f_4, the vibration dose value of the head (VDV_{head} - Equation 2.82),

$$VDV_i = \left[\int_0^T \left(\ddot{z}_i(t)\right)^4 dt\right]^{\frac{1}{4}} \tag{6.16}$$

(e) f_5, the crest factor of the head (CF_{head} - Equation 2.83) and

$$CF_i = \frac{max(\ddot{z}_i)}{rms(\ddot{z}_i)} \tag{6.17}$$

(f) f_6, the variance of the pitch angle (PTC - Equation 2.91).

$$PTC = \frac{1}{n}\sum_{j=1}^{n}(\theta_j - \overline{\theta})^2 = VAR(\theta) \tag{6.18}$$

The minimization of f_1, f_4 and f_5 provides good ride quality for the passengers based on ISO-2631, whereas the minimization of the remaining three, i.e. f_2, f_3 and f_6, decreases the body motions ensuring the road holding and providing good handling of the vehicle, as explained in Chapter 2.4.

6.2.2 Scenarios

In the first part of the analysis (Part A), we formulate three single-objective problems, with objective functions the terms f_1 (Case 1), f_2 (Case 2) and f_3 (Case 3), and a combination of them using weighting coefficients (Case 4 - as shown in Equation 5.7). These cases are obtained from Chapter 5 and used as a benchmark of the others, expecting to be at the edges of the Pareto Front as it shown in Figure 6.1. Also, the optimum solution of these four SOO cases, is obtained with the sorting algorithm (KE) and is compared with the optimums of the other parts.

In the next part (Part B), the approach proposed in this thesis, is applied and six (6) objective functions, widely used in the literature, are separated in main (3) and supplementary ones (3). The objective functions f_1, f_2 and f_3 are selected as the main ones in order to implement MOGA, while the three additional objective functions (f_4, f_5 and f_6) are selected supplementary ones so as to enhance the main ones. More specifically, the targets f_4 and f_5 enhance the ride comfort of the passenger and hence f_1, whereas target f_6 is related with the road holding of the vehicle enhancing targets f_2 and f_3. All the objective functions together are introduced to the sorting algorithm (KE), as shown in Figure 6.5. As far as Part C is concerned, all the above-mentioned objective functions ($f_1 - f_6$) are introduced to the MOGA, as shown in Figure 6.6. After obtaining the Pareto alternatives, they are

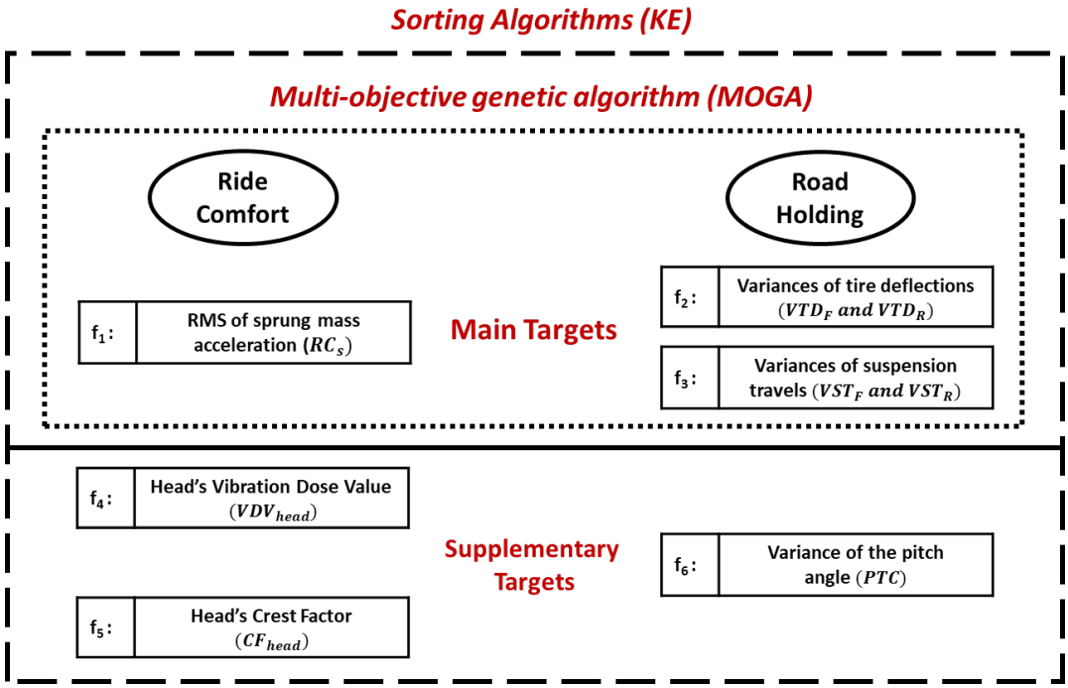

Figure 6.5: Approach of Part B

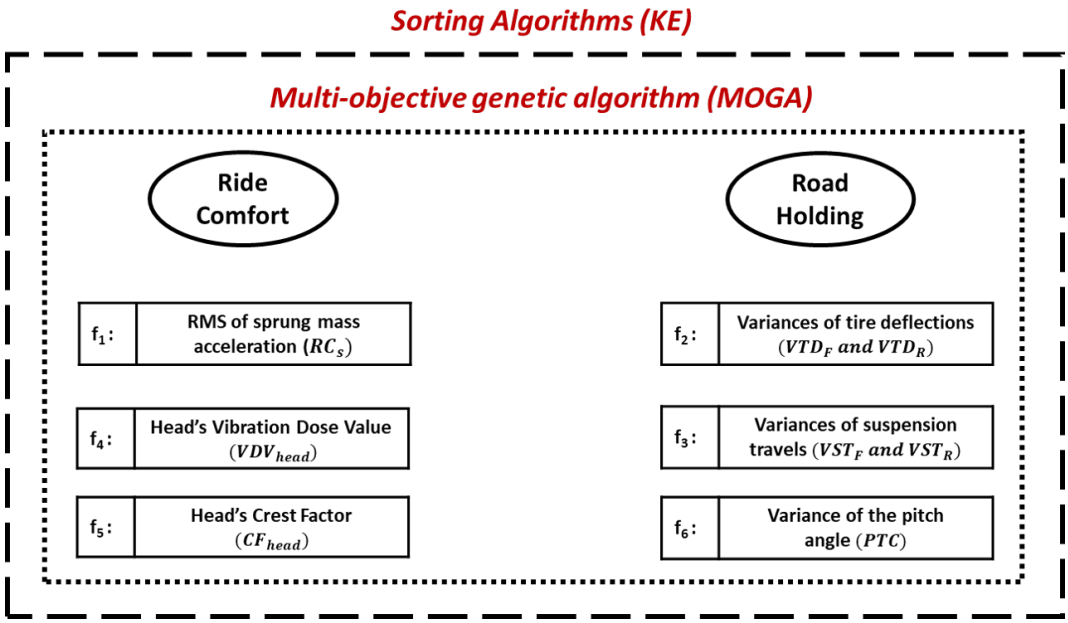

Figure 6.6: Approach of Part C

introduced in the sorting algorithm so as to seek the optimum solution among them. All the studied cases are presented in Table 6.1.

Scenarios			Objectives (f)	Threshold(ε)
Type	**Part**	**Cases**		
SOO	A	C_1	f_1	$\varepsilon = P_i[max(f_1);...;max(f_6)]$
		C_2	f_2	
		C_3	f_3	
		C_4	$w_1f_1 + w_2f_2 + w_3f_3$	
MOO	B	-	$f = [f_1;...;f_3]$	
	C	-	$f = [f_1;...;f_6]$	

Table 6.1: Optimization Scenarios

Regarding KE, In all the parts, a threshold is selected for the sorting algorithm, as shown in Equation 6.19:

$$\varepsilon = P_i[max(f_1);...;max(f_6)] \tag{6.19}$$

where P_i=[0.60, 0.55 , 0.65] is used for Part A, Part B and Part C respectively, so as to set the threshold ε and obtain only one optimum solution. The smaller the ε is, the k- ε optimality approaches the k-optimality method minimizing the possibilities of getting a single optimum solution. On the other hand, with a relatively high ε the variations in the change of k-levels become smoother. Therefore, ε is selected so as to be directly dependent with the objective functions and, in this respect, the maximum value of each objective among all the Pareto alternatives is used, as shown in Figure 6.19. Finally, the value of P_i is selected so as the k- ε algorithm to deliver only a single optimum solution (it is possible to deliver a set of solutions) from the Pareto Front, in order to compare the solutions of each Part. Part A, B and C are classified by the number of the main objectives and their optimization type which is either MOO or SOO (see Table 6.1, columns "Type" and "Objectives") and not by the value of P_i.

6.3 Results

The novelty of the proposed optimization approach (Part B) consists of the way the objectives are handled. The other two parts are selected based on the work of other researchers and are compared with Part B, so as to prove that it is able to provide a "more optimal" solution. Also, we aim to highlight the importance of separating the objectives to main and supplementary ones avoiding the inconsiderate selection of objective functions, which is noticed in the literature regarding vehicle suspension systems. Based on the above, Part A and C are considered the conventional optimization methods because of the trivial handling of their objectives. Thus, the optimization approach proposed in this thesis (Part B), is compared to them extensively in terms of convergence, computational time and quality of the solutions based on the suspension performance. Therefore, the results of the cases illustrated in Table 6.1 are presented in this section.

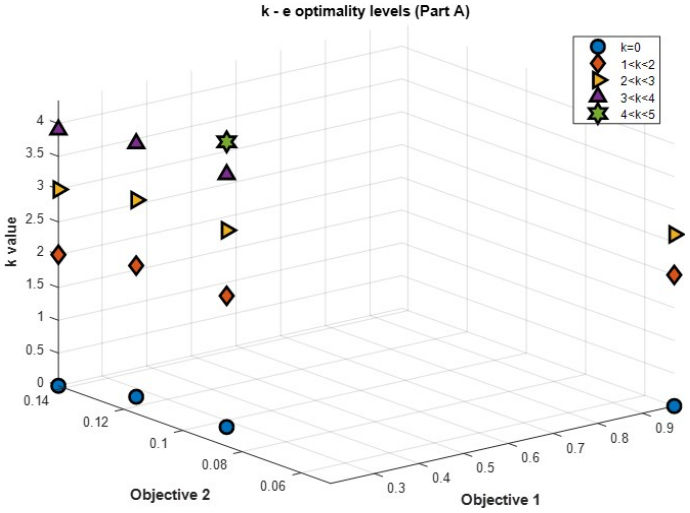

(a) Part A.

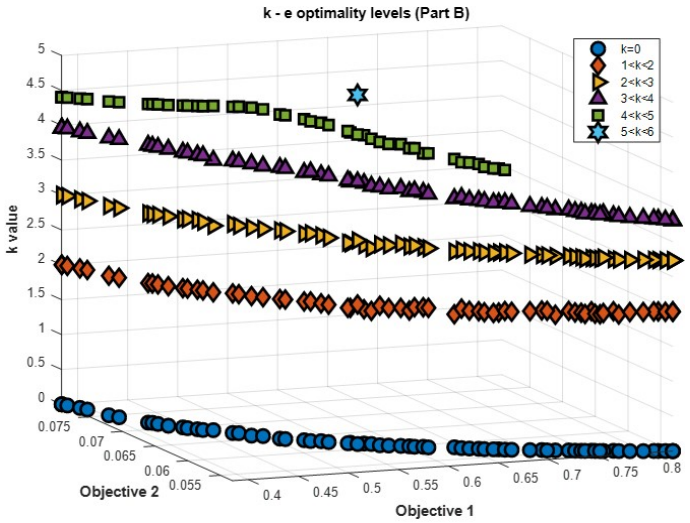

(b) Part B.

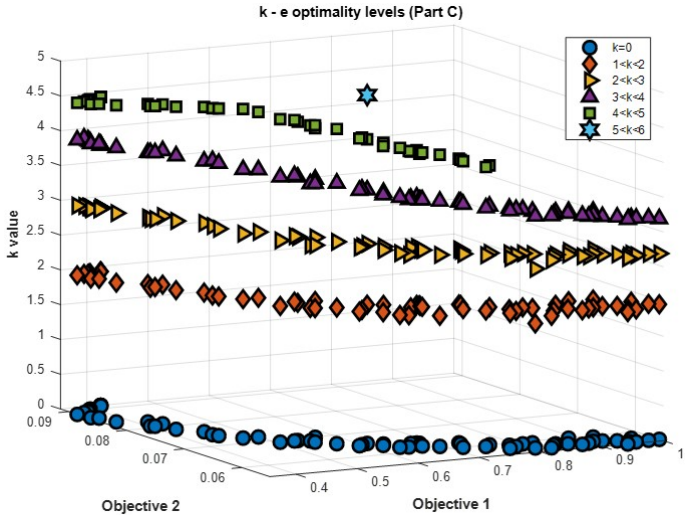

(c) Part C.

Figure 6.7: The optimal solutions of each part and their k-ε levels

More specifically, in Figure 6.7 the optimum selection among the alternatives for each Part is pointed out and the k levels of the ranked solutions are presented. Based on Figure 6.7a, the optimum solution for Part A is ranked above level four and below five, implying that the optimum solution is dominating to more than four targets out of six. The optimum solution of Part A is obtained in order to be compared with the optimum solutions of the other parts as a benchmark. Moreover, as far as Part B is concerned, the sorting algorithm proves the tendency of engineers and designers to move to the middle of the Pareto alternatives. It reached to an optimum solution of level five, i.e. it dominates five out of six objectives. Similarly, in Part C, a solution in the middle of the Pareto front of level five is obtained.

In addition to Figure 6.7, the Pareto Fronts for all the objectives are presented in Figure 6.8 with respect to f_1. Also, the optimum solutions obtained for each Part are pointed out in Figure 6.8 points out and are compared graphically. Additionally, all the SOO cases are presented in Figure 6.8. As expected, the solutions of the SOO problems ($C1$, $C2$ and $C3$) are located in the edges of the Pareto fronts of Part B and C or in the extension of their edges. On contrary, the pseudo-MOO ($C4$) is near the middle of the Pareto front validating its multi-objective character, despite being converted in a SOO problem with the balancing factors (Equation 5.7). The location of the SOO problems proves their single objective character and that the optimization algorithms minimize successfully their objective explicitly, neglecting all the other aspects. On the other hand, the position of the pseudo MOO problem indicates a good selection of weighting coefficients, despite being selected almost "randomly" considering that the engineer never knows the success or the failure of each selection. The illustration of these cases aims to validate if the optimization procedure managed to provide solutions covering the largest part of the feasible space of the problem, as shown in Figure 6.1.

According to Figure 6.8a, the main conflict in vehicle dynamics between ride comfort and vehicle stability is validated. Decreasing the value of f_1, i.e. increase of ride comfort, leads to the increase of f_2, and hence decrease of road holding. The Pareto fronts of Figure 6.8, validate the main idea of Part B, i.e. splitting the objective functions to main and supplementary in order to minimize their number in the optimization procedure. The extra targets, which are selected for the k-ε optimality method (f_4 - f_6), supplement the initial targets (f_1 - f_3) as described in the previous sections. This is proven by the fact that f_1 - f_6 (Figure 6.8e) presents the same conflict as $f_1 - f_2$ (Figure 6.8a)), and that f_1 - f_4 (Figure 6.8c)) and f_1 - f_5 (Figure 6.8d)) are almost strictly ascending functions regarding f_1, i.e. their decrease leads to the decrease of f_1 increasing the ride comfort. Another important remark based on Figure 6.8, is the convergence of the Pareto fronts. The Pareto front of Part B converges to solutions dominating the ones of all the other Parts. Thus, the use of less objective functions enabled the optimization to reach to better solutions and present a less scattered front due to the better convergence.

Another example of the worse convergence of Part C, is Figure 6.8e, which presents the Pareto front of f_5 vs. f_1. Based on Figure 6.8e, the value of the crest factor of the driver's head (f_5) tends to

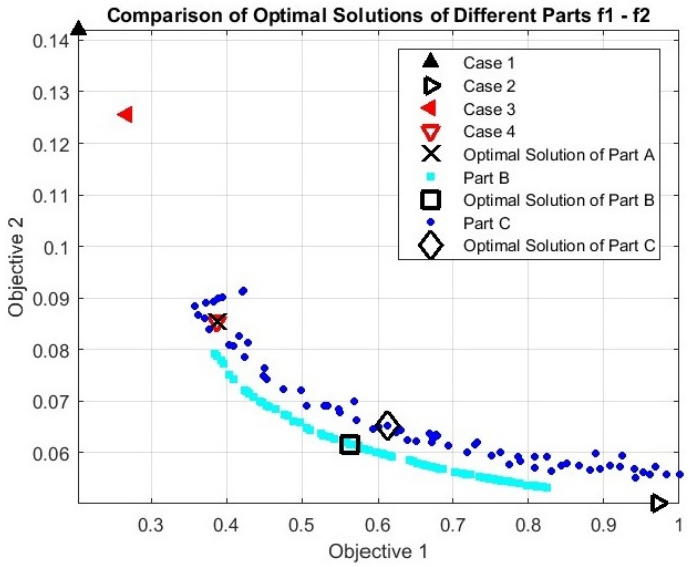

(a) $f_2 - f_1$.

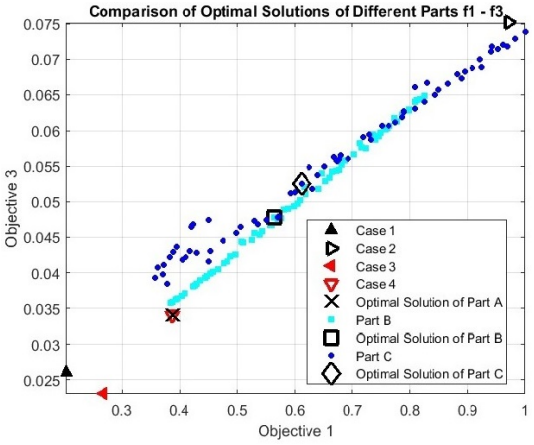

(b) $f_3 - f_1$.

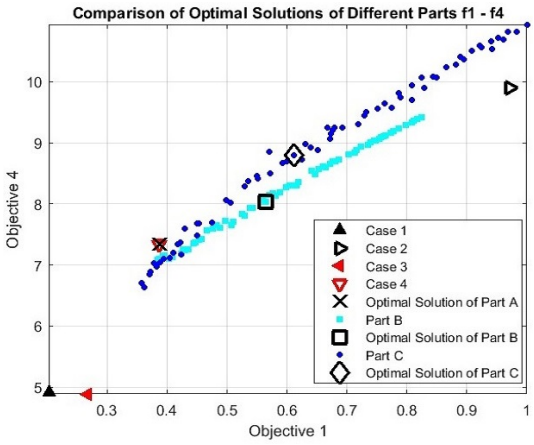

(c) $f_4 - f_1$.

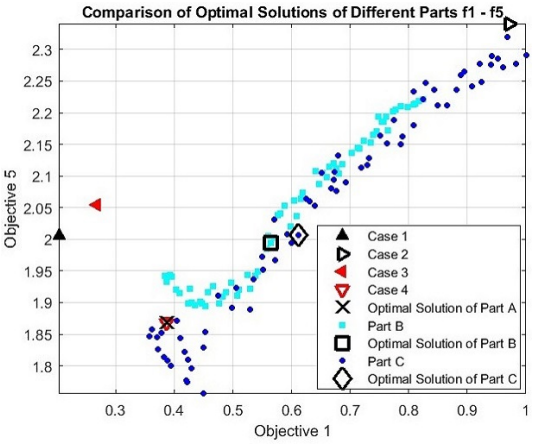

(d) $f_5 - f_1$.

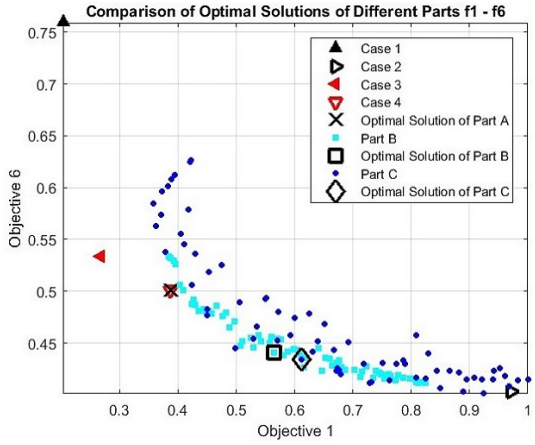

(e) $f_6 - f_1$.

Figure 6.8: Pareto fronts of the objectives for all the studied cases

increase for decreasing f_1 in a specific area of values of f_1 (f_1< 0.45), indicating a possible conflict between these two objectives. This conflict exposes the relation between the maximum value of the acceleration with its root mean square value, indicating that for low RMS values the maximum value of the acceleration tends to increase, and hence increase the value of the crest factor, based on Equation 2.83. This parabolic behavior in the relation between f_1 and f_5, for low values of f_1, is captured successfully in the front of the Part B due to the greater convergence of the problem. However, in Part C the crest factor continues to decrease with decreasing RC_s without capturing the parabolic behavior and misleading the selection of the optimum solution or the optimization in general. This remark is in agreement with the confusion that exists in the literature, regarding the use of the crest factor, its reliability as an index of ride comfort and its acceptable limits. Finally, from the Pareto fronts of all the objective, it is obvious that the sorting algorithm for Part B and Part C, reached to two solutions which seem similar based on their position in Figure 6.8a - 6.8e.

Moreover, in order to draw more concrete conclusions for these two solutions (Part B and C), they are compared with respect to the solution of Part A in terms of the optimum objective functions, optimum design variables and metrics indicating vehicle's performance. The optimum solutions of each Part, are presented in details in Tables 6.2, 6.3 and 6.4. At first, in Table 6.2 the values of the optimum objective functions are illustrated, while in Table 6.3 the values of the design variables are presented. Then, in Table 6.4, performance metrics are evaluated for the comparison of the optimum solutions. Finally, in Figure 6.9 the graphic comparison of the dynamic behavior of the vehicle for the three optimum solutions is presented so as to capture the effect of the different design variables.

Objective	**Value**			**Unit**
	Part A	**Part B**	**Part C**	
f_1	0.40	0.56	0.61	**m/s^2**
f_2	0.86	0.63	0.65	**mm**
f_3	0.34	0.47	0.52	**mm**
f_4	7.34	8.02	8.79	**m/s^2**
f_5	1.88	1.99	2.01	**m/s^2**
f_6	0.50	0.44	0.43	**rad**

Table 6.2: Comparison of the objective functions of the three optimum solutions

Based on Table 6.2, the optimum solutions of Part B and Part C are similar in terms of the values of the objectives with minor differences. Contrary to the optimum solution of Part A, the other two parts converged solutions with more emphasis on the road holding, i.e. f_2 and f_6, minimizing the suspension travels of both the rear and the front suspension system. However, the ride comfort is decreased by increasing f_1. This difference is expected considering Figure 6.8a, where the optimum solution of Part A is in the edge of the Pareto fronts, representing the optimal solution regarding the ride comfort (minimum value of f_1). Furthermore, this remark is also illustrated in Table 6.4. The suspension travel

Design Variable	Value			LB	UB	Unit
	Part A	Part B	Part C			
$K_{1_{F1}}$	63116	59610	75171	**32000**	**150000**	**N/m**
C_{F1}	3645	6819	7273	**2000**	**10000**	**N.s/m**
$K_{1_{R1}}$	66731	44882	70112	**32000**	**150000**	**N/m**
C_{R1}	2753	5393	4284	**2000**	**10000**	**N.s/m**
$K_{n1_{F1}}$	17.8	21.1	28.7	**0.5**	**30**	10^6 **N**/m^3
$K_{n1_{R1}}$	34.7	27.3	18.7	**0.5**	**30**	10^6 **N**/m^3

Table 6.3: Comparison of the design variables of the three optimum solutions

Performance Metric	Value			Unit
	Part A	Part B	Part C	
$RMS(\ddot{z}_s)$	0.62	0.75	0.79	**m/s**^{2}
MST_F	32.0	27.0	24.5	**mm**
MST_R	29.0	24.8	27.7	**mm**
$MAX(z_F)$	52.0	53.8	54.2	**mm**
$MAX(z_R)$	51.0	51.3	50.5	**mm**
$RATIO_F$	22.0	20.0	18.7	%
$RATIO_R$	29.0	26.5	16.4	%

Table 6.4: Comparison of the dynamic characteristics of the three optimum solutions based on the solution of Part A

is decreased in both cases compared to the solution of Part A. However, the suspension travel of front and rear suspension system has exchanged values in the optimum solution of Part B (ST_F=27 *mm* and ST_R=24 *mm*) and Part C (ST_F=24 *mm* and ST_R=27 *mm*). This is due the fact that the nonlinear part of the suspension system contributes more in the rear than in the front system in the solution of Part B ($Ratio_F$=20 % and $Ratio_R$=26.5 %). On the other hand, in the solution of Part C the front system has greater contribution of the nonlinear part ($Ratio_F$=18 % and $Ratio_R$=16 %) providing stiffer spring in the suspension system, as shown from Figure 6.11a and 6.11b. Moreover, in Figure 6.11a and 6.11b, the spring forces of Equation. 2.31 are compared for the optimum solutions of each Part, displaying the above-mentioned exchange. However, considering that f_2 is the mean value of the variances of the suspension travels, this exchange is not depicted in Table 6.2, as f_2 is at the same level in both solutions.

The similarity of these solutions, is also obvious in Figure 6.9, where performance metrics are compared presenting minor differences, which are more or less damping, as expected based on the values of the design variables. More specifically, in Part C, the damping coefficient is increased in both the front and the rear suspension system (C_{F1} and C_{R1}). On contrary, the differences of these two solutions with the one of Part A are depicted in Figure 6.9 - 6.10. The increase of the damping in the pitch

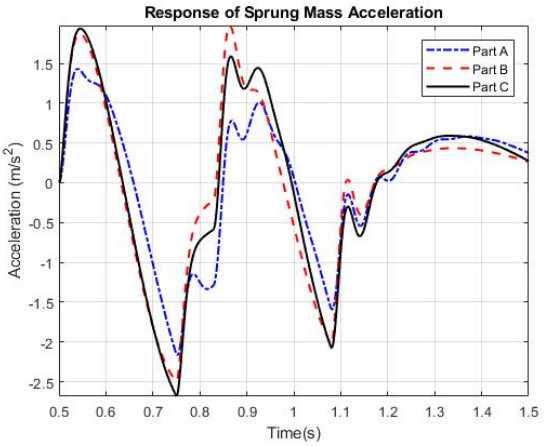

(a) Spung mass vertical acceleration.

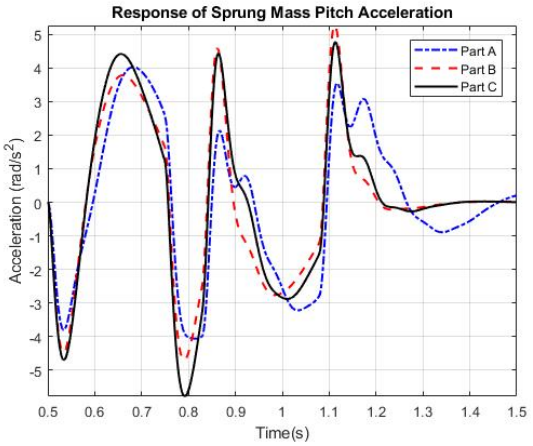

(b) Sprung mass angular acceleration.

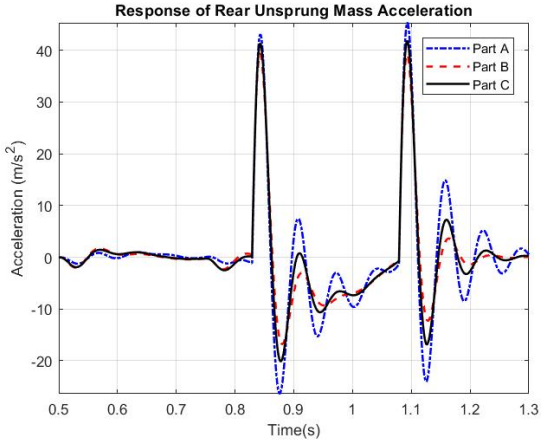

(c) Rear wheel vertical acceleration.

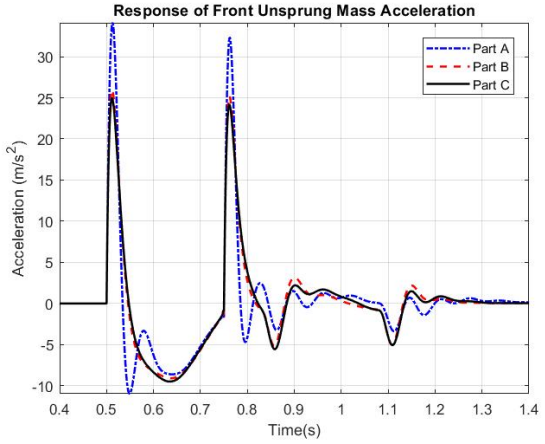

(d) Front wheel vertical acceleration.

Figure 6.9: Comparison of the dynamic behavior of the vehicle (1)

angle of the C.G. of the vehicle, which has led to the minimization of f_6, is illustrated in Figure 6.9b and Figure 6.10b. Moreover, the decrease of the suspension travel, and thus the increase of the road holding, occurred from the hardening of the suspension systems compared to the one of Part A, is depicted in Figure 6.9d and 6.10d and Figure 6.9c and 6.10c, respectively for both wheels. The peaks of the wheel accelerations have been decreased and their damping have been increased significantly minimizing their oscillatory behavior compared to the solution of Part A.

Last but not least, in Table 6.5, the computational time between Part A, B and C is compared. The cases of Part A are significantly faster than the other Parts, which was expected considering that they are SOO cases. However, the solutions of Part B and C are superior than the one of Part A. Also, in the MOO Parts (B and C), the optimization procedure compromise the conflicted objectives, contrary to Part A and, hence, the extra time needed is justified. The important remark of Table 6.5 is the fact

that Part B reached our expectations and apart from providing a "more optimal" solution, it converged almost 37% faster than Part C.

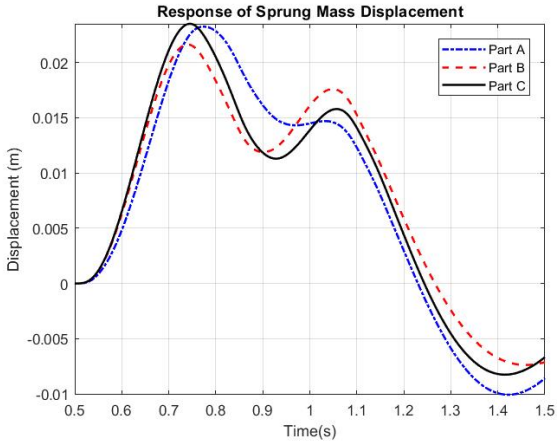

(a) Spung mass vertical displacement.

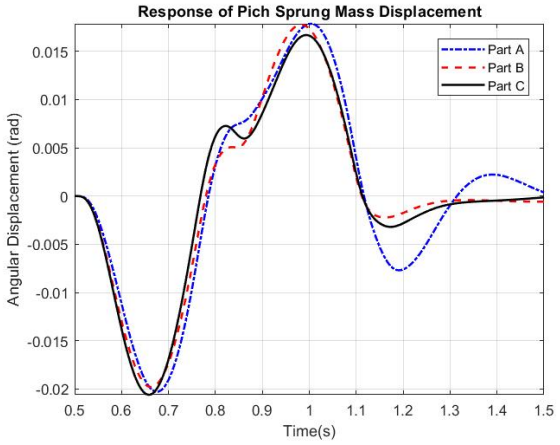

(b) Sprung mass angular displacement.

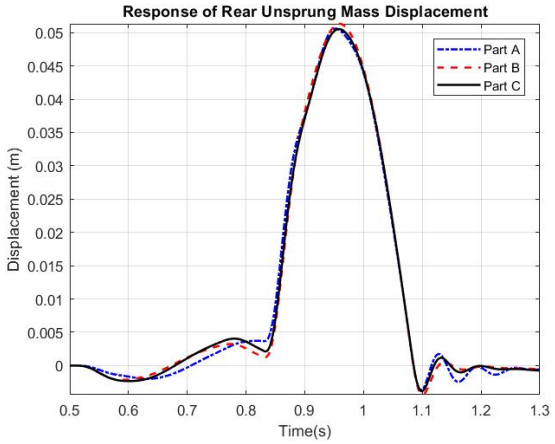

(c) Rear wheel vertical displacement.

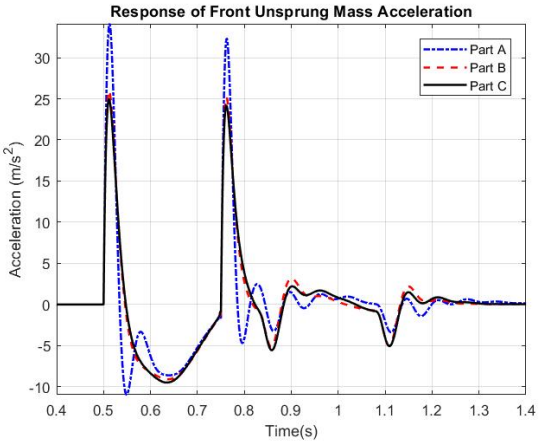

(d) Front wheel vertical displacement.

Figure 6.10: Comparison of the dynamic behavior of the vehicle (2)

		Part A	Part B	Part C
Total Computational Time (sec)	*C1*	9527	52708	90274
	C2	9437		
	C3	10549		
	C4	9779		

Table 6.5: Comparison of the computational time needed for the optimization scenarios of Table 6.1

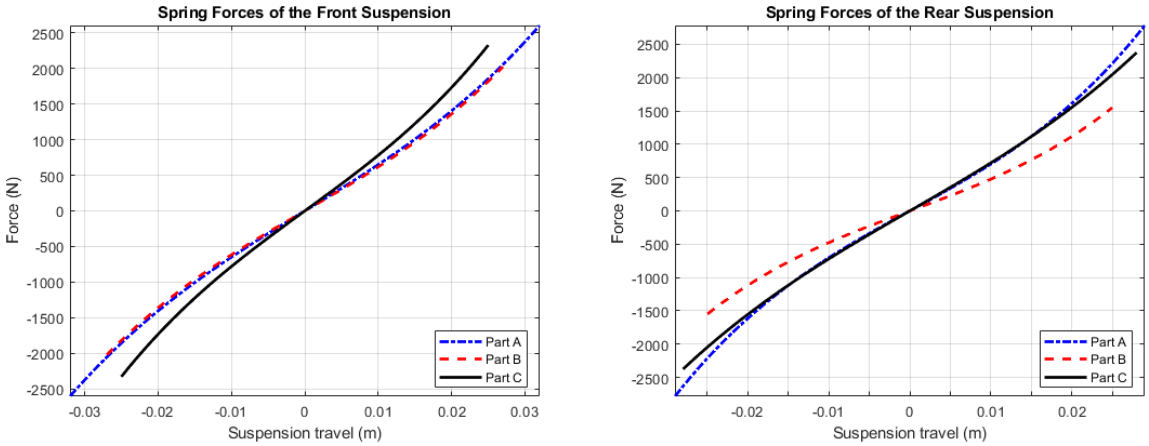

(a) Front Spring Force.

(b) Rear Spring Force.

Figure 6.11: Comparison of the dynamic behavior of the vehicle (3)

6.4 Conclusions

To sum up, this chapter focuses on the issue of the inconsiderate selection of objective functions that appears in literature in order to obtain the optimum design solution for the suspension system of a vehicle. In this respect, two MOO approaches are used and they are compared with few SOO cases in order to check their efficiency and their convergence. Also, a sorting algorithm is applied so as to obtain with validity the optimum solution among all the Pareto alternatives, and prove the superiority of Part B, and hence the importance of not exaggerating in the objective functions of the optimization.

First of all, the most important remark, which validated the purpose of this study, is the difference in the convergence between the Pareto alternatives of Part B and Part C. Splitting the optimization targets to main and supplementary ones in order to minimize the length of the objective function enabled the algorithm to reach to "more optimal" solutions which dominate all the others. This is proven also by the fact that the optimum solution of Part B is superior to the one of Part C, without being totally different or having design variables belonging to different family of solutions. Moreover, not only the convergence is better considering Figure 6.8, but also that the computational time gained from Part C is around 37% based on Table 6.5. In this chapter, the sorting algorithm is mainly used to prove the superiority of the Part B by pointing out its optimum solution and compare it with the one of Part A an C. However, the decrease in the computational time allows the engineer or the designer to provide this gained time to a sorting algorithm introducing to it more objectives so as to find the optimum design solution among the alternatives. Additionally, the better convergence pointed out in Part B, is proven by the fact that the Pareto alternatives, except from the expected conflict of ride comfort and road holding, indicated the one of the crest factor with the ride comfort that is mentioned extensively in the literature and described in Section 6.3 in details.

The main reason that various optimization techniques have been suggested through the years is trying so as to overcome the well-known automotive conflict between ride comfort and road holding. The level of its compromise depends highly from the suspension system's design. The trade-off between these objectives remains the same regardless the type of the suspension system and the only thing that changes regarding the suspension type is the level of the isolation. Thus, the proposed approach of this chapter is applicable to any other suspension type. In any case, the idea of the separation of the optimization objectives between main and supplementary ones should be followed in order to exploit the algorithm advantages. However, depending on the type of the suspension system, other constraints could be added such as the number of switches in an on-off or a continuous semi – active suspension instead the contribution of the nonlinear part in the spring force, used in the current work.

Consequently, based on all the above, it is important to select carefully the objective function in the optimization of the suspension system of a vehicle and not exaggerate in order to obtain an optimal solution which will not be the optimum because of misleading the optimization algorithm. Also, the separation of the objectives to main and supplementary could exploit the advantages of each algorithm and not only gain computational time but also quality in the solution as it is proven extensively in the current chapter.

CHAPTER 7

Multi-objective optimization of semi-active suspensions

In this chapter, a multi-objective genetic algorithm (MOGA) is applied to the vehicle model in order to optimize its suspension systems with respect to ride comfort and road holding. The suspension systems of the vehicle model operate with various SH control algorithms (SH-2, ADD and SH-ADD-2). Thus, three optimization scenarios with different control algorithms in the suspension systems are investigated in order to obtain their Pareto front and the set of optimal solutions. In contrast to existing works in the literature that focus mainly on the conflict between ride comfort and road holding, in this chapter we investigate the optimization of suspensions system with respect to more performance aspects as objectives.

Despite the importance of the extra objectives, the inconsiderate selection of objective functions grows the dimension of the optimization problem, costing computational time without providing "more optimum" solutions, as Papaioannou et al. described [27]. Thus, the approach based on KEMOGA algorithm [108], which is described in the previous chapter and minimizes the number of objective functions, is adopted in this chapter also. This approach suggests the separation of the objective functions to main and supplementary. The main objectives are used to the MOGA in order to obtain the Pareto front, while the supplementary ones are added in the sorting algorithm (KE) in order to rank the Pareto alternatives and vet the one solution with "something more" than the others. The supplementary objectives are performance metrics which either enhance the main ones or are of crucial importance in the design of the semi-active suspension. To sum up, in this work, the design of semi-active suspensions is investigated and the optimization approach based on KEMOGA algorithm is applied to a passenger vehicle in order to optimize its suspension systems. The suspension systems

operate with various SH control algorithms. Firstly, the vehicle model is optimized with respect to ride comfort and road holding with a multi-objective genetic algorithm (MOGA) by considering two performance indexes as objective functions. Then, a sorting algorithm (KE) is applied considering the extra objectives of the dissipation energy and the number of switches in the damper's states as objective functions due to their importance in the suspension design. Finally, the optimum solution of each case and the optimum among all are pointed out. Conclusions regarding the design solutions are extracted in addition with the benchmark of them in terms of their objective's values and their design variables.

7.1 Materials & Methods

7.1.1 Optimization Methods

In this chapter, a MOGA is combined with KE, as described in Chapter 5, for the optimization of semi-active suspension systems.

7.1.2 Simulation model

In the current chapter, the dynamic behavior of a passenger vehicle is investigated, as far as the vertical vibrations induced by the road surface are concerned. Different semi active suspension systems are applied to the vehicle model, so as to compare them and extract conclusions regarding their behavior. Moreover, a seat model is added on the sprung mass.

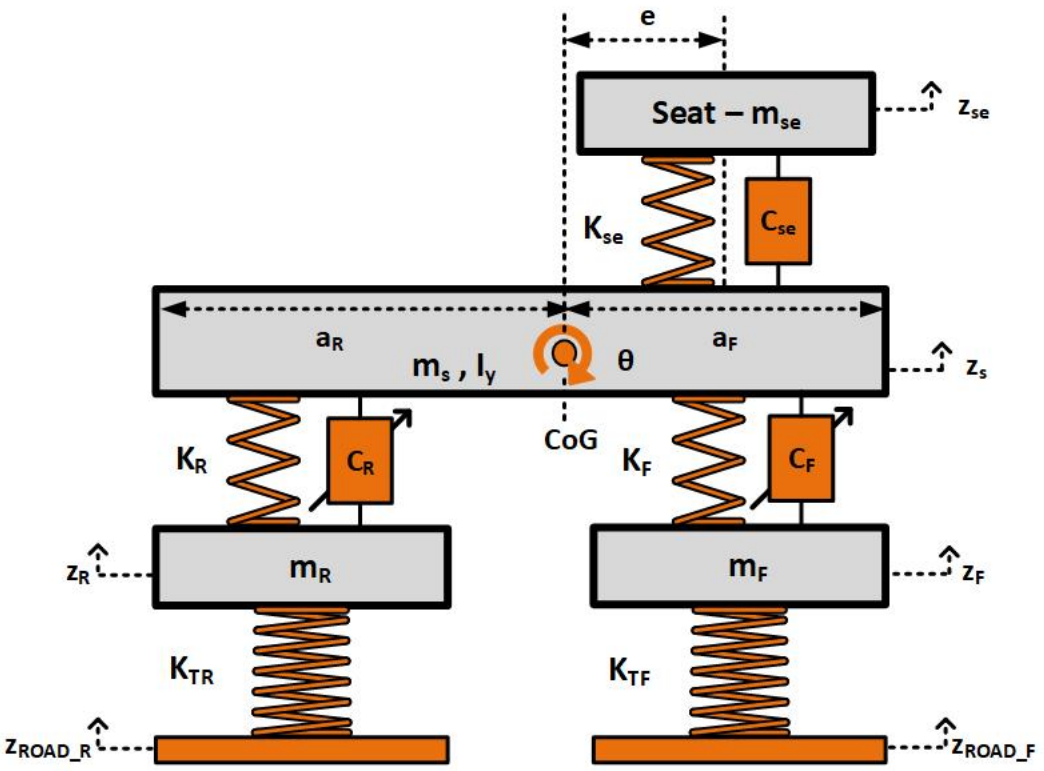

Figure 7.1: Half Car Model considering the front and the rear vehicle's wheel

A half car model (HC2 as descriped in Figure 2.3 of Chapter 2.1.3 is considered for analysis. The suspensions consist of linear springs (K_{F1} and K_{R1} as described in Equation 2.30), and controllable dampers (C_F and C_R) using SH algorithms, as described in Chapter 2.1.6. As far as the controllable dampers are concerned, they are operating with SH-2 (Equation 2.34), ADD (Equation 2.36),

SH-ADD-2 (Equation 2.39), SH-2-CDF (Equation 4.3) and SH-ADD-2-CDF (Equation 4.4). Additionally, the vehicle model is equipped with a seat model, as shown in Figure 7.1, which is placed at a distance of e (=0.4m) in front of the C.G of the vehicle. The parameters of the model are presented in Table 7.1.

Vehicle Model					
Parameter	**Unit**	**Values**	**Parameter**	**Unit**	**Value**
m_s	$[kg]$	520	a_F	$[m]$	0.91
I_z	$[kg\ m^2]$	473	a_R	$[m]$	1.55
m_R, m_F	$[kg]$	25	K_{TR}, K_{TF}	$[N/m]$	2.00 10^5
Seat Model					
Parameter	**Unit**	**Values**	**Parameter**	**Unit**	**Value**
m_{se}	$[kg]$	90	e	$[m]$	0.4
C_{se}	$[Ns/m]$	1200	K_{se}	$[N/m]$	30000

Table 7.1: Parameters of the HC2 vehicle and the PS seat model used in this chapter

7.1.3 Road Excitation

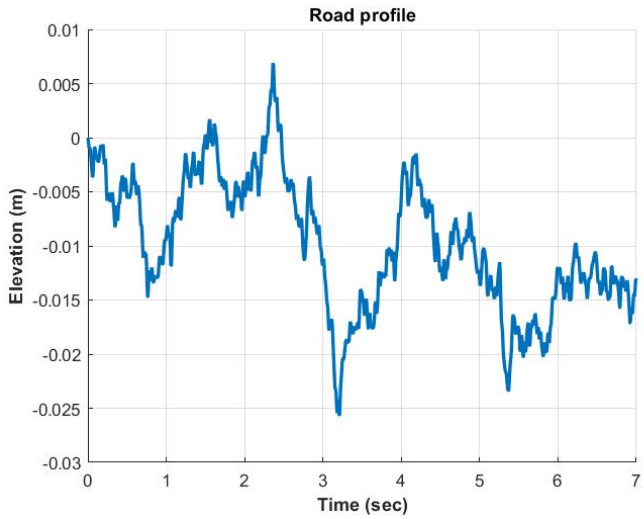

Figure 7.2: The random road profile generated based on ISO-8608 and applied to the vehicle model of this chapter.

In this chapter, a random road profile of Class C is generated, so as to optimize the controllable dampers under a severe road excitation with high speed. The vehicle is assumed to travel with a constant speed V (=50km/h) over a given road segment with length L_s (=100m). The profile is illustrated

in Fig. 7.2. The front and the rear wheels follow the same trajectory with a time delay $t_{distance}$, which is due to the distance $a_F + a_R$ of front and rear wheels and the vehicle's velocity (V).

7.2 Optimization Procedure

7.2.1 Genetic Algorithm

Objectives

As far as the MOGA is concerned, the main objectives, which represent the ride comfort and the road holding, are selected based on Chapter 5. After comparing the efficiency of various objective functions in different methods for the optimization of suspensions in Chapter 5, we proposed the RC_{se} and the average of VTD_F and VTD_R as the most appropriate objective functions in the design of suspensions. Thus, these performance metrics are selected for the MOGA and are presented in Equations 7.1-7.2:

$$f_1 = RC_{se} \tag{7.1}$$

$$f_2 = \frac{TD_F + TD_R}{2} \tag{7.2}$$

Using the above objective functions, three optimization scenarios, where the vehicle's suspensions operate with different control algorithms (SH-2, ADD and SH-ADD-2), are studied. These scenarios are presented in Table 7.2.

Design variables and their bounds

More specifically, for the optimization of the suspensions operating with SH-2 and ADD control algorithms, the damping coefficients of the controllable dampers ($C_{min,i}$ and $C_{max,i}$) and the spring stiffnesses (K_F and K_R) are selected as design variables, as shown in Table 7.2. As far as the SH-ADD-2 is concerned, the tuning coefficient α is added also as a design variable. Their bounds are presented in Table 7.3.

Constraints

The constraints used in the optimization problem are selected so as to incorporate the practical considerations into the design process and enhance the optimization targets. Thus, the maximum acceleration of the sprung mass (Equation 7.3), the maximum suspension travel (Equation 7.4), the maximum tire

Case	Description	Design Variable	Objective
1 2	SH-2 ADD	$[K_{F1};C_{max_{F1}};C_{min_{F1}};K_{R1};C_{max_{R1}};C_{min_{R1}}]$	$[f_1;f_2]$
3	SH-ADD-2	$[K_{F1};C_{max_{F1}};C_{min_{F1}};K_{R1};C_{max_{R1}};C_{min_{R1}},a]$	

Table 7.2: Optimization scenarios conducted with MOGA for obtaining their pareto fronts.

Design Variable	Unit	Bounds	
		Lower	Upper
K_{F1}, K_{R1}	$[N/m]$	15000	70000
$C_{min_{F1}}, C_{min_{R1}}$	$[N.s/m]$	500	2500
$C_{max_{F1}}, C_{max_{R1}}$	$[N.s/m]$	2500	5000
a (SH-ADD-2)	$[rad/s]$	10	60

Table 7.3: Bounds of Design Variables.

deflection (Equation 7.5) and the maximum displacement of the unsprung mass (Equation 7.6) are considered as constraints.

$$max(\ddot{z}_s) \leq 4.5\frac{m}{s^2} \tag{7.3}$$

$$MST_i \leq 0.13m \tag{7.4}$$

$$MTD_i \leq 0.05m \tag{7.5}$$

$$max(z_i) \leq 0.07m \tag{7.6}$$

where i=F_1, R_1 for front and rear tire and suspensions, respectively. The constraint of Equation 7.3 refers to the peak of the acceleration in order to maintain it in low levels, whereas the constraint of Equation 7.6 ensures a specific working space for the displacement of the suspension system, while the constraint of Equation 7.5 and Equation 7.4 enhance the objective of road holding demanding small tire deflections and small unsprung mass displacement.

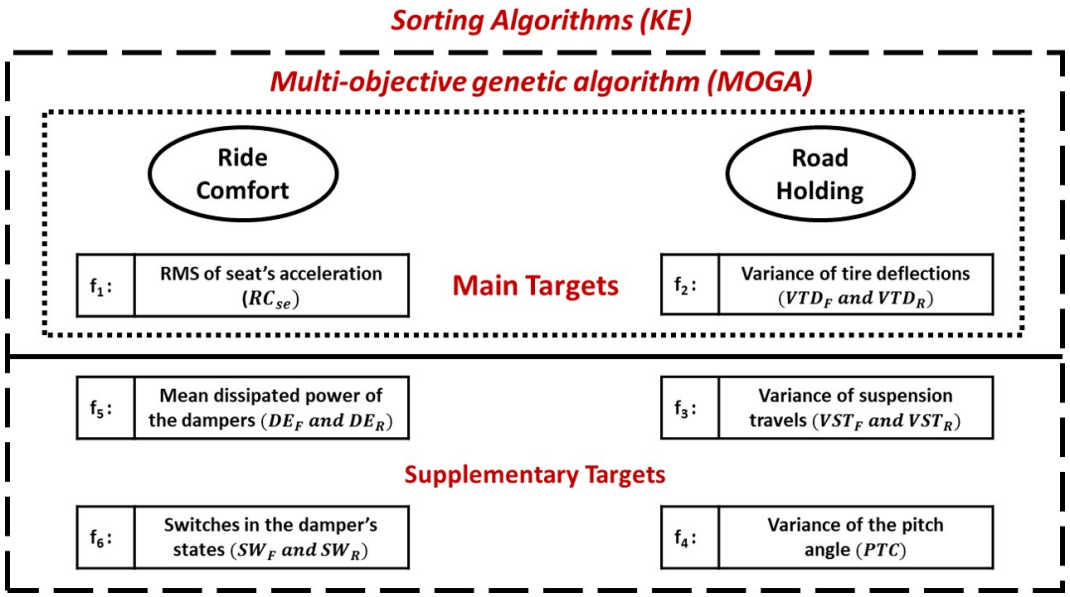

Figure 7.3: Optimization approach based on KEMOGA algorithm for minimizing the number of objective functions.

7.2.2 Sorting algorithm: k-ε optimality method

Objectives

Considering the issue of the inconsiderate selection of objective functions pointed out in the previous chapter [27], the objective functions of the MOGA are selected carefully and the approach proposed by them is applied in this work. The main objectives are used to the MOGA, while supplementary are added in the sorting algorithm (KE), as shown in Figure 7.3, in order to seek the optimum solution among the Pareto alternatives considering more performance aspects. The sorting algorithm (KE) is applied to five optimization cases, as shown in Table 7.4. Firstly, three cases are the ones having been optimized with the MOGA (SH-2, ADD and SH-ADD-2). Then, two more cases are generated, so as to apply the KE to them. More specifically, they are generated through the simulation of the vehicle model for the optimal solutions obtained from SH-2 and SH-ADD-2. However, the vehicle's suspensions operate with SH-2-CDF and SH-ADD-2-CDF.

As far as the supplementary objectives are concerned, they are selected either for enhancing the main ones (suspension travel and pitch angle) or because of their crucial importance in the design of the semi-active suspensions (dissipation energy and number of switches). Thus, four supplementary objectives are evaluated for the each optimal design solution (j) of the pareto fronts of each case in Table 7.4 and are presented in Equations 7.7-7.10.

$$f_3 = \frac{ST_F + ST_R}{2} \tag{7.7}$$

$$f_4 = PTC \tag{7.8}$$

$$f_5 = DE_F + DE_R \tag{7.9}$$

$$f_6 = SW_F + SW_R \tag{7.10}$$

The first two (f_3 and f_4) represent the suspension travel and the pitch angle of the vehicle. They are related with the road holding of the vehicle (f_2) and they are selected in order to enhance it. The next supplementary objective, f_5, represents the mean dissipated energy per second of both dampers. As Crews et al. [89] pointed out in their research through figures, the relation between the dissipation energy with ride comfort is complex, being both in conflict and not according to the range of values where it is investigated. In this chapter it is used in order to enhance ride comfort and consider the thermal performance of the damper in the suspensions design. Finally, the last supplementary objective (f_6) corresponds to the number of the switches in the dampers' states. This objective hasn't been considered from other researchers in the past for the design of semi-active suspensions and its minimization could provide many advantages. First of all, it aims to the decrease of the damper's components fatigue. Therefore, its components' expected life will be increased and the temperatures occurred in the fluid and the seals will be also decreased. Also, the decrease of f_6 will lead to the chatter's decrease and thus the decrease of the acceleration's response. Thus, this objective could be considered crucial for the design of the semi-active suspensions and based on the above, it should be incorporated in the design of semi-active suspensions as an extra objective.

In order to convert the values of all the objectives in the same level, the objectives are normalized for the shake of the sorting algorithm. More specifically, the vector of each objective is presented in Equation 7.11:

$$\vec{F}_{i,n} = \begin{bmatrix} f_{i,n,1} \\ f_{i,n,2} \\ \vdots \\ f_{i,n,j} \end{bmatrix} \tag{7.11}$$

where $n = 1,...,6$ is the n^{th} case study, $i = 1,...,6$ is the i^{th} objective function and j is each optimal solution from the pareto alternatives. Then, the vector of the objectives (F_i) for all the pareto alterna-

tives is normalized with its maximum value, as shown in Equation 7.12, in order to be used in KE and convert the values of all the objectives in the same level.

$$\overrightarrow{NF}_{i,n} = \vec{F}_{i,n} / max(\vec{F}_{i,n}) \tag{7.12}$$

Threshold (ε)

In all the parts of the analysis, a threshold was selected for the sorting algorithm so as to find the optimum solution among the optimal alternatives, as shown in Eq. 7.13

$$\varepsilon_i = P_i[max(\overrightarrow{NF}_{1,n}); ...; max(\overrightarrow{NF}_{6,n})] \tag{7.13}$$

where P_i=0.10-0.20 is used for all the scenarios, so as to set the threshold ε and obtain only one optimum solution. The value of ε was selected so as to be directly dependent with the objective functions. Thus, the maximum value of each objective among all the Pareto alternatives was used, while the value of P_i was selected so as to obtain one single optimum solution from the pareto alternatives of each case.

Cases	Description	Objectives	Thresholds (ε)
1	SH-2		
2	ADD		
3	SH-ADD-2	$[\overrightarrow{NF}_{1,n}; \overrightarrow{NF}_{2,n}; \overrightarrow{NF}_{3,n}; ...$	$\varepsilon = P_i * max(\overrightarrow{NF}_{i,n})$
4	SH-2-CDF	$\overrightarrow{NF}_{4,n}; \overrightarrow{NF}_{5,n}; \overrightarrow{NF}_{6,n};]$	
5	SH-ADD-2-CDF		

Table 7.4: Scenarios where the sorting algorithm (KE) is applied after having obtained the pareto fronts either from optimization or simulations.

7.3 Results

In this Section, the results of the optimization procedure are discussed using various figures and tables. Firstly, the Pareto fronts obtained from the MOGA regarding the optimization scenarios of Table 7.2 are presented in Figure 7.4a. The additional "pseudo" Pareto fronts, which occur from the simulation of the optimal solutions of SH-2 and SH-ADD-2 with the application of the CDF control strategy (SH-2-CDF and SH-ADD-2-CDF), are illustrated in Figure 7.4b. Additionally, the results of the sorting algorithm and the optimum design solution obtained for each case of Table 7.4 is pointed out in Figure 7.5. Furthermore, the k-ε levels and the optimum solution among all the case studies are presented

in Figure 7.6. Finally, the objectives of the optimum solution of each case study of Table 7.4 are illustrated in Table 7.5, in addition with the values of their design variables in Table 7.6.

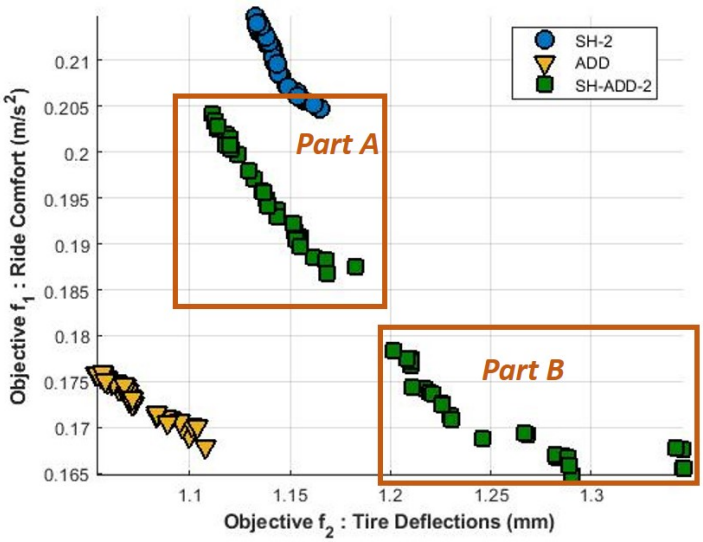

(a) The pareto fronts.

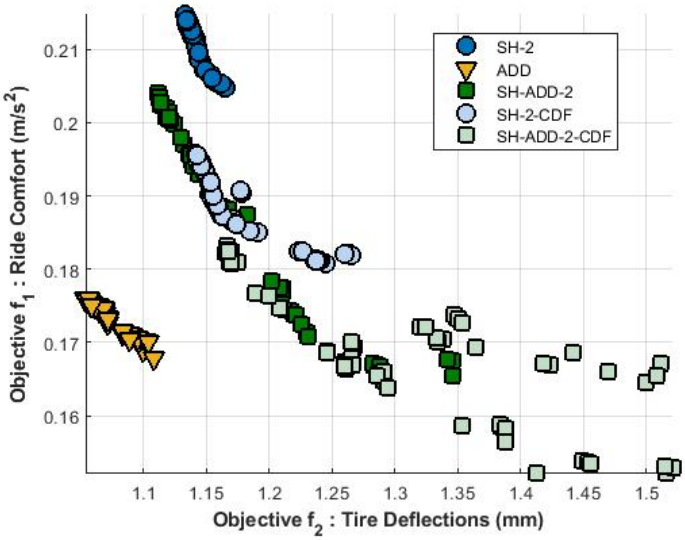

(b) The additional pseudo pareto fronts of CDF.

Figure 7.4: Comparison of the Pareto fronts provided by the MOGA, along with the pseudo pareto fronts occurred after applying to the optimal SH-2 and SH-ADD-2 the CDF control strategy.

More specifically, as far as the results of MOGA are concerned, the pareto fronts are presented in Figure 7.4a and the good convergence could be validated by the fact that all the pareto fronts have small dispersion and the optimal solutions are not scattered. Moreover, as far as the algorithms' results are concerned, based on their theory the SH-ADD-2 is a compromise of the complementary characteristics of SH-2 and ADD. The above remark is displayed in our results and the fact that the

pareto front of the SH-ADD-2 optimization scenario has converged to optimal solutions between the pareto fronts of SH-2 and ADD. Moreover, its pareto front is divided in two parts. The first part (Part A) has converged to solutions closer to SH-2, which have the same tire deflection with SH-2 but significant better comfort, whereas Part B has similar ride comfort levels with ADD but higher tire deflection values, thus less road holding.

Regarding the two "pseudo" pareto fronts (SH-2-CDF and SH-ADD-2-CDF), the optimal design solutions of the SH-2 and SH-ADD-2 optimization scenarios are applied to the vehicle model and it is simulated with the application of the CDF strategy in the control algorithms. Thus, the extra "pseudo" pareto fronts (SH-2-CDF and SH-ADD-2-CDF) are illustrated in Figure 7.4b. The SH-2-CDF case manages to improve significantly the ride comfort of the passengers, while it maintains objective f_2 in the same levels compared to SH-2. Also, the SH-2-CDF case provides solutions with similar characteristics with Part A of the SH-ADD-2, as pointed out in Figure 7.4a, illustrating the great effect of the CDF control strategy to the SH-2. The novel-distribution control strategy manages to make SH-2-CDF to operate similarly with a much better control algorithm such as SH-ADD-2. In addition, the application of CDF to SH-ADD-2 improves the ride comfort of the passengers compared to SH-ADD-2, but it decreases the road holding of the vehicle through the increase in the suspension travel. Furthermore, the "pseudo" pareto front of SH-ADD-2-CDF converges mainly to Part B of the SH-ADD-2, as pointed out in Figure 7.4a, while it provides few solutions (f_1 close to 0.18 m/s^2 and f_2 close to 1.16 mm) that dominate the ones of Part A of the SH-ADD-2 pareto front .

After obtaining the pareto fronts of the cases presented in Table 7.4 either from optimization (SH-2, ADD and SH-ADD-2) or from simulation (SH-2-CDF and SH-ADD-2-CDF), the KE sorting algorithm is implemented in order to seek the optimum design solution among their pareto alternatives (Table 7.4). The results are displayed in Figure 7.5 and all the subfigures (Figures 7.5a-7.5e) illustrate the relation of the main objective f_1 versus each one of the other objectives (f_2-f_6). In Figure 7.5a, the two main objectives (f_1 and f_2), which are used as objective functions in the MOGA, are plotted and the main conflict of the vehicle design between ride comfort and road holding is displayed. Furthermore, Figures 7.5b-7.5e present the supplementary objectives, which have been evaluated in order to be used for the KE, with respect to objective f_1 and display the conflicting or not behavior with ride comfort. As it is shown in Figures 7.5b-7.5c, f_3 and f_4 follow the conflict that was pointed out in Figure 7.5a because they supplement the objective of road holding and vehicle handling which are in conflict with comfort. Therefore, the role of enhancing them is proven.

On the other hand, in Figures 7.5d-7.5e a more complex relation is displayed regarding the relation of the objectives f_5 and f_6 with f_1, and thus ride comfort. As far as the number of the switches in the damper's states (f_5) is concerned, it is noticed in Figure 7.5d that all the cases (SH-2, ADD, SH-ADD-2, SH-2-CDF and SH-ADD-2-CDF) present significant variations among the switches of the optimal solutions of the pareto ($\pm$ 40). Also, some cases present conflicted relation with f_1 (SH-2-CDF and SH-ADD-2) while others not (SH-2). Moreover, as far as f_5 is concerned, SH-ADD-2-CDF

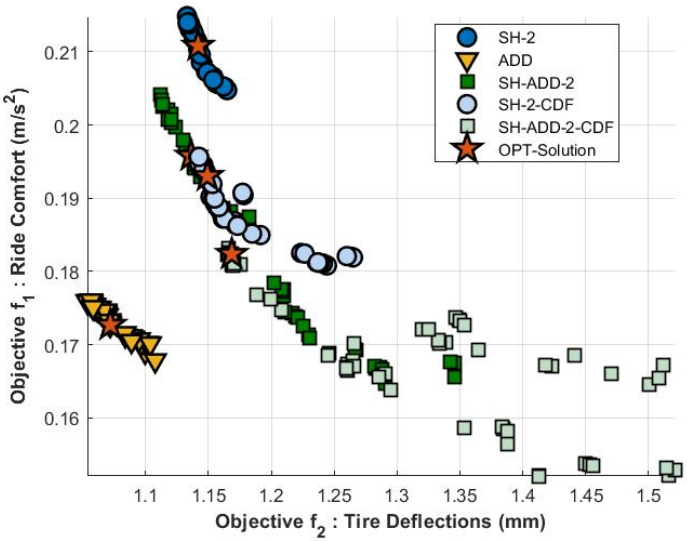

(a) f_1-f_2.

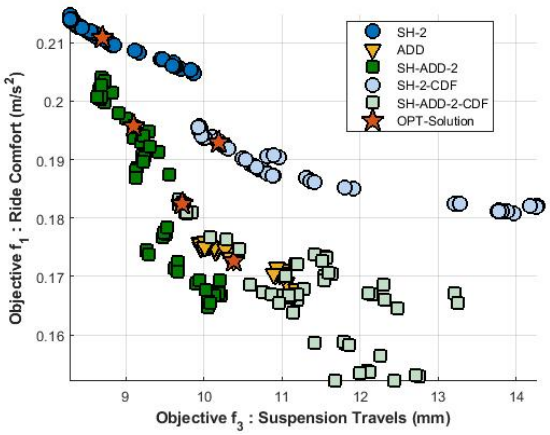

(b) f_1-f_3.

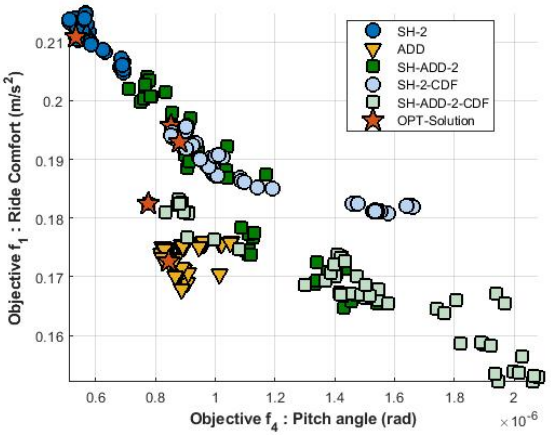

(c) f_1-f_4.

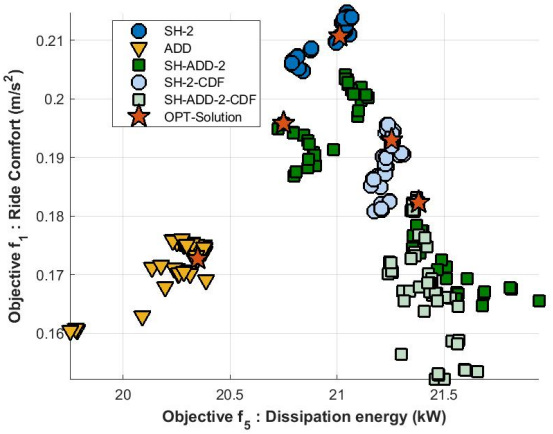

(d) f_1-f_5.

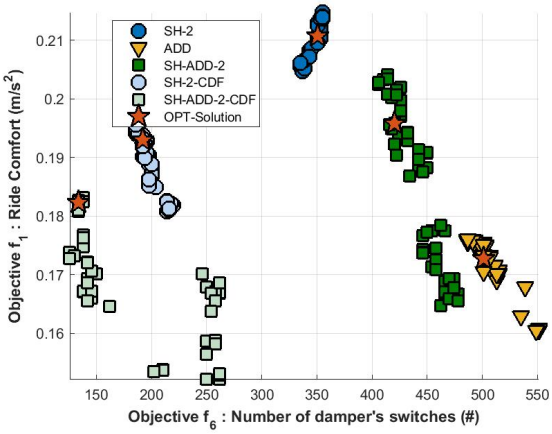

(e) f_1-f_6.

Figure 7.5: Comparison of the Pareto fronts provided by the MOGA and the optimum solutions obtained by KE for each optimization scenario of Table 7.4

has converged to a set of optimal solutions which consists of the two parts pointed out in Figure 7.4b. Both of them converge to two different but almost constant values for each part (Part A to ≈ 140 and Part B to ≈ 250). However, as it was mentioned before, the current objective is selected due to its importance in the design of the damper and its effect in the fatigue of the damper's components and the temperatures risen in them. As it shown in Figure 7.5d, the CDF control strategy when applied manages to decrease the number of the switches up to 50% compared to the traditional algorithms, i.e. SH-2 and SH-ADD-2 pareto front . Similarly with f_5, the dissipation energy (f_6) presents a complex relation, also, as shown in Figure 7.5e. In the cases of SH-2, ADD and SH-2-CDF, the last objective (f_6) presents non-conflicted relation with f_1, thus the decrease of the dissipation energy leads to the improvement in ride comfort. Although, the relation of f_1 with f_6 in the other cases (SH-ADD-2 and SH-ADD-2-CDF) is not clear, which is in accordance with the relation noticed in Crews et al. [89] pareto fronts. A possible explanation is the severe road excitation applied to the vehicle which is common both in this thesis and the one of Crews et al. [89].

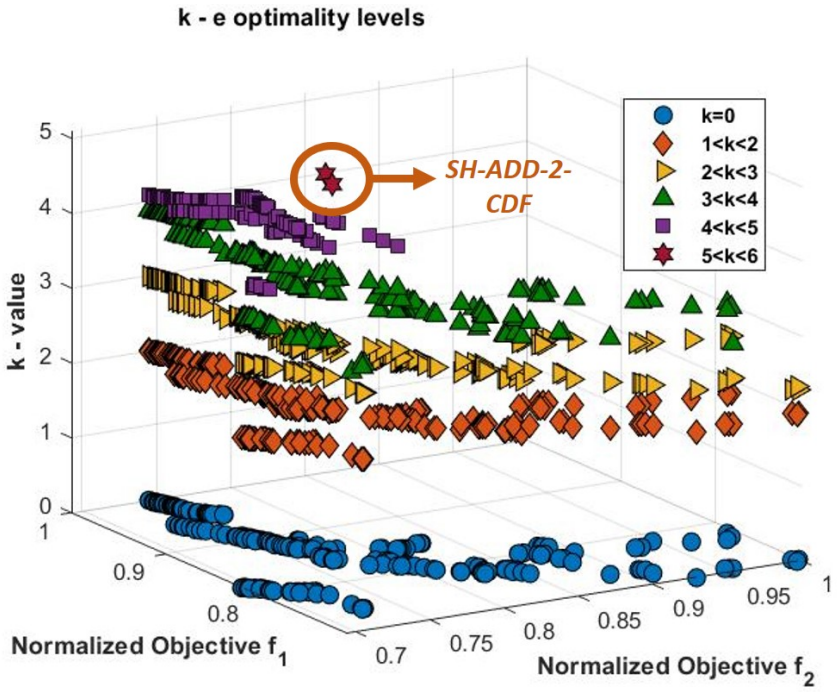

Figure 7.6: The k-ε levels of the optimal solutions occurred seeking the optimum among all the optimization scenarios of Table 6.

Furthermore, the optimum design solution of each case, which is delivered by KE, is pointed out in Figure 7.5. In all the cases, the optimum solutions are ranked above level five but below six from KE, implying that the solution is dominating to more than five objectives from the total six. Additionally, in the three cases (SH-2, ADD and SH-ADD-2), the optimum solution converged near the mid of the pareto front justifying the tendency of the designer to select this solution. On contrary, the optimum solutions of SH-2-CDF and SH-ADD-2-CDF are located to the edge of the pareto. Apart

from the optimum solutions of each case, in Figure 7.6 the optimum design solution among the pareto alternatives of all the cases of Table 7.4 are displayed. More specifically, the $k-\varepsilon$ levels are presented in a 3D plot with respect to the main objectives (f_1 and f_2). The "most optimum" solution is proven to be the optimum solution of SH-ADD-2-CDF (*OPT* 5) case and it is benchmarked against the other cases in terms of their objectives and their design variables in Tables 7.5 and 7.6 respectively.

Objective	Unit	OPT 1	OPT 2	OPT 3	OPT 4	OPT 5
		SH-2	ADD	SH-ADD-2	SH-2-CDF	SH-ADD-2-CDF
f_1	$[m/s^2]$	0.21	0.17	0.20	0.19	0.18
f_2	$[mm]$	1.14	1.07	1.14	1.15	1.17
f_3	$[mm]$	8.69	10.39	9.10	10.01	9.91
f_4	$[10^{-6}rad]$	0.53	0.84	0.85	0.89	0.81
f_5	$[kW]$	21.01	20.35	21.75	21.21	21.29
f_6	$[\#]$	351	501	420	182	134

Table 7.5: The values of the objectives of the optimum solutions of each case study of Table 7.4

Despite the superiority of *OPT* 5 against the other optimum solutions based on KE, it should be mentioned that also *OPT* 1 seems to provide high level vehicle performance. However, *OPT* 5 dominates mainly due to its performance in ride comfort and in the damper's switches, as shown in Tables 7.5. More specifically, *OPT* 5 manages to minimize the ride comfort close to the levels of the optimum value of ADD (*OPT* 2), which is the most comfort oriented and provided solutions with the best ride comfort. In addition, its suspension travel is less compared to the one of *OPT* 2 despite the improvement in comfort. Additionally, the number of the switches in the damper's states in *OPT* 5 is also decreased significantly compared to the other cases without any impact in the vehicles performance. This is also due to the control strategy applied to the suspensions, presented in Chapter 4, which mainly aims to achieve less temperatures and fatigue in the damper's components through a decrease in the switches and the chattering. Except from the pitch angle (f_5) of *OPT* 5 which is larger than SH-2 but smaller than the others, the rest objectives of *OPT* 5 have converged to similar values compared to the objectives of the other cases.

As far as the design variables are concerned, the values of each case are presented in Table 7.6. K_{S_F}, C_{max_F} and C_{max_R} have converged to very close values for all the cases, around 15200 N/m, 2540 Ns/m and 2600 Ns/m, respectively. On the other hand, K_{S_R}, C_{min_F} and C_{min_R} illustrate significant variations among the design variables of all the optimum solutions of each case. Also, regarding the general design of the suspensions, the rear suspension converge to a stiffer spring (K_{S_R}) compared to the front one, following the Olley's tuning [74] which is beneficial in high speeds as in our case study (V=50km/h). Likewise, the maximum coefficient (C_{max_F}) of the front damper is softer than the one of the rear damper (C_{max_R}), following also the above remark. On contrary, the minimum coefficient

Variable	Unit	OPT 1	OPT 2	OPT 3	OPT 4	OPT 5
		SH-2	ADD	SH-ADD-2	SH-2 CDF	SH-ADD-2 CDF
C_{min_F}	$[Ns/m]$	1490	1312	780	1536	1265
C_{max_F}	$[Ns/m]$	2532	2546	2537	2531	2567
C_{min_R}	$[Ns/m]$	1119	1225	1077	1267	1219
C_{max_R}	$[Ns/m]$	2663	2621	2680	2663	2598
K_{S_F}	$[N/m]$	15377	15177	15171	15374	15227
K_{S_R}	$[N/m]$	15933	16921	17451	15946	16441
α	$[rad/s]$	-	-	18.48	-	16.46

Table 7.6: The design variables of the optimum solutions of each case study of Table 7.4

(C_{min_F}) of the front damper is stiffer than the rear one (C_{min_R}), except OPT 3 which maintains Olley's tuning.

7.4 Conclusions

To sum up, in this chapter, the design of semi-active suspensions is investigated. An approach based on KEMOGA algorithm is applied to a passenger vehicle in order to optimize its suspensions. The semi-active suspensions operate with SH control algorithms, while a novel distribution-based control strategy is applied to some of them. The vehicle model is optimized with respect to ride comfort and road holding using a multi-objective genetic algorithm (MOGA). Each of these objectives is represented by performance indexes which are pointed out as the most appropriate in the literature. Then, a sorting algorithm (KE) is applied considering four extra indexes as objectives. More specifically, two of them enhance the road holding (the suspension travel and the pitch angle) and are widely used in the literature, while the other two are neglected but are important for the design of semi-active suspensions (the dissipation energy and the number of switches in the damper's states) as indicated in this work. The optimum solutions obtained by KE are presented and compared in terms of their objectives and their design variables.

Based on this work, firstly, the applicability and the efficiency of the approach based on KEMOGA algorithm [27] in semi-active suspensions is proven. The separation of the objectives to main and supplementary ones allowed the algorithm to provide optimum solutions, which not only have considered extra performance aspects but also they are attained without costing extra computational time compared to the case they are incorporated in the MOGA. Therefore, using this approach more performance aspects apart from the ride comfort and the road holding could be incorporated in the opti-

mization procedure. The above remark is even more important in case the extra performance aspects present a complex relation with the main objectives, such as the dissipation energy and the number of the switches, as shown in this work through Figures 7.5d-7.5e. Despite their importance for the design of semi-active suspensions, these performance aspects could be considered "inappropriate" main objective function being able to mislead the algorithm and demand more computational time for convergence due to the complex relation with ride comfort or road holding. However, with this approach they are introduced only in the sorting algorithm enabling the designer to include them as design criteria and introduce them in the design process without costing computational time and quality in the optimum solution.

Another important point illustrated in this chapter, is the significant improvement of the SH-2 and SH-ADD-2 with the application of CDF. This is proven initially by the fact that the pseudo-pareto fronts of SH-2-CDF and SH-ADD-2-CDF converged to solutions with better performance than the traditional algorithms in terms of the objectives' values Figure 7.5. More specifically, the CDF control strategy when applied, manages to decrease the number of the switches in the damper's states up to 50% in both algorithms. This change could increase the expected life of the damper's components and decrease significantly the elevated temperatures in the fluid and the seals of the damper. However, the improvement gained when applying CDF is more obvious to the case of SH-2, where the CDF control strategy improves the algorithm to the levels of SH-ADD-2, which is considered as a superior control algorithm in the literature. Finally, the optimum solution among all the cases obtained from KE is the one belonging to SH-ADD-2-CDF, which proves the superiority of the CDF approach among all the other cases according to the selected design criteria. The optimum design solutions had $k-\varepsilon$ levels between 5 and 6, i.e. it is dominating to five out of six objectives compared to the others which had $k-\varepsilon$ level under 4.

In conclusion, the optimization approach based on KEMOGA can be recommended as an effective methodology for the optimum design of semi-active suspensions, enabling the designer to incorporate extra performance indexes in the design process , such as the ones proposed in this chapter, without neglecting ride comfort and road holding.

CHAPTER 8

Optimization of seat suspensions

When a vehicle is employed with a high quality suspension system or it drives through smooth roads, the typical magnitude of the vibration entering the seat is low and the ride is comfortable. On the other hand, when the seat is exposed to high vibration magnitudes, it might not perform very well, resulting in a poor "ride" for the occupant, due to the lack of good suspension or an off-road ride. Therefore, in this thesis, after having optimized the primary suspension systems of a vehicle, the interest is turned on seat suspension systems and their optimization. The main conflict in the seat suspensions implies that the increasing initial deformation of the system ('static comfort') leads to better isolation of the accelerations and a more comfortable seat ('dynamic comfort'). Many researchers have focused on overcoming or at least suppress this conflict by modeling new suspension systems, such as the so called negative suspension systems. However, the modeling of new suspensions is not the only solution of improving the ride comfort of the passenger. The optimization is an equally important step in designing a seat and ensuring the required comfort of the driver and the safe handling of the working machine.

In this chapter, the comparison of four established isolators in seat design and the application of a novel one, are presented. More specifically, the comparison is conducted beteen the conventional suspension (PS), the ones of Carrella et al. (NSS1) [5–7], Le Thanh Danh et al. [9] (NSS2), Yan et al. [13] NSS3 and Antoniadis et al. [15, 119] (NSS4). The isolators are optimized using MOO algorithms (Pareto) and then their pareto fronts are compared. The optimum solutions occur for the excitation of the isolators with the response of the sprung mass of a vehicle, when it drives over random road profiles of different classes.

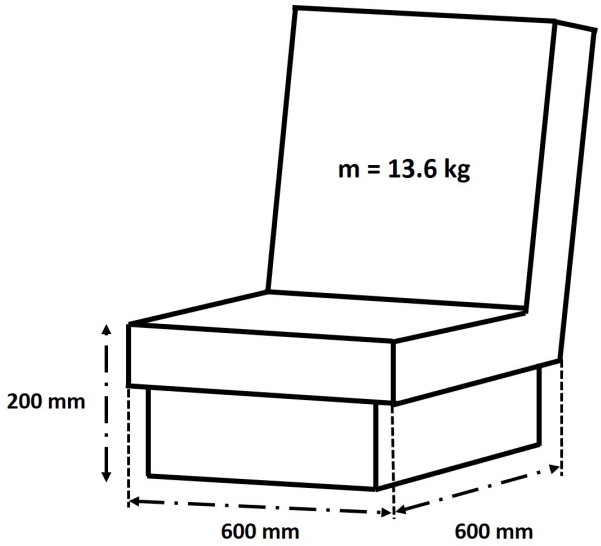

Figure 8.1: Seat from a commercial passenger vehicle and its dimensions applied as constraints in the optimization procedure

8.1 Materials & Methods

8.1.1 Simulation models

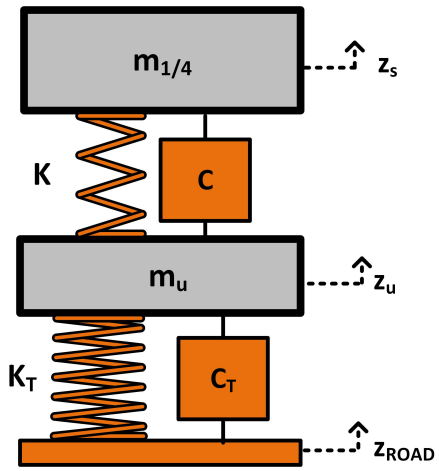

Figure 8.2: Quarter car model representing one wheel of the vehicle

This chapter concerns the suspension system of the seat, thus a simple vehicle model is selected so as to evaluate the vibrations of the sprung mass, i.e. vehicle's floor, in order to apply them as excitation in the seat models. Thus, the quarter car model (QC), as shown in Figure 8.2, is used so as to place the seat above. The parameters are selected from the literature so as to represent a passenger vehicle and are presented in Table 8.1.

Parameter	Unit	Value	Parameter	Value	Value
m_s	$[kg]$	285	m_u	$[kg]$	25
K_u	$[N/m]$	30000	C	$[Nm/s]$	2500
K_{Tu}	$[N/m]$	200000			

Table 8.1: Parameters of QC model used in this chapter

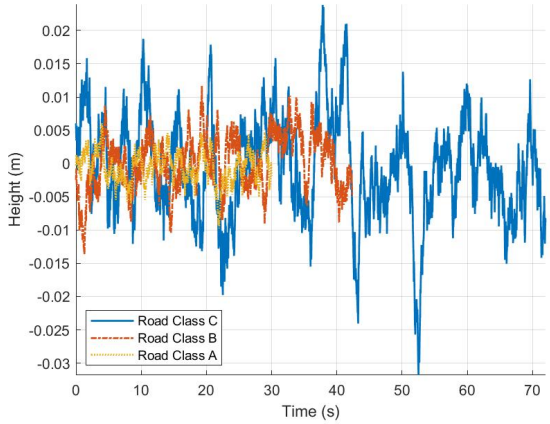

(a) Time Domain.

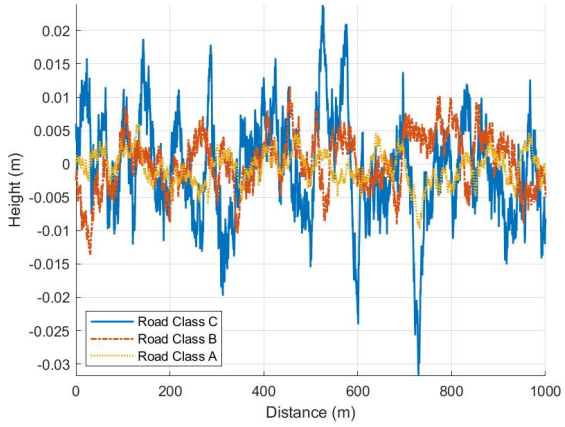

(b) Road's Trajectory generated using ISO8608

Figure 8.3: The random road profiles generated based on ISO-8608 and applied to the vehicle model of this chapter.

8.1.2 Road Excitation

Three random road profiles of Class A, B and C are generated using a sinusoidal approximation. The vehicle is assumed to travel with a constant speed V (120, 85 and 50 km/m respectively) over a given road segment with length ($L_s = 1000$m).

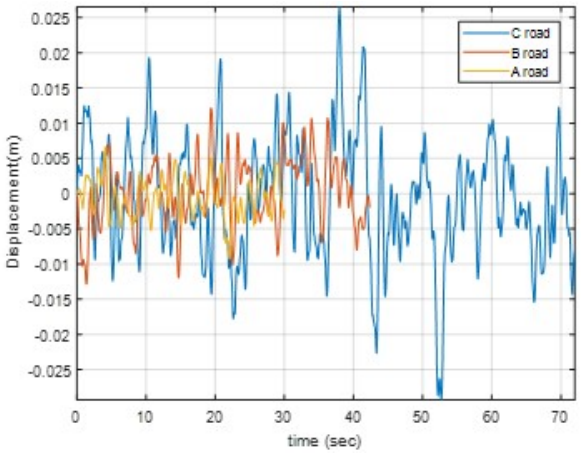

(a) Displacements.

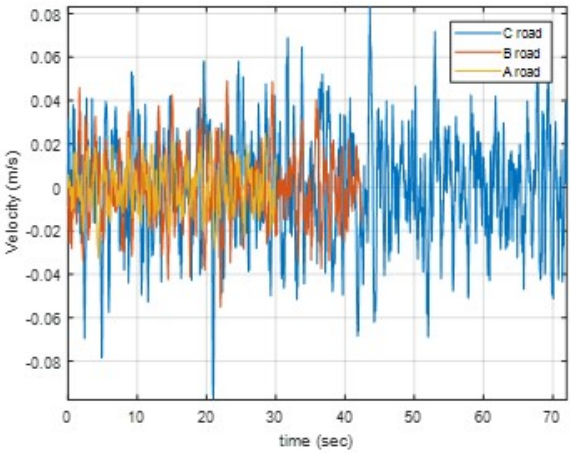

(b) Velocities

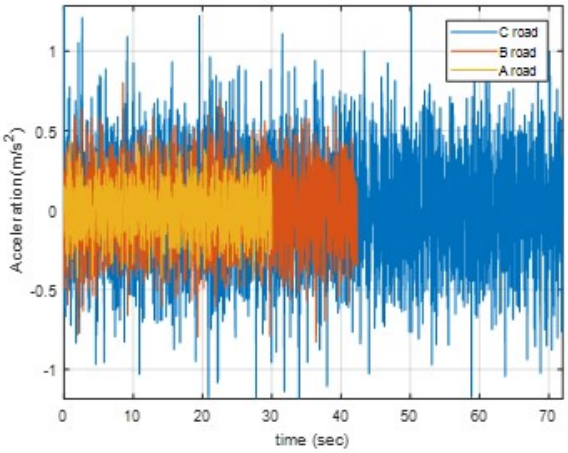

(c) Accelerations

Figure 8.4: Response of vehicle's sprung mass applied to seat models as excitations.

Previous researches have recommended that driving trials should have a duration of at least 2 h to accurately determine the performance of a seat. Porter et al. [142] demonstrated that although some seats are considered uncomfortable after 15 min, others that are initially considered comfortable become uncomfortable after about an hour. Also, previous research into commercial vehicle discomfort has implemented trial durations ranging from 60 s to 135 min [143–145]. Thus, in this chapter a duration around the minimum of these trials is used for our simulations.

The road profiles are illustrated in Figure 8.3, displaying both the time domain data (Figure 8.3a) and the trajectory of the road (Figure 8.3b).

8.1.3 Seat's Excitation

The road excitation presented in the previous section is used to excite the vehicle model and then the response of the sprung mass is used as an excitation of the seat model, considering it is the floor's vibration. More specifically, the displacements, the velocities and the accelerations of the sprung mass are presented in Figure 8.4.

8.2 Optimization Procedure

The objective functions are selected, so as to represent the two parts of the conflict in the design of seat suspensions, i.e. the comfort of the driver and the safe handling of the working machine. These two objectives represent the contribution of dynamic and static factors, respectively, to the overall discomfort, as shown in Figure 1.2. As far as the design variables are concerned, the key parameters both of the passive and the negative part of the suspension are selected. The bounds and the constraints applied to the optimization problem are set based on the dimensions of a commercial passenger seat, ensuring that the optimum solution will correspond not to only a comfortable seat but also to a compact structure applicable to a passenger vehicle seat. In Figure 8.1 the structures' total height, length and width are illustrated as they are measured from a seat of a commercial passenger vehicle. Additionally, the total mass of the seat and the passenger, 13.6 kg and 81.4 kg respectively, is used as the dof's mass (m) for the optimization of our system.

8.2.1 Objective Functions

The objective functions, which are selected in this chapter for overcoming the conflict appearing in seat suspensions, are:

1. f_1, as shown in Equation 8.1, the root mean square of the seat's vertical acceleration depicting the dynamic comfort, according to Equation 2.78 and Chapter 2.4.2:

$$f_1 = RC_{se} \tag{8.1}$$

2. f_2, as shown in Equation 8.2, the initial displacement of the mass depicting the static comfort and the safety of the machine handling:

$$f_2 = X_{ST} \tag{8.2}$$

   where the equation of X_{ST} varies based on the seat model and is displayed in Sections 2.2.2-2.2.5, which describe the design and the function of each suspension system.

For all the optimization scenarios that are implemented in this chapter, the objective functions are the same, as illustrated in Equation 8.1 - 8.2.

8.2.2 Design Variables, Bounds and Constraints

PS Model

As far as the PS Model shown in Figure 8.5 and described in Chapter 2.2.1 is concerned, the key parameters of the suspension system (K_v and C_v) are selected as the design variables of the optimization. The design variables and their bounds are shown in Table 8.2. Also, the constraints, as presented in Table 8.3, are selected so as to ensure acceptable levels of ride comfort (Constraint 1) based on ISO2631 [96] and the initial deformation of the system to be maximum the half of the structures' total height (0.1 m - Constraint 2).

#	Design Variable	Unit	Lower Bound	Upper Bound
1	K_v	$[N/m]$	$1.0\ 10^4$	$1.5\ 10^5$
2	C_v	$[N.s/m]$	$2.0\ 10^2$	$2.5\ 10^3$

Table 8.2: Upper and lower bounds of the design variables of the PS Model

#	Constraints
1	$RC_{se} < 1\ m/s^2$
2	$X_{ST} < 0.1$ m

Table 8.3: Constraints of PS Model

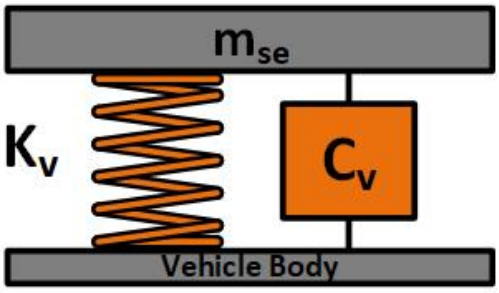

Figure 8.5: Passive seat suspension system with linear spring and damper (PS)

NSS1 Model

Regarding the NSS1 Model, as presented in Figure 8.6 and described in Chapter 2.2.2, the design variables and their bounds are depicted in Table 8.4. The first two design variables (γ and α) are selected, so as to optimize the "negative" function of the mechanism. Thus, the geometrical parameter γ is bounded so as the angle of the inclined springs (θ_o) could be between 0 and 90^o. Additionally,

the third one (a_o) is selected for keeping the dimensions of the structures insided the desired levels. The final design variable (C_v) is one of the key parameters of the passive suspension system, while, in contrast to PS Model, the spring constant (K_v) isn't selected as a design variable. Based on the analysis of Section 2.2.2, the initial deformation of the structure occurs from $X_{ST} = \sqrt{L_o^2 - a_o^2}$, where $L_o = \alpha_o/\gamma$. Also, the stiffness of the vertical spring results from $K_v = mg/X_{ST}$, based on Hooke's Law in the equilibrium position. Considering also that γ and a_o are already selected as design variables and K_v is a function of them, the K_v is not included as an extra design variable. Finally, the constraints, applied to the current scenario (NSS1 Model) and shown at Table 8.5, are the same with the PS Model.

#	Design Variable	Unit	Lower Bound	Upper Bound
1	γ	-	0.01	0.99
2	α	-	0.00	5.00
3	a_o	$[m]$	0.10	0.30
4	C_v	$[N.s/m]$	$2.0*10^2$	$2.5*10^3$

Table 8.4: Upper and lower bounds of the design variables of NSS1 Model

#	Constraints
1	$RC_{se} < 1\ m/s^2$
2	$X_{ST} < 0.1\ m$

Table 8.5: Constraints of NSS1 Model

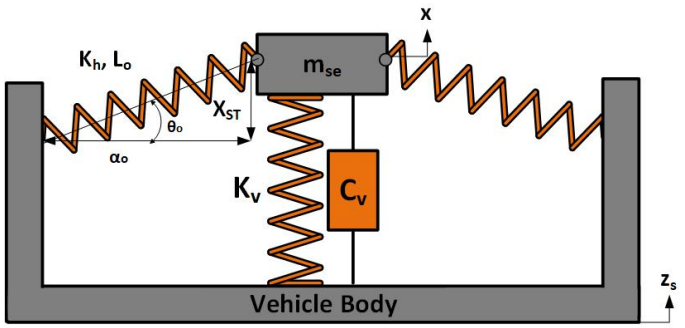

Figure 8.6: Seat suspension system based on Carrella et al. [5–7] at a random position x under the excitation of z_s (NSS1)

NSS2 Model

As far as the NSS2 Model illustrated in Figure 8.7 of Chapter 2.2.3, the boundaries in the design variables are determined by the analysis of Le et al. [8, 10, 146] and are obtained as follows. The ratio of the spring stiffnesses (α) is limited to 0 to 1, based on the theory of the current suspension system described in Section 2.2.3. The other three design variables (L_o, b and a_o) are selected based on the

structure dimensions shown in Figure 8.1. In accordance with the procedure of the NSS1 Model, the only key parameter of the passive suspension system, which is selected as a design variable, is the damping coefficient (C_v). Similarly, the initial deformation is $X_{ST} = \sqrt{b^2 - (a_o - L_o)^2}$ and thus, based on Hooke Law the spring's coefficient results from $K_v = mg/X_{ST}$. Hence, there is no need to consider K_v as a design variable, considering that it's a function of the other design variables.

The constraints used in the current model, apart from the first two that remain the same with the previous models (Constraints 1 and 2), are oriented so as to ensure that the system will attain the maximum possible range where its dynamic stiffness will be almost zero and the "QZS" characteristics of the mechanism (Constraints 3-5) will be maintained.

#	Design Variable	Unit	Lower Bound	Upper Bound
1	α	–	0.00	1.0
2	L_o	$[m]$	0.10	0.3
3	a_o	$[m]$	0.10	0.3
4	b	$[m]$	0.05	0.3
5	C_v	$[N.s/m]$	$2.0*10^2$	$2.5*10^3$

Table 8.6: Upper and lower bounds of the design variables of NSS2 Model

#	Constraints
1	$RC_{se} < 1\ m/s^2$
2	$X_{ST} < 0.1$ m
3	$\alpha < \frac{\gamma_1}{2(1+\gamma_1-\gamma_2)}$
4	$\gamma_2 - 1 < \gamma_1$
5	$\gamma_2 > 1$

Table 8.7: Constraints of NSS2 Model

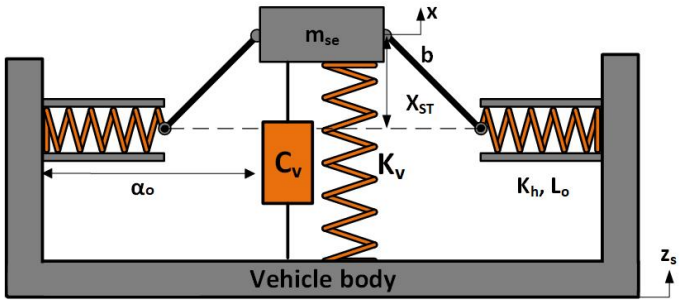

Figure 8.7: Seat suspension model system on T. D. Le et al. [8–12] at a random position x under the excitation of z_s (NSS2)

NSS3 Model

The design variables of this model (NSS3), as presented in Figure 8.8 and described in Chapter 2.2.4), are defined similarly with the previous models. The ratio of spring stiffnesses are selected to be bounded between 0 and 5. In addition, the radiuses R and r and the dimension d are limited up to 0.25 m taking into account the available space of the seat structure, as shown in Figure 8.1. Also, in accordance with the other models, the damping coefficient (C_v) is selected as a design variable, while the K_v is excluded. The exclusion is due to the fact that the initial deformation of the system is $X_{ST} = \sqrt{(R+r)^2-(d+r)^2}$, and K_V occurs to be a function of all the other design variables considering that $K_v = mg/X_{ST}$.

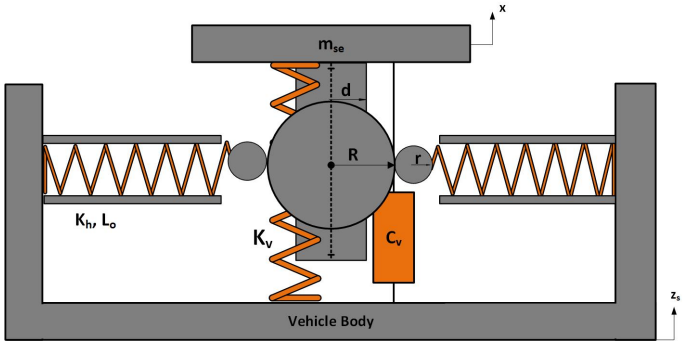

Figure 8.8: Seat suspension system based on Yan et al. [13] at a random position x under the excitation of z_s (NSS3)

#	Design Variable	Unit	Lower Bound	Upper Bound
1	α	-	0.00	5.00
2	R	$[m]$	0.01	0.25
3	d	$[m]$	0.00	0.25
4	r	$[m]$	0.01	0.25
5	C_v	$[N.s/m]$	$2.0*10^2$	$2.5*10^3$

Table 8.8: Upper and lower bounds of the design variables of NSS3 Model

As far as the constraints are concerned, Constraints 1 and 2 are the same with all the other models. The radius of the inner disk is selected to be greater than the one of the outer (Constraint 3), in order to ensure that the roller will be in contact with the cam for a greater range of suspension travels. In this respect, and for ensuring the contact of the roller with cam in the extreme positions, the initial precompression u_2 of the horizontal springs is selected equal to 0.001 m, for the design of the model. Finally, for greater ease in the construction of such a system and for securing the greater range of possible seat displacements, the Constraint 4 is added. Its importance is pointed out in the results of the current model, where the optimization results for various values of μ (0.5, 0.6, 0.7, 0.8 and 0.9) are illustrated.

#	Constraints
1	$RC_{se} < 1\ m/s^2$
2	$X_{ST} < 0.1$ m
3	R > r
4	μ*R > d

Table 8.9: Constraints of NSS3 Model

NSS4 Model

The final optimization scenario is the one of NSS4 Model, which involves the optimization of the KDamper design as presented in Figure 8.9 and described in Chapter 2.2.5. In accordance to all the other cases, the design variables are selected so as to ensure either the "negative" function of the mechanism or the dimensions of the structure. More specifically, in this case the first three design variables (a_o, L_o and b) are for design and dimension reasons, while the last four are the key parameters of the suspension system (K_S, K_v, K_h *and* C_v). In contrast to all the other models, the spring constant is not possible to be excluded from design variables. The initial displacement of the system is $X_{ST} = \left[(m+m_d)g - f_{N0}\right]/K_S$, and includes also f_{N0}. Also, as far as the internal mass is concerned, its mass is selected to be constant and equal to 1 kg, i.e. approximately 1% of the mass of the entire load applied to the system. Finally, regarding the constraints, apart from the ones applied to all the models (Constraints 1 and 2), which ensure measurable levels of ride comfort and the initial deformation of the system to be maximum the half of the structures' total height, a third one is applied. The variable c_I is bounded to small values ($-0.1 < c_I < 0.1$), so as to increase the linearity in the behavior of the suspension system and design it more stable.

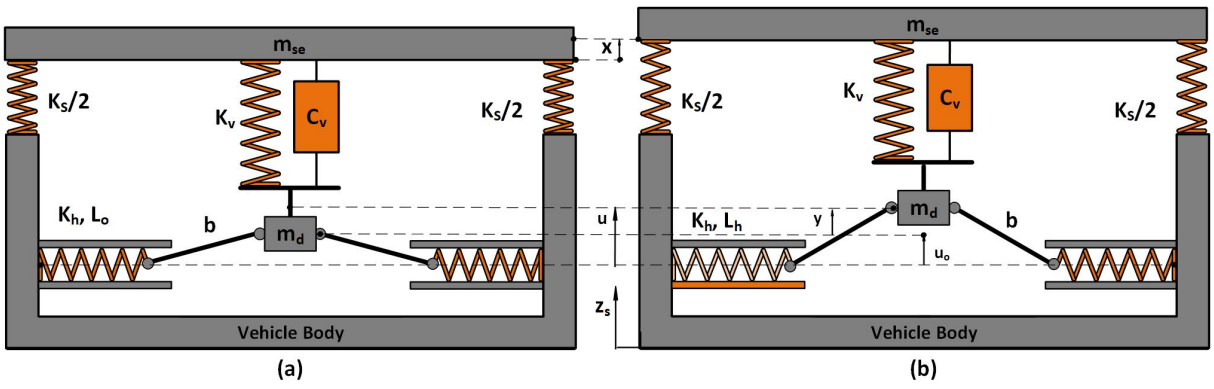

Figure 8.9: Seat suspension system based on Antoniadis et al. [14, 15] the left in the static equilibrium and the right at a random position x under the excitation of z_s (NSS4)

#	Design Variable	Unit	Lower Bound	Upper Bound
1	α_o	$[m]$	0.10	0.30
2	L_o	$[m]$	0.10	0.30
3	b	$[m]$	0.10	0.30
4	K_S	$[N/m]$	$1.0*10^4$	$1.5*10^5$
5	K_v	$[N/m]$	$2.0*10^3$	$7.0*10^4$
6	K_h	$[N/m]$		
7	C_v	$[N.s/m]$	$2.0*10^2$	$2.5*10^3$

Table 8.10: Upper and lower bounds of the design variables of NSS4 Model

#	Constraints
1	$RC_{se} < 1\ m/s^2$
2	$X_{ST} < 0.1$ m
3	$-0.1 < c_I < 0.1$

Table 8.11: Constraints of NSS4 Model

8.3 Optimal design

In this chapter, as it was mentioned, KDamper design (NSS4 Model) is tested in a seat suspension and the results are presented. Thus, in order to extract conclusions regarding its behavior, it is compared with four other established vibration isolators (PS, NSS1, NSS2 and NSS3). For the purpose of their comparison the five isolators are optimized in respect to the ride comfort and the safety of the machine handling applying constraints aiming not only to a compact structure able to fit in a passenger vehicle but also to a comfortable seat. The optimum compromise of the above-mentioned conflict is obtained through the solution of two MOO problem applying two excitations to the isolators. The excitations correspond to the response of a vehicle's sprung mass, while it drives over two random road profile of Class A and B. Hence, in order to extract important conclusions, the results of each model are presented both by comparing the Pareto fronts for the road profile of class A (Pareto A) and of Class B (Pareto B), but also the design variables of the two optimization scenarios. Additionally, the common solutions from the two Pareto Fronts are illustrated. However, considering that its really difficult for the genetic algorithms to converge in the same solutions not only in different optimization problems (different excitations in the current study) but also in the same optimization problem, the common solutions are found considering a certain percentage of difference between the optimum design variables of the two excitations.

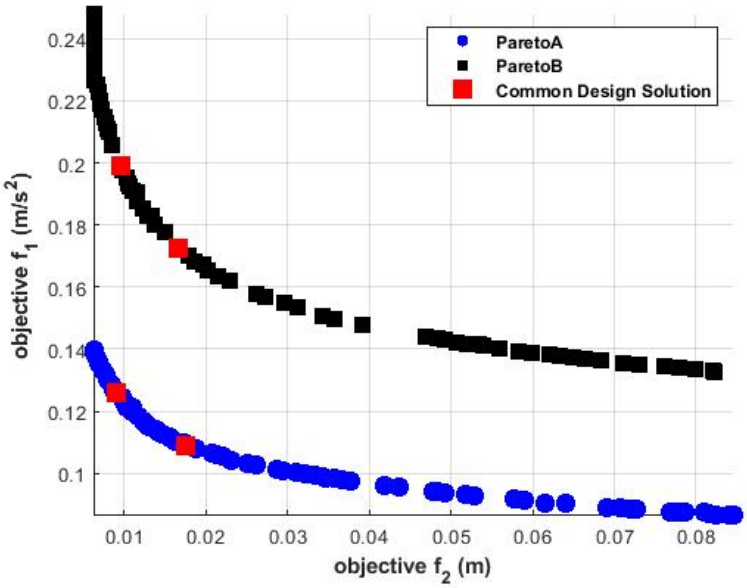

Figure 8.10: Comparison of the Pareto Fronts of PS Model for Road A and Road B

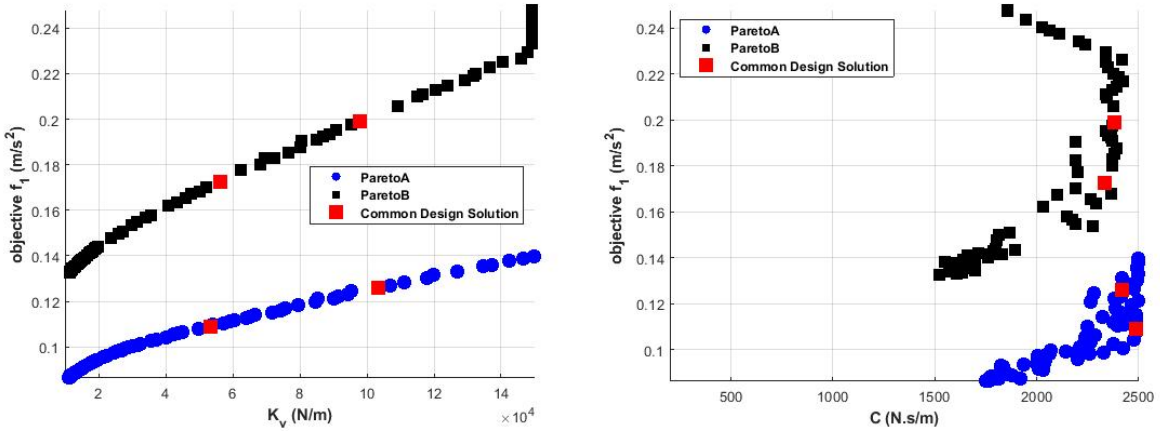

(a) K_v (N/m) . (b) C_v (N.s/m) .

Figure 8.11: The optimum design variables of PS Model occured from the Pareto front vs. the Objective f_1 (m/s^2)

8.3.1 PS Model

The first model is the conventional linear suspension. As show in Figure 8.10, Pareto B increases the values of f_1, hence the levels of ride comfort, around 35% in all the range of the optimum solutions occurred. Additionally, the initial displacements are almost the same, for both of the Pareto fronts including solutions between 0.006 to 0.09 m. Moreover, despite the fact that the majority of the solutions of Pareto B could be corresponded to optimum solutions of Pareto A, only two have similar

design variables (Figure 8.11a - 8.11b) in both the Pareto Fronts, considering an acceptable difference less than 7 %. Thus, only these two optimum design solutions of seat model, occurred for a vehicle driving over a road profile of class A, could be also used for a vehicle driving over a road profile of class B. Furthermore, these two solutions have exactly the same objectives values (f_1 and f_2) as presented in 8.10. Finally, the lack of high dispersion in the data of Figure 8.11a - 8.11b, displays the high convergence of the optimization algorithm.

8.3.2 NSS1

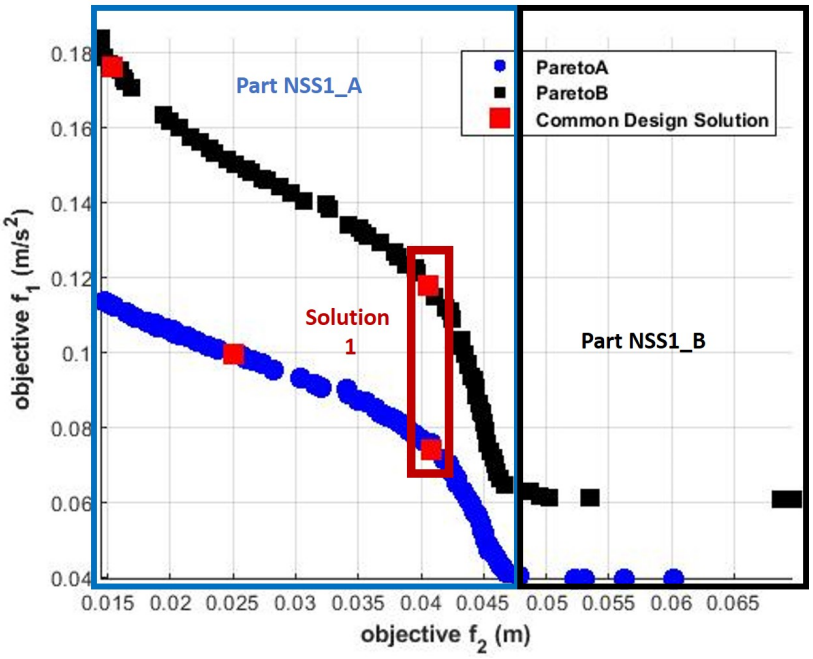

Figure 8.12: Comparison of the Pareto Fronts of NSS1 model for Road A and Road B

The second model, studied in this chapter, is the first using negative structures (NSS1 Model). Based on the comparisons of the two Pareto Fronts in Figure 8.12, the optimum solutions could be divided in:

- Part NSS1_A, for initial deformations between 0.01 to 0.045 m, and
- Part NSS1_B, for initial deformations around 0.045 to 0.07 m.

This separation is due to the fact that all the solutions of Part NSS1_B have equal f_1, but varying f_2. These solutions could be ignored considering that they have the same ride comfort and increasing initial deformation and both of these objectives are set for minimization. Thus, the one with the minimum value of f_2 could be kept. As far as the ride comfort is concerned, it decreases essentially

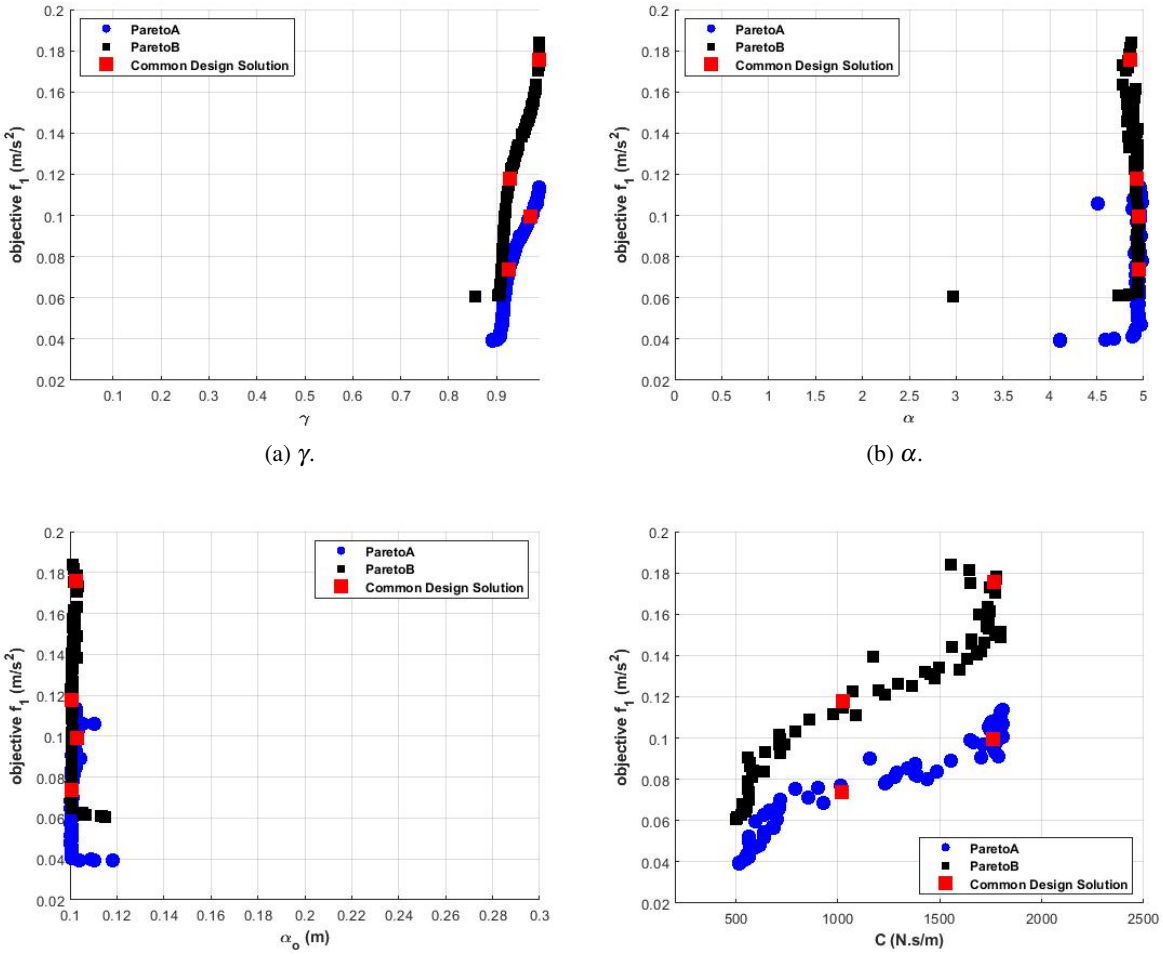

(a) γ. (b) α.

(c) α_o (m) . (d) C (N.s/m) .

Figure 8.13: The optimum design variables of NSS1 Model occurred from the Pareto front vs. the Objective f_1 (m/s^2)

by roughening the road profile. The values of f_1 of Pareto B have been increased around 40 % compared to the ones of Pareto A for Part NSS1_A and around 30 % for Part NSS1_B. On the other hand, in the PS Models, as shown in Figure 8.10, this increase is uniform in all the range of the optimum solutions and is around 40%. The smaller increase, noticed for Part NSS1_B, corresponds in higher displacements and implies that the better performance of this suspension mechanism occurs for higher initial displacements. However, regarding the initial deformation (f_2), its range is exactly the same in both the Pareto fronts, excluding a few solutions belonging to Part NSS1_B of the Pareto fronts.

AS far as the design variables (Figure 8.13a - 8.13d) are concerned, despite the fact that the majority of the solutions of Pareto B could be corresponded to the optimum solutions of Pareto A, only two of them have close values of design variables considering an acceptable difference of 2 %. However,

only one of them (Solution 1) presents also the close values in the objectives of the optimum solution according to Figure 8.12. Thus, only one optimum solution among the Pareto alternatives of Pareto A could be used for a seat designed also for Pareto B conditions. Furthermore, the ratio of the horizontal and vertical stiffnesses (α) has converged to the upper bound, showing the need of the mechanism for stiffer springs in the negative structure. Similar behavior is noticed in the distance of the wall (α_o) which has converged to the lower bound, as shown in the optimization procedure and Table 8.4. Finally, the lack of high dispersion in the data of Figure 8.13a - 8.13d, shows the high convergence of the optimization algorithm.

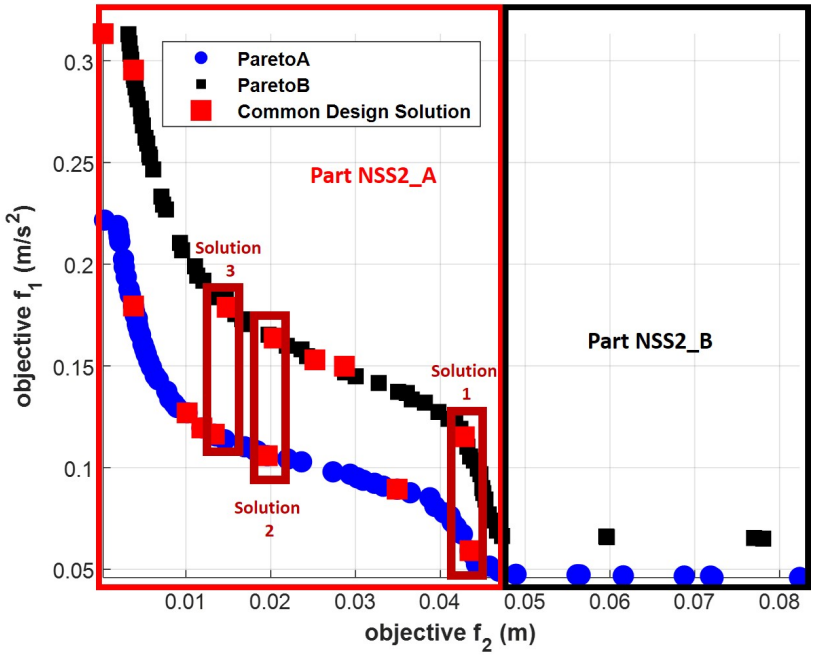

Figure 8.14: Comparison of the Pareto Fronts of NSS2 model for Road A and Road B

8.3.3 NSS2

The third model studied is the extension of NSS1(NSS2). Based on the comparisons of the two Pareto Fronts in Figure 8.14, the optimum solutions could be divided in:

- Part NSS2_A for initial deformations between 0.01 to 0.045 m, and
- Part NSS2_B for initial deformations around 0.045 to 0.083 m.

As also mentioned in NSS1, these solutions could be ignored considering they provide the equal values of f_1 for increasing f_2. As far as the ride comfort is concerned, the values of f_1 in Pareto B have increased around 30 % in all the range of the optimum solutions occurred, decreasing ride

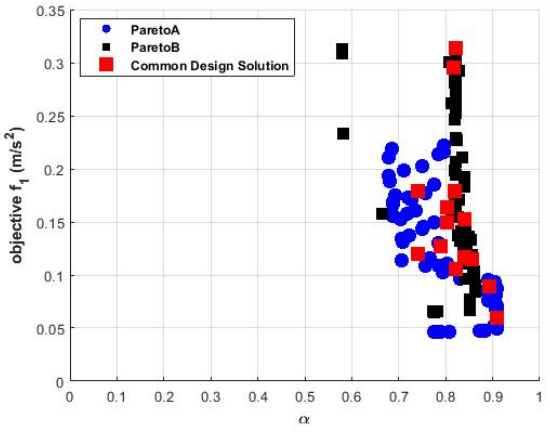

(a) α.

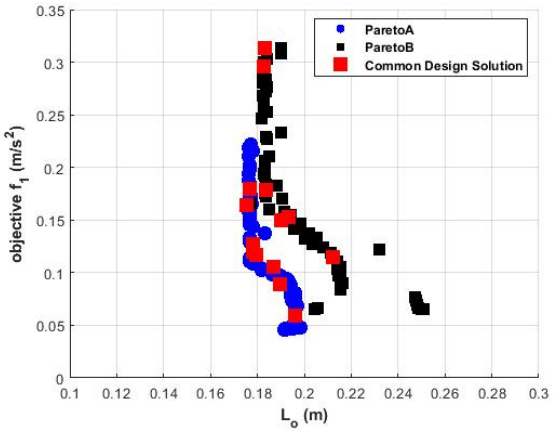

(b) L_o.

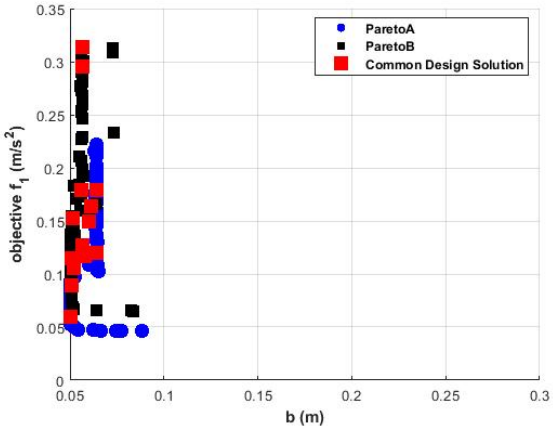

(c) b (m) .

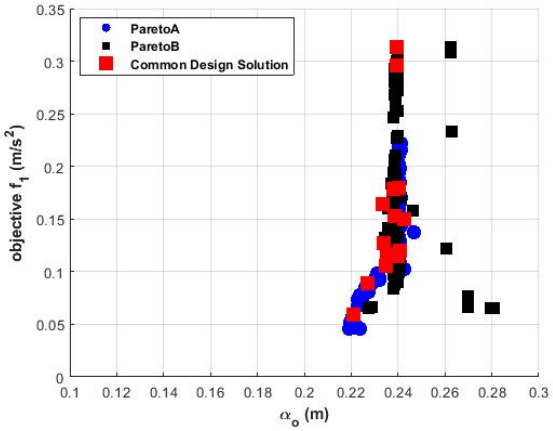

(d) α_o (m) .

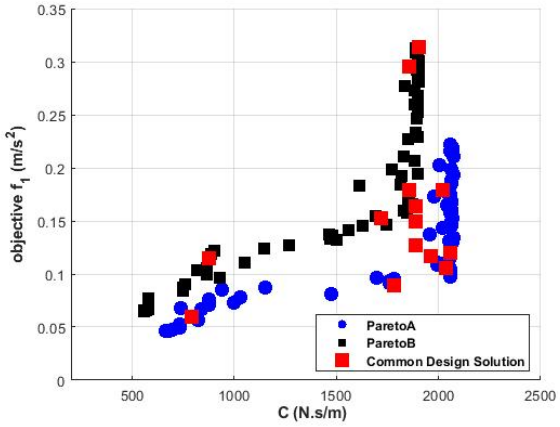

(e) C (N.s/m) .

Figure 8.15: The optimum design variables of NSS2 Model occured from Pareto front vs. the Objective f_1 (m/s^2)

comfort essentially. Regarding the initial displacement, in accordance to the NSS1 model, the range of the initial displacements is exactly the same in both the Pareto fronts.

As far as the design variables are concerned (Figure 8.15a - 8.15e), in contrast to the previous model, the majority of them has converged to different values comparing the optimum design variables of Pareto A with the ones of Pareto B. However, the comparison of the design variables of the two Pareto Fronts resulted in six common solutions with up to 7% difference in the values of the design variables, as shown in Figure 2.11. Although, the values of their objectives (f_1 and f_2) are almost the equal to three (Solution 1, 2 and 3) out of six common solutions, as outlined in Figure 2.11. Thus, only these three could be used for both road profiles providing optimal behavior. In addition, the length of the bar have converged to the lower bound, especially for Pareto B, showing the need of the mechanism to decrease the length of the bar for higher vibration isolation. Whereas, all the other design variables have converged to similar values. Finally, similarly with the other models, the convergence could be outlined through the lack of any dispersion in the figures of both the design variables and the Pareto Fronts.

8.3.4 NSS3

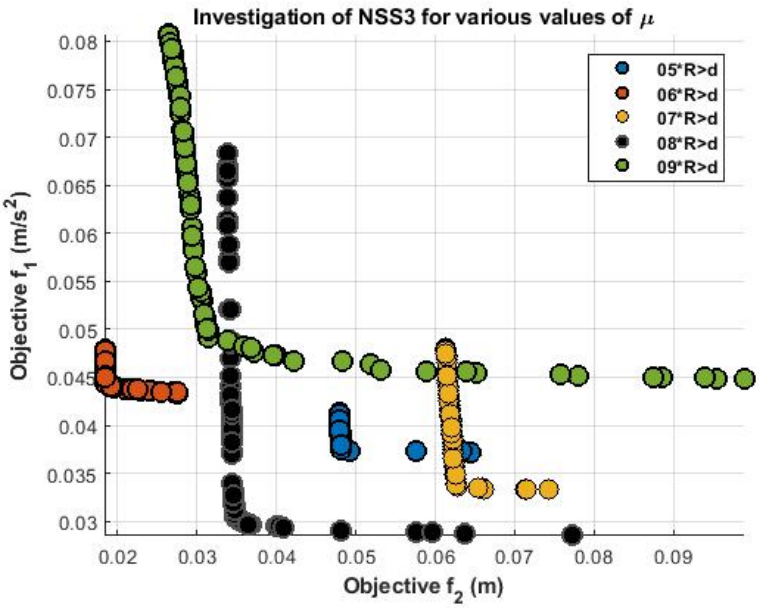

Figure 8.16: Investigation of the optimization of NSS3 model for various different values of μ of the Constraint 4 of Table 8.9

The next model studied is the NSS3 model. The importance of Constraint 4 in Table 8.9 is outlined in Section 2.2.4, affecting both the range of the seat's displacements and the ease of the construction. Thus, its impact on the Pareto A, is investigating by varying variable μ (0.9*R, 0.8*R, 0.7*R, 0.6*R and 0.5*R) in the optimization scenario and thus, Constraint 4 of Table 8.9, as shown in Figure 8.16.

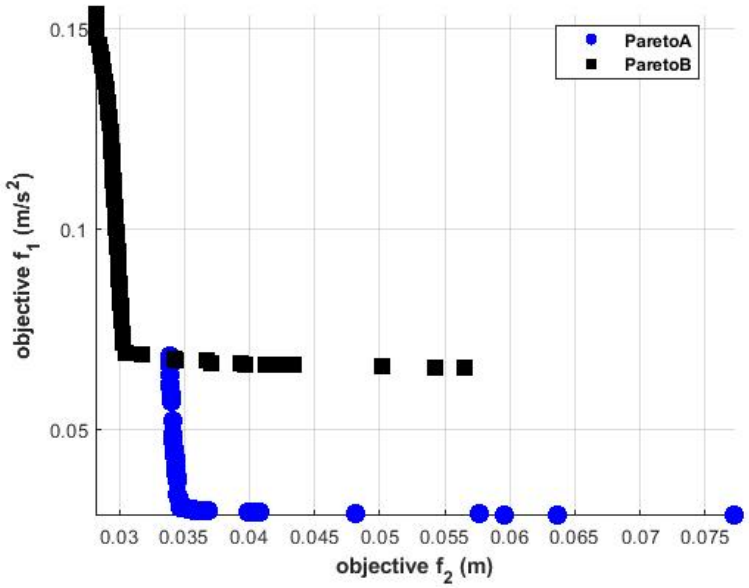

Figure 8.17: Comparison of the Pareto Fronts of NSS3 model for Road A and Road B

Based on Figure 8.16, using $\mu = 0.8$ delivers the optimum compromise of f_1 with f_2 and provides small initial deformations and great levels of comfort (low values of f_1).

Having concluded to the best value of the Constraint 4, the comparison of Pareto A and B is illustrated in Figure 8.17. Both the Pareto Fronts consist of almost two vertical lines, providing a single optimum solution each. Pareto B has converged to a solution with smaller initial deformation than Pareto A, which verifies the ability of the current mechanism to compromise better the conflict of static and dynamic comfort in difficult road conditions and particular off-road ones. Additionally, the increase comparing the two Pareto fronts in terms of objective f_1 is similar to the other models and around 40%. Furthermore, the singularity of the solutions in both fronts and their differences are depicted from their optimal design variables (Figure 8.18a-8.18e). In contrast to the "dimensioning variables" (R, d and r), which have converged to similar values, the stiffness ratio and the damping coefficients have delivered solutions with important differences. This differences doesn't allow the existence of common solutions between Pareto A and B, even by setting an acceptable difference up to 50%. Thus, the adaptability of the current seat model is in question. Finally, in accordance to the previous models, the convergence of the optimization is depicted in all the figures of this scenario, where there is no dispersion in the data of the optimum solutions.

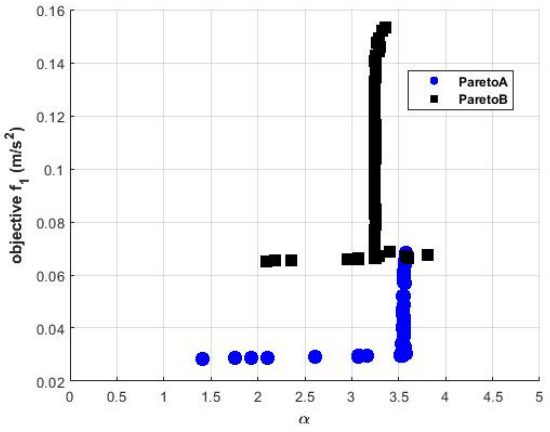

(a) α.

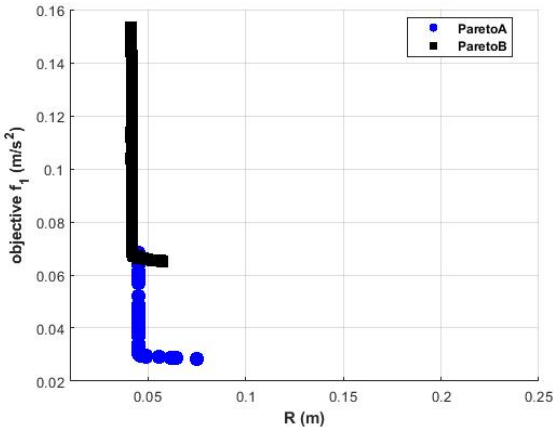

(b) R.

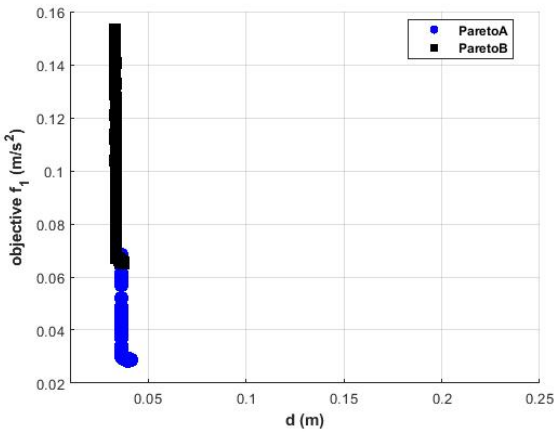

(c) d (m) .

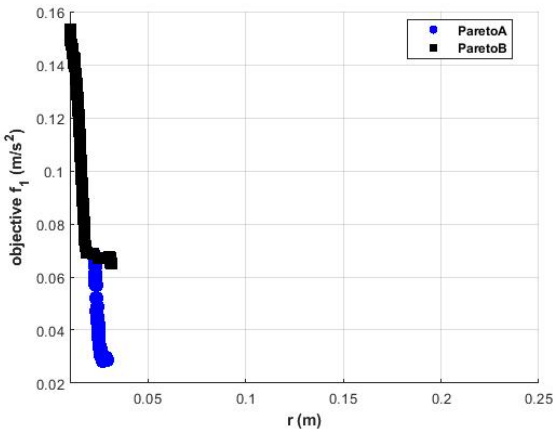

(d) r (m) .

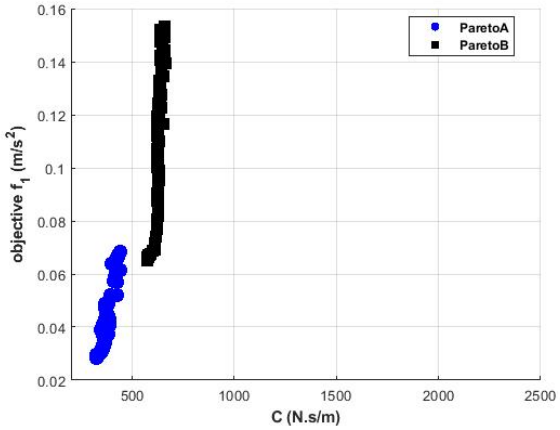

(e) C (N.s/m) .

Figure 8.18: The optimum design variables of NSS3 Model occurred from the Pareto front vs. the Objective f_1 (m/s^2)

8.3.5 NSS4

The final model studied in this work is the KDamper design, which has never been applied in a seat suspension before. Based on the comparisons of the Pareto Fronts of the two road profiles in Figure 8.14, it is shown that the optimum solutions could be divided in two Parts:

- Part NSS4_A, for initial deformations between 0.006 to 0.013 m, where there are corresponding solutions for both the Pareto fronts, and
- Part NSS4_B, for initial deformations between 0.013 to 0.024 m, where Pareto B hasn't delivered any solutions.

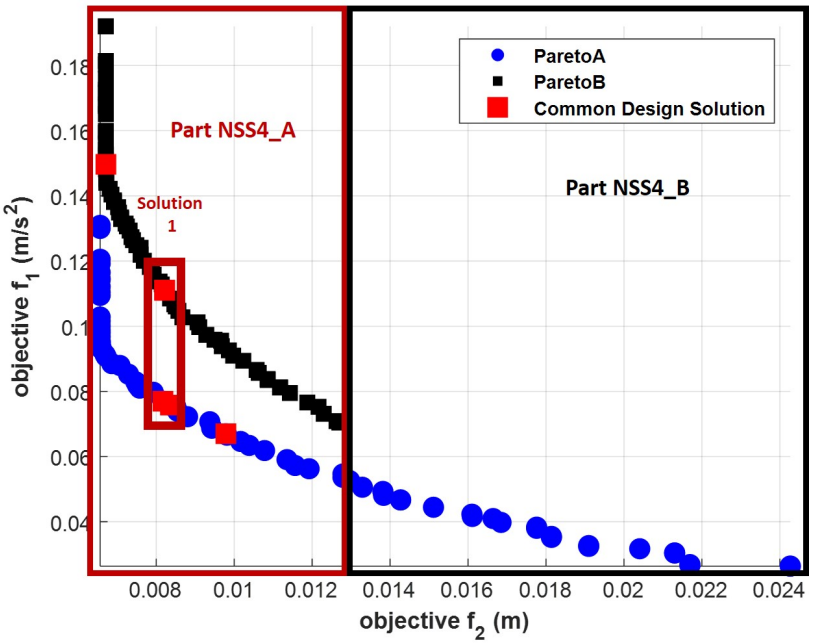

Figure 8.19: Comparison of the Pareto Fronts of NSS4 model for Road A and Road B

In contrast to the previous models, the comparison of the two Pareto Fronts illustrate non corresponding solutions in Part NSS4_B, which are solutions with larger values of f_2. For Part NSS4_*B* the increase noticed in the objective f_1 is around 20-30% comparing Pareto A with Pareto B and it is the smallest one between all the NSS models studied. Additionally, the current model delivered not only the smallest values of f_1 among all the models but also the smallest initial deformations. This remark highlights the main advantage of the current vibration isolator, which is similar stiffness with the conventional systems but greater isolation.

As far as the range of the initial displacements (f_2) is concerned, they vary between the two Pareto Fronts, although this difference is not significant considering that both ranges are really small. Additionally, the largest initial deformation delivered for Part B is smaller than the one of Pareto A,

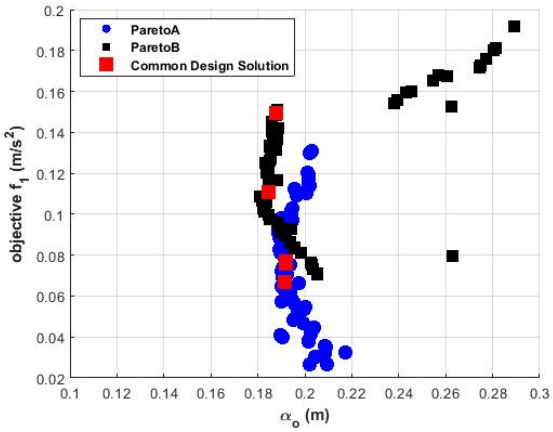

(a) α.

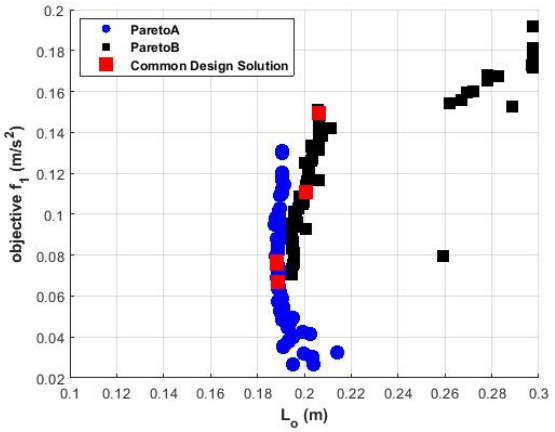

(b) L_o.

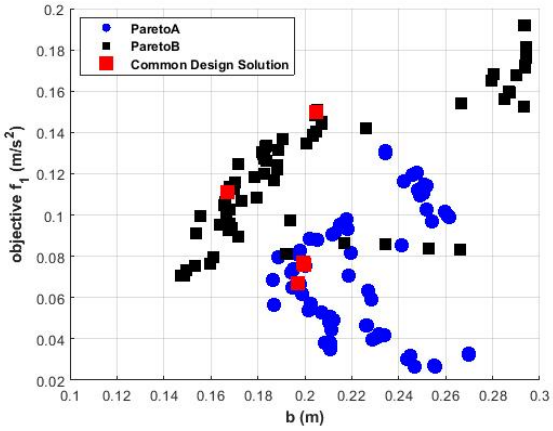

(c) b (m) .

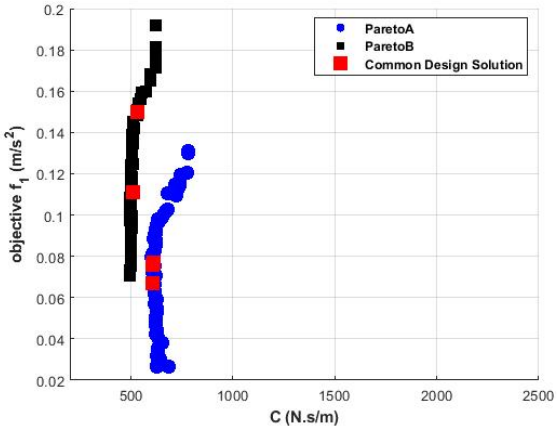

(d) α_o (m) .

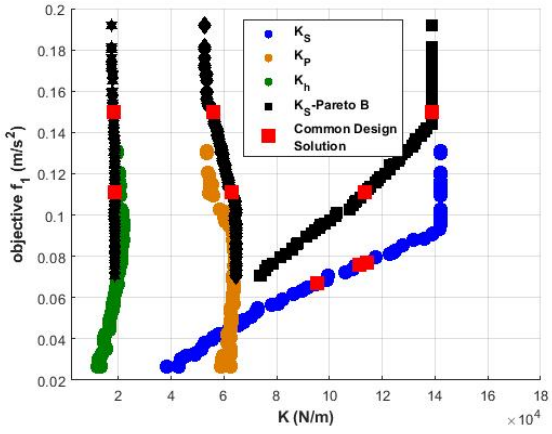

(e) C (N.s/m) .

Figure 8.20: The optimum design variables of NSS4 Model occurred from the Pareto front vs. the Objective f_1 (m/s^2)

implying that NSS4 suspension mechanism provides good static comfort even for rougher road profiles. Furthermore, while the road profile becomes more intense, the optimization algorithm converges for α_o, b and C to slightly larger values than the solutions of Pareto A, as shown in Figure 8.20a- 8.20e. On contrary, Figure 8.20e illustrates that the spring stifnesses have converged to exactly the same area of optimum solutions. Due to the above remark, in order to find common solutions between the optimum solutions of Pareto A and B, the acceptable difference was set up to 15%, delivering three common ones. However, only the one of them illustrates also same values in f_1 and f_2. Finally, once more, the convergence is verified with the figures of the design variables and the Pareto Fronts.

8.4 Dynamic Analysis

In this Section, after presenting the original Pareto Fronts occurred for all the seat models, a modification is applied in the optimum solutions of the original Pareto Front and the comparison of all the modified is presented in Figure 8.22. Then, three types of analysis are used for comparing the models and extracting conclusions for the levels of the isolation of each model, as well as for the adaptability and the universality of the models in different excitations corresponding to different road classes and in different seated passengers.

1. **Analysis 1:** All the optimum solutions of the Pareto Fronts are applied to the models. Afterwards, they are simulated for another two excitations, which correspond to the vibrations induced to the sprung mass of a passenger vehicle while it drives over two additional road profiles of different classes (B and C). The two "pseudo" Pareto Fronts for the additional excitations are compared to the initial one.

2. **Analysis 2:** All the optimum solutions of the Pareto Fronts are applied to the models. Then, the system's mass (m = passenger + seat = 95 kg) is varied by adding and removing 20 kg from the initial mass, i.e. the passenger of the seat is changed. The extra two "pseudo" Pareto Fronts, occurred from the simulations of the seat models with the other two masses, are compared to the initial one.

3. **Analysis 3:** Based on the Pareto theory, the edges of the occurred Front, represent the optimum solutions of the two objectives in case of a single objective optimization problem, whereas the mid solution of the Pareto front corresponds to the best compromise of the two objectives, as shown in Figure 8.21. Thus, three solutions (Edge 1, Edge 2 and Mid) based on Figure 8.21, are selected for each model. After adding the passenger model, as described in Chapter 2.3, to the seat models, and converting mass m to only the seat mass (=13.6 kg), instead of both the seat and the passenger, the optimum solutions are applied in the models. The seat to head transmissibilities of these designs, as described in Equation 2.86 for i=head, for each solution (Edge 1, Edge 2 and Mid) are presented and compared between all the models.

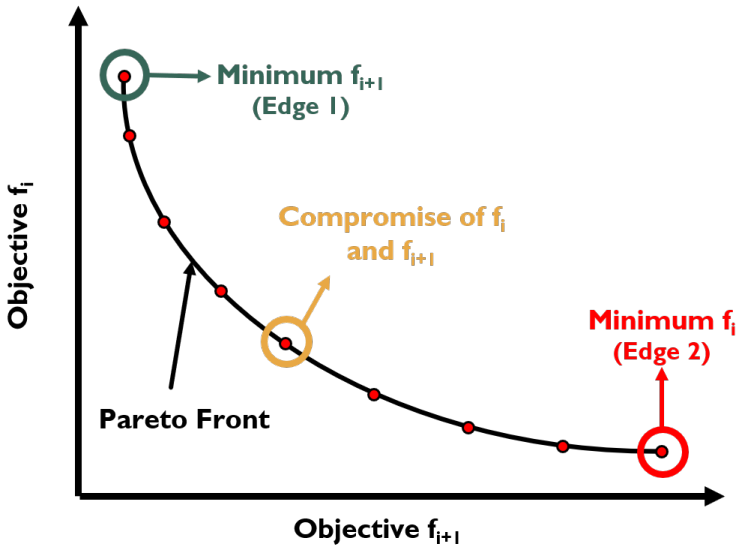

Figure 8.21: Theory of the Pareto Front based on which the three solutions of **Tool 3** are selected.

8.4.1 Comparison of Pareto Fronts

The original Pareto Fronts (Pareto A of previous chapter) are illustrated in Figure 8.22a. As shown in Figure 8.22a, NSS1, NSS2 and NSS3 delivered solutions with equal Objective f_1 and varying f_2. Thus, considering that the optimization is implemented for the minimization of these objectives (f_1 and f_2), all these solutions are excluded except from the solution with the minimum f_2 among them. Similarly, this behavior is noticed in NSS4 model, but with solutions with the equal f_2 and decreasing f_1. Hence, they are also excluded apart from the solution with the minimum f_1. After these modifications, the comparison of the final Pareto Fronts is illustrated in Figure 8.22b.

8.4.2 Different Road Profiles

All the optimum solutions of the Pareto Fronts (Pareto A of previous chapter) are applied to the seat models described in Sections 2.2.1 - 2.2.5. Afterwards, they are simulated for another two excitations, which correspond to the vibrations induced to the sprung mass of a vehicle while it drives overtwo additional road profiles of classes B and C. The two "pseudo" Pareto Fronts for the additional excitations are compared with the initial one obtained from the optimization of the model. Thus, the comparison of this analysis is presented in Figure 8.23. In addition to the comparison of the Pareto fronts for the three road excitations, the levels of ISO2631 regarding ride comfort are presented in all the subfigures of Figure 8.23, when the objective f_1 is close to marking the seat uncomfortable. Furthermore, the percentage of the change in Objective f_1 (m/s^2) by roughening the road profile from A to B and A to C, is presented in Table 8.12 for the optimum solutions of Edges 1 and 2 of each seat model.

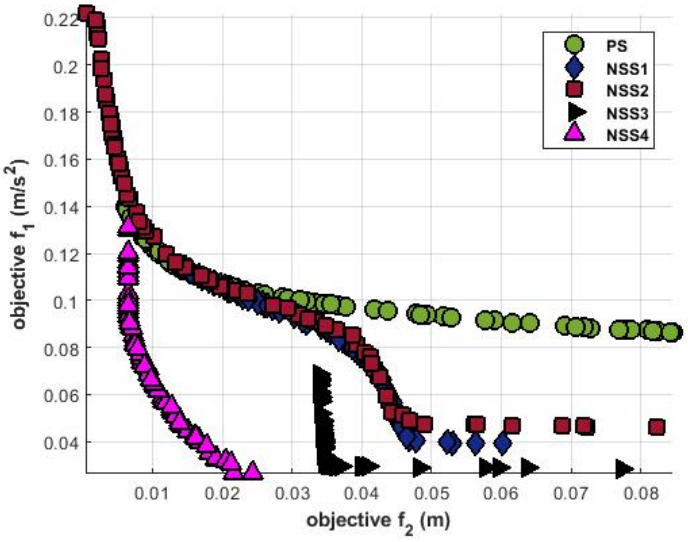

(a) The original.

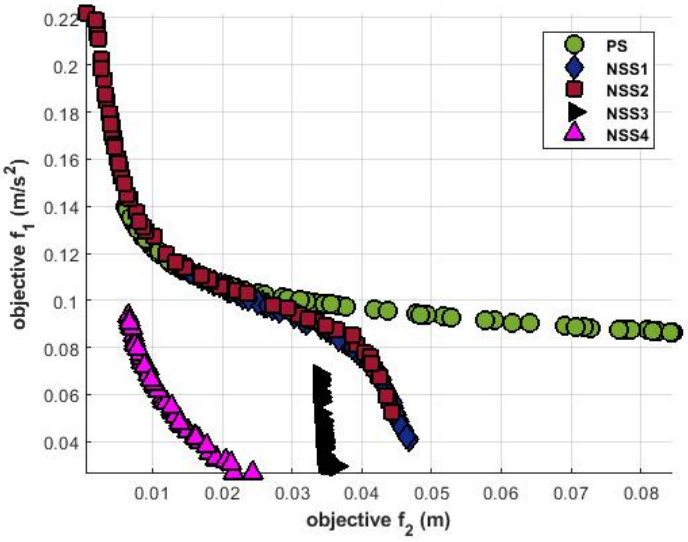

(b) The modified

Figure 8.22: The comparison of the optimal solutions occurred from the Pareto fronts (PS, NSS1, NSS2, NSS3 and NSS4).

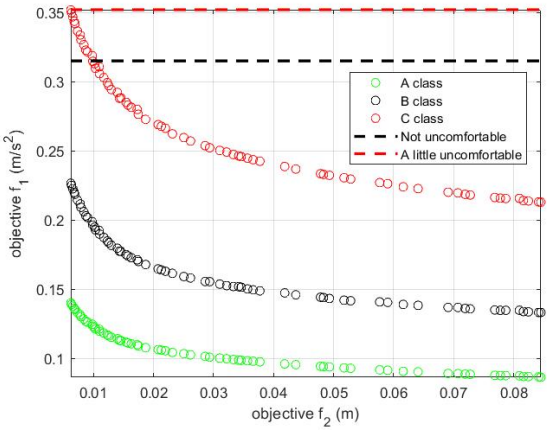

(a) PS.

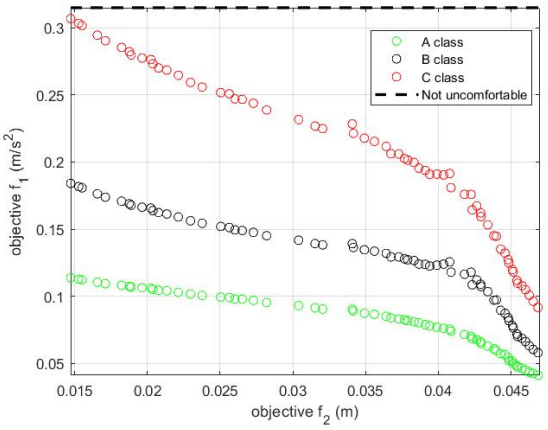

(b) NSS1

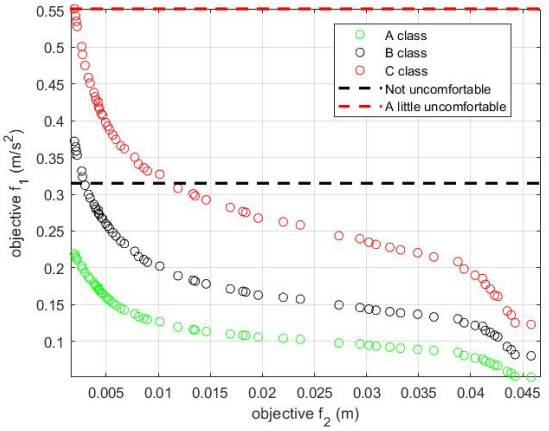

(c) NSS2

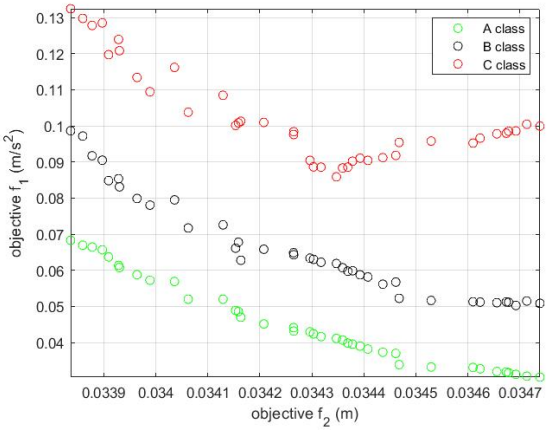

(d) NSS3

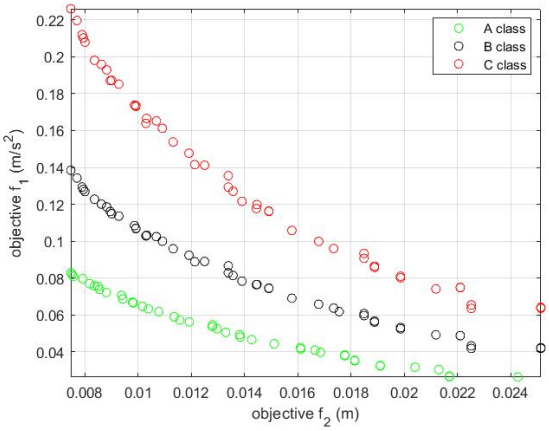

(e) NSS4

Figure 8.23: The comparison of all the optimum solutions of the Pareto Front simulated for another two excitations corresponding to the vibrations induced to the vehicle while driving over road classes B and C.

Model	Values		Percentage compared with Road A			
	Road A (m/s^2)		**Road B** (%)		**Road C** (%)	
	Edge 1	**Edge 2**	**Edge 1**	**Edge 2**	**Edge 1**	**Edge 2**
PS	0.14	0.09	62	54	152	147
NSS1	0.11	0.04	62	41	170	123
NSS2	0.22	0.05	70	56	152	139
NSS3	0.07	0.03	47	67	94	196
NSS4	0.08	0.03	67	60	173	142

Table 8.12: The effect of driving under different road profile on the objective f_1 (m/s^2) of the Edges 1 and 2 in comparison with the main case of Road A.

As it was expected, when the road roughens from A→B→C, the levels of comfort decrease , making the ride uncomfortable. However, in our work, the interest is turned on the level of change and how uncomfortable the seat design has became. As far as the conventional suspension (PS) is concerned, the results are shown in the Figure 8.23a. The increase noticed from A→B and B→C is not the same, as it could be seen from Figure 8.23a and Table 8.12. The change in Objective f_1,while the road profile is roughen from A to B, is around 60%, as it could be seen from the change in the optimum solutions of Edge 1 and Edge 2 of Road B. On contrary, the ride comfort is worsen up to 150% when the road class changes from A to C, which is more than the double of the percentage from A→B (60%), showing the lack of uniformity. Additionally, the changes of objective f_1 noticed in Table 8.12 for both cases (A→B and A→C), indicate a uniform change for all the optimum solutions of the Pareto Front. However, for some optimum solutions, when the road roughens from A to C, the ride becomes a little uncomfortable, based on ISO2631 [96].

The above remark regarding the lack of uniformity when the road profiles roughens could be identified also in the other models. NSS1, NSS2 and NSS3 have increased objective f_1 significantly less in Edge 2 compared to Edge 1. This point presents the better isolation of the above suspension mechanisms when the f_2 is larger. Regarding the smaller initial deflections, the NSS2 model presents a little uncomfortable optimum solutions not only for Road C but also for Road B. Last but not least, the suspension mechanism with the greater isolations in all the road profiles, are the NSS3 and the NSS4 models. Despite the fact that the NSS3 in the current analysis shows to be able to manage all the road profiles, the suspension design demands an initial deflections around 3.5 cm based on Figure 8.23d. Similarly, vibration isolation could be noticed for NSS1 and NSS2 with an initial deformation around 4.0-4.5 cm. On contrary, the above isolation, and greater, is achieved from NSS4 model with an initial deformation around 1.2 - 2.4 cm, as shown in Figure 8.23e.

8.4.3 Different Masses

In the next type of analysis, all the optimum solutions of the Pareto Fronts are applied to the models. Then, the system's mass (m = passenger + seat = 95kg) is changed by adding and removing 20 kg from the initial mass, i.e. changing the passenger of the vehicle. The extra two "pseudo" Pareto Fronts, occurred from the simulations of the seat models described in Section 2.2.1 - 2.2.5 with the heavier and the lighter passenger, are compared to the initial one. In order to conduct this analysis, the K_v is modified for each passenger in order to keep the initial displacement of the systems constant and equal to the one of the optimum solution, as occurred with the initial mass (95 kg). This modification is implemented to NSS1, NSS2 and NSS3 models, which in order to function properly demand a constant initial deformation and a predefined load. This modification considers the designs of negative stiffness structures described in the literature, where seats containing the above negative structures use mechanisms offering this function. Also, this change is not applied in PS and NSS4 model, because there is no malfunction issues with the change of the initial deformation of the system. Hence, the initial deformation is able to change without costing ride comfort or safety in the machine handling.

More specifically, the less sensitive model with respect to the passenger's mass is illustrated in the case of the conventional suspension (PS), as shown in Figure 8.24a. Based on Figure 8.24a, the change of f_1, as evaluated in the Edges 1 and 2 compared to the initial Pareto front obtained from the optimization (m = 95 kg) (Table 8.13), negligible. However, there is an significant change in the initial deformations of the optimum solution, as displayed in Figure 8.24a, which is a disadvantage regardless the lack of sensitivity in Objective f_1. Similar behavior with PS model, is captured in NSS1 and NSS2 models. Although, as mentioned previously, the negative structures of these mechanisms start to contribute more in the vibration isolation above a value of initial deformation (f_2) around 0.03 m and 0.04 m for NSS1 and NSS2 respectively. Above these values of f_2, the change in the passenger's mass affects the ride comfort essentially, as shown in Table 8.13. More particularly, the variation of Objective f_1 in Edge 2, when the passenger's mass is increased, is around 74 and 163 % for NSS1 and NSS2 respectively, while when the mass is decreased is around 140 % for both. Although, in contrast to Edge 2, Edge 1 presents an negligible change for both the cases ($\pm$10%) .

The NSS3 suspension system is the most sensitive with respect the passenger's mass, because it illustrates variations up to 211 and 377 % for Edge 2, as presented in Table 8.13. There (Edge 2) the optimum solution of this model lies. The above remark is also outlined in Figure 8.24d where the "pseudo" Pareto, for both deccreased and increased passenger's mass, have changed their inclination compared to the initial Pareto, displaying significant variations in the vibration levels. On the other hand, the suspension system with the best adaptability is the NSS4, where the variations evaluated in Objective f_1 are up to 20 %. These variations occur in Edge 2 of the decreased mass, where the levels of f_1 are already low.

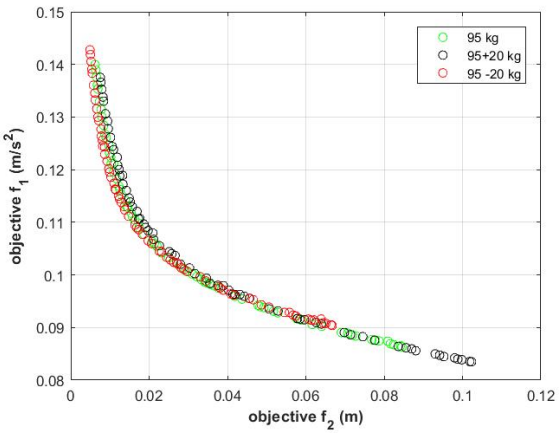

(a) PS.

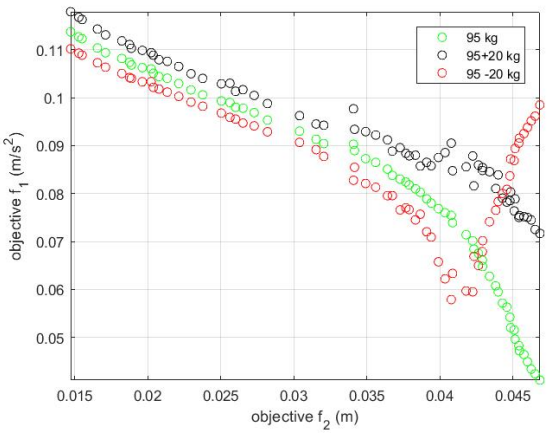

(b) NSS1

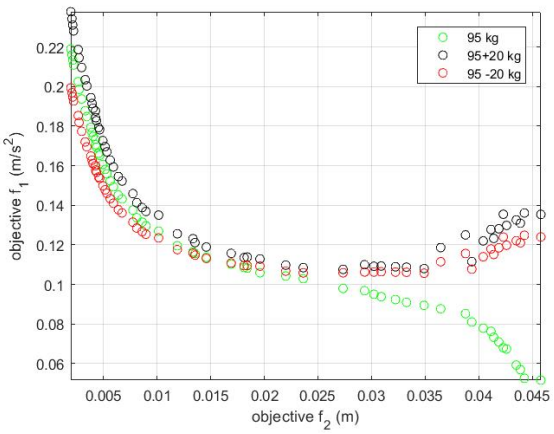

(c) NSS2

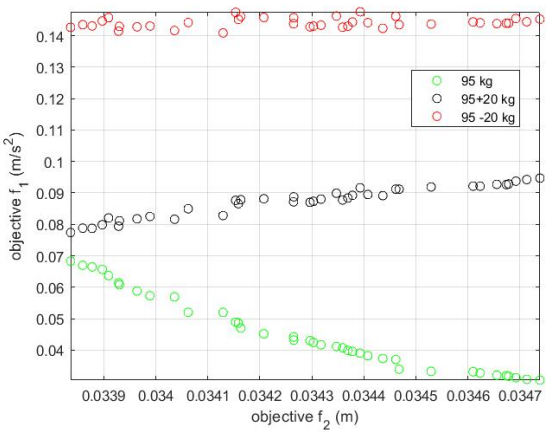

(d) NSS3

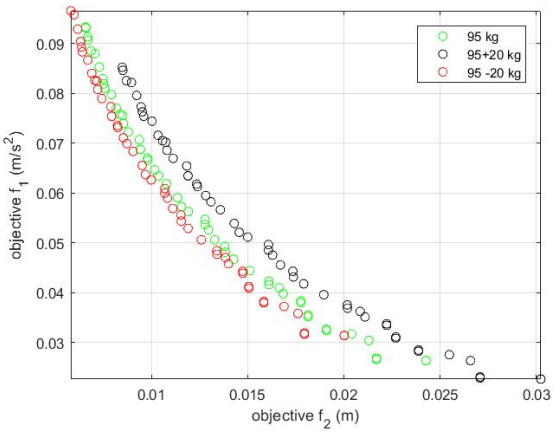

(e) NSS4

Figure 8.24: The comparison of all the optimum solutions of the Pareto Front simulated for another two masses corresponding to different passengers.

Model	Values		Percentage compared with Road A			
	Mass m (kg)		Increase (%)		Decrease (%)	
	Edge 1	Edge 2	Edge 1	Edge 2	Edge 1	Edge 2
PS	0.14	0.09	-2	-3	2	5
NSS1	0.11	0.04	4	74	-3	140
NSS2	0.22	0.05	9	163	-9	140
NSS3	0.07	0.03	13	211	107	377
NSS4	0.08	0.03	-9	8	3	19

Table 8.13: The effect of changing the passenger on the objective f_1 (m/s^2) of the Edges 1 and 2 in comparison with the main case of a passenger of mass (m).

8.4.4 Seat's Transmissibility

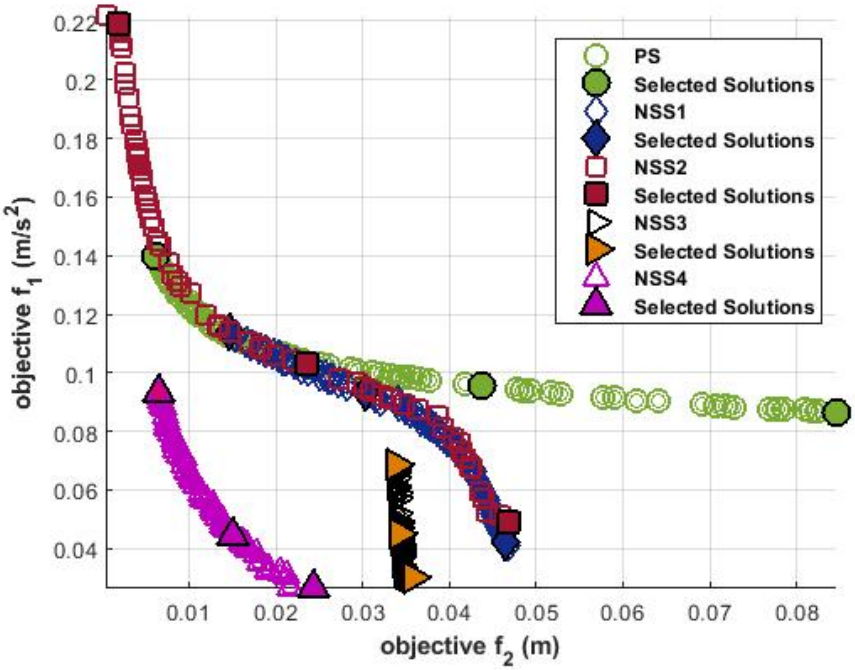

Figure 8.25: The optimal solutions of the Pareto Fronts (PS, NSS1, NSS2, NSS3 and NSS4) selected for the evaluation of the transmissibilities T = $\ddot{z}_{w_{head}}/\ddot{z}_s$ for **Analysis 3**

Based on the Pareto theory, the edges of the front represent the optimum solutions of the two objectives in case of single objective optimization problem with these as objectives. The mid solution of the Pareto front corresponds to the one of the best compromise of the two objectives, as shown in Figure 8.21. Thus, these solutions (Edge 1, Edge 2 and Mid), as pointed out in Figure 8.21, are identified

for each model based on the above and are displayed in Figure 8.25. After adding the passenger of Chapter 2.3 to the seat models, the optimum solutions are applied in the seat suspensions. Through the simulations, the seat to head transmissibilities, as presented in Equation 2.86, are evaluated for each solution (Edge 1, Edge 2 and Mid) and are presented in Figure 8.26.

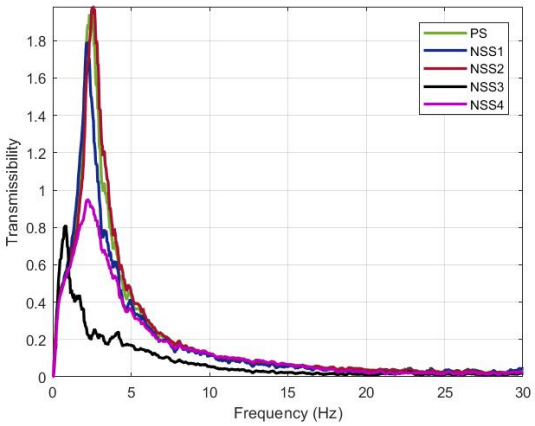

(a) Edge 1.

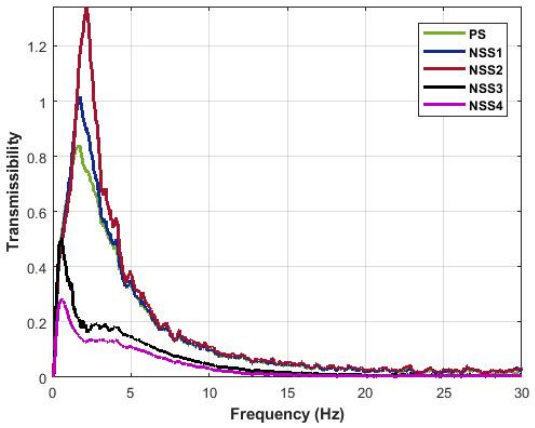

(b) Mid

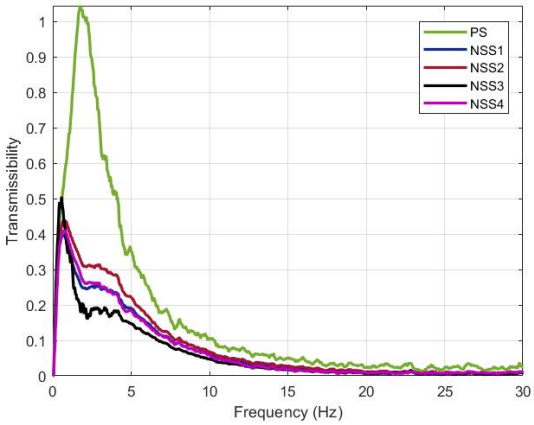

(c) Edge 2

Figure 8.26: The comparison of the transmissibilities from seat to head (T = $\ddot{z}_{w_{head}}/\ddot{z}_s$) for the three optimum solutions of the Pareto front occurred for each vehicle model (PS, NSS1, NSS2, NSS3 and NSS4).

As shown in Figure 8.26a, despite the fact that PS, NSS1 and NSS2 and NSS4 illustrate the same natural frequency, NSS4 model manages to isolate the vibrations to a greater extend. Also, NSS4 and NSS4 operate as a soft suspension system in contrast to the rest which function as a foam sprung seat. However, NSS3 is not comparable to the other models, because it displays smaller resonance frequency and more damping, but with much higher value in the initial deformation (f_2), as shown in Figure 8.25.

In Figure 8.26b, where the compromise of the dynamic and static factors lies, the isolation of NSS4 and NSS3 is greater than all the other models. Apart from the smaller peaks illustrated in NSS4 and NSS3, the resonance frequency is moved around 0.56 Hz, as shown in Figure 8.26b. The value of their resonance frequency is almost outside the area of interest regarding ride comfort, i.e. 0.5-8 Hz, whereas the other models display their resonance frequency around 1.8 Hz. Similar behavior is displayed in Figure 8.26c, where in addition to NSS3 and NSS4 the other negative structures present the same resonance frequency, on contrary with the PS model which still is around 1.8 Hz. The reasoning of this similarity is the fact that the Edge 2 solutions of the Pareto Fronts of NSS1, NSS2, NSS3 and NSS4, selected in Figure 8.25, display the same levels of ride comfort (f_1) whereas the initial deformation varies from 0.046 (NSS1 and NSS2), 0.035 (NSS3) and 0.024 m (NSS4).

8.5 Conclusions

8.5.1 Optimal Design

To sum up, in this chapter five different isolators with negative stiffness elements are implemented in vehicle seats. One of the implemented isolators is the KDamper design, which has never been tested in a seat but has proven to be efficient in other applications. All the isolators are optimized with excitations corresponding to the response of the sprung mass of a vehicle, which drives over a road profile of Class A and B. The optimization problem is a multi-objective one, aiming to improve the ride comfort of the passengers and the safety of the machine handling. The purposes of the optimization applied are:

- To obtain the optimal designs (Figure 8.11, 8.13, 8.15, 8.18 and 8.20) of all the studied seat suspensions for a structure intended to be installed in a passenger vehicle and investigate the applicability and universality of each system.
- To compare the optimum solutions occurred from the multi-objective optimization and the Pareto method, both between different road profiles for each model (Figure 8.10, 8.12, 8.14, 8.17 and 8.19) but also between the all the seat models for each road profile (Figure 8.27a and 8.27b).
- To check the efficiency of the KDamper design through the above comparisons with the other established isolators in the vehicle's seat suspension design.

More specifically, as far as the suspension systems are concerned, the conventional system (PS) functions similar with NSS1 and NSS2 for values of f_2 up to 0.02 m, whereas, for larger deformations, the function of the negative system contributes more in the overall performance of the isolator. Hence, the optimization of NSS models delivers solutions with much better ride comfort than PS Model, when

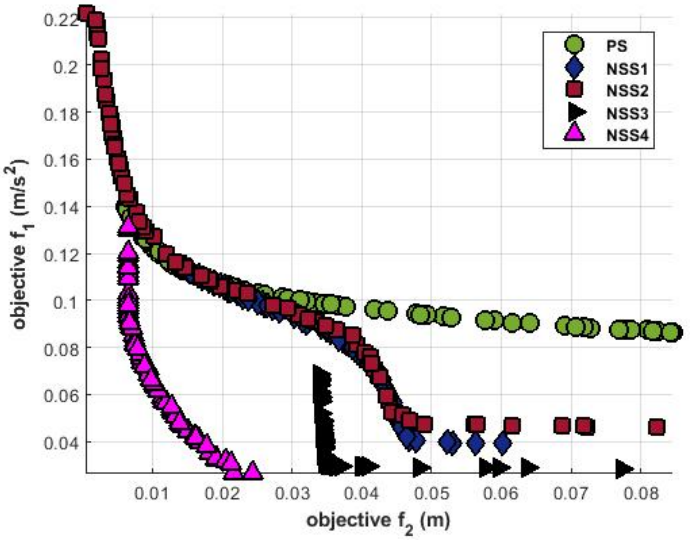

(a) .

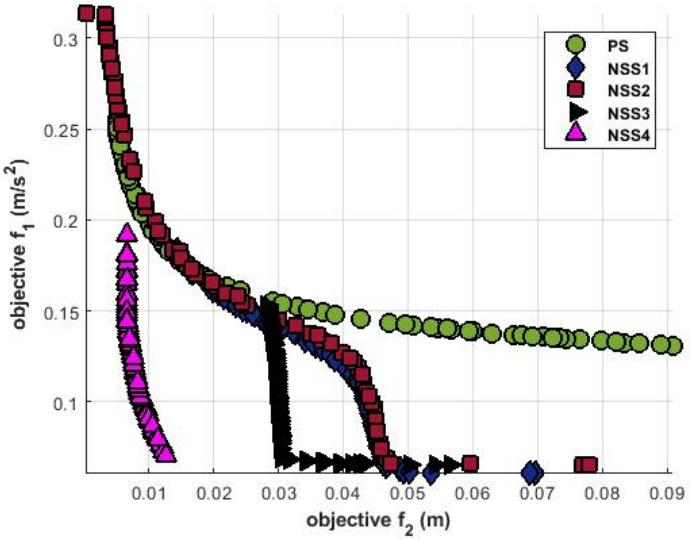

(b) .

Figure 8.27: Comparison of the Pareto Fronts occurred for all the seat models (PS, NSS1, NSS2, NSS3 and NSS4) having been optimized for (a) Road Profile of Class A and (b) Road Profile of Class B

f_2 is larger than 0.02 m. This remark points out the main disadvantage of these structures, which is their need for space and larger initial deformations, as noticed in both the road profiles (Figure 8.27a and 8.27b) of all the cases studied. Furthermore, the fact that the NSS3 model almost delivered a single optimum solution in both the optimization cases (road Class A and B), illustrates its lack of alternatives. However, this solution is the one together with NSS4 with the best ride comfort between all the models in both the road profiles.

As far as the KDamper design (NSS4) is concerned, it not only delivers one of the optimum solutions with the greatest ride comfort (small f_1) in both Pareto A and B, but also with the smallest initial displacement (f_2) among all the Pareto alternatives of all the models (PS, NSS1, NSS2, NSS3 and NSS4). Additionally, the optimization of NSS4 model delivered solutions with worse ride comfort than NSS3 model, but only when it minimized the objective f_1 80% more (0.006 m compared to 0.035 m for NSS3 model). This remark is outlined also by the fact that the best solution of NSS4 Model in terms of ride comfort (minimum f_1), has the same f_1 with NSS3, but with an initial deformation around 30% smaller. This is the main advantage of the KDamper design, that it provides much better isolation and damping without reducing the overall stiffness of the system. Furthermore, the solution of NSS4 with the minimum initial deflection (f_2), functions like PS model in both Pareto A and B. Hence, the area with the smallest initial deformations, around 0.005 m, could be avoided as a possible design solution due to the fact that it could be obtained by a PS model also. Moreover, the common solutions of Pareto A and Pareto B, with similar design variables, showed the adaptability and universality of NSS4 model to different road profiles, whilst NSS3 model wasn't able to deliver any common solutions between Pareto A and Pareto B.

8.5.2 Dynamic Analysis

To sum up, in this chapter an extended comparison of five isolators intended to be installed in a passenger vehicle, is implemented. The suspension mechanisms are optimized for an excitation corresponding to the vibrations induced to a vehicle while driving in a road profile of Class A. Specific constraints and bounds to the design variables are applied to the optimization problem aiming to not only a compact structure but also a comfortable one. The results of the optimization procedure are used in order to conduct further dynamic analysis by investigating the sensitivity of these suspension systems to different seated passengers and to excitations corresponding to rougher road profiles.

In conclusion, the NSS4 model has proven to be superior than all the other mechanisms not only in terms of the objectives of the optimum solutions but also in terms of its adaptability in different road profiles and its sensitivity in different passenger's masses. The simulation with different excitations and passenger's mass displayed the disadvantages of NSS3, which illustrated the greatest variations. Also, based on the analysis of this work, it is obvious that all the suspension systems studied are able to provide similar vibration isolation with their initial deformation varying, while NSS4 illustrates the smallest one among the models and is around 0.024 m. Last but not least, NSS4 and NSS3 are able to decrease their resonance frequency really low (around 0.56 Hz) and almost outside the area of interest for ride comfort (0.5-8 Hz).

CHAPTER 9

Conclusions

The current thesis focuses on the optimization of both primary and secondary vehicle suspension systems . A primary suspension system cannot eliminate the compromise between the parts of the most prominent conflict in automotive industry, i.e. the passenger's ride comfort and the vehicle's stability. However, they are able to combine the above-mentioned parts optimally. Considering the importance of a good suspension design, in this thesis, the optimization procedure of a primary suspension system is studied extensively. Firstly, the most common vehicle models are compared and investigated in order to conclude in terms of their suitability. The results illustrate the ability of lower accuracy models to cope well and that they should be preferred most of the times. Also, anti-roll bars and tire dampers should be neglected when the ride comfort is investigated, whereas they have to be included when simulations regarding road holding are conducted.

Before the study of the optimization procedure, the research for a high quality suspension system focused on semi-active suspensions and resulted in the development of a novel distribution-based control strategy for skyhook control algorithms. The CDF controller is applied to two different SH control algorithms and is tested by using a quarter car model excited by four different road excitation. The results illustrate an increase of up to 13 % in the ride comfort of the passengers and increase of 6 % in the road holding of the vehicle compared to the traditional algorithms. Both of these are achieved by minimizing the number of switches of the damping ratio up to 80%.

Afterwards, an assessment of the optimization procedure of passive suspensions in SOO and pseudo-MOO problems is conducted with respect to the efficiency of both the objective functions and the optimization algorithms. The results outline the importance of tire deflection and highlight the fact

that it should be preferred as main target in the SOO problems of suspension systems instead of the vehicle body acceleration, which is the most common in the literature. Moreover, the suggestion of using a dynamic penalty function, which includes the additional objectives weighted one order of magnitude lower,proved successful managing to converge to more optimal solutions.

Later, the thesis proved that the inconsiderate selection of objective functions noticed in the literature and the use of more than one objective for the same performance aspect, doesn't help the Pareto Method to converge to more "optimal" solutions. As a solution, an approach, which handles the objectives by dividing them in main and supplementary, is described and aims to decreasing the demanded computational time and allowing the MOGAs to be attractive again in the design of suspension systems. At the same time, this approach enables the suspension designers to consider more objectives in the optimization procedure. Applying this approach, the merits are exploited and the computational time required for convergence is essentially increased ($\pm$ 37 %), compared to a case study where many objective functions are introduced to MOGA.

Meanwhile, the conclusions from the assessment of the optimization procedure and the approach presented in this thesis are applied to various semi-active suspensions, which also adopt the novel control strategy. In this thesis, the supplementary objectives selected for the optimization of semi-active suspensions is the dissipated energy and the number of switches in the damper's state. The results proved the applicability and the efficiency of the approach for handling the objective function in semi-active suspensions is proven. In addition, the application of CDF controller is validated with a higher accuracy model and manages to decrease the number of the switches in the damper's states up to 50 % compared to the traditional algorithms.

Finally, considering that the optimum design of a primary suspension system is not the only prerequisite for ride comfort, this thesis investigates the design of seat suspension systems. More specifically, a novel isolator with embedded negative stiffness elements (KDamper), which has proven efficient in other applications, is applied in a seat suspension and is benchmarked against the most common isolators in seat design, conducting an extensive dynamic analysis. This thesis proves the adaptability and universality of KDamper under different excitations corresponding to different road classes and for different seated passengers. Its the resonance frequency is decreased around 0.56 Hz, almost outside the are of interest in ride comfort. At the same time, it provides the most compact and comfortable optimum design solutions among all the other models.

Nomenclature

Vehicle Simulation Models

Parameter	Unit	Description	Subscript	Description
z	$[m]$	vertical motion coordinate of mass (m_s)	s	sprung mass
φ	$[rad]$	roll motion coordinate of mass (m_s)	u	unsprung mass
θ	$[rad]$	pitch motion coordinate of mass (m_s)	K	spring
z_{road}	$[m]$	road excitation	C	damper
F	$[N]$	forces applied to the subsystems	T	tire
M	$[Nm]$	moments applied to the subsystems	l	linear
m	$[kg]$	mass	nl	nonlinear
k	$[N/m]$	spring stiffness	AR	antiroll bar
c	$[Ns/m]$	damping coefficient	F	front axle
I_x	$[kgm^2]$	longitudinal moment of inertia	R	rear axle
I_y	$[kgm^2]$	lateral moment of inertia	1	right wheel
b	$[m]$	distance between CG and each side	2	left wheel
a	$[m]$	distance between CG and each axle	x	x-axis
w	$[m]$	track width	y	y-axis
ST	$[m]$	suspension travel		
$\dot{ST}$	$[m/s]$	suspension stroke velocity		
TD	$[m]$	tire deflection		

Seat Simulation Models		
Parameter	**Unit**	**Description**
x	$[m]$	displacement of mass (m) from the desired static E.P.
$\dot{x}$	$[m/s]$	velocity of mass (m)
$\ddot{x}$	$[m/s^2]$	acceleration of mass (m)
m_{se}	$[kg]$	total mass of seat (13.6 kg) and passenger (81.4 kg)
K_h	$[N/m]$	horizontal spring stiffness
K_v	$[N/m]$	vertical spring stiffness
C_v	$[Ns/m]$	damping coefficient
X_{ST}	$[m]$	initial deformation of vertical spring
L_o	$[m]$	initial length of underformed horizontal spring
a_o	$[m]$	distance from the wall
α	-	spring stiffness ratio (K_h/K_v)
Additional Nomenclature for NSS1		
θ_o	$[deg]$	initial angle of horizontal spring
Additional Nomenclature for NSS2		
b	$[m]$	bar length
Additional Nomenclature for NSS3		
R	$[m]$	cam radius
r	$[m]$	roller radius
d	$[m]$	distance from cam center
u_2	$[m]$	precompression of horizontal spring (=0.01 m)
Additional Nomenclature for NSS4		
K_S	$[N/m]$	vertical spring's stiffness
b	$[m]$	bar length
u_o	$[m]$	distance from horizontal level
m_d	$[kg]$	inner mass (=1 kg)

Performance Metrics		
Parameter	**Unit**	**Description**
t_r	$[s]$	rise time
t_p	$[s]$	peal time
t_s	$[s]$	settling time
SST	$[-]$	steady state value
M_p	$[-]$	peak value
M_{OV}	$[-]$	overshoot value
RC_i	$[m/s^2]$	weighted RMS acceleration of the ith system
CF_i	$[m/s^2]$	crest factor of the acceleration response of the ith system

Performance Metrics		
Parameter	**Unit**	**Description**
VDV_i	$[m/s^2]$	vibration dose value of the acceleration response of the ith system
$MTVV_i$	$[m/s^2]$	maximum transient vibration value
TR	$[-]$	transmissibility of an input acceleration signal to an output acceleration signal
$STHT$	$[-]$	transmissibility seat-to-head for i=head in TR
VST	$[m]$	variance of the suspension travel of the ith suspension
MST	$[m]$	maximum value of the suspension travel of the ith suspension
VTD	$[m]$	variance of the tire deflection of the ith tire
MTD	$[m]$	maximum value of the tire deflection of the ith tire
PTC	$[rad]$	pitch angle of the vehicle body
DE	$[kW]$	mean dissipated power of the of damper of the ith suspension
SW	$[\#]$	the switches between the states of a semi-active damper

Bibliography

[1] Mansfield NJ. Human Response to Vibration. ; 2005.

[2] Rill G. Vehicle modeling by subsystems. Journal of the Brazilian Society of Mechanical Sciences and Engineering. 2006 dec;28(4):430–442. Available from: http://www.scielo.br/scielo.php?script=sci{_}arttext{&}pid=S1678-58782006000400007{&}lng=en{&}nrm=iso{&}tlng=en.

[3] Savaresi SM, Poussot-Vassal C, Spelta C, et al. Semi-Active Suspension Control Design for Vehicles. ; 2010.

[4] Griffin MJ, Erdreich J. Handbook of Human Vibration. Vol. 90. ; 1991.

[5] Carrella A, Brennan MJ, Waters TP. Static analysis of a passive vibration isolator with quasi-zero-stiffness characteristic. Journal of Sound and Vibration. 2007;301(3-5):678–689.

[6] Carrella A, Brennan MJ, Waters TP, et al. On the design of a high-static-low-dynamic stiffness isolator using linear mechanical springs and magnets. Journal of Sound and Vibration. 2008; 315:712–720. Available from: www.elsevier.com/locate/jsvi.

[7] Carrella A, Brennan MJ, Waters TP, et al. Force and displacement transmissibility of a nonlinear isolator with high-static-low-dynamic-stiffness. International Journal of Mechanical Sciences. 2012;55(1):22–29. Available from: http://dx.doi.org/10.1016/j.ijmecsci.2011.11.012.

[8] Le TD, Kyoung Kwan A. Active pneumatic vibration isolation system using negative stiffness structures for a vehicle seat. Journal of Sound and Vibration. 2014 feb; 333(5):1245–1268. Available from: https://www.sciencedirect.com/science/article/pii/S0022460X13009000.

[9] Le TD, Ahn KK. A vibration isolation system in low frequency excitation region using negative stiffness structure for vehicle seat. Journal of Sound and Vibration. 2011;.

[10] Le TD, Ahn KK. Experimental investigation of a vibration isolation system using negative stiffness structure. International Journal of Mechanical Sciences. 2013;70:99–112. Available from: http://dx.doi.org/10.1016/j.ijmecsci.2013.02.009.

[11] Le TD, Nguyen PT. Dynamic simulation of seat suspension system with virtual prototyping technology. Journal of Advanced Mechanical Design, Systems, and Manufacturing. 2017; 11(5):1–11.

[12] Le TD, Nguyen VAD. Low frequency vibration isolator with adjustable configurative parameter. International Journal of Mechanical Sciences. 2017;134(September 2016):224–233.

[13] Yan Z, Zhu B, Li X, et al. Modeling and analysis of static and dynamic characteristics of nonlinear seat suspension for off-road vehicles. Shock and Vibration. 2015;2015.

[14] Antoniadis I, Chronopoulos D, Spitas V, et al. Hyper-damping properties of a stiff and stable linear oscillator with a negative stiffness element. Journal of Sound and Vibration. 2015;.

[15] Antoniadis IA, Kanarachos SA, Gryllias K, et al. KDamping: A stiffness based vibration absorption concept. JVC/Journal of Vibration and Control. 2016;24(3):588–606.

[16] Tyan F, Hong YF, Tu SH, et al. Generation of random road profiles. Journal of Advanced Engineering. 2009;4(2):151–156.

[17] Koulocheris D, Papaioannou G, Chrysos E. A comparison of optimal semi-active suspension systems regarding vehicle ride comfort. IOP Conference Series: Materials Science and Engineering. 2017;252(1).

[18] Faris WF, BenLahcene Z, Hasbullah F. Ride quality of passenger cars: an overview on the research trends. International Journal of Vehicle Noise and Vibration. 2012;8(3):185. Available from: http://www.inderscience.com/link.php?id=48169.

[19] Papaioannou G, Dineff AM, Koulocheris D. Comparative study of different vehicle models with respect to their dynamic behavior. International Journal of Automotive and Mechanical Engineering. 2019;(FOR PUBLICATION).

[20] Cao D, Song X, Ahmadian M. Editors' perspectives: Road vehicle suspension design, dynamics, and control. Vehicle System Dynamics. 2011;.

[21] Koulocheris D, Papaioannou G. Dynamic analysis of the suspension system of a heavy vehicle through experimental and simulation procedure. In: 25th JUMV International Automotive Conference "Science and Motor Vehicles"; Vol. 13; 2015. p. 187–199.

[22] Koulocheris D, Papaioannou G. Experimental evaluation of the vertical wheel loads of a heavy vehicle validated with an optimized half car model. In: 11th HSTAM International Congress on Mechanics; 2016. p. 27–30.

[23] Koulocheris D, Papaioannou G, Christodoulou D. Multi-objective optimization of a heavy vehicle nonlinear suspension system. In: 11th HSTAM International Congress on Mechanics; 2016. p. 27–30.

[24] Koulocheris D, Papaioannou G, Christodoulou D. An approach for multi-objective optimization of vehicle suspension system. IOP Conference Series: Materials Science and Engineering. 2017;252. Available from: http://stacks.iop.org/1757-899X/252/i=1/a=012037?key=crossref.b5b8d118209e69517acffe2a3afe5a0a.

[25] Koulocheris D, Papaioannou G, Christodoulou D. Optimal design solution among pareto alternatives for vehicle nonlinear suspension system. In: 26th JUMV International Automotive Conference "Science and Motor Vehicles"; Vol. 15; 2017. p. 174–188.

[26] Koulocheris D, Papaioannou G, Christodoulou D. Assessment of the optimization procedure for the nonlinear suspension system of a heavy vehicle. International Journal for Vehicle Mechanics, Engines and Transportation Systems. 2016;42(2):19–35.

[27] Papaioannou G, Koulocheris D. An approach for minimizing the number of objective functions in the optimization of vehicle suspension systems. Journal of Sound and Vibration. 2018 nov;435:149–169. Available from: https://linkinghub.elsevier.com/retrieve/pii/S0022460X1830508X.

[28] Alkhatib R, Jazar GN, Golnaraghi MF. Optimal design of passive linear suspension using genetic algorithm. Journal of Sound and Vibration. 2004;275(3-5):665–691.

[29] Silveira M, Pontes BR, Balthazar JM. Use of nonlinear asymmetrical shock absorber to improve comfort on passenger vehicles. Journal of Sound and Vibration. 2014;333:2114–2129. Available from: https://ac.els-cdn.com/S0022460X13010195/1-s2.0-S0022460X13010195-main.pdf?{_}tid=b03d71d4-5b39-4be3-bf74-69d455d84c73{&}acdnat=1524994102{_}f268e6a1d932818733deef7dc637f543.

[30] Gadhvi B, Savsani V, Patel V. Multi-Objective Optimization of Vehicle Passive Suspension System Using NSGA-II, SPEA2 and PESA-II. Procedia Technology. 2016;23:361–368. Available from: http://linkinghub.elsevier.com/retrieve/pii/S2212017316300391.

[31] Pollini NO, Lavan O, Amir O. Adjoint sensitivity analysis and optimization of hysteretic dynamic systems with nonlinear viscous dampers. Structural and Multidisciplinary Optimization. 2017;.

[32] Ahmadian M. On the isolation properties of semiactive dampers. Journal of Vibration and Control. 1999;5(2):217–232.

[33] Ihsan SI, Faris WF, Ahmadian M. Analysis of control policies and dynamic response of a Q-car 2-DOF semi active system. Shock and Vibration. 2008;15(5):573–582. Available from: http://iospress.metapress.com/content/T088743X6NJ5N420.

[34] Ihsan SI, Ahmadian M, Faris WF, et al. Ride performance analysis of half-car model for semi-active system using RMS as performance criteria. Shock and Vibration. 2009;16(6):593–605.

[35] Do AL, Sename O, Dugard L, et al. An Extension of Mixed Sky-hook and ADD to Magneto-Rheological Dampers. In: 4th IFAC Symposium on System, Structure and Control; 2010.

[36] Sharp RS, Crolla DA. Road Vehicle Suspension System Design - a review. Vehicle System Dynamics. 1987;16(3):167–192.

[37] Hrovat D, Margolis DL, Hubbard M. An Approach Toward the Optimal Semi-Active Suspension. Journal of Dynamic Systems, Measurement, and Control. 1988;110(3):288.

[38] Tseng HE, Hrovat D. State of the art survey: active and semi-active suspension control. Vehicle System Dynamics. 2015 jul;53(7):1034–1062. Available from: http://www.tandfonline.com/doi/full/10.1080/00423114.2015.1037313.

[39] Čorić M, Deur J, Kasać J, et al. Optimisation of active suspension control inputs for improved vehicle handling performance. Vehicle System Dynamics. 2016;54(11):1574–1600. Available from: https://doi.org/10.1080/00423114.2016.1177655.

[40] Čorić M, Deur J, Xu L, et al. Optimisation of active suspension control inputs for improved vehicle ride performance. Vehicle System Dynamics. 2016;54(7):1004–1030. Available from: http://www.tandfonline.com/action/journalInformation?journalCode=nvsd20.

[41] Jalili N, Esmailzadeh E. Optimum Active Vehicle Suspensions With Actuator Time Delay. Journal of Dynamic Systems, Measurement, and Control. 2001;123(1):54. Available from: http://dynamicsystems.asmedigitalcollection.asme.org/article.aspx?articleid=1408825.

[42] Bouazara M, Richard MJ. An optimization method designed to improve 3-D vehicle comfort and road holding capability through the use of active and semi-active suspensions. European Journal of Mechanics, A/Solids. 2001;20(3):509–520.

[43] Bouazara M, Richard MJ, Rakheja S. Safety and comfort analysis of a 3-D vehicle model with optimal non-linear active seat suspension. Journal of Terramechanics. 2006;43:97–118. Available from: www.elsevier.com/locate/jterra.

[44] Nguyen QH, Choi SB, Park YG. An analytical approach to optimally design of electrorheological fluid damper for vehicle suspension system. Meccanica. 2012;47:1633–1647. Available from: http://www.ssslab.com.

[45] Prabakar RS, Sujatha C, Narayanan S. Optimal semi-active preview control response of a half car vehicle model with magnetorheological damper. Journal of Sound and Vibration. 2009;.

[46] Prabakar RS, Sujatha C, Narayanan S. Response of a quarter car model with optimal magnetorheological damper parameters. Journal of Sound and Vibration. 2013;.

[47] Ahmadian M, Simon DE. An Analytical and Experimental Evaluation of Magneto Rheological Suspensions for Heavy Trucks. Vehicle System Dynamics. 2002;37:38–49. Available from: http://www.tandfonline.com/action/journalInformation?journalCode=nvsd20.

[48] Ahmadian M, Sandu C. An experimental evaluation of magneto-rheological front fork suspensions for motorcycle applications. International Journal of Vehicle Systems Modelling and Testing. 2008;3(4):296–311. Available from: http://dx.doi.org/10.1504/IJVSMT.2008.025405.

[49] Ahmadian M. Magneto-rheological suspensions for improving ground vehicle's ride comfort, stability, and handling. Vehicle System Dynamics. 2017;55(10):1618–1642. Available from: https://doi.org/10.1080/00423114.2017.1323106.

[50] Papaioannou G, Koulocheris D. Optimization of skyhook control strategies and an alterna-tive approach for the operational conditions. In: Proceedings of ISMA2018 and USD2018; Leuven, Belgium; 2018. Available from: http://past.isma-isaac.be/downloads/isma2018/proceedings/Contribution{_}372{_}proceeding{_}3.pdf.

[51] Papaioannou G, Koulocheris D. Multi-objective optimization of semi-active suspension systems using KEMOGA algorithm. Engineering Science and Technology, an International Journal. 2019;(FOR PUBLICATION). Available from: http://dx.doi.org/10.1016/j.jestch.2015.07.004.

[52] Beard GF, Griffin MJ. Discomfort of seated persons exposed to low frequency lateral and roll oscillation: Effect of backrest height. Applied Ergonomics. 2016 may;54:51–61. Available from: https://www.sciencedirect.com/science/article/pii/S0003687015301101?via{%}3Dihub.

[53] Mansfield NJ, Mackrill J, Rimell AN, et al. Combined Effects of Long-Term Sitting and Whole-Body Vibration on Discomfort Onset for Vehicle Occupants. ISRN Automotive Engineering. 2014 jan;2014:1–8. Available from: https://www.hindawi.com/archive/2014/852607/.

[54] Gündoğdu Ö. Optimal seat and suspension design for a quarter car with driver model using genetic algorithms. International Journal of Industrial Ergonomics. 2007;37(4):327–332.

[55] Maciejewski I, Meyer L, Krzyzynski T. Modelling and multi-criteria optimisation of passive seat suspension vibro-isolating properties. Journal of Sound and Vibration. 2009;.

[56] Maciejewski I, Kiczkowiak T, Krzyzynski T. Application of the Pareto-optimal approach for selecting dynamic characteristics of seat suspension systems. Vehicle System Dynamics. 2011;49(12). Available from: http://www.tandfonline.com/action/journalInformation?journalCode=nvsd20.

[57] Abbas W, Emam A, Badran S. Optimal Seat and Suspension Design for a Half-Car with Driver Model Using Genetic Algorithm. Intelligent Control and Automation. 2013;4(May):199–205. Available from: http://www.scirp.org/journal/PaperInformation.aspx?paperID=31745.

[58] Rahman MS, Kibria KMG. Investigation of vibration and ride characteristics of a five degrees of freedom vehicle suspension system. Procedia Engineering. 2014;90:96–102.

[59] Drehmer LRC, Paucar Casas WJ, Gomes HM. Parameters optimisation of a vehicle suspension system using a particle swarm optimisation algorithm. Vehicle System Dynamics. 2015;53(4):449–474.

[60] Shangguan WB, Shui Y, Rakheja S. Kineto-dynamic design optimisation for vehicle-specific seat-suspension systems. Vehicle System Dynamics. 2017;55(11):1643–1664. Available from: http://www.tandfonline.com/action/journalInformation?journalCode=nvsd20.

[61] Haiping Du, Weihua Li, Nong Zhang. Integrated Seat and Suspension Control for a Quarter Car With Driver Model. IEEE Transactions on Vehicular Technology. 2012 nov;61(9):3893–3908. Available from: http://ieeexplore.ieee.org/document/6263316/.

[62] Yao HJ, Fu J, Yu M, et al. Semi-active H control of seat suspension with MR damper. Journal of Physics: Conference Series. 2013;412(1).

[63] Segla S, Trišović N. Optimization of Semi-active Seat Suspension. American Journal of Mechanical Engineering. 2013;1(10):221–225. Available from: http://pubs.sciepub.com/ajme/1/7/14.

[64] Ning D, Sun S, Zhang J, et al. An active seat suspension design for vibration control of heavy-duty vehicles. Journal of Low Frequency Noise, Vibration and Active Control. 2016;.

[65] Papaioannou G, Voutsinas A, Koulocheris D, et al. Dynamic performance analysis of vehicle seats with embedded negative stiffness elements. Vehicle System Dynamics. 2019;(FOR PUBLICATION).

[66] Papaioannou G, Voutsinas A, Koulocheris D. Optimal design of passenger vehicle seats with the use of negative stiffness elements. Proc IMechE Part D : Journal of Automobile Engineering. 2019;(FOR PUBLICATION).

[67] Barethiye VM, Pohit G, Mitra A. Analysis of a quarter car suspension system based on non-linear shock absorber damping models. International Journal of Automotive and Mechanical Engineering. 2017;.

[68] Ahmadian M, Vahdati N. Transient dynamics of semiactive suspensions with hybrid control. Journal of Intelligent Material Systems and Structures. 2006;.

[69] Shirahatti A, Prasad P, Panzade P, et al. Optimal design of passenger car suspension for ride and road holding. Journal of the Brazilian Society of Mechanical Sciences and Engineering. 2008;30(1):66–76. Available from: http://www.scielo.br/scielo.php?script=sci{_}arttext{&}pid=S1678-58782008000100010{&}lng=en{&}nrm=iso{&}tlng=en.

[70] Gobbi M, Papalambros P. Optimization of Ground Vehicle Systems. Vehicle System Dynamics. 2013;43(6):241–261. Available from: http://dx.doi.org/10.1201/b15560-10.

[71] Seifi A, Hassannejad R, Hamed MA. Optimum design for passive suspension system of a vehicle to prevent rollover and improve ride comfort under random road excitations. Proceedings of the Institution of Mechanical Engineers, Part K: Journal of Multi-body Dynamics. 2016;230(4):426–441. Available from: http://journals.sagepub.com/doi/10.1177/1464419315618034.

[72] Shim T, Ghike C. Understanding the limitations of different vehicle models for roll dynamics studies. Vehicle System Dynamics. 2007;45(3):191–216.

[73] Shim T, Velusamy PC. Improvement of vehicle roll stability by varying suspension properties. Vehicle System Dynamics. 2011;49(1-2):129–152.

[74] Cao J, Li P, Liu H. An interval fuzzy controller for vehicle active suspension systems. IEEE Transactions on Intelligent Transportation Systems. 2010;.

[75] Faris WF, Ihsan SI, Ahmadian M. Transient and steady state dynamic analysis of passive and semi-active suspension systems using half-car model. International Journal of Modelling, Identification and Control. 2009;6(1):62. Available from: http://www.inderscience.com/link.php?id=23531.

[76] Ihsan SI, Faris WF, Ahmadian M. Dynamics and control policies analysis of semi-active suspension systems using a full-car model. Int J Vehicle Noise and Vibration J Vehicle Noise and Vibration. 2007;3(4):370–405.

[77] Karnopp D, Crosby MJ, Harwood RA. Vibration Control Using Semi-Active Force Generators. Journal of Engineering for Industry. 1974 may;96(2):619. Available from: http://manufacturingscience.asmedigitalcollection.asme.org/article.aspx?articleid=1443734.

[78] Sammier D, Sename O, Dugard L. Skyhook and H∞ Control of Semi-active Suspensions: Some Practical Aspects. Vehicle System Dynamics. 2003;39(4):279–308. Available from: http://www.tandfonline.com/doi/abs/10.1076/vesd.39.4.279.14149.

[79] Savaresi SM, Silani E, Bittanti S. Acceleration-Driven-Damper (ADD): An Optimal Control Algorithm For Comfort-Oriented Semiactive Suspensions. Journal of Dynamic Systems, Measurement, and Control. 2005 jun;127(2):218. Available from: http://dynamicsystems.asmedigitalcollection.asme.org/article.aspx?articleid=1410764.

[80] Savaresi SM, Spelta C. Mixed Sky-Hook and ADD: Approaching the Filtering Limits of a Semi-Active Suspension. Journal of Dynamic Systems, Measurement, and Control. 2007; 129(4):382. Available from: http://dynamicsystems.asmedigitalcollection.asme.org/article.aspx?articleid=1412349.

[81] Savaresi SM, Spelta C. A Single-Sensor Control Strategy for Semi-Active Suspensions. IEEE Transactions on Control Systems Technology. 2009 jan;17(1):143–152. Available from: http://ieeexplore.ieee.org/document/4729738/.

[82] Van Der Sande TP, Besselink IJ, Nijmeijer H. Rule-based control of a semi-active suspension for minimal sprung mass acceleration: Design and measurement. Vehicle System Dynamics. 2016;54(3):281–300.

[83] Nie S, Zhuang Y, Liu W, et al. A semi-active suspension control algorithm for vehicle comprehensive vertical dynamics performance. Vehicle System Dynamics. 2017;55(8):1099–1122. Available from: https://doi.org/10.1080/00423114.2017.1299871.

[84] Fischer D, Isermann R. Mechatronic semi-active and active vehicle suspensions. Control Engineering Practice. 2004;12:1353–1367. Available from: https://ac.els-cdn.com/S0967066103001771/1-s2.0-S0967066103001771-main.pdf?{_}tid=8b80a432-6fb1-4be7-a540-e9775d2605fe{&}acdnat=1525174232{_}407b20131c06f21f90505c075ed58e0b.

[85] Akutain XC, Vinolas J, Savall J, et al. Comparing the performance and limitations of semi-active suspensions. International Journal of Vehicle Systems Modelling and Testing. 2007;2(3):296–314. Available from: https://pdfs.semanticscholar.org/3a60/4b9d240f89cf5150ec60f90b63fcbe74d898.pdf.

[86] Poussot-Vassal C, Spelta C, Sename O, et al. Survey on Some Automotive Semi-Active Suspension Control Methods : a Comparative Study on a Single-Corner Model. Vol. 44. IFAC; 2011. Available from: http://dx.doi.org/10.3182/20110828-6-IT-1002.00446.

[87] Colina A, Lerma G, Cabanes I, et al. New Advances in Mechanisms, Transmissions and Applications. In: Proceedings of the 2nd New Advances in Mechanisms, Transmissions

and Applications; Vol. 17; 2014. Available from: http://link.springer.com/10.1007/978-94-007-7485-8.

[88] Smith MC, Swift SJ. Power dissipation in automotive suspensions. Vehicle System Dynamics. 2011;49:59–74.

[89] Crews JH, Mattson MG, Buckner GD. Multi-objective control optimization for semi-active vehicle suspensions. Journal of Sound and Vibration. 2011;330(23):5502–5516. Available from: http://dx.doi.org/10.1016/j.jsv.2011.05.036.

[90] Eslaminasab N, Vahid A O, Golnaraghi F. Nonlinear analysis of switched semi-active controlled systems. Vehicle System Dynamics. 2011;49(1-2):291–309.

[91] Tsampardoukas G, Stammers CW, Guglielmino E. Hybrid balance control of a magnetorheological truck suspension. Journal of Sound and Vibration. 2008;317(3-5):514–536.

[92] Tsampardoukas G, Stammers CW, Guglielmino E. Semi-active control of a passenger vehicle for improved ride and handling. Proceedings of the Institution of Mechanical Engineers, Part D: Journal of Automobile Engineering. 2008;222(3):325–352.

[93] Ahmadian M, Song X, Southward SC. No-Jerk Skyhook Control Methods for Semi-active Suspensions. Journal of Vibration and Acoustics. 2004;126(4):580. Available from: http://vibrationacoustics.asmedigitalcollection.asme.org/article.aspx?articleid=1470711.

[94] Liu Y, Waters TP, Brennan MJ. A comparison of semi-active damping control strategies for vibration isolation of harmonic disturbances. Journal of Sound and Vibration. 2005;280(1-2):21–39.

[95] Margolis DL, Goshtasbpour M. The Chatter of Semi-Active On-Off Suspensions and its Cure. Vehicle System Dynamics. 1984;13(3):129–144.

[96] International Organization for Standardization. Mechanical vibration and shock- Evaluation of human exposure to whole-body vibration - Part 1 : General requirements, ISO 2631-1 : 1997, 1997; 1997.

[97] Crolla DA, Abouel Nour AM. Power losses in active and passive suspensions of off-road vehicles. Journal of Terramechanics. 1992;29(1):83–93.

[98] Karnopp D. Power Requirements for Traversing Uneven Roadways. Vehicle System Dynamics. 1978;7(3):135–152.

[99] Kuznetsov A, Mammadov M, Sultan I, et al. Optimization of a quarter-car suspension model coupled with the driver biomechanical effects. Journal of Sound and Vibration. 2011;330(12):2937–2946. Available from: http://dx.doi.org/10.1016/j.jsv.2010.12.027.

[100] Sun L, Cai X, Yang J. Genetic algorithm-based optimum vehicle suspension design using minimum dynamic pavement load as a design criterion. Journal of Sound and Vibration. 2007; 301(1-2):18–27.

[101] Nariman-Zadeh N, Salehpour M, Jamali A, et al. Pareto optimization of a five-degree of freedom vehicle vibration model using a multi-objective uniform-diversity genetic algorithm (MUGA). Engineering Applications of Artificial Intelligence. 2010;23(4):543–551. Available from: http://dx.doi.org/10.1016/j.engappai.2009.08.008.

[102] Moradi A, Nafchi AM, Ghanbarzadeh A, et al. Optimization of linear and nonlinear full vehicle model for improving ride comfort vs. road holding with the bees algorithm. In: 2011 IEEE Colloquium on Humanities, Science and Engineering, CHUSER 2011; 2011. p. 17–22. Available from: http://ieeexplore.ieee.org/lpdocs/epic03/wrapper.htm?arnumber=6163712.

[103] Nagarkar MP, Vikhe Patil GJ, Zaware Patil RN. Optimization of nonlinear quarter car suspension–seat–driver model. Journal of Advanced Research. 2016;7(6):991–1007.

[104] Nagarkar M, Bhalerao Y, Patil GV, et al. Multi-Objective Optimization of Nonlinear Quarter Car Suspension System - PID and LQR Control. In: Procedia Manufacturing; 2018.

[105] Marler RT, Arora JS. Survey of multi-objective optimization methods for engineering Maximum objective function values. Structural and Multidisciplinary Optimization. 2004;26:369–395. Available from: https://link.springer.com/content/pdf/10.1007{%}2Fs00158-003-0368-6.pdf.

[106] Konak A, Coit DW, Smith AE. Multi-objective optimization using genetic algorithms: A tutorial. Reliability Engineering and System Safety. 2006;.

[107] Gobbi M, Levi F, Mastinu G. Multi-objective stochastic optimisation of the suspension system of road vehicles. Journal of Sound and Vibration. 2006;298(4-5):1055–1072.

[108] Gobbi M. A k, k-ε optimality selection based multi objective genetic algorithm with applications to vehicle engineering. Optimization and Engineering. 2013;14(2):345–360.

[109] Das I. A preference ordering among various Pareto optimal alternatives. Structural Optimization. 1999;18(1):30–35. Available from: http://link.springer.com/10.1007/BF01210689.

[110] Taboada HA, Coit DW. Multi-objective scheduling problems: Determination of pruned Pareto sets. IIE Transactions (Institute of Industrial Engineers). 2008;.

[111] Venkat V, Jacobson SH, Stori JA. A Post-Optimality Analysis Algorithm for Multi-Objective Optimization. Computational Optimization and Applications. 2004;28:357–372.

[112] Zhu Y, Dopico D, Sandu C, et al. Dynamic Response Optimization of Complex Multibody Systems in a Penalty Formulation Using Adjoint Sensitivity. Journal of Computational and Nonlinear Dynamics. 2015;10.

[113] Lee CM, Goverdovskiy VN. A multi-stage high-speed railroad vibration isolation system with "negative" stiffness. Journal of Sound and Vibration. 2011;331:914–921. Available from: https://ac.els-cdn.com/S0022460X11007541/1-s2.0-S0022460X11007541-main.pdf?{_}tid=ef99fc39-f74d-4c2b-8c1a-1b6240746961{&}acdnat=1531901568{_}7449fdf7c238d41698aac7d44cf205c3.

[114] Lee CM, Goverdovskiy VN, Sotenko AV. Helicopter vibration isolation: Design approach and test results. Journal of Sound and Vibration. 2016;366:15–26. Available from: https://ac.els-cdn.com/S0022460X15006999/1-s2.0-S0022460X15006999-main.pdf?{_}tid=398c5a7c-8c7e-4646-b778-ab9cf80e67aa{&}acdnat=1531901680{_}0db36ad811c324dc3ca6064e9fa330cf.

[115] Wang X, Liu H, Chen Y, et al. Beneficial stiffness design of a high-static-low-dynamic-stiffness vibration isolator based on static and dynamic analysis. International Journal of Mechanical Sciences. 2018 jul;142-143:235–244. Available from: http://linkinghub.elsevier.com/retrieve/pii/S002074031733223X.

[116] Zhou J, Wang X, Xu D, et al. Nonlinear dynamic characteristics of a quasi-zero stiffness vibration isolator with cam-roller-spring mechanisms. Journal of Sound and Vibration. 2015; 346(1):53–69. Available from: http://dx.doi.org/10.1016/j.jsv.2015.02.005.

[117] Zhao L, Zhou C, Yu Y, et al. Hybrid modelling of driver seat-cushion coupled system for metropolitan bus. Journal of Low Frequency Noise, Vibration and Active Control. 2017; 36(3):214–226.

[118] Kim JH, Marin LS, Dennerlein JT. Evaluation of commercially available seat suspensions to reduce whole body vibration exposures in mining heavy equipment vehicle operators. Applied Ergonomics. 2018 sep;71:78–86. Available from: http://linkinghub.elsevier.com/retrieve/pii/S0003687018300899.

[119] Antoniadis I, Kyriakopoulos K, Papadopoulos E. Hyper-Damping Behavior of Stiff and Stable Oscillators with Embedded Statically Unstable Stiffness Elements. International Journal of Structural Stability and Dynamics. 2017;17(5):1–15.

[120] Sapountzakis E, Syrimi P, Pantazis I, et al. KDamper concept in seismic isolation of bridges with flexible piers. Engineering Structures. 2017 dec;153:525–539. Available from: https://linkinghub.elsevier.com/retrieve/pii/S0141029616305004.

[121] Huang X, Su Z, Hua H. Application of a dynamic vibration absorber with negative stiffness for control of a marine shafting system. Ocean Engineering. 2018 may;155:131–143. Available from: https://www.sciencedirect.com/science/article/pii/S0029801818301963.

[122] Chronopoulos D, Antoniadis I, Collet M, et al. Enhancement of wave damping within metamaterials having embedded negative stiffness inclusions. Wave Motion. 2015;58:165–179. Available from: http://dx.doi.org/10.1016/j.wavemoti.2015.05.005.

[123] Liang CC, Chiang CF. Modeling of a Seated Human Body Exposed to Vertical Vibrations in Various Automotive Postures. Industrial Health. 2008;46(2):125–137. Available from: http://joi.jlc.jst.go.jp/JST.JSTAGE/indhealth/46.125?from=CrossRef.

[124] Antoniadis IA, Sapountzakis IE, Design M, et al. Base acceleration absorption of structures using the KDAMPER. In: 11th HSTAM International Congress on Mechanics; 2016. p. 27–30.

[125] Abbas W, Abouelatta OB, El-azab MS, et al. Application of genetic algorithms to the Optimal Design of Vehicle's Driver - seat Suspension Model. Proceedings of the World Congress on Engineering. 2010;II.

[126] Demic M, Lukic J, Milic Ž. Some Aspects of the Investigation of Random Vibration Influence on Ride Comfort. Journal of Sound and Vibration. 2002;253(1):109–128. Available from: http://linkinghub.elsevier.com/retrieve/pii/S0022460X0194252X.

[127] Wang W, Rakheja S, Boileau PÉ. Relationship between measured apparent mass and seat-to-head transmissibility responses of seated occupants exposed to vertical vibration. Journal of Sound and Vibration. 2008 jul;314(3-5):907–922. Available from: https://www.sciencedirect.com/science/article/pii/S0022460X08000461.

[128] Rahmatalla S, DeShaw J. Effective seat-to-head transmissibility in whole-body vibration: Effects of posture and arm position. Journal of Sound and Vibration. 2011 dec; 330(25):6277–6286. Available from: https://www.sciencedirect.com/science/article/pii/S0022460X11006158.

[129] Tufano S, Griffin MJ. Nonlinearity in the vertical transmissibility of seating: the role of the human body apparent mass and seat dynamic stiffness. Vehicle System Dynamics. 2013;51(1):122–138. Available from: http://www.tandfonline.com/action/journalInformation?journalCode=nvsd20.

[130] Georgiou G, Verros G, Natsiavas S. Multi-objective optimization of quarter-car models with a passive or semi-active suspension system. Vehicle System Dynamics. 2007;45(1):77–92.

[131] Rao KD. Modeling, simulation and control of semi active suspension system for automobiles under MATLAB Simulink using PID controller. In: IFAC Proceedings Volumes (IFAC-

PapersOnline); Vol. 3. IFAC; 2014. p. 827–831. Available from: http://dx.doi.org/10.3182/20140313-3-IN-3024.00094.

[132] Hu Y, Chen MZ, Sun Y. Comfort-oriented vehicle suspension design with skyhook inerter configuration. Journal of Sound and Vibration. 2017;405:34–47. Available from: http://dx.doi.org/10.1016/j.jsv.2017.05.036.

[133] International Organization for Standardization. Mechanical vibration-Road surface profiles-Reporting of measured data; 1995. Available from: https://www.iso.org/standard/71202.html.

[134] Andren P. Power spectral density approximations of longitudinal road profiles. International Journal of Vehicle Design. 2006;40.

[135] Poussot-Vassal C, Savaresi SM, Spelta C, et al. A methodology for optimal semi-active suspension systems performance evaluation. Decision and Control CDC 2010 49th IEEE Conference on. 2010;:2892–2897Available from: http://ieeexplore.ieee.org/lpdocs/epic03/wrapper.htm?arnumber=5718058.

[136] Walck C, Group PP. Hand-book on statistical contributions for experimentalists. 2007;(September):26–35. Available from: http://www.stat.rice.edu/{~}dobelman/textfiles/DistributionsHandbook.pdf.

[137] Poussot-Vassal C, Spelta C, Sename O, et al. Survey and performance evaluation on some automotive semi-active suspension control methods: A comparative study on a single-corner model. Annual Reviews in Control. 2012;36:148–160. Available from: https://ac.els-cdn.com/S1367578812000120/1-s2.0-S1367578812000120-main.pdf?{_}tid=022eb900-a557-43fb-8d07-d3bff3bbaf11{&}acdnat=1530537430{_}8696c88a8122517763ee1dbeba0b2a05.

[138] Valášek M, Novák M, Šika Z, et al. Extended Ground-Hook-New Concept of Semi-Active Control of Truck's Suspension. Vehicle System Dynamics. 1997;27:289–303. Available from: http://www.tandfonline.com/action/journalInformation?journalCode=nvsd20.

[139] Goncalves FD, Ahmadian M. A Hybrid Control Policy for Semi-Active Vehicle Suspensions. Shock and Vibration. 2003;10(1):59–69. Available from: http://www.hindawi.com/journals/sv/2003/897173/abs/.

[140] Sankaranarayanan V, Oncu S, Ozcan D, et al. Vehicle Chassis Control Using Adaptive Semi-Active Suspension. IFAC Proceedings Volumes. 2008;41:4677–4682.

[141] Carrillo VM, Aguirre O, Taboada H. Applications and performance of the non-numerical ranking preferences method for post-Pareto optimality. Procedia Computer Science. 2011;6:243–248. Available from: http://dx.doi.org/10.1016/j.procs.2011.08.045.

[142] Porter JM, Gyi DE, Tait HA. Interface pressure data and the prediction of driver discomfort in road trials. Applied Ergonomics. 2003;34:207–214. Available from: https://ac.els-cdn.com/S0003687003000097/1-s2.0-S0003687003000097-main.pdf?{_}tid=880613b1-b36e-4b4d-bf95-48d14007b24f{&}acdnat=1533474302{_}974d51eda976dc350e2bf87cca02ec60.

[143] Gyi DE, Porter J. Interface pressure and the prediction of car seat discomfort. Applied Ergonomics. 1999 apr;30(2):99–107. Available from: https://www.sciencedirect.com/science/article/pii/S0003687098000180.

[144] Kolich M. Automobile seat comfort: occupant preferences vs. anthropometric accommodation; 2003. Available from: https://ac.els-cdn.com/S0003687002001424/1-s2.0-S0003687002001424-main.pdf?{_}tid=be8e7392-becb-42ec-a037-df228f97cf11{&}acdnat=1533477748{_}a5dbc12ecc6b1cbbe0b1a98beaf62b57.

[145] Sammonds GM, Fray M, Mansfield NJ. Effect of long term driving on driver discomfort and its relationship with seat fidgets and movements (SFMs). Applied Ergonomics. 2017;.

[146] Le TD, Bui MTN, Ahn KK. Improvement of Vibration Isolation Performance of Isolation System Using Negative Stiffness Structure. IEEE/ASME Transactions on Mechatronics. 2016; 21(3):1561–1571.